UNIVERSIDAD
DE GRANADA

Instituto de Astrofísica de Andalucía,
Consejo Superior de Investigaciones Científicas
(IAA-CSIC)

Characterization of exo-atmospheres with transmission spectroscopy

Thesis submited by Alejandro Sánchez López
For the degree of Doctor of Philosophy

Supervisors: Manuel López Puertas
and Bernd Funke

Programa de Doctorado
en Física y Ciencias del Espacio Granada, September 2019

Editor: Universidad de Granada. Tesis Doctorales
Autor: Alejandro Sánchez López
ISBN: 978-84-1306-393-5
URI: http://hdl.handle.net/10481/58360

Dedicado a mi familia

Alejandro

Agradecimientos

Un doctorado no es cosa menor. Dicho de otra manera: es cosa mayor. Quiero decir que es complicado mantener la salud mental durante estos cuatro años y, no nos vamos a engañar, no empecé cuerdo, pero tampoco acabo sano. Aunque creo que sí algo más sesudo. Probablemente el reto más grande fue empezar casi de cero, ya que no había una línea de investigación en atmósferas de exoplanetas en el Instituto de Astrofísica de Andalucía. Así, creo que mi paso de estudiante a aprendiz de investigador tuvo una curva de dificultad un tanto empinada. Es por ello que tengo que dar las gracias a las personas encargadas de la dirección de este viaje: mis supervisores Manuel López Puertas y Bernd Funke. Ambos orientaron esta tesis en la buena dirección cuando yo no era capaz de hacerlo. Creo que, al final, hemos conseguido construir una nave de último modelo capaz de moverse por esta burbuja exoplanetaria, que no deja de crecer.

Por supuesto, muchas gracias al resto de componentes del Grupo de Amósferas Planetarias Terrestres (Miguel Ángel, Maya, Francisco, Sergio y María José) por las charlas, los consejos y, en general, por la formación. De la misma manera, he de agradecer a Pedro Amado todo el tiempo que me ha dedicado y el entusiasmo que ha demostrado por el desarrollo de este trabajo. Igualmente, esta tesis es mejor gracias a la compañía en el IAA durante parte o todo este viaje de Aythami (durante la primera y crucial semana), Clara, Zaira, Manuel Lampón y Agor.

During the second year of my travels I stayed in Leiden for a few months and this ship acquired one of its most powerful tools. I have to say a big Thank you to Professor Ignas Snellen, Javi and both Pauls (Mollière and Wilson) for their hospitality during the cold Dutch autumn. You integrated me from the very first day, taught me a lot, and created an environment in which I believe I made a giant leap forward. And all of it among great laughs! In the end, that CCF peak grew.

Speaking of Leiden, this thesis is dedicated to the over-an-hour walk from my room in Warmond to the Leiden observatory, to the croquette spread on bread, to the boats over my head, and to the regrettably huge hamburger near

the Nieuwe Rijn. Oh, and before I forget... Most specially, this thesis is dedicated to Peter, the spider that perched on the most perfect web I have ever witnessed outside of my window for three months. Rest in pieces, Parker. The snow took you and I shall not pity you.

Gracias familia por patrocinarme todos estos años, en particular desde que nací. Los artículos y eso están bien, pero el combustible de esta tesis son el apoyo incondicional, el arroz caldoso, los 200 duros que se gastaron en enseñarme, el cocido, escuchar mis ataques de histeria, la paella, quizá otro ataque de histeria, las gachas manchegas y, a quien vamos a engañar, esto es realmente una excusa para, públicamente, mentar qué comidas me gustan. ¡Así da gusto!

Esta tesis de seguro no sería posible sin la gente que he conocido en Granada durante este lustro (o antes): Sam, Pablo Aldana, José Felixiano, Pablo Villegas, David, Claudia, Cristina... Hemos vivido, viciado, desahogado y comido juntos mucho. Ojalá poner un Comedores UGR en cada ciudad, pueblo, villa o asentamiento temporal de esta canica azul. También gracias a la gente de fuera, especialmente a Marco. ¿Qué te voy a decir? Hemos derrotado a Atheon, Crota, Oryx, Aksis y casi le zurramos a Calus. Por no hablar de las incontables horas de vuelo por la Vía Láctea. Las escuadras no se olvidan. En general, gente, una buena parte de esta tesis es también vuestra.

Y colorín colorado este cuento se ha acabado. Once años en Granada llegan a su fin. Si tuviese que quedarme con algo de todo esto, nunca escogería las tapas antes que a ti Ana. Esto es más obra tuya que mía. Bueno, en realidad no, pero ya sabes por dónde voy. Me salvaste la vida cuando acabé enterrado bajo varios gramos de nieve en Holanda y con una maleta llena de comida (oh, gracias Salmorejo por tu contribución a este trabajo). Es más, me protegiste de un lunar malicioso y de cuando me quedé ciego y perdí la voz un par de veces. ¡Eternamente agradecidos! Para cuando leas esto, ya serás Doctora en física estadística y, además, especializada en redes neuronales, así que cuento contigo para diseñar la IA de nuestra nave. Eyes up, guardian!

I am also grateful for financial support from the spanish Ministerio de Ciencia e Innovación and Ministerio de Economía y Competitividad, the Fondo Europeo de Desarrollo Regional (FEDER/ERF), the Agencia Estatal de Investigación, and the Fondo Social Europeo under grants BES-2015-073500, ESP2014-54362-P and ESP2017-87143-R.

Preface

"The exploration of the cosmos is a voyage of self-discovery."

Carl Sagan

This thought, finding unimaginably far away the answers to the questions of our world, is the surprising result of countless (and not myopic) primates that turned their gaze to the stars. In essence, the search and characterization of new planets, hosted by the myriad stars surrounding us, is driven by an unstoppable desire to be contextualized.

This idea is also at the foundation of this thesis, which is developed in the framework of the collective effort to find and characterize an Earth-like planet. It is a grain of sand that contributes to discover how unique our planet is, to shed light on the origin and evolution of the solar system planets, and to answer if there are similar habitable worlds out there that could host life (see, e.g., Seager et al., 2016). To that end, we usually study the composition and temperature of the atmospheres using spectroscopy. That is, by analyzing the electromagnetic radiation that is absorbed, emitted, or scattered by the atmospheric compounds in different frequencies (see, e.g., Burrows, 2014b).

This analysis provides us with essential information about the present state, formation, and evolution of the planet. Thus, the field of spectroscopic characterization of the atmosphere of extrasolar planets, or *exoplanets*, is extremely fruitful. The analysis techniques, the technology of the instruments, and our knowledge are taking a giant step forward. This allows us to study increasingly smaller exoplanets, which results in a maelstrom of surprising results (Charbonneau et al., 2002; Tinetti et al., 2007; Snellen et al., 2008; Snellen et al., 2010; Brogi et al., 2012; Anglada-Escudé et al., 2016; Demory et al., 2016; Ribas et al., 2018). Among these discoveries, it is worth noting that we have found that the majority of stars (and there are hundreds of thousands of them only in our galaxy) host planetary systems. Moreover, the rocky planets such as Mercury, Venus, the Earth, or Mars, are very common (see, e.g., Butler et al., 2006). The desired counterexample to the current unicity of life could be in any of them and, if found, it would possibly provide unexpected answers for which science

must ask the correct questions.

The discovery of the first worlds orbiting distant stars was made between 1992 and 1994, when two objects with masses similar to that of Earth and one similar to the Moon, were found orbiting the pulsar PSR1257 + 12 (Wolszczan and Frail, 1992; Wolszczan, 1994). A year later, Mayor and Queloz (1995) found the first gas giant exoplanet, 51 Pegasi b, with half the mass of Jupiter, orbiting a main-sequence Solar-like star (51 Pegasi). This exoplanet defied many previous assumptions. This was because 51 Pegasi b was orbiting at a distance of only 0.05 UA from its star (i.e., nearly eight times closer than Mercury orbits our Sun). Hence, the orbital period (or year) for this exoplanet is of only four days.

Currently, the planetary formation models cannot reproduce the formation of a planet orbiting at such a small distance from the host star. In fact, it is thought that these exoplanets might have formed at larger distances and then migrated inwards in the planetary disk (Lin et al., 1996; Dawson and Johnson, 2018; Heller, 2018). Another surprising result is that, at that distance, the equilibrium temperature of 51 Pegasi b is predicted to be around 1300 K, which is much hotter than any of the solar system's planets. In addition, it is expected that the gravitational influence of the star produced a synchronization of the orbital and rotation periods of the planet due to tidal forces. Thereby, 51 Pegasi b likely shows the same side to the star permanently (Rasio et al., 1996; Marcy et al., 1997).

These findings are commonly considered the starting point of the field of investigation of exoplanets. 51 Pegasi b became the first of a new category of planets, which was unknown at the moment since it has no analogue in the solar system: the hot Jupiters. With these first examples and the 4055 confirmed exoplanets[1], we have found that the Universe has a wide variety of exoplanets in terms of masses, radii, orbital distances, host stars, composition and temperature of the atmospheres, among others (see, e.g., Madhusudhan, 2019).

The majority of known exoplanets have been found by using two techniques: the search for *transits* and the study of the *stellar radial velocity*. The former is based on the decrease of the stellar flux we receive when an exoplanet is passing in front of its host star, as seen from the Earth. In this configuration, a portion of the stellar light is temporarily blocked by the exoplanet and thus, it does not reach our telescopes. The probability of an exoplanet transiting its host star from our perspective decreases the larger its orbital distance is. Therefore, it is not surprising that most of the confirmed transiting exoplanets orbit very close-in.

The latter of the aforementioned techniques (i.e., the stellar radial velocity) studies the periodic motion induced in the star by the gravitational influence of the exoplanet. That is, the gravitational pull of the exoplanet produces a

[1]This is the current number of confirmed exoplanets as of September 15th 2019; https://exoplanetarchive.ipac.caltech.edu/

small, though detectable, oscillation or *wobble* of the star, which manifests in a Doppler shift of the stellar radiation. Thus, when the exoplanets orbit very close-in, this interaction is strong and easier to detect. Therefore, the majority of exoplanets detected with this technique also corresponds to gas giants at short orbital periods.

Naturally, it is much easier to detect such large and massive exoplanets than rocky worlds. To illustrate this, let us assume an exoplanet like Jupiter, and another one like the Earth, orbiting a distant Sun-like star. The exo-Jupiter planet induces an oscillation of amplitude $\sim$30 m/s in the star, whereas the exo-Earth's induced oscillation is of only around 10 cm/s. This small oscillation, two orders of magnitude lower than that produced by the gas giant, presents a challenge for our instruments. Current spectrographs can measure oscillations down to about $\sim$ 20 cm/s (see, e.g., ESPRESSO at the Very Large Telescope; Pepe et al., 2010). However, a precision of 10 cm/s or better is a realistic objective during the coming decade for ground-based observatories (e.g., it is the target precision of ESPRESSO and it will be very much improved with the future E-ELT; Pasquini et al., 2008).

Fortunately, we can find other potentially habitable exoplanets hosted by smaller and colder stars. In this case, the relative effect produced by the exoplanet becomes larger (although these stars are fainter). In this scenario, the search for Earth-like exoplanets in terms of mass and radius is already possible with current instrumentation. In order to provide a classification of how likely a planet is habitable for us, a first attempt is to define the so-called *habitable zone* (HZ; Kasting et al., 1993). That is, the annulus of orbital distances at which a planet would receive a stellar flux such, that liquid water could persist on its surface (i.e., moderate surface temperatures).

The HZ is thus constrained in its inner region by the strong stellar flux that can induce a *runaway greenhouse effect* in the exoplanet's atmosphere (or *exo-atmosphere*). At smaller distances, the surface temperature of the exoplanet would not allow for liquid water to exist for a long time. In its outer region, the HZ is constrained by the weak stellar fluxes. In this scenario, the surface temperature of the exoplanet is expected to be too cold for water to be in a liquid state, regardless of the potential greenhouse gases in the exo-atmosphere.

With this definition, the boundaries of the HZ depend directly on the spectral type of the star, being closer for small and cold stars, such as M dwarfs ($\sim$ 3000 K), than for G-type stars like our Sun ($\sim$ 6000 K). However, the HZ represents only a first estimation of the potential habitability of an exoplanet. In general, it is very hard to establish its real inner and outer regions accurately, since many other factors are equally important (and perhaps more) for habitability.

Venus is a close example of a planet that is similar to Earth in terms of its mass and size, but orbits closer than the inner boundary of the HZ of the

solar system. This rather small distance could be the reason for the runaway greenhouse effect of Venus' atmosphere, which could have caused a rapid evaporation of all liquid water on its surface in the past (Kulikov et al., 2006). In fact, the water vapor could later be photodissociated by the stellar radiation. Subsequently, several escape processes arising from the atmospheric dynamics could have yielded a loss of hydrogen and oxygen atoms to space (Lammer et al., 2006). As a result, the atmosphere of Venus is extremely dry, toxic for life as we know it, and has a extreme surface temperature ($\sim 462\,^{\circ}\mathrm{C}$) and pressure ($\sim 90$ atm).

However, we can illustrate that the HZ is only an approximation for habitability studies by using, again, an example from our own system. The planet Mars orbits within the Sun's HZ, although close to its outer limit. However, the surface conditions of Mars are cold ($-55\,^{\circ}\mathrm{C}$), and its atmosphere is about 168 times less dense than that of Earth. Moreover, it is formed mainly by carbon dioxide (95%). Its low mass (roughly 0.1 times the mass of Earth) might have caused a continuous reduction of its internal heat flux, which yielded poor dynamics at its core. Because of this, the planetary dynamo, which is thought to be responsible for the magnetic field in the Earth[2], was turned off (see, e.g., Ruiz, 2014). Thus, Mars' atmosphere was unprotected from the solar wind, and was likely eroded to its present low density (Jakosky et al., 2018).

Therefore, a planet with (potentially) temperate and wet surface conditions in the HZ can turn into a dry and cold world due to its intrinsic nature. The knowledge of many other parameters is then necessary to determine the potential habitability of an exoplanet. For instance, habitability is likely greatly dependent on the initial composition, the occurrence of natural cycles that recycle the atmospheric constituents (e.g., the carbon cycle on Earth), the dynamics at the planetary core, the presence of an ozone layer that shields the surface against ultraviolet radiation, the stellar activity, etc.

Interestingly, we can infer a lot of information about these features by studying the atmospheres of these planets. Let us assume that we are curious aliens that are equipped with the necessary technology to study our pale blue dot (Sagan, 1997). By using our advanced technology and observing at visible and near infrared wavelengths, we could be able to obtain evidences of the presence of ozone (O_3, Chappuis band between 400 and 650 nm), molecular oxygen (O_2, 760 nm) and water vapor (H_2O, ~ 700 nm) well mixed globally in the atmosphere. This information will probably trigger a revolution due to its potential implications.

Firstly, molecular oxygen is the canonical oxidizing species (i.e., gains electrons easily). For this reason, it is not expected to be present in large abundances

[2]The theory of the dynamo in the Earth's core states that the rotation and convection of the molten metals (mainly iron) in the core generate and sustain the magnetic field of the planet (see, e.g., Christensen, 2006).

in an atmosphere but trapped in other atmospheric compounds and in the planetary surface. For instance, this is the case of Venus or the early Earth (see also the so-called *Great Oxidation Event* of the Earth; Goldblatt et al., 2006). Thus, in order to accumulate oxygen in the atmosphere, there has to be a sources that constantly provides it with this compound (e.g., oxygenic life, photodissociation of other compounds, etc.).

Furthermore, the presence of ozone could be linked to the photodissociation of molecular oxygen in the atmosphere. In this case, it would also indicate that oxygen is likely being produced constantly for hundreds or millions of years (Walker, 1978). Due to the ozone's absorption in the Hartley's band ($200 - 300\,\mathrm{nm}$), we could also expect the planetary surface to be protected from ultraviolet radiation, which could help the potential lifeforms prosper.

Next, the study of the planetary flux, when compared to that of an ideal *blackbody*[3] (Kirchhoff, 1860; Planck, 1901), would provide us with a rough measurement of the planetary equilibrium temperature ($\sim 288\,\mathrm{K}$, or $15\,^{\circ}\mathrm{C}$). This temperature is compatible with the presence of liquid water on the surface, which could explain the observation of water vapor also in the planet's atmosphere (i.e., due to regular evaporation).

Continuing our analyses of the near infrared radiation, we could identify the presence of methane (CH_4) and carbon dioxide (CO_2). The presence of CO_2 can be linked to a greenhouse effect that allows for moderate temperatures to occur. However, the presence of globally mixed methane would represent a major surprise. Methane is an easily reducing species (i.e., it loses electrons easily). Hence, it is not expected to observe both O_2 and CH_4 well mixed in the atmosphere, with the required abundances to explain the observed absorption features. These observations would then constitute an evidence for the planetary atmosphere being out of the so-called *oxidation-reduction* equilibrium (Catling and Claire, 2005; Seager, 2014), which requires a powerful mechanism that constantly maintains these conditions.

These findings in the atmosphere of the distant pale blue exoplanet would be an evidence, although not confirmation, of the potential habitability of that exoplanet for life as we know it. However, such confirmation is likely only possible by having in-situ measurements or, closer to science-fiction, by receiving an intelligent message that is hard or impossible to replicate randomly (Sagan and Drake, 1975; Atri et al., 2011).

Back to our human forms, such amount of information can be derived from studying the atmosphere of our blue marble by means of the absorbed, reflected, and emitted light. These observations have actually been recorded by using

[3]Theoretical body that absorbs all incident radiation. Moreover, a blackbody emits radiation at all wavelengths, peaking the emission at shorter wavelengths the larger the temperature of the body is. This model is a good approximation for the emission of electromagnetic radiation by a real body.

instruments that we have sent to space and oriented towards our planet to, again, contextualize ourselves, studying the Earth as an exoplanet. This is the case, for instance, of the *Earthshine* measurements (Turnbull et al., 2006), the spectra gathered by the *Deep Impact Extended Investigation* (Robinson et al., 2011), or those obtained by the *Mars Global Surveyor* (Christensen and Pearl, 1997). Also, see a discussion about these in Seager (2014).

As we will see in this thesis, the study of exoplanet atmospheres — similar or not to Earth and other planets of the solar system — is a highly fruitful area of science. In particular, hot Jupiters and Neptunes, and super-Earths[4], accessible with current instruments, have become perfect astronomical laboratories where we can develop and test our knowledge on, i) planetary and atmospheric formation and evolution (Moses et al., 2012; Mollière et al., 2015; Brewer et al., 2017), ii) the influence of the host star on the exoplanet, which phenomena drive their atmospheric dynamics (Rauscher and Menou, 2013; Showman et al., 2013; Mollière et al., 2015; Amundsen et al., 2016), and iii) the composition and pressure-temperature conditions of the exo-atmospheres (Snellen et al., 2008; Burrows, 2014a; Demory et al., 2016; Line et al., 2016; Sing et al., 2016; Birkby, 2018; Alonso-Floriano et al., 2019a; Sánchez-López et al., 2019).

Fortunately, we can now find planets similar in mass and size to Earth relatively close to the solar system by taking advantage of the study of M-type dwarf stars[5]. For instance, Proxima b was discovered very recently. Proxima b is a rocky exoplanet with a minimum mass of 1.3 times that of Earth that orbits in the HZ of the closest star to our solar system, Proxima Centauri (Anglada-Escudé et al., 2016). Shortly after, seven planets with masses between the martian and terrestrial ones were found orbiting the TRAPPIST-1 star. The first three of them are within the HZ of this star (Gillon et al., 2016, 2017). In fact, the first attempts to characterize these exoplanets are already taking place. By using the Hubble space telescope, Wit et al. (2016) were able to obtain a combined transmission spectrum of the exoplanets TRAPPIST-1b and TRAPPIST-1c. The authors found an almost flat transmission spectrum, in which no trace of atmospheric compounds could be observed. Thus, they concluded that, if these exoplanets have atmospheres, these would be dense and without clouds (for instance, consistent with high contents in water vapor), or similar to that of Venus (i.e., with a dense cloud coverage).

And these are not the only pleasant encounters, as we have also known of the existence of Barnard's Star b, a super-Earth candidate in the outer limit of the HZ of our second-closest star, Barnard star (Ribas et al., 2018). Moreover, two candidates to Earth-like planets have been found around our third-closest start,

[4]Rocky planets with masses ranging from, roughly, 2 to 10 Earth masses. That is, exoplanets smaller than Jupiter or Neptune, but notably more massive than Earth.

[5]Typically, these have masses, radii, and luminosities smaller than 40%, 50%, and 10% those of the Sun, respectively (Chabrier et al., 1996).

Teegarden's star (Zechmeister et al., 2019b), providing even further evidence of the potential ubiquity of worlds similar in size and mass to our very own orbiting in the HZ of their stars.

In the years to come, the atmospheric characterization of these small exoplanets will become increasingly precise, as our knowledge and analysis techniques develop and the new generations of spatial and ground-based telescopes arrive (see, e.g., Pallé et al., 2011; Barstow and Irwin, 2016; Kreidberg and Loeb, 2016; Turbet et al., 2016; Lovis et al., 2017; Snellen et al., 2017; Madhusudhan, 2019). The motivation to find one of these Earth-like worlds, potentially similar to our home, will be the engine that allows us to evolve the exoplanetary science to, in the future, take our voyage of self-discovery to a new pale blue dot.

Objectives of the thesis

In this general context, the main objective of this thesis is the investigation and characterization of the atmospheres of hot Jupiters during the primary transit. To that end, we will use the technique based on the cross-correlation of high-resolution spectra obtained with the CARMENES spectrograph with synthetic models of the exo-atmosphere. This study will allow us to determine the presence of molecular species and to study the dynamics of exo-atmospheres. Moreover, we will analyze the sensitivity of the measurements to the abundance of compounds and to the exo-atmospheric temperature.

In particular, the *main objectives of this thesis* are:

i) To adapt our tools for the computation of the radiative transfer, which have been widely validated in the study of the solar system, to the geometry of exoplanetary systems. This will provide us with the necessary tools to calculate synthetic spectra of the exo-atmospheres.

ii) To learn and optimize the cross-correlation technique of high resolution spectra with exo-atmospheric models. The optimized technique will allow us to precisely identify the presence of molecular species and to investigate the exo-atmospheric dynamics.

iii) To understand the CARMENES instrument and its capabilities for exo-atmospheric science. This includes submitting proposals for the obtention of high-resolution data of hot Jupiters, analyzing the quality of the measurements, discussing potential improvements with the CARMENES Consortium, etc.

iv) To apply the developed techniques to the characterization of the atmospheres of the hot Jupiters HD 189733 b and HD 209458 b. We will analyze

the data recorded during their primary transits with the two channels of the CARMENES spectrograph, covering wavelengths in the visible and the near-infrared. Additionally, we will contextualize our results with previous studies of these exoplanets.

Summary and structure of the thesis

In **chapter** 1, we present an introduction to the techniques used to find exoplanets and characterize their atmospheres. We focus on those that are most relevant to the context of this thesis. We first describe three detection methods. The first one based on the analysis of the radial velocity of the star; the second one consists on analyzing the exoplanet's primary transit; and the third one images the exoplanets directly.

Consecutively, we introduce the main techniques developed to characterize the atmospheres of known exoplanets. In particular, we describe the obtention of transmission spectra during the primary transit, which are fundamental in the chapters with original scientific contributions of this thesis. We also discuss the characterization of exo-atmospheres by studying the radiation coming from the illuminated side of the exoplanet during the secondary eclipse, despite not being fully explored in this thesis. Similarly, we introduce the elaboration of phase curves, of great relevance on this research field. Lastly, we discuss the most relevant characterization method for the original chapters of this thesis: the cross-correlation of high-resolution spectra with models of the exo-atmospheric absorption.

In **chapter** 2, we present an introduction to the basic atmospheric physics needed to understand exoplanetary systems and the research undertaken in this thesis. We begin by presenting the equation of hydrostatic equilibrium, of fundamental importance in the study of atmospheres of planets. We will then present the main contributions to the atmospheric temperature profile, and under which conditions the atmospheres are in radiative-convective equilibrium. Next, we will discuss the modeling of the composition of the atmospheres, based on the assumption of chemical equilibrium, by minimizing the Gibbs free energy. Moreover, we will compare the results of these models with those obtained when considering processes far from the equilibrium, such as photodissociation and vertical transport. Thus, we will discuss the first studies making use of networks of chemical kinetics verified in laboratories. In this context, we will discuss the study of the ratio between carbon and oxygen atoms in the exo-atmospheres, which holds invaluable information about the chemistry, formation and evolution of the exoplanets. Additionally, we will discuss the atmospheric dynamics and circulation in hot Jupiters, which are responsible for the distribution of thermal energy and chemical compounds in their exo-atmospheres.

We will then continue introducing the phenomena affecting the shape of the

absorption and emission spectral lines. In particular, we describe the natural, Doppler, and Lorentz broadenings, and the convolution of these mechanisms. The latter constitutes the real observed shape of the rotational-vibrational spectral lines (Voigt line shape) in the spectral regions studied in this thesis (visible and near infrared wavelengths). At this point, we will introduce the equation of radiative transfer, whose resolution reveals the state of the radiative field in each atmospheric layer. Here, we will introduce the KOPRA algorithm to solve the radiative transfer equation. In particular, we will discuss the adaptation of this algorithm to the geometry of the exoplanet systems undertaken within this thesis. Moreover, we will validate the synthetic spectra of exo-atmospheres generated with KOPRA, both in transmission and emission, against those generated with other algorithms developed by diverse research groups.

In **chapter** 3, we will present an in-depth description of the technique based on the cross-correlation of high resolution measurements with models of the exo-atmospheric absorption. In particular, we focus on transmission spectra gathered during the primary transit of exoplanets, both in the visible and near infrared, with the spectrograph CARMENES (Calar Alto, Almería). Here, we will describe all the steps involved in the data analysis. These include the removal of "hot" pixels, the normalization of spectra, and the masking of the spectral regions most affected by the Earth's atmospheric absorption. Consecutively, we will elaborate on the removal of the Earth's tellurics and the stellar features of the spectra. In this thesis, this step will be carried out by using the Sysrem algorithm, which performs a principal component analysis. Next, we will combine the weak planetary signal across all wavelengths and in time by cross-correlating the residual spectra with model templates computed with KOPRA. Lastly, we will describe the main metrics used to determine the significance of the signal: the calculation of the signal-to-noise ratio of the cross-correlation functions and the application of a Welch t-test.

In the following chapters, we present the original scientific contributions and results of this thesis.

Specifically, in **chapters** 4 and 5, we apply the cross-correlation technique discussed in chapter 3 to high resolution data taken with CARMENES in the near infrared (NIR). These measurements consist of transit data for the two canonical hot Jupiters HD 189733 b and HD 209458 b, respectively. In both cases, we will remove the telluric and stellar contributions using Sysrem. This algorithm is used in a conservative way for the dataset of HD 189733 b, whereas we develop an optimization for each of the spectral orders of CARMENES in the case of HD 209458 b. This is done by following previous results by other groups, which used similar instrumentation. Next, we describe the inputs used in the computation of the atmospheric models with KOPRA, which are based on the latest results obtained in the literature for the pressure-temperature ($p-T$) and abundance profiles of these exoplanets.

Using these model templates, we present in both chapters a detection of water vapor in the atmospheres of the hot Jupiters HD 189733 b and HD 209458 b. In particular, for HD 189733 b, we will describe the detection of this molecule by using its two most absorbent bands covered by the CARMENES NIR channel separately. Also, we will discuss the low sensitivity of this technique to the $p-T$ and abundance profiles used in the computation of the models. In addition, we report a non-detection of methane in the exo-atmosphere of HD 189733 b, which is in line with previous results for this exoplanet.

Consecutively, we will study the possibility of recovering the water vapor signal by cleaning the telluric contribution using the MOLECFIT algorithm. To do so, we cross-correlate the residual spectra after applying MOLECFIT with the model templates computed with KOPRA, which results in a non-detection of water vapor.

With the aim of obtaining precise information about the $p-T$ and abundance profiles in HD 189733 b, we use the *inverse-injection* technique. This technique aims at finding the best-fitting model that best cancels the water vapor cross-correlation signal. In this context, we will discuss how our capabilities to determine the best fit model are affected by the intrinsic degeneration of the relevant parameters used in the calculation of the models (e.g., the reference pressure and radius of the exoplanet, the temperature profile, the abundance of the molecules, and the contribution of clouds and hazes).

In the case of HD 209458 b, we discuss the detection of water vapor, principally using its absorption band at around 1 μm. This is the detection of water vapor using the bluest wavelengths to date. In addition, we will discuss the possible explanations for not finding the water vapor signal robustly in the two most absorbent bands in the dataset of HD 209458 b, which were clearly identified in the dataset of HD 189733 b. Among these reasons, we will elaborate on the impact of the signal-to-noise ratio of the observations, and the variability of the observing conditions during the transit of HD 209458 b, on our capabilities to obtain the water vapor signal with this technique.

For both exoplanets and in both chapters, we study the presence of significant Doppler shifts of the cross-correlation signals. These are an indication of strong winds flowing from the day- to the night-side across the terminator of these hot Jupiters. We will compare both results and contextualize them we the predictions of global circulation models developed by other research groups. Furthermore, as a result of the comparison of the water vapor signal in both exo-atmospheres, we will obtain evidences of HD 189733 b being more affected by the extinction of atmospheric aerosols than HD 209458 b, which is in good agreement with previous literature results.

In **chapter** 6, we analyze the measurements taken with the CARMENES visible channel for the hot Jupiters HD 189733 b and HD 209458 b during their primary transits in three observation nights for each exoplanet. To that end,

we adapt the methods described in the previous chapters to this new spectral interval. Next, we discuss the preliminary results we obtained for each observation night separately, and combining the information of the respective nights for each exoplanet. Our preliminary results reveal a water vapor detection in the atmosphere of HD 209458 b. In addition, the non-detection in HD 189733 b supports our previous results and the literature findings for this exoplanet being rather hazy. Thus, these spectral features in the optical are obscured by a steep scattering slope in the exo-atmosphere of the latter.

Finally, in **chapter** 7, we present the main conclusions of this thesis. In particular, we focus on the implications of our detections of water vapor and how they fit in the previous knowledge about the hot Jupiters HD 189733 b and HD 209458 b. In addition, we discuss the scientific cases that, in the future, might use our results to expand the knowledge about exo-atmospheres further.

Prefacio

"El estudio del universo es un viaje al autodescubrimiento."

Carl Sagan

Este pensamiento, intentar hallar inimaginablemente lejos las respuestas a las incógnitas de nuestro mundo, es el sorprendente resultado de milenios en los cuales incontables primates (no miopes) dirigieron los ojos al cielo. En esencia, la búsqueda y caracterización de nuevos planetas, acogidos por la miríada de estrellas que nos rodean, está motivada por un deseo imparable, y hasta conmovedor, de contextualizarnos. Esta idea es también la raíz de esta tesis doctoral, que se enmarca en la carrera trepidante por encontrar un planeta similar a la Tierra y caracterizar su atmósfera. Es un esfuerzo por aportar un granito de arena que contribuya a esclarecer cuán único es este planeta, que dé pistas sobre el origen y evolución de la Tierra y de los otros cuerpos del sistema solar, que ayude a responder si existen mundos similares, si son habitables para el ser humano y, en última instancia, si existe vida de cualquier tipo en ellos (véase también, por ejemplo, Seager et al., 2016). Para ello, solemos acudir al estudio de la composición y temperatura de sus atmósferas a través de la espectroscopía. Esto es, mediante el estudio de la radiación electromagnética que absorben, emiten o dispersan los componentes de la atmósferas en distintas frecuencias (véase, por ejemplo, Burrows, 2014b).

Este análisis nos proporciona información esencial sobre el estado actual del astro y nos aporta pistas sobre sus condiciones de formación y evolución. Así, el campo de la caracterización espectroscópica de las atmósferas de planetas extrasolares, o *exoplanetas*, orbitando en torno a otras estrellas lejanas, goza de una envidiable salud. Las técnicas de análisis, la tecnología de la instrumentación y nuestro conocimiento evolucionan a pasos agigantados. Esto, a su vez, nos permite estudiar planetas cada vez más pequeños y se materializa en una vorágine de resultados impactantes (Charbonneau et al., 2002; Tinetti et al., 2007; Snellen et al., 2008; Snellen et al., 2010; Brogi et al., 2012; Anglada-Escudé et al., 2016; Demory et al., 2016; Ribas et al., 2018). Entre estos hallazgos, y retomando la idea recogida por Carl Sagan (Sagan et al., 1980), cabe destacar

el descubrimiento de que la mayoría de las estrellas (y existen cientos de miles de millones de ellas solo en nuestra galaxia) albergan sistemas planetarios en los cuales los cuerpos rocosos como Mercurio, Venus, la Tierra o Marte, son muy comunes (véase, por ejemplo, Butler et al., 2006). El deseado contraejemplo a la, por ahora, unicidad de la vida, puede estar en cualquiera de esos planetas y, posiblemente, vendrá con inesperadas respuestas para las cuales la ciencia ha de plantear las preguntas correctas.

El descubrimiento de los primeros mundos en torno a otras estrellas se produjo entre 1992 y 1994, cuando dos objetos de masa parecida a la terrestre, y uno de masa similar a la lunar, fueron hallados orbitando al púlsar PSR1257+12 (Wolszczan and Frail, 1992; Wolszczan, 1994). Apenas un año después, Mayor and Queloz (1995) encontraron el primer planeta de tipo joviano, 51 Pegasi b, (la mitad de masivo que Júpiter) acogido por una estrella tipo solar (51 Pegasi), en plena secuencia principal. Sin embargo, la sorpresa fue mayúscula al comprobar que el exoplaneta 51 Pegasi b desafiaba todas las ideas preconcebidas hasta esa fecha. Este exoplaneta orbitaba a tan solo 0.05 UA de su estrella, una distancia casi ocho veces más pequeña que aquella a la que Mercurio orbita nuestro Sol. Esto se traduce en periodos orbitales (o años) que duran apenas cuatro días.

Hasta el día de hoy, los modelos de formación planetaria no pueden reproducir la formación de un exoplaneta a esa distancia, de manera que se piensa que estos cuerpos han migrado hasta esa posición desde un lugar de origen a distancias orbitales mucho mayores (Lin et al., 1996; Dawson and Johnson, 2018; Heller, 2018). Otro dato impactante es que, a esa distancia, la temperatura de equilibrio de 51 Pegasi b puede estimarse en torno a los 1300 K, muy por encima de la de ninguno de los planetas del sistema solar. Además, es de esperar que la influencia gravitatoria de la estrella cercana produzca una sincronización de los periodos de rotación y orbital del planeta a través de enormes fuerzas de marea, de manera que 51 Pegasi b probablemente muestra constantemente la misma cara a su estrella (Rasio et al., 1996; Marcy et al., 1997).

El cúmulo de hallazgos inesperados en este sistema es popularmente aceptado como el pistoletazo de salida del campo de estudio de exoplanetas. 51 Pegasi b se convirtió en el primero de una categoría planetaria que era desconocida hasta la fecha al no tener análogo en el Sistema Solar: los Jupiteres calientes. Con estos primeros ejemplos y los 4055 exoplanetas confirmados hasta ahora[6] mediante distintas metodologías, la ciencia ha encontrado que el Universo nos guardaba una gran variedad de exoplanetas, abarcando amplios intervalos de masas y radios planetarios, distancias orbitales, estrellas anfitrionas, composición y temperatura de las atmósferas, entre otros parámetros (véase, por ejemplo, Madhusudhan, 2019).

La mayoría de planetas que conocemos se han encontrado mediante dos métodos: la búsqueda de *tránsitos* y el estudio de las *velocidades radiales este-*

[6]Con fecha de 15 de septiembre de 2019; https://exoplanetarchive.ipac.caltech.edu/

lares. El primero se basa en el decrecimiento del flujo estelar recibido por nuestros telescopios cuando un exoplaneta cruza la línea de visión entre la Tierra y la estrella. En esta configuración, deja de llegarnos la radiación de una sección de la estrella debido al disco planetario, que la bloquea temporalmente. Debido a que la probabilidad de que un planeta transite a su estrella, desde nuestra línea de visión, se reduce cuanto mayor sea la distancia orbital, la mayoría de exoplanetas encontrados con esta técnica corresponde a mundos que orbitan muy cerca de sus estrellas.

El segundo de los citados métodos estudia los movimientos inducidos en la estrella por la fuerte interacción gravitatoria con el planeta. Esto es, la atracción gravitatoria del planeta se traduce en una pequeña (pero detectable) oscilación o bamboleo de la estrella, que se manifiesta en un corrimiento Doppler de la radiación estelar. Así, cuando los planetas orbitan muy cerca de la estrella, esta interacción es más fuerte y fácil de detectar. Por lo tanto, no es de extrañar que la mayoría de los exoplanetas identificados con este método corresponda a gigantes gaseosos con muy cortos periodos orbitales.

Naturalmente, es mucho más facil detectar planetas grandes y masivos que mundos terrestres con estas técnicas. Para ejemplificar esto, consideremos un exoplaneta como Júpiter, y otro como la Tierra, en orbita en torno a una estrella lejana como el Sol. El planeta exo-Júpiter induce una oscilación de amplitud $\sim$30 m/s en su estrella, mientras que la exo-Tierra solo produce oscilaciones al nivel de, aproximadamente, 10 cm/s. Este nivel de sensibilidad, dos órdenes de magnitud inferior al necesario para un gigante gaseoso, representa un gran desafío para la instrumentación actual, la cual está alcanzando el nivel de sensibilidad de $\sim$ 20 cm/s en los espectrógrafos más recientes (véase, por ejemplo, ESPRESSO en el Very Large Telescope; Pepe et al., 2010). No obstante, sensibilidades cercanas o incluso mejores que 10 cm/s son un objetivo realista para la instrumentación en observatorios terrestres durante la próxima década (esta es la sensibilidad que se prevee alcanzar con ESPRESSO y superar con, por ejemplo, el instrumento CODEX en el futuro telescopio E-ELT; Pasquini et al., 2008).

Afortunadamente, podemos encontrar otros mundos potencialmente habitables hospedados por estrellas más pequeñas y frías. Al reducir el tamaño de la estrella estudiada, el efecto producido por planetas más pequeños es proporcionalmente mayor (aunque estas estrellas son menos brillantes). En este escenario, la búsqueda de planetas de radio y masa similares a los terrestres es posible con la sensibilidad actual. Para catalogar estos exoplanetas por su posible habitabilidad, uno de los primeros pasos es la definición de la llamada *zona habitable* (ZH; Kasting et al., 1993). Esto es, el anillo de distancias orbitales en las que un planeta recibiría un flujo estelar tal, que permitiría una temperatura superficial moderada, y la presencia de agua líquida en superficie.

La ZH está por tanto delimitada en la zona interna por los fuertes flujos

estelares que pueden producir un efecto invernadero desbocado en la atmósfera. A distancias más cercanas a esta, la temperatura superficial de un hipotético planeta como la Tierra podría elevarse a cientos de grados, vaporizando el agua líquida. Por otra parte, el borde externo de la ZH está definido por la distancia a la cual el flujo estelar es tan débil que los posibles gases de efecto invernadero (como el CO_2) no podrían mantener la superficie del planeta por encima del punto de congelación del agua.

Con esta definición, la posición y extensión de la ZH depende directamente del tipo espectral de la estrella, estando más cerca para estrellas pequeñas y frías (como enanas de tipo M con temperaturas superficiales $\sim 3000\,\mathrm{K}$), y más lejos para una estrella más grande y caliente (como las estrellas de tipo G, o solar, con temperaturas $\sim 6000\,\mathrm{K}$). Sin embargo, la ZH es solo una primera aproximación a la determinación de la habitabilidad de un exoplaneta. En general, es difícil establecer una definición exacta para los bordes de la misma, pues una gran cantidad de factores adicionales tienen papeles igual de relevantes que el de la distancia orbital a la hora de determinar las condiciones en el astro.

Venus es un ejemplo cercano de planeta similar a la Tierra, en terminos de tamaño y masa, y situado ligeramente fuera del borde interno de la ZH de nuestro sistema solar (esto es, más cerca del Sol que el borde interno de la ZH). A esta distancia, Venus presenta un efecto invernadero desbocado que pudo evaporar toda el agua de su superficie (Kulikov et al., 2006). En este escenario, el vapor de agua resultante puede ser fotodisociado en la atmósfera por la radiación solar incidente y, posteriormente, diversos procesos de escape producidos por la dinámica atmosférica pueden producir la pérdida de los átomos de hidrógeno y oxígeno al espacio (Lammer et al., 2006). Como resultado, la atmósfera de Venus es extremadamente seca, tóxica para la vida como la de la Tierra y poseé condiciones extremas de presión ($\sim$ 90 atm) y temperatura ($\sim 462\,^{\circ}\mathrm{C}$) en su superficie.

Sin embargo, podemos evidenciar el carácter aproximado de la ZH, nuevamente, con un ejemplo de nuestro propio sistema. El planeta Marte orbita al Sol dentro de la ZH solar, aunque cerca de su borde externo. No obstante, las condiciones superficiales marcianas son frías ($-55\,^{\circ}\mathrm{C}$), su atmósfera es en torno a 168 veces menos densa que la de la Tierra y, además, está formada en un 95% por dióxido de carbono. Su baja masa (en torno a 0.1 veces la masa de la Tierra) pudo traducirse en una continua disminución del flujo de calor en el interior del planeta, ligado a un empobrecimiento de la dinámica del núcleo (véase, por ejemplo, Ruiz, 2014). Estas condiciones probablemente fueron la causa de que la dinamo de escala planetaria, responsable de generar el campo magnético en nuestro planeta[7], detuviese su funcionamiento en Marte. Despo-

[7]La teoría de la dinamo en el núcleo de la Tierra, compuesto principalmente de hierro fundido, establece que los movimientos de rotación y convección del fluido conductor generan y mantienen el campo magnético de nuestro planeta (véase, por ejemplo, Christensen, 2006).

jada de un campo magnético protector, la atmósfera marciana quedó expuesta a los potentes vientos solares que, en el transcurso de miles de millones de años, la erosionaron hasta su ténue densidad actual (Jakosky et al., 2018).

Así, un planeta potencialmente cálido y húmedo, orbitando dentro de la ZH de su estrella, puede evolucionar a un mundo seco y frío debido a sus circunstancias intrínsecas. Así, son muy importantes para catalogar un exoplaneta como habitable para el ser humano su composición inicial, el desarrollo de diversos ciclos naturales de reclicaje de la atmósfera (como, por ejemplo, el ciclo del carbono en la Tierra), la dinámica interna, la producción de una capa de ozono que proteja la superficie de la radiación ultravioleta, la actividad estelar, entre muchos otros factores.

Curiosamente, podemos extraer gran cantidad de información sobre estos fenómenos en los planetas a través del estudio de sus atmósferas. Supongamos momentáneamente que somos, usted y yo, intrépidos alienígenas equipados con la tecnología necesaria para estudiar meticulosamente nuestro punto azul pálido, orbitando en torno a una lejana estrella (Sagan, 1997). Utilizando nuestra avanzado tecnología y observando en las longitudes de onda del espectro visible e infrarrojo, podríamos ser capaces de observar indicios de ozono (O_3, banda de Chappuis entre 400 y 650 nm), oxígeno molecular (O_2, 760 nm) y vapor de agua (H_2O, ~ 700 nm) bien mezclados en la atmósfera del planeta. Esta información supondría, probablemente, una revolución por sus potenciales implicaciones.

Primeramente, el oxígeno molecular es la especie oxidante por excelencia (esto es, que capta electrones fácilmente), de manera que no es habitual ver altas concentraciones de este compuesto bien mezcladas en toda una atmósfera. De hecho, es de esperar que el oxígeno esté atrapado de otras maneras y en compuestos oxidados en superficie. Este es, por ejemplo, el caso de Venus o de la Tierra cuando surgió la vida oxigénica (véase, por ejemplo, la llamada *época de la gran oxidación* terrestre; Goldblatt et al., 2006). Por tanto, la acumulación de O_2 en la atmósfera requiere la existencia de una fuente constante que aporte dicho compuesto (por ejemplo, vída oxigénica, fotodisociación de otros compuestos, etc.).

Por su parte, la presencia de ozono puede ligarse a la fotodisociación del oxígeno molecular en la atmósfera. En ese caso, podría ser indicativo de que el O_2 lleva siendo producido constantemente cientos o miles de millones de años (Walker, 1978). Además, permitiría deducir que una parte significativa de la radiación ultravioleta estelar no alcanza la superficie del planeta. Esto es debido a la absorción del ozono en la llamada *banda de Hartley*, en torno a $200-300$ nm. De haber vida en el planeta, la absorción de radiación ultravioleta por el ozono favorecería su prosperación.

Seguidamente, el estudio del flujo emitido por la atmósfera, comparado con la emisión ideal de un cuerpo negro[8] (Kirchhoff, 1860; Planck, 1901), propor-

[8]Cuerpo teórico que absorbe toda la radiación que incide sobre él. Además, el cuerpo negro

cionaría una evidencia directa de la temperatura de equilibrio en la superficie del planeta, en torno a $\sim 288\,\mathrm{K}$ ($15\,^{\circ}\mathrm{C}$). Esta temperatura es compatible con la presencia de agua líquida en la superficie del planeta. Así, el alto contenido en vapor de agua atmosférico bien mezclado podría ser indicativo de la presencia de mares u océanos.

El análisis de la radiación que recibiríamos desde el exoplaneta en el infrarrojo nos revelaría, además de la ya descubierta contribución de H_2O, dos nuevas sorpresas en forma de metano (CH_4) y dióxido de carbono (CO_2). La presencia de CO_2 podría ligarse al efecto invernadero que permite temperaturas templadas en superficie. Pero es la presencia de CH_4 bien mezclado el gran descubrimiento en este intervalo espectral. Y es que, si el oxígeno es la especie oxidante por excelencia, el metano es un compuesto que reduce fácilmente (es decir, suministra electrones fácilmente). Por lo tanto, no es de esperar que la concentración relativa de ambos compuestos, necesaria para explicar las observaciones, se mantenga de forma estable. Es decir, existe una evidencia directa de que la atmósfera del punto pálido azul se encuentra fuera del llamado equilibrio *oxidación-reducción* (Catling and Claire, 2005; Seager, 2014), lo cual necesita de un potente mecanismo que constantemente mantenga estas condiciones.

Estos descubrimientos en la atmósfera de un exoplaneta significarían para nosotros alienígenas una evidencia, aunque no confirmación, de la hospitalidad de ese nuevo mundo para la vida tal y como la conocemos. Sin embargo, tal confirmación es, probablemente, solo alcanzable a través de medidas in situ o, rozando el dominio de la ciencia-ficción, tras la recepción de un mensaje inteligente difícil o imposible de replicar aleatoriamente (Sagan and Drake, 1975; Atri et al., 2011).

De vuelta a nuestra forma humana, tal cantidad de información puede extraerse de nuestra canica azul a través del estudio de la radiación emitida, reflejada y absorbida por nuestra atmósfera. Este tipo de medidas han sido tomadas en el pasado utilizando los instrumentos que, a lo largo de las décadas, hemos enviado al espacio y orientado hacia nuestra propia casa para, una vez más, contextualizarnos, imaginándonos la Tierra vista como un exoplaneta. Tal es el caso de, por ejemplo, las medidas *Earthshine* (Turnbull et al., 2006) y espectros terrestres tomados con los instrumentos de la misión *Deep Impact Extended Investigation* (Robinson et al., 2011) o con la *Mars Global Surveyor* (Christensen and Pearl, 1997). Además, véase una discusión sobre los mismos en Seager (2014).

Como veremos en esta tesis, el estudio de la atmósfera de exoplanetas, parecidos o no a la Tierra u otros planetas del sistema solar, es una ciencia muy

emite radiación electromagnética de todas las frecuencias, teniendo el pico de emisión una mayor frecuencia cuanto más alta sea la temperatura del cuerpo. Este modelo es una buena primera aproximación a la emisión de radiación por parte de los cuerpos reales.

fructífera. En concreto, los jupiteres y neptunos calientes y las supertierras[9], accesibles con la instrumentación actual, se han convertido en perfectos laboratorios astronómicos. En ellos, desarrollamos y contrastamos nuestros conocimientos sobre, i) la formación y evolución planetaria y atmósferica (Moses et al., 2012; Mollière et al., 2015; Brewer et al., 2017), ii) la influencia de la estrella anfitriona en los exoplanetas y qué regímenes gobiernan en sus dinámicas atmosféricas (Rauscher and Menou, 2013; Showman et al., 2013; Mollière et al., 2015; Amundsen et al., 2016) y iii) su composición y condiciones de presión y temperatura (Snellen et al., 2008; Burrows, 2014a; Demory et al., 2016; Line et al., 2016; Sing et al., 2016; Birkby, 2018; Alonso-Floriano et al., 2019a; Sánchez-López et al., 2019).

Afortunadamente, podemos encontrar planetas similares en tamaño y masa a la Tierra relativamente cerca del sistema solar aprovechando las ventajas del estudio de estrellas enanas de tipo M[10]. Muy recientemente, se descubrió Próxima b, un planeta rocoso con una masa mínima 1.3 veces la terrestre en la ZH de la estrella más cercana a la Tierra, Próxima Centauri (Anglada-Escudé et al., 2016). Poco después, siete planetas con masas comprendidas entre la marciana y la terrestre fueron hallados en torno a la estrella TRAPPIST-1, estando tres de ellos en su ZH (Gillon et al., 2016, 2017). De hecho, los primeros intentos de caracterización del sistema TRAPPIST-1 ya están en marcha. Utilizando el telescopio espacial Hubble, Wit et al. (2016) obtuvieron un espectro de transmisión combinado de los exoplanetas TRAPPIST-1b y TRAPPIST-1c. Estos autores encontraron un espectro de transmisión prácticamente plano en el que no se observa la presencia de ningún compuesto atmosférico. Así, concluyeron que, de poseer atmósferas, éstas podrían ser densas y sin nubes (por ejemplo, consistentes con altos contenidos de vapor de agua), o ser parecidas a la del planeta Venus (esto es, una densa cobertura de nubes).

Y no han sido estos los únicos encuentros agradables, ya que también hemos conocido de la existencia de Barnard's Star b, un candidato a super-Tierra en el límite externo de la ZH de la segunda estrella más cercana, llamada Estrella de Barnard (Ribas et al., 2018). Además, dos candidatos a planeta similares a la Tierra han sido descubiertos en torno a la tercera estrella más cercana a la Tierra, la estrella de Teegarden (Zechmeister et al., 2019b), aportando incluso más evidencias de la potencial ubicuidad de los mundos similares en tamaño y masa al nuestro orbitando en la ZH de sus estrellas.

En los próximos años, la caracterización de la atmósfera de estos pequeños exoplanetas será cada vez más precisa, a medida que desarrollamos nuestros conocimientos y técnicas de análisis y llegan las nuevas generaciones de tele-

[9]Planetas rocosos con masas entre $2 - 10$ veces la terrestre. Es decir, menos masivos que Júpiter o Neptuno, pero notablemente más masivos que la Tierra.

[10]Típicamente, éstas tienen masas, radios y luminosidades inferiores a un 40%, 50% y 10% los del Sol, respectivamente (Chabrier et al., 1996).

scopios terrestres y espaciales (véanse, por ejemplo, Pallé et al., 2011; Barstow and Irwin, 2016; Kreidberg and Loeb, 2016; Turbet et al., 2016; Lovis et al., 2017; Snellen et al., 2017; Madhusudhan, 2019). La motivación por encontrar uno estos mundos lejanos, pero potencialmente parecidos a nuestra casa, será el motor que nos permita evolucionar la ciencia de exoplanetas para, en el futuro, llevar nuestro viaje por el autodescubrimiento a un nuevo punto pálido azul.

Objetivos de la tesis

En este contexto general, el objetivo de esta tesis es la investigación y caracterización de la atmósfera de Jupiteres calientes durante el tránsito primario. Para ello, se utilizará la técnica de correlación cruzada de espectros de alta resolución, tomados con el espectrógrafo CARMENES, con modelos sintéticos de la exo-atmósfera. Esto nos permitirá determinar la presencia de especies moleculares y estudiar la dinámica de éstas. Además, analizaremos la sensibilidad de las medidas a la abundancia de compuestos y a la temperatura de las exo-atmosferas.

En particular, los *principales objetivos de esta tesis* son:

i) Adaptar nuestras herramientas para el cálculo del transporte radiativo, ampliamente validadas en el estudio del sistema solar, a la geometría de sistemas exoplanetarios. Esto nos permitirá contar con las herramientas necesarias para el cálculo de espectros sintéticos de la atmósfera de exoplanetas.

ii) Aprendizaje y optimización de la técnica de correlación cruzada de espectros de alta resolución con modelos de la exo-atmósfera. Dicho estudio nos permitirá contar con herramientas punteras para identificar especies moleculares e investigar la dinámica de las atmósferas de exoplanetas.

iii) Entender el instrumento CARMENES y sus capacidades para observar atmósferas de exoplanetas. Esto incluye la escritura de propuestas de observación, analizar la calidad de los datos obtenidos, discutir potenciales mejoras con el Consorcio CARMENES, etc.

iv) Aplicación de las técnicas aprendidas a las observaciones de los Jupiteres calientes HD 189733 b y HD 209458 b. Analizaremos los datos tomados durante sus tránsitos primarios con los dos canales del espectrógrafo CARMENES, observando en el visible y en el infrarrojo. Adicionalmente, contextualizaremos nuestros resultados con los estudios anteriores realizados para estos exoplanetas.

Resumen y estructura de la tesis

En el **capítulo** 1 presentamos una introducción a las técnicas de búsqueda de exoplanetas y de caracterización de sus atmósferas más relevantes en el contexto de esta tesis. En primer lugar, comenzamos describiendo el método de detección de exoplanetas basado en la monitorización de la velocidad radial de las estrellas. En segundo lugar, introducimos el método que utiliza los tránsitos primarios de los exoplanetas para detectar su presencia. En tercer lugar, describimos la técnica de detección de exoplanetas mediante la toma directa de imágenes de los mismos.

A continuación, introducimos las principales técnicas desarrolladas para la caracterización de las atmósferas de los exoplanetas confirmados. En concreto, describimos la toma de espectros de trasmisión durante el tránsito primario, fundamentales para los capítulos con contribuciones científicas originales de esta tesis. A pesar de no haberse estudiado en profundidad en este trabajo, discutimos también la caracterización de exo-atmósferas mediante el estudio de la cara iluminada de los exoplanetas durante el eclipse secundario. Igualmente, introducimos la elaboración de curvas de fase por su gran relevancia en este campo científico. Por último, discutimos el método de caracterización más relevante para los capítulos originales de esta tesis, la correlación cruzada de espectros de alta resolución con modelos de la exo-atmósfera.

En los capítulos 2 y 3 introducimos las nociones de física atmosférica, transporte radiativo y análisis de datos de alta resolución más relevantes para esta tesis. Además, desarrollamos las técnicas existentes para aplicarlas en los capitulos con resultados científicos originales de esta tesis.

Especificamente, en el **capítulo** 2 presentamos una introducción a la física atmósferica básica para entender los sistemas exoplanetarios y la investigación realizada en esta tesis. Comenzaremos presentando la ecuación de equilibrio hidrostático, de importancia capital en el estudio de atmósferas planetarias y estelares. Seguidamente, estudiaremos las principales contribuciones al perfil de temperatura de las atmosferas planetarias y en qué condiciones éstas alcanzan el llamado equilibrio radiativo-convectivo. Seguidamente, discutiremos el modelado de la composición química de las atmósferas, basado en la asunción de equilibrio químico, mediante la minimización de la energía libre de Gibbs. Además, compararemos los resultados de estos modelos con aquellos que se obtienen al considerar procesos alejados del equilibrio, como la fotodisociación y el transporte vertical. Así, discutimos los primeros estudios que hacen uso de redes de cinética química verificadas en el laboratorio. En este contexto, discutiremos el estudio del cociente entre átomos de carbono y oxígeno en las exo-atmosferas, el cual nos puede aportar una valiosa información sobre la química, formación y evolución de los exoplanetas. Adicionalmente, discutiremos la dinámica y circulación atmosféricas en Jupiteres calientes, responsables de distribuir la energía

térmica y los compuestos en sus exo-atmósferas.

Proseguiremos con la introducción de los fenómenos que afectan a la forma de las líneas espectrales de absorción o emisión de los compuestos. En particular, describiremos los mecánismos de ensanchamiento natural, Doppler y Lorentz, y la convolución de los mismos. Esta convolución constituye la forma real de las líneas rotacionales-vibracionales observadas (perfil de línea Voigt) en las regiones espectrales estudiadas en esta tesis (visible e infrarrojo). En este punto, introduciremos la ecuación del transporte radiativo, cuya resolución nos revela el estado del campo radiativo en cada capa atmosférica. Aquí, introduciremos el algoritmo KOPRA para la resolución de la ecuación del transporte radiativo. En concreto, también discutiremos la adaptación de este algoritmo a la geometría de sistemas exoplanetarios que hemos realizado en esta tesis. Además, validaremos los espectros sintéticos de exo-atmósferas generados con KOPRA, en transmisión y emisión, frente a aquellos generados con otros algoritmos desarrollados por diversos grupos de investigación.

En el **capítulo** 3, presentaremos pormenorizadamente la técnica de correlación cruzada de espectros de alta resolución con modelos sintéticos de la absorción de las exo-atmósferas durante el tránsito primario. Específicamente, en esta tesis analizaremos los datos tomados con el espectrógrafo CARMENES. Aquí, describiremos todos los pasos realizados durante el análisis de los datos. Esto incluye la limpieza de rayos cósmicos, la normalización de los espectros y el enmascarado de las regiones espectrales más afectadas por la atmósfera terrestre. Seguidamente, expondremos de qué manera se eliminan las líneas de absorción y emisión terrestres y estelares. En esta tesis, haremos uso del algoritmo Sysrem, que ejecuta un análisis de componentes principales. A continuación, combinaremos la débil señal del planeta en el intervalo espectral cubierto, realizando una correlación cruzada de los espectros residuales con los modelos creados con KOPRA. Por último, describiremos las principales metodologías para medir la significancia de las señales: el cálculo de la relación señal/ruido de las funciones de correlación cruzada y la realización de tests-t de Welch.

En los capítulos que siguen, presentaremos las contribuciones y resultados científicos originales de esta tesis.

Concretamente, en los **capítulos** 4 y 5 aplicamos la técnica introducida en el capítulo 3 a datos tomados por el instrumento CARMENES en el infrarrojo cercano (NIR, por sus siglas en inglés). Dichos datos abarcan los tránsitos primarios de los jupiteres calientes HD 189733 b y HD 209458 b, respectivamente. En ambos casos, eliminamos la contribución telúrica (esto es, de la atmósfera de la Tierra) y estelar utilizando el algoritmo Sysrem. Este algoritmo es empleado de manera conservadora para HD 189733 b, mientras que desarrollamos una optimización para cada uno de los órdenes espectrales de CARMENES en el caso de HD 209458 b, siguiendo las pautas de publicaciones anteriores. Posteriormente, describimos la computación de modelos de la absorción de la exo-atmósfera de

los respectivos jupiteres calientes con KOPRA, utilizando los resultados más recientes de la bibliografía para sus perfiles de presión-temperatura y de abundancias.

Utilizando los modelos calculados, presentamos en estos capítulos las detecciones de vapor de agua en las atmósferas de HD 189733 b y HD 209458 b. En particular, para HD 189733 b, detallamos la detección de H_2O utilizando las dos bandas de absorción completamente cubiertas por el canal NIR de CARMENES. Además, discutimos la poca sensibilidad de esta técnica a los perfiles utilizados en la generación de los modelos y reportamos la no detección de metano en esta exo-atmósfera.

A continuación, estudiamos la posibilidad de recuperar la señal de agua, esta vez utilizando el algoritmo MOLECFIT para eliminar la contribución telúrica en esta técnica. Para ello, realizaremos la correlación cruzada de los espectros corregidos de telúricas con esta herramienta con los modelos generados con KOPRA. Así, discutimos la no detección de vapor de agua cuando se usa este algoritmo.

Con el objetivo de obtener información precisa de la temperatura y abundancia de agua en la exo-atmósfera, utilizamos la técnica de la *inyección inversa*. Esta técnica tiene como objetivo estudiar qué modelos de la exo-atmósfera cancelan mejor la señal de correlación cruzada. En este contexto, discutiremos cómo influye la degeneración en los parámetros relevantes para el cálculo de los modelos (por ejemplo, el radio y presión de referencia del exoplaneta, la abundancia de agua o la contribución de nubes y aerosoles) en nuestra capacidad para determinar el mejor ajuste.

Por otra parte, para HD 209458 b, discutimos la detección de H_2O, principalmente usando la banda de absorción parcialmente cubierta en torno a 1 μm. Esta es la detección de una señal de vapor de agua en un exoplaneta a través de las longitudes de onda más cercanas al visible hasta la fecha. Además, discutiremos las posibles razones por las que la señal no se encuentra con solidez, en este caso, usando las dos bandas más absorbentes cubiertas en el NIR con CARMENES. Entre ellas, destacaremos el fuerte impacto de la relación señal/ruido y la variabilidad de la atmósfera terrestre durante las observaciones en nuestra capacidad para detectar agua con esta técnica.

Para ambos exoplanetas, y en ambos capítulos, estudiaremos la presencia de corrimientos Doppler significativos de la señal de vapor de agua. Esto es una evidencia de la presencia de fuertes vientos en sus atmósferas, fluyendo desde la cara iluminada a la oscura. Compararemos ambos resultados y los pondremos en contexto con las predicciones de los modelos de circulación planetaria desarrollados por diversos grupos. Fruto de la comparación de las señales de agua detectadas en ambas exo-atmósferas, discutiremos la posible mayor abundancia de aerosoles en la atmósfera de HD 189733 b, con respecto a la de HD 209458 b, lo cual es consistente con resultados previos para estos exoplanetas.

En el **capítulo** 6, analizaremos los datos tomados para los Jupiteres calientes HD 189733 b y HD 209458 b durante el tránsito primario en diversas noches de observación con el canal visible de CARMENES. Para ello, adaptaremos la metodología aplicada en los capítulos anteriores al nuevo intervalo espectral. Seguidamente, expondremos los resultados preliminares obtenidos para cada noche por separado, y combinando la información obtenida a través de la correlación cruzada en los respectivos tránsitos de cada exoplaneta. Nuestros resultados preliminares revelan la primera detección de vapor de agua utilizando longitudes de onda en el espectro visible en HD 209458 b. Adicionalmente, los resultados respaldan una mayor extinción por aerosoles atmosféricos en el exoplaneta HD 189733 b, lo cual está en línea con nuestros resultados previos y otros estudios recientes.

Finalmente, en el **capítulo** 7, presentaremos las conclusiones principales de esta tesis. En concreto, nos centraremos en las implicaciones que tienen nuestras detecciones de vapor de agua sobre los conocimientos previos de la composición y dinámica de la atmósfera de ambos Jupiteres calientes estudiados. Adicionalmente, discutiremos los casos científicos que, en el futuro, podrían hacer uso de nuestros resultados para expandir el conocimiento sobre exo-atmosferas.

Contents

List of Figures

List of Tables

Chapter 1

Introduction

1.1 How do we find exoplanets?

Detecting planets orbiting distant stars (i.e., *exoplanets*) is one of the most challenging tasks of modern science. In fact, the first confirmed exoplanet was not published until nearly the end of the 20^{th} century (Wolszczan and Frail, 1992; Wolszczan, 1994). This is better understood when considering that the size, mass and flux of these planets usually are orders of magnitude lower than those of their host stars. Moreover, the light emitted by most of the confirmed exoplanets is buried inside the bright glare of their host stars, since they have very close-in orbits ($\sim 0.05\,\text{AU}$), which makes them very difficult to detect. This, however, does not come as a surprise, since this configuration (i.e., a short orbital period) favors the detection probabilities. For instance, the typical flux ratio in the visible for an exo-Jupiter orbiting at $\sim 0.05\,\text{AU}$ around a Sun-like star is of about 10^{-4}, which is detectable for current instrumentation (Angerhausen et al., 2015; Kreidberg, 2017). On the contrary, if the orbital distance were of $\sim 5\,\text{AU}$ (i.e., that of Jupiter), the flux ratios would be of only 3×10^{-9} (Board et al., 2019). The challenge is even greater for Earth-like exoplanets (orbiting at $\sim 1\,\text{AU}$), as this ratio drops to 5×10^{-10}.

Within the last three decades, scientists have developed several procedures to detect and/or confirm exoplanet candidates (Deeg and Belmonte, 2018, see Fig. 1.1). Most of these methods rely on the impact that the exoplanet produces on the light emitted by the star, which then travels towards us. In the following, we briefly describe the three detection methods that are most relevant for this thesis: the radial velocity, transit and direct imaging techniques. We also describe their optimal application scenario and their limitations. In depth descriptions of other methods, such as astrometry, gravitational microlensing, pulsar timing, among others, can be found in references such as, for example, Deeg and Belmonte (2018).

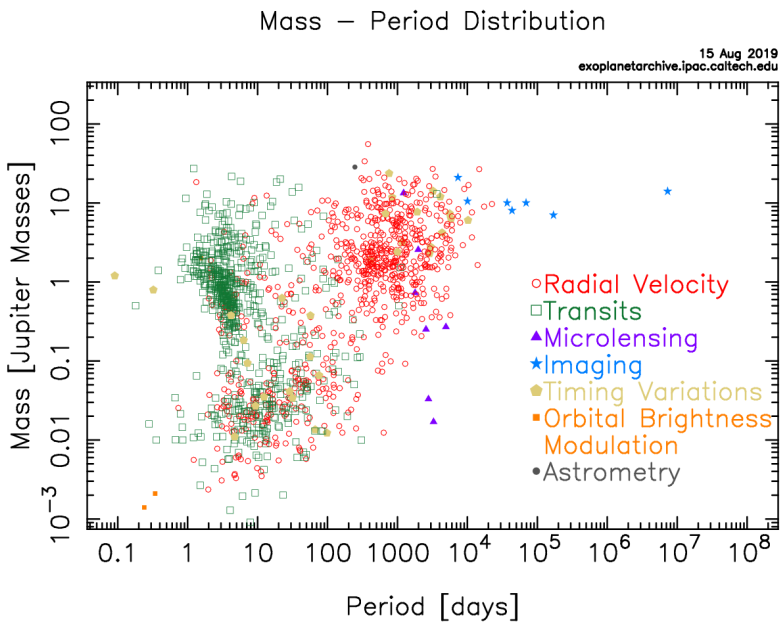

Figure 1.1: Mass – period distribution of confirmed exoplanets as of 21th August 2019. Different colors and markers represent the different techniques used. *Image credit:* NASA Exoplanet Archive.

1.1.1 Radial velocity

One of the most successful detection methods is the Radial Velocity (RV) method, also referred to as the Doppler method. This technique takes advantage of the fact that neither the star nor the exoplanet orbit one another, but both of them orbit the common center of mass of the system. Therefore, the RV technique is usually referred to as an "indirect" detection procedure, since it focuses of the reflex motion of the host star due to the presence of the planetary companion, and not on the exoplanet itself. By monitoring the light emitted by the star in a time-scale that encompasses several points of the exoplanet orbital phase, we can measure a Doppler shift of the stellar lines, i.e. a blueshift of the lines when the star is pulled towards us and a redshift when it moves away from the Earth. This Doppler-shift measurements reveal a "wobble" of the star as it moves towards and away from us (see Fig. 1.2). The modulation of this motion is then given by a Keplerian function in which the semi-amplitude of the RV variation of the star (K) can be expressed in the form (see, e.g., Wright and Gaudi, 2013)

$$\mathrm{K} = \left(\frac{2\pi G}{P}\right)^{1/3} \frac{M_p \sin(i)}{(M_p + M_*)^{2/3}} \left(1 - e^2\right)^{-1/2}, \tag{1.1}$$

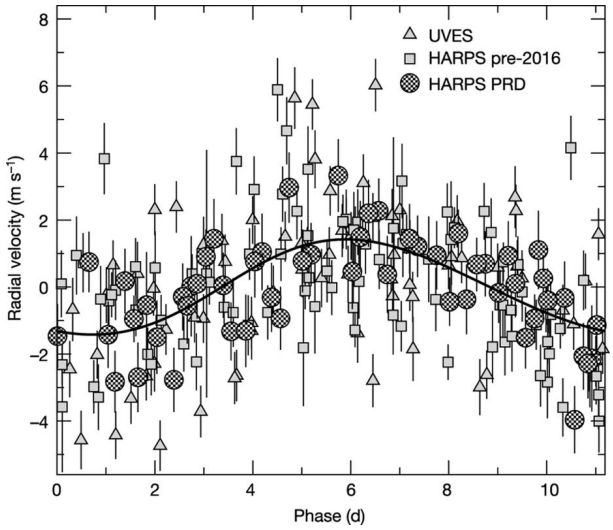

Figure 1.2: Phase-folded radial velocities of Proxima Centauri at the 11.2 d period of the exoplanet candidate Proxima b. Triangle markers are measurements within the Pale Red Dot campaign with HARPS, square markers show HARPS data gathered before 2016, and circles depict UVES data. The black line is the Keplerian best-fit for the data. *Image credit:* Figure taken from Anglada-Escudé et al. (2016).

where G is the Newton's gravitational constant, P is the planetary orbital period, M_p is the mass of the exoplanet, i is the inclination of the planetary orbit, M_* is the mass of the star, and e is the eccentricity of its orbit. The amplitude of this motion towards the observer is thus $\propto M_p \sin(i)$, which is a lower limit of the planetary mass depending on i. However, the inclination of the orbit is unknown when using this method alone and requires additional techniques to be determined.

In light of Eq. 1.1, the amplitude of the orbital motion and, in turn, the amplitude of the Doppler-shift, becomes larger the closer and more massive the exoplanet is. Also, this technique greatly benefits from the study of low-mass stars (e.g., M dwarfs), for which the amplitude of this motion becomes larger. This technique only allows us to estimate the minimum mass of the exoplanet, although it does not provide any information about its radius. If we are to detect Solar System analogs, from Jupiter- to Earth-like bodies, we need increasingly precise instruments. In particular, the RV amplitude induced in a Solar-type star by a Jupiter-like exoplanet orbiting at 1 AU is roughly 30 m/s, whereas it is of only 9 cm/s for an Earth twin at that distance (see, e.g., Wright, 2017).

In the last decade, the improved technology of spectrographs (i.e., their stability and calibration) and telescopes and the development of advanced data analysis procedures have been able to achieve the $10\,\mathrm{m\,s^{-1}}$ level (see e.g., the RV precisions of CARMENES, Quirrenbach et al., 2016, 2018; Reiners et al., 2018b). This explains the observed bias towards massive exoplanets, which

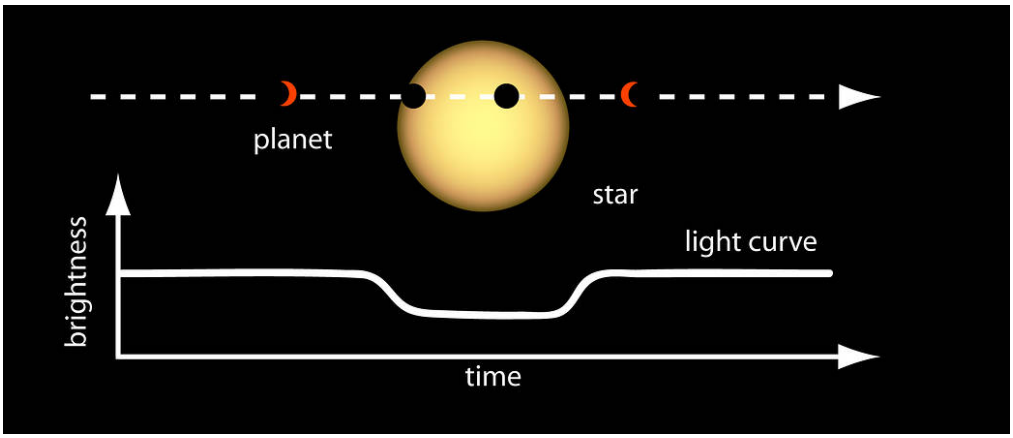

Figure 1.3: Basic sketch of the geometry of a transiting extrasolar system. The primary transit occurs as the planet passes in front of its host star from the Earth's perspective. Consequently, a dip is observed in the stellar brightness. *Image credit:* Figure taken from NASA Ames, https://www.nasa.gov/ames.

maximize the observed amplitude with the RV technique (see open red circles in Fig. 1.1). However, new instrumentation already in operation can push this precision already down to the $10 - 20\,\mathrm{cm/s}$ level (see, e.g., ESPRESSO, Pepe et al., 2014). If we now combine the new and more precise instruments with observations of smaller and less massive stars, this technique already allows us to detect Earth-mass exoplanets in the habitable zone of low-mass stars, such as M dwarfs (Anglada-Escudé et al., 2016; Ribas et al., 2018; Zechmeister et al., 2019b). In the coming decade, the challenge of detecting Earth analogues with this technique will require ultra-stable spectrographs that can reliably reach the level of 1 cm/s with access to a large collecting area (Pepe and Lovis, 2008; Wright, 2017).

1.1.2 Transits

In planetary systems with a large enough inclination with respect to our Solar System (i.e. nearly edge-on systems), exoplanets can be detected as their orbits put them periodically in front of their host stars (from the Earth's line-of-sight). This is known as the *primary transit* (see Fig. 1.3). The geometric probability for a transit to occur, at least partially (Winn, 2010; Deeg and Alonso, 2018), is given by:

$$p_{\mathrm{transit}} = \left(\frac{R_* \pm R_p}{a}\right)\left(\frac{1 + e\cos\omega}{1 - e^2}\right), \tag{1.2}$$

where R_* and R_p are the radii of the star and the exoplanet, respectively, ω is the observer's celestial longitude, and a is the semi-major axis of the exoplanet's

orbit[1]. In the case of a circular orbit, assuming $R_p \ll R_*$, and averaging over ω, the transit probability reduces to:

$$p_{\text{transit}} = \frac{R_* + R_p}{a} \simeq \frac{R_*}{a}. \tag{1.3}$$

In the case of a transit, this configuration yields a small reduction in the received stellar flux during a photometric time-series of the system, as the planetary disk blocks part of the light (see Fig. 1.3 and the top right inset in Fig. 1.4). To first order, the fraction of blocked flux, also known as *transit depth* ($\frac{\Delta F}{F}$), can be expressed as the ratio of areas between the exoplanet and the star:

$$\frac{\Delta F}{F} = \left(\frac{R_p}{R_*}\right)^2, \tag{1.4}$$

where we have neglected the exoplanet's night-side flux and assumed that the stellar disk has a uniform brightness.

In the case of a hot Jupiter in a 0.05 AU orbit around a Sun-like star ($P \sim 3$ days), the probability of observing a transit is, roughly, of a 10% and the depth of the transit would be of $\sim 1\%$, which is easily detectable with current instruments (see, e.g., Brown et al., 2001). However, for an Earth analogue at 1 AU, the transit probability drops to about 0.5%, with a small transit depth of 0.08% (Odunlade and Pauline, 2010; Deeg and Alonso, 2018). This is the reason behind this technique finding the majority of exoplanets at very close-in orbits, with short orbital periods (see green open squares in Fig. 1.1). In particular, transits of Earth-mass planets are more easily found with this method by looking at smaller stars. Although the transit probability is compromised in this case, the relative transit depth increases and the overall probability of detecting the small exoplanet is favored (e.g. Charbonneau et al., 2009). Nevertheless, although the transit technique is very fruitful, the vast majority of exoplanetary systems do not suffice the necessary conditions for presenting transits (i.e., unfavorable system inclination, undetectable planets with current instrumentation, etc.).

It is useful to define the *equatorial crossing time*, which is the duration of the transit if the system were completely edge-on (i.e., an impact parameter $b = 0$), as

$$T_{equ} = \frac{R_* P}{\pi a} \simeq \left(\frac{3P}{\pi^2 G \rho_*}\right)^{1/3}, \tag{1.5}$$

where ρ_* is the stellar density. With this definition, we are able to estimate the duration of any transit, T, as a function of b by calculating

$$T \simeq T_{eq}\left(1 - b^2\right)^{1/2}. \tag{1.6}$$

Hence, by monitoring several transits of the exoplanet we can infer its orbital period, which can then be used to calculate the stellar density using Eq. 1.13

[1] One may rewrite this expression in terms of the orbital period by using Kepler's third law.

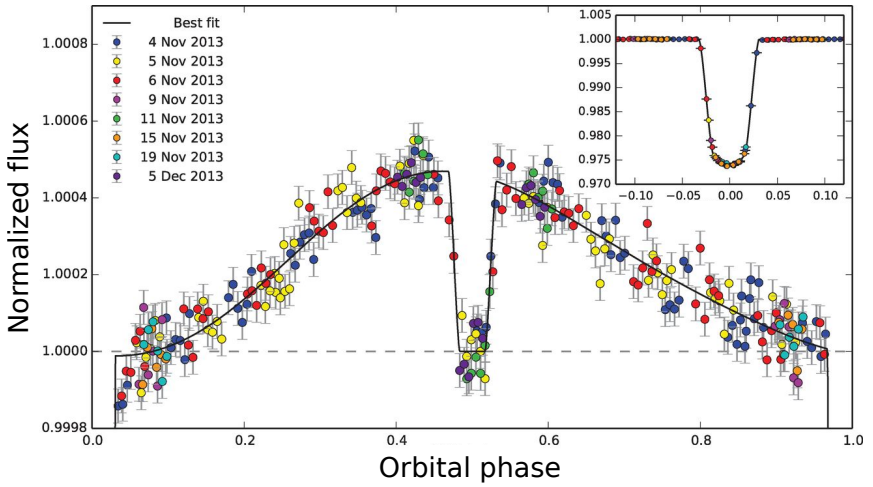

Figure 1.4: Band-integrated phase curve of the hot Jupiter WASP-43 b. The data have been binned in time and normalized with respect to the stellar flux. The different colors correspond to different observations with the *Hubble Space Telescope*. The normalized flux during the primary transit is depicted in the top right inset at an orbital phase around 0.0. The secondary eclipse can be seen at orbital phase of around 0.5. *Image credit:* Figure adapted from Stevenson et al. (2014).

(Wright and Gaudi, 2013). Interestingly, by combining the transit and RV methods, we can use these parameters in Eq. 1.1 (assuming $M_p \ll M_*$) to determine the mass function of the exoplanet, defined as $(M_p \sin i)^3 / M_*^{2/3}$. At this point, if the stellar mass was known from other measurements or modeled, we would be able to calculate the inclination of the orbit by means of the impact parameter and, hence, we would obtain a precise measurement of the planet's mass (Barragan, 2018). These parameters are then used to make preliminary hypothesis about the planetary density and hence composition, which opens a window for its characterization.

For transiting systems, as the exoplanet continues its orbit after the primary transit, we can observe the irradiated hemisphere of the exoplanet. In this configuration, the reflected stellar light and the emitted light from the planetary atmosphere add up to the light emitted by the star itself and, therefore, we can observe an overall increase of the received flux from the system. This is the so-called *phase curve* of the exoplanet, which further confirms its presence (see Fig. 1.4). As the planet is occulted by the star, the received flux decreases again and we can only see the original emission from the star itself. This is referred to as the *secondary eclipse*.

Additional planetary companions can be detected in systems with confirmed transiting exoplanets by searching for *Transit Timing Variations* (TTVs, see olive pentagons in Fig. 1.1). These are periodic shifts in the transit time interval produced by the gravitational influence of another exoplanet on the transiting

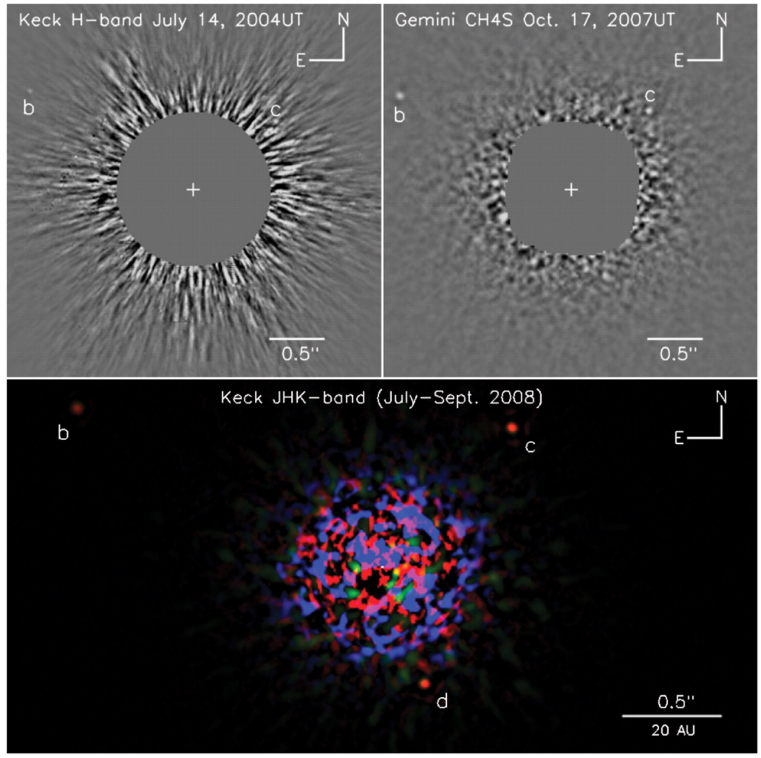

Figure 1.5: Discovery of three exoplanets in the HR 8799 system: HR 8799 b c d. The obtention of such result required the use of Angular Differential Imaging (ADI) processing. The image obtained with the Keck telescope on July 2004 is depicted in the top left panel. In the top right panel the GEMINI image recorded in October 2007 is shown. The bottom panel shows the J-, H- and K-band combined images obtained at two different epochs (i.e. July and September 2008) with the Keck telescope. The residual noise at the expected position of the star is left unmasked in the bottom panel. *Image credit:* Figure taken from Marois et al. (2008).

one. In fact, the detection of TTVs allows for a direct determination of the planetary masses, even without RV measurements of the star (Steffen et al., 2012; Agol and Fabrycky, 2018).

1.1.3 Direct Imaging

A direct detection of exoplanets is viable by using the High-Contrast Imaging technique (HCI, see crimson stars in Fig. 1.1). In fact, this is the key feature distinguishing this technique from those presented above, which rely on indirect measurements. The light coming directly from the exoplanet not only represents a solid evidence for its existence, but also carries invaluable information about its current condition and internal structure (Brown and Burrows, 1990).

In order for an exoplanet to be directly imaged with state-of-the-art instrumentation, we need to restrict our observations to those systems in which the

point-like light received from the exoplanet can be spatially separated from that emitted by the host star, which outshines the exoplanet completely otherwise. This step is mainly hindered by two factors: On the one hand the diffraction of the light in the aperture of the instrumental optics bears a certain spatial extension which is inversely proportional to the aperture's size and proportional to the wavelength. Thus, the point-source light appears as an Airy pattern that, in the case of circular apertures, corresponds to an Airy function (Brown and Burrows, 1990). That is, a central light peak and concentric illuminated rings with decreasing strength away from it. Therefore, in order to separate the star from the planet we need them to be separated by an angular distance $\theta > 1.22\frac{\lambda}{D}$, being λ the wavelength and D the diameter of the aperture.

The other factor limiting our capabilities of separating the point-like sources from the star and the exoplanet is the variability of our own atmosphere, which is changing constantly and, usually, rapidly. This turbulent behaviour diffracts the light coming from the star and the exoplanet in random directions producing visible changes in their brightness and position[2]. This unwanted effect masks the extrasolar systems with star-planet separations smaller than the so-called *seeing limit*. Nevertheless, this distortion is successfully mitigated by the use of the *adaptive optics* technology (AO, see e.g., SPHERE at the Very Large Telescope, Beuzit et al., 2008). AO is based on the measurement of optical aberrations and the operation of several deformable mirrors that can compensate the wavefront aberrations, which are induced by the atmospheric turbulence (Babcock, 1953; Guyon, 2018). Hence, AO unmasks many systems that were inaccessible before. In addition, the use of coronagraphs, which block the light from the star on the telescope's axis, enhances by several orders of magnitude the planet-star contrast ratios (Snellen et al., 2015).

Overall, only massive and bright exoplanets such as those around young stars ($\sim 1\,\mathrm{Gyr}$) and orbiting at least at $\sim 5\,\mathrm{AU}$ are suitable to be discovered and studied by using this technique with current technology (Bowler, 2016). In fact, a Jupiter-like exoplanet orbiting a Sun-like star at Jupiter's orbital distance in an extrasolar system at 10 pc would require a sensitivity in the order of 10^{-7} in the near infrared for an angular separation of $0.5''$ (Madhusudhan, 2019), which is about three orders of magnitude weaker than the currently measurable signals. Interestingly, the detection of the exoplanets and the characterization of their exo-atmospheres are done simultaneously with this technique. This is because the light coming from the exoplanet has direct information on the presence of atmospheric compounds and the temperature profile, in a similar way as for emission spectra during the secondary eclipse.

To mention a few examples, the exoplanets orbiting the star HR 8799 were directly imaged by Marois et al. (2008, 2010) (see Fig. 1.5), a Jupiter-like exoplanet around HD 95086 was also directly imaged by Rameau et al. (2013a,b),

[2]This is the reason why the stars twinkle when observed from the ground.

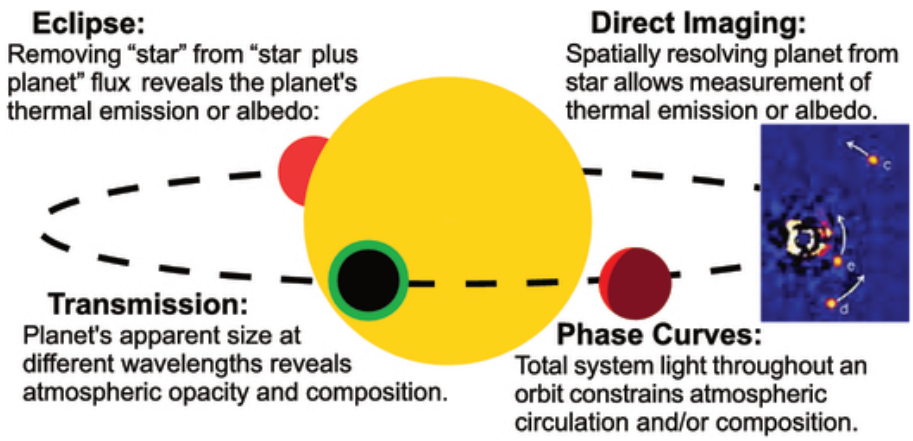

Figure 1.6: Different techniques designed for the characterization of transiting exoplanet systems. The primary transit allows us to obtain transmission spectra that probes the terminator region of the exo-atmosphere (green annulus). As the orbit continues, we can monitor the received flux for different planetary orbital phases to characterize the illuminated hemisphere gradually. Before and after the secondary eclipse (i.e., when the star is between the Earth and the exoplanet) we can compare the flux received from the star with and without the exoplanet's contribution to obtain the emission spectrum from the dayside of the latter. In addition, some systems allow for a direct imaging of the exoplanets, hence providing an isolated measurement of the exo-atmosphere. *Image credit:* Figure taken from Crossfield (2015).

β Pictoris b was observed by Bonnefoy et al. (2013) and Currie et al. (2013), etc. Future instrumentation at large ground-based telescopes (see, e.g., the EPICS instrument on the future 39 m E-ELT telescope, Kasper et al. (2010)) with improved AO systems, and new space instruments (e.g., the James Webb Space Telescope and the future NASA's *WFIRST*) will push this technique further enabling the study of smaller, dimmer and closer-in exoplanets (Noecker et al., 2016; Beichman and Greene, 2018; Madhusudhan, 2019).

1.2 How do we characterize the exo-atmospheres?

Acquiring knowledge about the size, mass and orbital periods of exoplanets is crucial for their study. However, in order to further characterize these bodies, we need to study the light that interacts with their atmospheres. This light has two major contributions: Scattered and reflected stellar photons, mainly in the visible (VIS), and photons emitted by the constituents of the atmosphere in the Infrared (IR) thermally. The fraction of the total stellar radiation that is re-emitted back out into space at all wavelengths and phase angles is known as the *Bond Albedo*, and its knowledge is crucial in the estimation of the energy budget of the exo-atmosphere which, in turn, allows us to estimate the equilibrium temperature of the body. This has been widely studied in the past by analyzing the thermal radiation emitted by exoplanets (Charbonneau et al., 2005; Knutson

et al., 2007a; Hansen, 2008; Demory et al., 2012, 2016).

Sometimes, the relevant information does not come from the arriving photons in our telescopes, but from the missing ones at certain wavelengths. That is, the compounds in the atmosphere of exoplanets absorb part of the stellar radiation at certain wavelengths and each one of them imprints a unique absorption pattern in the spectra. Thus, the basic analysis procedure for exo-atmospheric characterization is based on identifying unique spectral features that can be attributed to certain constituents (e.g., water vapour, methane, carbon monoxide, etc.). There are, however, other relevant processes that severely impact the light we receive from exoplanets. For instance, the presence of atmospheric aerosols can be inferred from evidences of scattering. In the case of Rayleigh scattering[3], the strong spectral dependence (i.e. $\sim \lambda^{-4}$) results in stronger extinctions towards shorter wavelengths and hence, the spectra show a scattering slope (Etangs et al., 2008a,b; Sing et al., 2011, 2014). Moreover, the presence of clouds in the atmosphere can lead to a partial or complete blockage of photons coming from the deepest layers of the atmosphere. Thus, the gathered spectra appears almost flat with a surprising lack of spectral features (Demory et al., 2013; Morley et al., 2013; Knutson et al., 2014; Kreidberg et al., 2014; Mbarek and Kempton, 2016; MacDonald and Madhusudhan, 2017; Espinoza et al., 2018).

Furthermore, some exoplanets have been shown to present evaporating atmospheres (see, e.g., Owen, 2019). Typically, this occurs in close-in exoplanets in extreme irradiation environments, which induce a hydrodynamic escape in their atmospheres. That is, their upper atmospheres expand faster than the planetary escape velocities and, hence, particles can be lost to space. The escape of hydrogen atoms has been studied in the past by, for example, probing the Lyman-α feature (see, e.g., Vidal-Madjar et al., 2003), or, very recently, the helium triplet absorption (see, e.g., Spake et al., 2018). Interestingly, the envelope of escaping particles can expand asymmetrically, thus forming cometary-like tails (see, e.g., Nortmann et al., 2018).

Out of the thousands of exoplanets known at the time of writing, only $\sim$ 100 exo-atmospheres have been detected so far either from space telescopes or ground-based instrumentation (Madhusudhan, 2019). In this section, we will describe some of the characterization techniques for different configurations of the star – exoplanet system, their limitations, and future prospects. We will restrict ourselves to the most relevant techniques, which are based on transmission and emission spectroscopy during the primary transit and secondary eclipse of exoplanets, respectively, the study of phase curves, and the analysis by using high dispersion spectroscopy with ground-based spectrographs.

[3]Rayleigh scattering describes the elastic scattering of light produced by spheric particles which are much smaller than the wavelength of the photons.

1.2.1 Transmission spectroscopy in the primary transit

Transit spectroscopy is one the most successful techniques for characterizing exoplanet atmospheres. As the exoplanet transits in front of its host star (see, e.g., Figs. 1.3 and 1.6), we can perform a multi-wavelength study of the light blocked by the exoplanet with photometric or spectroscopic measurements. Why are multi-wavelength observations extremely relevant for atmospheric characterization? To answer this fundamental question, let us assume a transparent atmosphere at all wavelengths, except for those corresponding to known excitation levels of a certain compound. When observing the transit at wavelengths in which the atmosphere is transparent, the transit depth corresponds to that of the planetary disk (i.e. optically thick at all wavelengths). On the contrary, when probing at the *fingerprint* wavelengths of the constituents of the exo-atmosphere, the transit depth appears deeper, as if the planetary radius was larger. The stronger the absorption at a certain wavelength, the deeper the transit depth and the larger the exoplanet's apparent radius is. The transit geometry allows us to probe a small but key fraction of the exo-atmosphere, the annulus (see green annulus in Fig. 1.6) corresponding to the *terminator*, which is the atmospheric region between the irradiated and the dark side of the exoplanet.

Usually, the observed transiting exoplanets are tidally locked and the terminator becomes a highly dynamic region, driven by often extreme temperature gradients (Demory et al., 2016; Caldas et al., 2019). These, in turn, trigger powerful winds that tie to the redistribution of energy in the atmosphere as a whole (Showman and Polvani, 2011; Showman et al., 2013). Moreover, condensates are expected to form at the terminator, as condensible species are pushed to lower temperatures (see, e.g., Fortney, 2005; Moses et al., 2011; Marley et al., 2013; Morley et al., 2013).

The idea of the characterization of exo-atmospheres using transit measurements is not new, as it was already proposed at the beginning of the current century (Seager and Sasselov, 2000; Brown, 2001). In essence, the difference between the *in-transit* spectra and the *out-of-transit* spectra, normalized by the *out-of-transit* spectra, provides us with the so-called *transmission spectrum*, which encodes the absorption from the exoplanet (i.e., the solid disk and the atmosphere). The first successful detections of absorption at the sodium doublet and in the Lyman-α line by using transmission spectra in the primary transit of the hot Jupiter HD 209458 b arrived shortly after with the results obtained by Charbonneau et al. (2002) and Vidal-Madjar et al. (2003), respectively. These findings contributed to further develop the field, which was consolidated in following years with many more solid detections of atomic and molecular features (Tinetti et al., 2007; Burrows et al., 2008; Désert et al., 2008; Snellen et al., 2008; Madhusudhan and Seager, 2009; Wyttenbach et al., 2015; Casasayas-Barris et al., 2017; Nortmann et al., 2018).

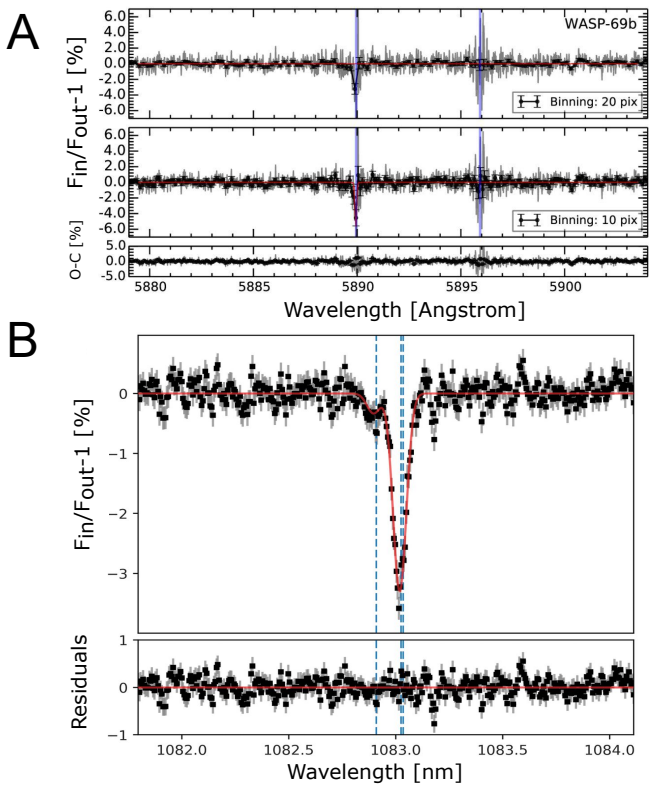

Figure 1.7: A: Detection of sodium in the atmosphere of WASP-69 b with the HARPS-North instrument. B: Detection of the Helium I triplet features in WASP-69 b with the CARMENES instrument. *Image credit:* Figures A and B adapted from Casasayas-Barris et al. (2017) and Nortmann et al. (2018).

In Fig. 1.7, we show examples of some of the detections with the largest significances obtained by using transmission spectroscopy. In particular, Fig. 1.7A presents a detection of sodium in the atmosphere of the hot Jupiter WASP-69 b at the 5-σ level (Casasayas-Barris et al., 2017). Such results might be used, along with new data, to characterize the atmosphere of this hot Jupiter by analyzing the line profiles of the doublet (see Sect. 2.2). Moreover, Fig. 1.7B shows the first ground-based detection of the helium triplet absorption at a signal-to-noise ratio of 18 (Nortmann et al., 2018). The study of the helium triplet feature in exo-atmospheres is a nascent field that has opened a new window for the study of atmospheric escape in strongly irradiated atmospheres (see, e.g., Oklopčić and Hirata, 2018; Spake et al., 2018). In particular, the high spectral resolution that can be achieved by ground-based instrumentation (even at 4 m-class telescopes) provides an absorption profile that contains information not only on the helium density (and hence on the hydrogen density), but also on the dynamics (i.e., velocities) of the thermospheres and the escape rate of these evaporating

atmospheres (see, e.g., Nortmann et al., 2018; Salz et al., 2018; Lampón et al., 2019).

In addition, other works have aimed at the study of the Rayleigh scattering slope and cloud coverage in hot Jupiter atmospheres. From this analyses, a classification of the hot Jupiter atmospheres can be established as a function of their haziness (see Fig. 1.8 and Sing et al., 2016). The extinction by atmospheric hazes and the presence of clouds at the terminator of exoplanets can partially, or completely, obscure the atmospheric fingerprints. Therefore, the observation of almost featureless spectra provides information about the presence of volatiles, the mean molecular weight, among other parameters of the exo-atmospheres (Sing et al., 2011; Kreidberg et al., 2014; Barstow et al., 2016; Sing et al., 2016; MacDonald and Madhusudhan, 2017).

The occultation of stellar photons by the planetary disk produces a decrease in the received brightness which is proportional to the ratio between the areas, in accordance with Eq. 1.4. However, the apparent disk of the exoplanet appears larger at the frequencies corresponding to strong atomic or molecular transitions of the atmospheric compounds. That is, the height of the outer optically thick atmospheric layer, also referred to as the *effective height*, $r_{\mathrm{eff},\,\nu}$, depends on the frequency ν at which we probe the exo-atmosphere. Thus, the transit depth depends on the frequency-dependent area of the atmospheric annulus, as seen from the Earth, in the form:

$$\frac{\Delta F_\nu}{F_\nu} = \frac{(R_p + r_{\mathrm{eff},\,\nu})^2 - R_p^2}{R_*^2} = \frac{2R_p r_{\mathrm{eff},\,\nu} + r_{\mathrm{eff},\,\nu}^2}{R_*^2} \simeq \frac{2R_p r_{\mathrm{eff},\,\nu}}{R_*^2}, \tag{1.7}$$

where, in the last step, we have used that $r_{\mathrm{eff},\,\nu}$ is small when compared to R_p. This still holds even for gas giant exoplanets, despite having a more expanded atmosphere and larger radii than rocky worlds. Thus, although the transit depth for gas giants in close-in orbits can be of about 1%, the variations around this value when probing at different wavelengths are small, of the order of $\sim 10^{-3} - 10^{-4}$ at best (Crossfield, 2015). Fortunately, these small transit depth variations are detectable with current instrumentation, allowing us to infer the presence of exo-atmospheric absorbers such as sodium, potassium, water vapor, methane, carbon monoxide, carbon dioxide, hydrogen cyanide, titanium and/or vanadium oxide, etc.

Interestingly, we can estimate the transit signal that would be expected for a certain exoplanet so as to determine the feasibility of its characterization with this technique (see, e.g., Sing, 2018). This can be done by using the atmospheric scale height, given by

$$H = \frac{\kappa_B T}{\mu g}, \tag{1.8}$$

where κ_B is the Boltzmann constant, T is the temperature, μ is the mean mass of the atmospheric particles, and g is the gravitational acceleration. The scale

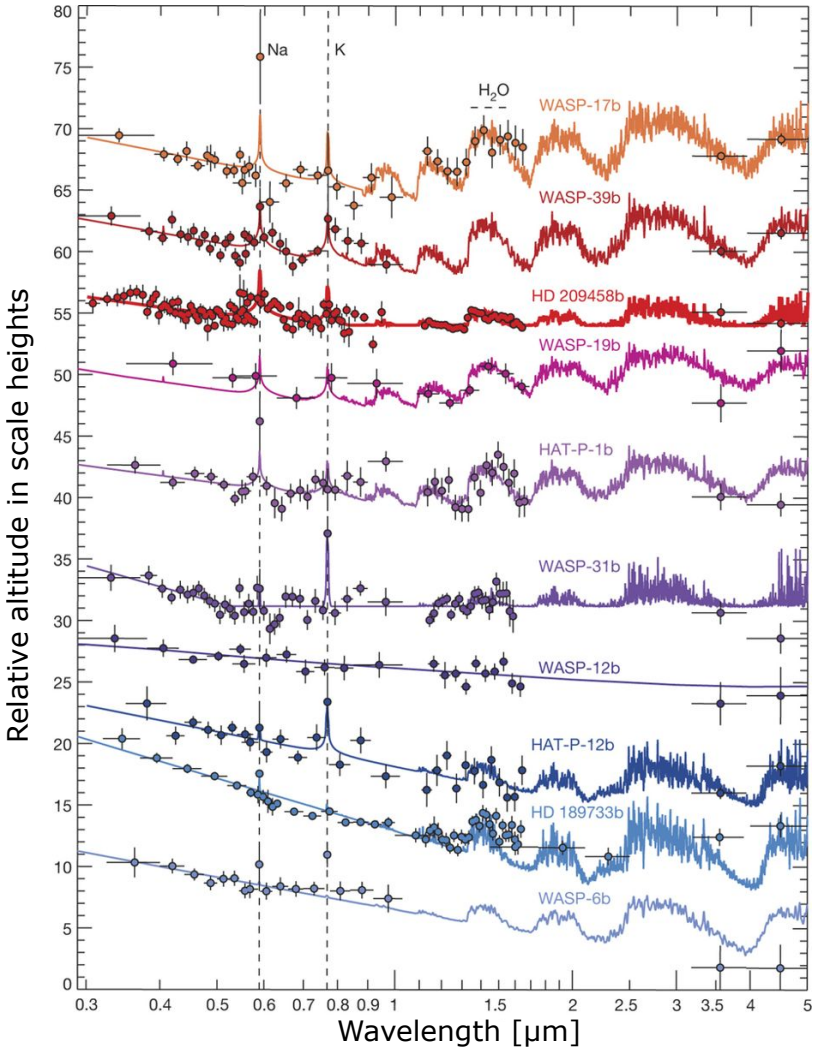

Figure 1.8: Transmission spectra in the primary transit for several hot Jupiters gathered with different space instrumentation. The best-fit models are shown for each exoplanet. The spectra have been offset in the vertical axis for clarity. We can observe rather clear atmospheres (e.g., WASP-17 b, WASP-39 b), the influence of scattering by hazes at optical wavelengths (e.g., HAT-P-12 b, HD 189733 b) and the impact of clouds in exoplanets with flat spectra (e.g., WASP-31 b, WASP-12 b). *Image credit:* Figure adapted from Sing et al. (2016).

height represents the altitude at which the atmospheric pressure decreases by a factor of e with respect to the zero altitude reference[4]. Alternatively, the scale height can be viewed as the thickness that an atmosphere would have above the reference planetary radius if it had a constant pressure and temperature, equal

[4]In the Earth's atmosphere, $H = 8.5\,\mathrm{km}$ if $T = 290\,\mathrm{K}$. For a typical hot Jupiter, at $T \sim 1000\,\mathrm{K}$, $H \sim 360\,\mathrm{km}$.

to those at the reference radius. Thereby, we can approximate the annular area of one scale height of the exo-atmosphere by calculating:

$$\mathcal{A} = \frac{(R_p + H)^2 - R_p^2}{R_*^2}. \tag{1.9}$$

In addition, taking into account that $H \ll R_p$ even in the case of hot Jupiters, this expression reduces to

$$\mathcal{A} \simeq \frac{2R_pH}{R_*^2}, \tag{1.10}$$

which is very similar in form to Eq. 1.7, but neglects the dependency with the frequency (the frequency dependent area of the exo-atmosphere will be explored in Sect 2.4.1). In this way, an estimation of the expected signal for many exoplanets is rather easy to compute, although it does not representent an accurate characterization of the objects. In fact, this quantity has to be weighted by the V magnitude of the star, which will determine if the signal-to-noise ratio of the observations is high enough to allow for the characterization of the exo-atmospheres.

For instance, the expected signal for the two most well-studied hot Jupiters, HD 189733 b and HD 209458 b, is of $\mathcal{A} \sim 0.02\%$, whilst other exoplanets such as WASP-39 b have a much larger transit signal, of $\sim 0.07\%$ (see, e.g., Fig. 5 in Sing, 2018). However, the first two exoplanets orbit rather bright stars with $V \sim 7.6$, whereas the latter orbits a much dimmer star with $V \sim 12$. Thus, although the atmosphere of WASP-39 b can be studied due to its large transit signal (Fischer et al., 2016), HD 189733 b and HD 209458 b present more advantageous conditions for a succesfull characterization due to the larger magnitude of their host stars. Moreover, the majority of known transiting exoplanets orbit dim stars ($V > 11$) at transit signals $< 0.02\%$, which is the reason behind the difficulty for characterizing the majority of known transiting exoplanets by using transmission spectroscopy.

1.2.2 Emission spectroscopy and phase curves

We now shift our attention to studying exoplanet atmospheres by analyzing their emitted and reflected fluxes. When the appropriate geometry conditions are met, exoplanets are eclipsed by their stars at the moment of superior conjunction (see Fig. 1.6). Right before and after this secondary eclipse, the flux received from the system is slightly larger due to the incoming exoplanet's flux (see Fig. 1.4). Thus, the incoming flux with stellar and planetary components, normalized by the stellar flux (i.e., measured, for instance, at superior conjunction) yields the planetary spectrum which bears unique information about its main absorbent species and temperature at different pressure levels.

We can estimate the dip in the light curve when the exoplanet is eclipsed by the star as

$$\frac{\Delta F_\nu}{F_\nu} = \frac{F_p R_p^2}{F_p R_p^2 + F_* R_*^2} \sim \frac{F_p R_p^2}{F_* R_*^2}, \tag{1.11}$$

where F_p is the flux coming from the dayside of the exoplanet and F_* is the stellar flux. In fact, we can approximate this expression by assuming blackbody emissions and introducing the Planck's function $\mathcal{B}_{\nu,T}$. Also, we can take into account that the planetary flux is the sum of two contributions. That is, the planet's own thermal emission and the reflection of the stellar light, which will depend on the planet's Bond albedo, $\mathcal{A}_B = (3/2)\mathcal{A}_g$, where $\mathcal{A}_g$ is the geometric albedo, which is defined as the ratio of planet's brightness, as seen from the light source, with respect to that of a *Lambert sphere*[5]. Thus, we obtain (Esteves et al., 2015; Tarnas, 2016):

$$\frac{\Delta F_\nu}{F_\nu} = \left(\frac{R_p}{R_*}\right)^2 \frac{\mathcal{B}_{\nu,T_{eq}} + \mathcal{B}_{\nu,T_{eff}} \left(R_*/a\right)^2 \mathcal{A}_g}{\mathcal{B}_{\nu,T_{eff}}}, \tag{1.12}$$

where T_{eq} and T_{eff} are the planet's atmospheric equilibrium temperature and the stellar effective temperature, respectively. By imposing a balance between the incoming and outgoing flux in the exo-atmosphere, both temperatures are related by

$$T_{eq} = T_{eff} \left(\frac{f\,(1-\mathcal{A}_B)\,R_*^2}{4a^2}\right)^{1/4}, \tag{1.13}$$

where f is the heat redistribution factor, which equals 1/4 for isotropic models (Burrows, 2014b). Thus, in the case of a typical hot Jupiter, we can expect a dimming in brightness in the NIR of about $\Delta F/F \sim 10^{-3}$ (Brogi, 2014).

In a similar way as for transmission spectroscopy, the dimming in brightness will change with frequency. That is, the photosphere of the exoplanet is located at the atmospheric region at which the transition from an optically thick (i.e., opaque) to an optically thin (i.e, transparent) regime occurs at a certain frequency. This means that for those ν at which the exo-atmosphere is almost transparent, we will probe its deeper regions. On the contrary, for those frequencies at which the atmosphere is optically thick we will probe higher-altitude layers (see, e.g., Line et al., 2013).

For instance, in the scenario of a decreasing temperature with altitude, the flux received at optically thick frequencies will be lower than that of the flux continuum. That is, the bulk spectrum at those frequencies is formed at high atmospheric layers, for which the temperature and, in turn, the emitted flux, is lower. On the contrary, the flux continuum is mainly formed at the deepest layers, which have a higher temperature.

[5] A Lambert sphere is an ideal, flat, and diffusing surface, whose radiance is independent of the angle at which it is observed (Esteves et al., 2013).

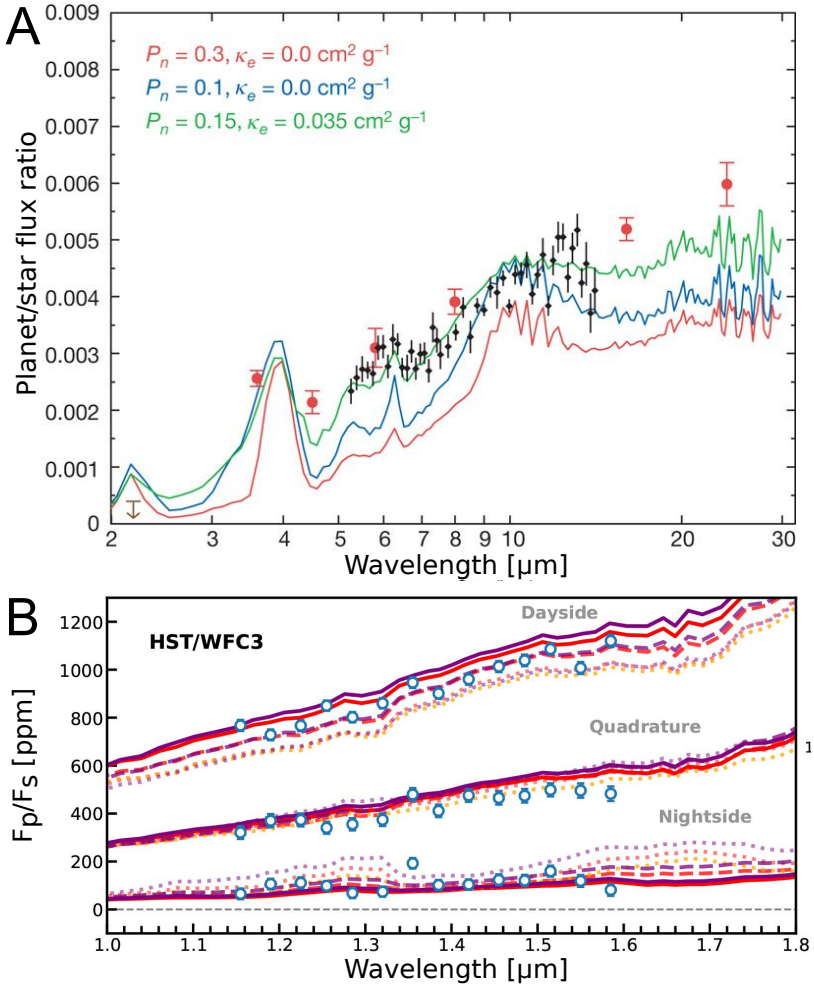

Figure 1.9: A: Flux ratio between the exoplanet HD 189733 b and its host star. Black data points were obtained with the Spitzer Space Telescope's Infrared Spectrograph (IRS). Red data are the broadband measurements taken with all Spitzer detectors (IRAC, IRS and the Multiband Imaging Photometer). Different models are shown as a function of the heat redistribution parameter (P_n) and the upper atmospheric opacity (κ_e). B: Phase-resolved spectra for the day-side, night-side and at quadrature of WASP-18 b taken with the HST/WFC3. A range of global circulation models is shown. *Image credit:* Figure A adapted from Grillmair et al. (2008). Figure B adapted from Arcangeli et al. (2019).

The opposite occurs in the case of atmospheres with inversion layers, for which the temperature increases with altitude in some regions (i.e., stratospheres). Thus, studying the flux received at optically thick frequencies would result in the appearance of emission features. That is, the flux received at those frequencies is larger than at the continuum, since the probed temperature is higher. Hence, this technique also allows us to detect compounds in the exo-

atmosphere by constructing the so-called planetary *dayside spectrum* (see, e.g., Fig. 1.9A).

Furthermore, we can also monitor the evolution of the received flux with time in order to cover a wide range of planetary orbital phases. We can then analyze the obtained light curve in order to identify differences in the received flux when the day- or the night-side of the exoplanet face the line of sight from the Earth. These observations, spanning different orbital phases across one or multiple orbits, are known as *phase curves* (see, e.g., Fig. 1.9B). In the case of extreme temperature gradients between the illuminated and non-illuminated hemispheres of the exo-atmosphere, we would observe a sinusoidal behaviour of the light curve, with its maximum brightness occurring right before and after the secondary eclipse. That is, when nearly the whole illuminated hemisphere is pointing towards the Earth (see, e.g., Fig. 1.4, and Knutson et al., 2012; Stevenson et al., 2014; Demory et al., 2016). Naturally, the flux received will be minimum at the times right before and after the transit, when we can only observe the night hemisphere (see Fig. 1.9B). The difference between the maximum and minimum flux received can be used to infer the effectiveness of the redistribution of thermal energy in the atmosphere. This provides invaluable information, for instance, about the atmospheric dynamics (see, e.g., Showman and Polvani, 2011; Showman et al., 2013).

In addition, phase-curves can also provide information about the atmospheric constituents. A particularly interesting scenario is that observed for some exoplanets that present brightness peaks occurring after the secondary eclipse (i.e., also referred to as *post-occultation*). For instance, this is the case of the exoplanets Kepler-7 b, Kepler-8 b, Kepler-12 b, and Kepler-41 b (see, e.g., Esteves et al., 2015). Interestingly, in the case of Kepler-7 b, the post-occultation brightness peak can be linked to a non-uniform cloud coverage of the exo-atmosphere (Demory et al., 2013; Hu et al., 2015; Muñoz and Isaak, 2015; Muñoz, 2018). Linear polarization of the reflected stellar light by the exo-atmosphere can be analyzed so as to infer information about the particle size and optical properties of these condensates. Specifically, this can be studied by using broadband polarimetry (see, e.g., Berdyugina et al., 2011; Bott et al., 2016) or, alternatively, by using high-dispersion spectro-polarimetry coupled with a cross-correlation analysis (see, e.g., Moutou et al., 2007; Muñoz and Isaak, 2015; Muñoz, 2018).

1.2.3 High dispersion spectroscopy

One of the most successful techniques applied to the characterization of exo-atmospheres is that based on the use of high dispersion spectroscopy (HDS, $R \sim 50\,000 - 100\,000$) and a cross-correlation analysis. In particular, we can take advantage of the fact that close-in exoplanets move much faster than their host stars. In fact, the radial component of their orbital velocities can be in

the order of 100 km/s, which is $\sim 1000\times$ larger than that corresponding to the star. Therefore, the resulting velocity change of the exoplanet with respect to the Earth (i.e., tens of km/s) is detectable in the planetary lines by using high-resolution spectra. That is, if we monitor the stellar light, we will find that the absorption lines of the exoplanet's atmosphere are Doppler shifted and can be differentiated from those of the Earth and the star (Snellen et al., 2010; Brogi et al., 2012).

Another crucial aspect of this technique is that it allows us to resolve thousands of rotational-vibrational lines in the considered spectral interval ($N_{\rm lines}$) and, hence, to combine their information so as to enhance the planetary signal by a factor of $\sqrt{N_{\rm lines}}$. We can now use this to attempt the challenging detection of molecular features, which are even weaker than atomic absorption lines (e.g. H_2O absorption features are in the order of 10^{-5} in the NIR, whilst the sodium or the helium I triplet features can reach strengths of about $1-4\,\%$, Nortmann et al., 2018). A usual procedure to merge this information is to cross-correlate the observed spectra with a template of the expected exo-atmospheric absorption. In fact, the standard procedure is to Doppler-shift the model template in a wide range of planetary radial velocities and, consecutively, cross-correlate these shifted templates with the data. In the case of a positive detection, we would expect to observe larger cross-correlation values along the expected radial velocities of the planet during transit (see Fig. 1.10A). By co-adding this information (i.e., cross-correlation values) over time, we can construct a *Cross-Correlation Function* (CCF) in which the entire absorption from the exoplanet materializes in a CCF peak (see Fig. 1.10B).

This technique is sensitive enough to provide some insights of the atmospheric dynamics in the form of approximate measurements of the average wind velocity in the probed exo-atmosphere. This is because once the spectra have been properly shifted to the rest-frame of the exoplanet, it is still possible to observe an extra blue or redshift of the signal in some cases (Snellen et al., 2010; Brogi et al., 2018; Alonso-Floriano et al., 2019a; Sánchez-López et al., 2019). The additional Doppler-shift can be explained by invoking strong winds in the upper layers of the exo-atmosphere, which are in fact predicted for hot Jupiters (Rauscher and Menou, 2013; Showman et al., 2013; Amundsen et al., 2016).

The high-resolution instrumentation used to perform this kind of studies is only available in ground-based observatories due to the necessary instrumental volume[6]. This introduces a new challenge: The cleaning of the absorption features of the Earth's atmosphere (the *tellurics* from now on). This is arguably the most delicate step of the technique, since the telluric signal is orders of magnitude stronger than any of the target features and dominates the recorded spectra and thus, we need to remove it carefully so as to preserve the wanted information. However, as we discuss in more detail in Chapter 3, the telluric

[6]Launching these instruments to space is financially too expensive.

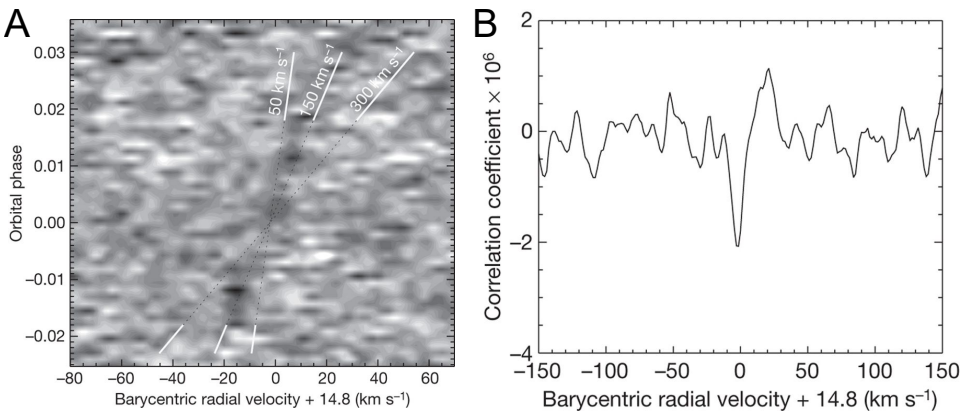

Figure 1.10: A: Cross-correlation values as a function of the planetary orbital phase and velocity. A model of the exo-atmospheric CO absorption has been used as a template for the cross-correlation. The CO signal can be seen as a trail of cross-correlation values (in black) along the expected planet's velocities during transit (with a semi-amplitude of the orbital velocity, $K_p \sim 150$ km/s). B: Co-adding of the cross-correlation values of panel A along the 150 km/s trail. A detection of CO in HD 209458 b is evidenced by a significant cross-correlation peak. *Image credit:* Figures A and B taken from Snellen et al. (2010).

lines do not shift their wavelength with respect to the observatory (i.e., the change is negligible when compared to that of the exoplanet absorption lines). Thus, we will use this to separate them from the exoplanet lines, which have large and changing Doppler shifts.

This technique delivered the first successful molecular detection when it was applied by Snellen et al. (2010) to the CRyogenic high-resolution InfraRed Echelle Spectrograph (CRIRES) on the Very Large Telescope (VLT). CRIRES was then used to find the cross-correlation signal produced by the absorption of CO in the atmosphere of HD 209458 b. Ever since, the field of spectroscopic characterization at high spectral resolution using cross-correlation flourished. For instance, the signatures of water vapor, CO, Fe and TiO have been found in different transiting exoplanets at 8-m class telescopes (Birkby et al., 2013; Kok et al., 2013; Schwarz et al., 2015; Brogi et al., 2016; Nugroho et al., 2017; Hoeijmakers et al., 2018a).

More recently, HDS has been applied with great success at smaller, 4-m class telescopes equipped with highly-stabilized spectrographs. Water vapor has been the priority target in these cases in the last few years due to the forest of strong lines it presents in the NIR. For instance, H_2O was detected in the transit spectra of HD 189733 b by Brogi et al. (2018) and the dayside spectra of HD 102195 b by Guilluy et al. (2019) using GIANO at the Telescopio Nazionale Galileo (TNG). Additionally, water vapor was detected in Alonso-Floriano et al. (2019a) on the same exoplanet and, shortly after, in HD 209458 b by Sánchez-López et al. (2019) by using its absorption bands at $\sim 1.0\,\mu$m, $\sim 1.15\,\mu$m, and $\sim 1.4\,\mu$m

individually and simultaneously with the NIR channel of CARMENES (Calar Alto high-Resolution search for M dwarfs with Exoearths with Near-infrared and optical Échelle Spectrographs, Quirrenbach et al., 2016, 2018).

A great advantage of HDS is that it is by no means restricted to the study of transmission spectra. As was also discussed in the previous section, HDS and cross-correlation can be used to study the polarization of reflected stellar light by the exoplanet's atmosphere during the secondary eclipse to infer information about atmospheric condensates (see, e.g., Moutou et al., 2007; Muñoz and Isaak, 2015; Muñoz, 2018). In addition, several hot Jupiters that do not transit their host star have already been analyzed. Such is the case of τ Boo b (Brogi et al., 2012; Lockwood et al., 2014), HD 179949 b (Brogi et al., 2014), 51-Pegasi b (Brogi et al., 2013; Birkby et al., 2017), HD 88133 b (Piskorz et al., 2016) or Upsilon Andromedae b (Piskorz et al., 2017).

HDS can be combined with other existing techniques for the characterization of exo-atmospheres. For instance, a succesful detection of CO was achieved by Snellen et al. (2014) in the exoplanet β Pictoris b by combining HDS with *High Contrast Imaging* (HCI). In fact, the combination of both techniques provides better detection significances than with any of these techniques individually. In this case, HDS+HCI allowed the authors to measure the spin of β Pictoris b by studying the rotational broadening of the combined line profile. Furthermore, HDS has also been coupled with *integral-field spectroscopy* (IFS) at medium-resolution ($R \sim 5000$, see, e.g., OSIRIS on the Keck Telescope or SINFONI on the VLT) that use adaptive optics for succesful detections of carbon monoxide and water vapor in the exoplanets β Pictoris b and HR8799b (Hoeijmakers et al., 2018b; Roche et al., 2018, respectively). The latter technique is also referred to as *molecule mapping*.

In recent years, a new technique has been devised for the combination of HDS analyses with *Low Dispersion Spectroscopy* (LDS) in works such as Brogi et al. (2017) and Brogi and Line (2019). Whereas ground-based data is not sensitive to the absolute level of absorption in the exo-atmosphere due to the required procedures to eliminate the Earth's atmospheric contamination, space-observations can provide us with such measurements. However, not even the combination of HDS and LDS can provide with a unique solution for the atmospheric parameters, but rather a probability-based mapping of the parameter space. This is because of the large degeneracies found in the contribution of several quantities (e.g., temperature, mixing ratios, reference radius and pressure in the exo-atmosphere) to the absolute absorption (Heng and Kitzmann, 2017).

The methods introduced here for using HDS and a cross-correlation analysis constitute the basis of this thesis and will be applied to different exoplanets in the following chapters. Therefore, we will expand on each of the steps of this technique in Chapter 3.

Chapter 2

Modeling of exoplanet atmospheres

The modeling of exoplanet atmospheres is naturally essential in order to extract information about our available data, or make accurate predictions that guide future exoplanet research. When we aim at characterizing atmospheres, we always face the challenge of acquiring deep knowledge of their composition (i.e. the abundance profile of its compounds) as well as the temperature profile, and how these change with altitude or, equivalently, pressure. The atmospheric structure reveals itself in the spectra we observe. That is, the absorber amounts and the temperature at each atmospheric layer determine the optical depths, line profiles, etc.

In this chapter, we will introduce basic atmospheric physic concepts used in the modeling of exoplanet atmospheres by following, mainly, Gordon and McBride (1994), Fitzpatrick (2001), Lopez-Puertas and Taylor (2002), Showman et al. (2013), Venot et al. (2015), Mollière (2017), and Madhusudhan (2019). Additionally, we will introduce the radiative transfer equation and its formal solution based on Lopez-Puertas and Taylor (2002) and Dullemond (2012). This will provide us with the basic knowledge and the necessary tools to simulate the transmittances for photons of a wide range of wavelengths travelling through the atmospheres. Next, we will apply the radiative transfer theory using the Karlsruhe Optimized and Precise Radiative Transfer Algorithm (KOPRA, Stiller et al., 1998, 2002), which is used in this thesis to obtain models of the transmission spectra of exoplanets for different abundance and pressure-temperature profiles. In particular, we describe the integration over the atmospheric annulus, as seen from the Earth, probed during the primary transit (i.e. the terminator, Ehrenreich et al., 2006) so as to obtain the transmission spectra. Afterwards, we validated our tools by comparing our simulated exo-atmospheric spectra with those produced by other well-tested algorithms.

2.1 Notions of atmospheric physics

In its most basic definition, atmospheric physics applied to planets and exoplanets aims at understanding the physical processes that govern the behavior of the atmospheric layers. That is, we need to understand the atmospheres in terms of fluid dynamics and evaluate the results of radiative transfer and chemical models. In this section, we will discuss some of the most important notions to understand such complex systems.

2.1.1 Hydrostatic equilibrium equation

Atmospheres are very complicated systems formed by an uncountable number of particles that interact following non-trivial relationships. However, a fundamental notion about atmospheric physics can be derived by simplifying these complex systems into a parcel of gas of thickness Δr and cross-sectional area A, located at a height r above the surface of the planet. On the one hand, the force that pushes the parcel of gas upwards is simply $p_{\text{below}}(r)\,A$, where $p_{\text{below}}(r)$ is the pressure at the height r. On the other hand, the fluid above the parcel generates a force that pushes it downwards by $-p_{\text{above}}(r+\Delta r)\,A$. Naturally, the parcel of gas has a certain weight which is given by $-\rho g A \Delta r$, where ρ is the density of the gas in the parcel and g is the gravitational acceleration. If we assume an equilibrium state for the parcel of gas, the sum of all forces must be zero. Hence,

$$p_{\text{below}}(r)\,A - p_{\text{above}}(r+\Delta r)\,A - \rho g A \Delta r = 0. \tag{2.1}$$

By assuming that the width of the parcel is infinitesimally small (dr), we can consider $p_{\text{above}} - p_{\text{below}} = dp$ and this expression simply reduces to its most recognizable form:

$$\frac{dp}{dr} = -\rho g, \tag{2.2}$$

where, assuming the ideal gas equation, the pressure is given by

$$p = \frac{\rho \kappa_B T}{\overline{m}}, \tag{2.3}$$

where κ_B is the Boltzmann constant, T is the temperature, $\overline{m}$ is the mean molecular mass, and ρ is the density of an atmospheric layer at a vertical distance r.

Thus, Eq. 2.2 is the so-called *hydrostatic equilibrium equation*, where we have implicitly neglected viscosity terms, and assumed spherical symmetry and that the vertical velocities in the atmosphere are very small, although not zero (Fitzpatrick, 2001; Lopez-Puertas and Taylor, 2002; Mollière, 2017). Thereby, atmospheres are prevented from collapsing into a thin and dense layer above the surface by the pressure-gradient and, at the same time, they are prevented from expanding and diffusing into space due to gravity.

2.1.2 The pressure-temperature profile of exoplanetary atmospheres

The pressure-temperature ($p - T$) structure in the atmosphere of a planet is a result of multiple contributions to its overall energy budget. There are two major energy sources that heat atmospheric gases. Firstly, the stellar photons reaching the atmosphere are absorbed or scattered and heat up the gases, fuel the atmospheric circulation, photodissociate molecules (initiating chemical reaction chains), etc. In the case of tidally-locked hot Jupiters, this is of particular importance since an hemisphere of the planet is constantly being irradiated. The stellar flux impinging on the top of the atmosphere (TOA) can be estimated by:

$$F_{*,TOA} \propto \mathcal{B}_\nu \left(T_{\text{eff}}\right) \frac{R_*^2}{a^2}, \tag{2.4}$$

where $\mathcal{B}_\nu \left(T_{\text{eff}}\right)$ is the Planck function at the temperature T_{eff}, which is the effective temperature of the star, and a is the orbital distance of the planet.

Secondly, and specially for the case of gas giants, the planet's interior is itself radiating due to its internal temperature[1] and thus, the atmosphere receives a second contribution, affecting mainly its deepest atmospheric layers. The flux emitted by the planet's interior can be estimated by using the Stefan-Boltzmann law:

$$F_{\text{int}} = \sigma T_{\text{int}}^4, \tag{2.5}$$

where σ is the Stefan-Boltzmann constant and T_{int} is the internal temperature of the planet, arising from its core.

In the stationary state, the stellar and planetary irradiation are not heating and, certainly, not cooling the atmosphere anymore. In order to reach such steady state, the energy cannot accumulate in any atmospheric layer. In other words, all incoming energy at a specific layer needs to be redistributed either by collisions, by radiation of the gases, by transporting material to other layers (i.e., convection), etc. In the following, we discuss the basic mechanisms that drive the atmosphere to the stationary state in its upper and lower regions.

Radiative-convective equilibrium

In the upper atmospheric layers, in which the opacity is small due to the low density, the reradiation of the incoming energy is already an efficient mechanism for maintaining the steady state (i.e., no cooling nor heating). Hence, such atmospheric region is said to be in *radiative equilibrium* (see atmospheric regions

[1]The internal heat of planets can be produced by the contraction of the planet, remaining heat from the planetary formation, the decaying of radioactive elements (e.g., ^{235}U, ^{238}U, ^{232}Th, or ^{40}K), friction, among others (see, e.g., Jaupart and Mareschal, 2010; Komacek and Youdin, 2017).

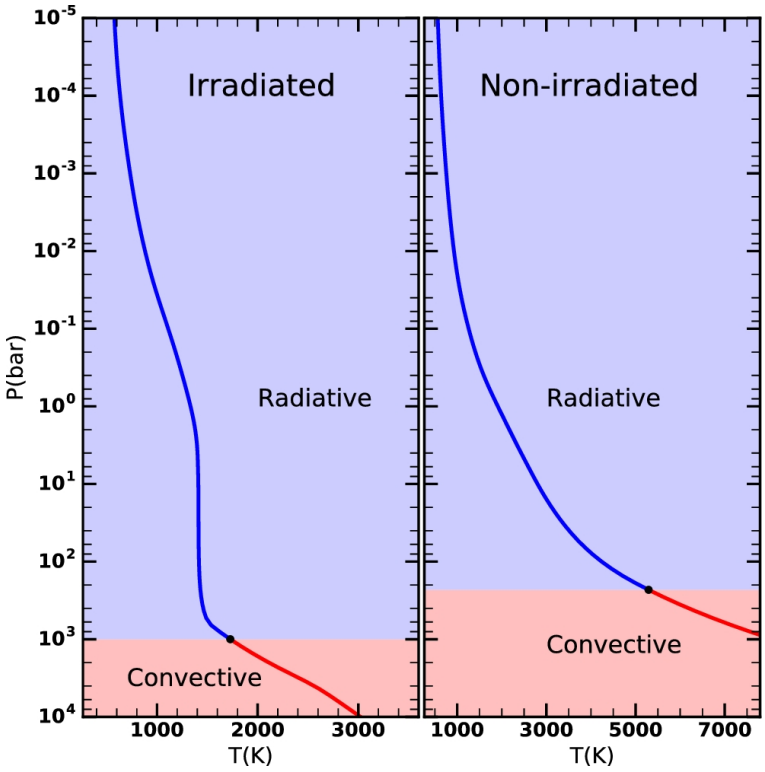

Figure 2.1: Pressure-temperature profiles for an irradiated (left) and non-irradiated atmosphere (right) of a Jupiter-like exoplanet. The atmospheric region shaded in red represents the layers which are unstable against convection, whereas the layers shaded in blue show the atmosphere in radiative equilibrium. The transisition point is marker by a black dot. *Image credit:* Figure taken from Gandhi and Madhusudhan (2017).

shaded in blue in Fig. 2.1). The condition that must be fullfilled for radiative equilibrium to accur can be written as follows:

$$\int_0^\infty \kappa_\nu \left(\overline{L}_\nu - \mathcal{B}_\nu \right) d\nu = 0, \tag{2.6}$$

where κ_ν is the absorption coefficient, $\overline{L}_\nu$ is the mean radiance of the radiation field. This equation establishes that the energy absorbed at an atmospheric layer (encoded in $\overline{L}_\nu$) must be balanced by the emission of the layer itself (given by B_ν), hence ensuring the temperature profile is not perturbed. Note that this does not apply to a single frequency, ν, but to the integration over the whole spectrum. That is, energy can be absorbed at ultraviolet frequencies and then re-emitted in the infrared. The other case would correspond to monochromatic radiative equilibrium, which is not treated here.

However, in the lowest atmospheric layers, which are optically thick, radiation stops being an efficient mechanism for transporting the energy. This

is because the emitted photons are quickly absorbed, since the density is now orders of magnitude larger than in the upper regions. Therefore, the atmosphere becomes *convectively unstable* (see atmospheric regions shaded in red in Fig. 2.1). That is, hot gas blobs are transported to the upper layers, whereas cold gas blobs fall to low altitudes. In this case, Eq. 2.6 needs to include an additional term so as to include the convective flux, $F_{\rm conv}$:

$$\int_0^\infty \kappa_\nu \left(\overline{L}_\nu - \mathcal{B}_\nu\right) d\nu + \frac{\rho g}{4\pi}\frac{dF_{\rm conv}}{dp} = 0. \tag{2.7}$$

Typically, convection is treated by using *mixing length theory*, which has the so-called mixing length, l_{mix}, as its only free parameter (see, e.g., Kippenhahn et al., 2012; Gandhi and Madhusudhan, 2017; Mollière, 2017). Thus, mixing length theory allows us to calculate $F_{\rm conv}$ and, also, to estimate the mean path traveled by the rising hot gas blobs before they brake and mix with the surrounding colder gas. This distance is often assumed to be of the order of one atmospheric scale height.

2.1.3 Atmospheric equilibrium chemistry

The current chemical composition of an atmosphere provides key information about the planet's formation conditions and evolution. Gas giants are expected to preserve their primary H_2-He atmospheres, whereas rocky bodies tend to modify their atmospheres by outgassing. In the latter case, the atmosphere becomes rich in heavier compounds such as N_2, H_2O, CH_4, CO_2, CO, etc. Moreover, precise knowledge of the chemistry at each atmospheric layer allows us to better understand the atmospheric optical depth, which directly impacts its energy budget, its temperature structure, and the dominant processes at each atmospheric region (e.g., diffusion, mixing mechanisms, etc.). This is because the distribution and abundance of absorbent species in the atmosphere will determine whether the atmosphere is optically thin or thick at a specific wavelength and thus, which fraction of photons is absorbed or scattered.

A fully-fleshed model that simulates the time evolution of a mixture of gases until a stationary state is reached, while also including non-equilibrium processes (i.e., vertical transport or photolysis) is computationally expensive (see Sect. 2.1.4). Because of this, some approximations are commonly used in the literature when a less refined description is sufficient for our purposes, or when computational time is to be optimized. One of such procedures are the thermochemical models based on *Gibbs minimizers* (Gordon and McBride, 1994; Mollière, 2017), which allow us to estimate the abundances in the stationary state of the atmospheric components ($t \to \infty$), without requiring any prior knowledge of how the system actually evolved to equilibrium. This approach is of particular interest for the lower atmospheric layers (i.e., at pressures larger

than 1 bar), which are expected to be in chemical equilibrium due to the high density and temperature (Madhusudhan, 2019).

The thermodynamic potential G (called the Gibbs *free energy*) is given by

$$G = U + pV - TS, \tag{2.8}$$

where U is the internal energy of the gas, V its volume, and S the entropy. By taking the total differential of this equation we obtain

$$\begin{aligned} dG &= dU + pdV + Vdp - TdS - SdT \\ &= TdS - pdV + \sum_{i=1}^{N_s} \mu_i\,(p,\,T)\,dN_i + pdV + Vdp - TdS - SdT \\ &= Vdp - SdT + \sum_{i=1}^{N_s} \mu_i dN_i, \end{aligned} \tag{2.9}$$

which follows from the first law of thermodynamics[2], where $\mu_i\,(p,\,T)$ and N_i are the chemical potential at a constant $(p,\,T)$ and the number of moles of the species i, respectively, and N_s is the number of species.

The second law of thermodynamics requires that the entropy of an isolated system always increases over time, $\Delta S > 0$. Thus, Eq. 2.8 immediately translates in an always decreasing Gibbs free energy. Therefore, in the limit of $t \to \infty$, the atmosphere has evolved into a stationary state of minimum G and hence, all state functions are constant over time. As such, we may re-write Eq. 2.9 for this limit, at a constant pressure and temperature as

$$dG = \sum_{i=1}^{N_s} \mu_i\,(p,\,T)\,dN_i. \tag{2.10}$$

Therefore,

$$G = \sum_{i=1}^{N_s} \mu_i\,(p,\,T)\,dN_i + cst. \tag{2.11}$$

For a mixture of N_s compounds, the abundances that correspond to the equilibrium state of the atmosphere can be obtained by minimizing Eq. 2.11. This can be done by imposing a constraint: The number of atoms of each element in the atmosphere, $N_{\rm atoms}$, must remain constant. Mathematically, this can be written as

$$\sum_{i=1}^{N_s} a_{ji} N_i = b_j, \tag{2.12}$$

[2]The first law of thermodynamics states that $dU = \delta Q - \delta W = TdS - pdV + \sum_i \mu_i\,(p,\,T)\,dN_i$ for closed systems and reversible processes of a thermodynamic system formed by different species that may react chemically. In this expression, W is the mechanical work done by the system to its surroundings and is given by $\delta W = -pdV$, and the heat added to the system is given by $\delta Q = TdS$.

where a_{ji}, called *stoichiometric factors*, are the kilogram-atoms of the element j per kilogram-mole of species i, and b_j are the respective constant values. This is an archetype example of a mathematical optimization problem which can be treated by applying the method of *Lagrange multipliers*. This method allows us to find the local maxima and minima of a given function subjected to a specific number of constraints (e.g., Eq. 2.12). From the Lagrange multiplier theorem, we know that the wished minimum for the Gibbs free energy is a stationary point of the so-called *Lagrangian function*, $\mathcal{L}$, which must satisfy the given constraints. In particular, at the minimum, it holds that the gradient of the function can be written as a linear combination of the gradients of the given constraints. The coefficients of the combination (λ_j) are known as the *Lagrange multipliers*. The Lagrangian function is given in our case by

$$\mathcal{L}\left(N_{i=1,...,N_s},\, \lambda_{i=1,...,N_{atoms}}\right) = \sum_{i=1}^{N_s} \mu_i\left(p,\, T\right) N_i - \sum_{j=1}^{N_{\rm atoms}} \lambda_j \left[\sum_{i=1}^{N_s} a_{ji} N_i - b_j\right], \tag{2.13}$$

and by imposing $\nabla\mathcal{L} = 0$, where

$$\nabla = \frac{\partial}{\partial N_1}, ..., \frac{\partial}{\partial N_s}, \frac{\partial}{\partial \lambda 1}, ..., \frac{\partial}{\partial \lambda_{N_{\rm atoms}}}, \tag{2.14}$$

we can now solve for the critical points of $\mathcal{L}$. Thus, the expected equilibrium abundances are those that minimize the Gibbs free energy.

Although this approach neglects important phenomena taking place during the system's evolution to a stationary state, it allows for a speeding up of the calculations. For this reason, this procedure is widely used in the literature and is in the basis of several well-tested algorithms such as, e.g., the NASA's CEA code (Gordon and McBride, 1994; McBride and Gordon, 1996) or *petit*CODE (Mollière et al., 2015; Mollière, 2017; Mollière et al., 2017).

Other works simplify the modeling of the atmospheric chemistry further by fixing a uniform mixing ratio for the observable atmospheric species. That is, a constant abundance for the atmospheric compounds is set at each pressure point, calculated as $X_i \equiv n_i/n_{tot}$ (see, e.g., Line et al., 2016; MacDonald and Madhusudhan, 2017). Thereby, no calculation of the atmospheric chemistry is performed, which speeds up the calculations at the expense of their accuracy.

2.1.4 The importance of disequilibrium chemistry

Despite its fast delivery of results, thermochemical models based on Gibbs minimizer algorithms neglect important phenomena such as the photodissociation (driven mostly by the UV stellar flux impinging on the atmosphere), or the vertical transport (mixing and molecular diffusion processes) that are key at pressures below 1 bar. In fact, photochemical processes are expected to dominate at $p < 10^{-3}$ bar due to the increased ultraviolet radiation and low density.

In addition, vertical mixing is expected to drive the composition in the region $10^{-3} < p < 1$ bar (Madhusudhan, 2019). In the past years, much effort has been put into developing complex models that include such non-equilibrium processes and simulate the evolution of the system until it reaches a stationary state.

These models should better reproduce the expected atmospheric conditions in any planet. In the case of hot Jupiters, which are of particular interest in this thesis, this is specially important, because their atmospheres are heavily irradiated. Therefore, their atmospheres are likely very far from an equilibrium state. 1D photochemical models usually assume an input for the $p-T$ profile of the exoplanet and then solve for the time evolution of the so-called *continuity equation* given by

$$\frac{\delta n_i}{\delta t} = P_i - n_i L_i - div\left(\Phi_i \overrightarrow{e_r}\right), \tag{2.15}$$

where n_i is the number density of the considered species (given in cm^{-3}), t is the time, P_i is the production rate of species i in $\mathrm{cm}^{-3}\mathrm{s}^{-1}$, L_i is the specific loss rate of species i in s^{-1}, $\overrightarrow{e_z}$ is the flow velocity vector in the vertical direction, r, and Φ_i is a vertical flux that accounts for diffusion (Venot et al., 2012, 2018). This flux is parametrized by means of the *vertical diffusion equation* in the form

$$\Phi_i = -n_i D_i \left[\frac{1}{n_i}\frac{\delta n_i}{\delta r} + \frac{1}{H_i} + \frac{1}{T}\frac{dT}{dz}\right] - n_i K_{\mathrm{eddy}} \left[\frac{1}{y_i}\frac{\delta \chi_i}{\delta z}\right], \tag{2.16}$$

with D_i being the molecular diffusion coefficient in $\mathrm{cm}^{-2}\mathrm{s}^{-1}$, H_i the scale height of species i, K_{eddy} the eddy diffusion coefficient given in $\mathrm{cm}^{-2}\mathrm{s}^{-1}$, and χ_i the mixing ratio of species i. Under these circumstances, in the case of considering N_s species, the problem becomes a set of N_s coupled and non-linear differential equations whose resolution is non-trivial.

The first attempt at calculating non-equilibrium abundances for hot Jupiters was performed in Liang et al. (2003), where the authors explored the photodissociation processes that lead to the presence of atomic hydrogen in the upper atmosphere of the hot Jupiter HD 209458 b. Later, in Line et al. (2010), thermochemically derived mixing ratios for relevant molecules such as CO, H_2O, CO_2 and CH_4 were compared with those provided by photochemical models in the atmosphere of the hot Jupiter HD 189733 b. Their findings hint at photochemistry and vertical mixing[3] severely affecting the concentration of these important compounds in hot Jupiter atmospheres. Specifically, they found vertical transport, which is not taken into account in the thermochemical models of Sect. 2.1.3, to be the strongest contribution to the abundances we may observe in transiting exoplanets.

[3] If the convective mixing timescale (τ_{mix}) is shorter than the chemical kinetics timescale (τ_{chem}), some "disequilibrium" species may elevate in the atmosphere until the condition $\tau_{\mathrm{mix}} = \tau_{\mathrm{chem}}$ is fulfilled. The altitude at which this happens varies from one species to another and is known as the *quench level* for that species (see, e.g., Visscher and Moses, 2011).

In the following years, an interesting discussion raised regarding the verification of kinetic chemical networks[4] via experiments. In spite of the interesting results obtained with several photochemical models, such as those of Zahnle et al. (2009a,b), Line et al. (2010), and Moses et al. (2011), these were not based on experimental data. Hence, their results and conclusions might not be fully correct. Since then, chemical kinetic networks have been developed for the $p-T$ range usually expected for hot Jupiters (i.e., $0.001 - 100$ bar, and $300 - 2500$ K), with the necessary rate coefficients and their temperature dependencies, for many of the possible chemical reactions, and using data validated in laboratory experiments (Venot et al., 2012, 2018). By using data tested in environments that resemble the atmospheric conditions of hot Jupiters, it is possible to develop reliable 1D models and achieve more confident abundance predictions for their atmospheres. However, this also brings up the question of the completeness of such networks and the lack of experimental chemical kinetic rates for the required pressure-temperature ranges.

Since most of the work in this thesis has been devoted to analyzing the atmospheres of the hot Jupiters HD 189733b b and HD 209458 b, it is worth summarising briefly the main results obtained in recent works (see, e.g., Venot et al., 2012) by means of the experimentally tested kinetic chemical network ($\sim$ 2000 possible chemical reactions including H, C, O, N, and hydrocarbons with two C atoms). Their model for the abundances of the main absorbent species in the atmospheres of HD 189733 b and HD 209458 b can be seen in Fig. 2.2 (adapted from their work). Their results show that both exo-atmospheres are expected to present thermochemical equilibrium at pressures larger than 10 bar. For HD 209458 b, vertical transport is found to have a profound impact on the abundances of HCN, NH_3, and CH_4 at pressures lower than 1 bar. Despite the large UV stellar flux received in its atmosphere, the authors found that photodissociation does not play a major role in the abundances. In fact, the high temperature of its atmosphere shortens the chemical reaction timescale, making it smaller than that of photodissociation. Hence, the atmospheric compounds react with other species before they can be photodissociated. For the slightly colder HD 189733 b, their results present a more out-of-equilibrium atmosphere, more impacted by the photodissociation and vertical transport of gases.

In particular, the abundances of HCN (blue dashed lines in Fig. 2.2) and NH_3 (black dashed lines in Fig. 2.2) are greatly affected by considering disequilibrium processes, even in the lower atmosphere ($P \sim 1$ bar). In fact, these two species have been observed for the first time in transit spectra using high dispersion spectroscopy in both exoplanets very recently (Cabot et al., 2018; Hawker et al., 2018). These detections provide evidence of these species being rather abundant and globally distributed in both exo-atmospheres, which is in good agreement

[4] A database of possible (and often reversible) chemical reactions involving a user-specified list of compounds in the atmosphere.

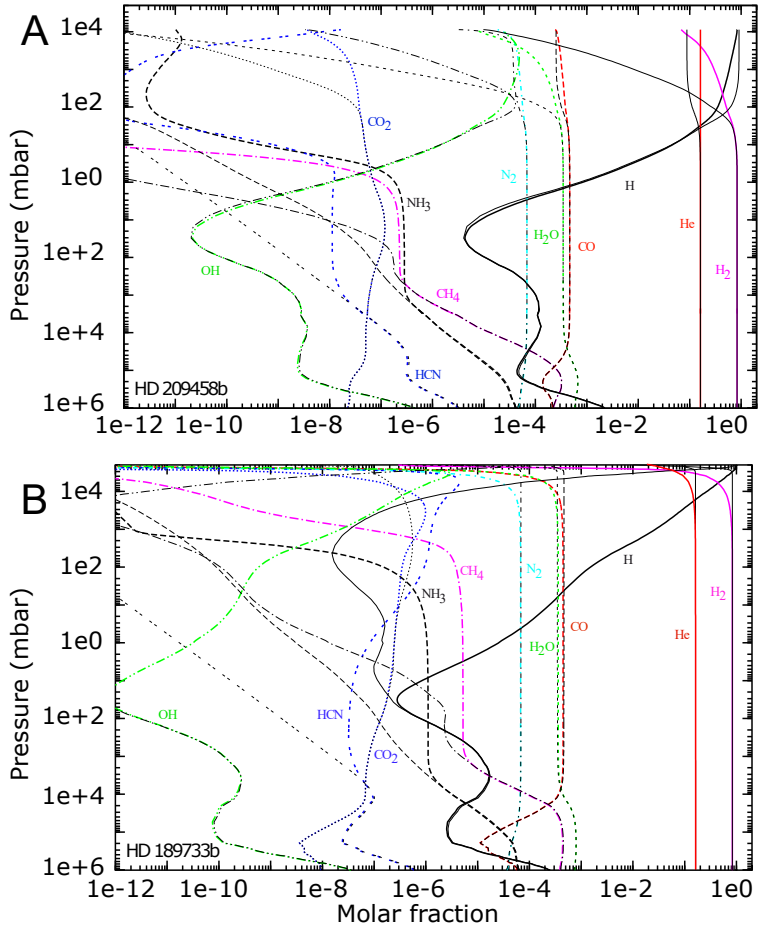

Figure 2.2: Comparison of the model abundance profiles obtained for the hot Jupiters HD 209458 b (A) and HD 189733 b (B) for several absorbent species by using photochemical models (color lines) and thermochemical models (thin black lines). *Image credit:* Figure adapted from Venot et al. (2012).

with the disequilibrium chemistry model predictions.

2.1.5 C/O ratio

The ratio of carbon to oxygen atoms (C/O ratio) provides invaluable information about the chemistry, formation, and evolution of exoplanets (see, e.g., Öberg et al., 2011; Moses et al., 2012; Madhusudhan et al., 2017). This quantity can be studied for gases and grains of material in the protoplanetary disk (see Fig. 2.3A). The state of matter varies with the orbital distance, since the received stellar flux diminishes towards larger distances. Carbon- and oxygen-bearing gases will condense into icy grains at the orbital distance at which the

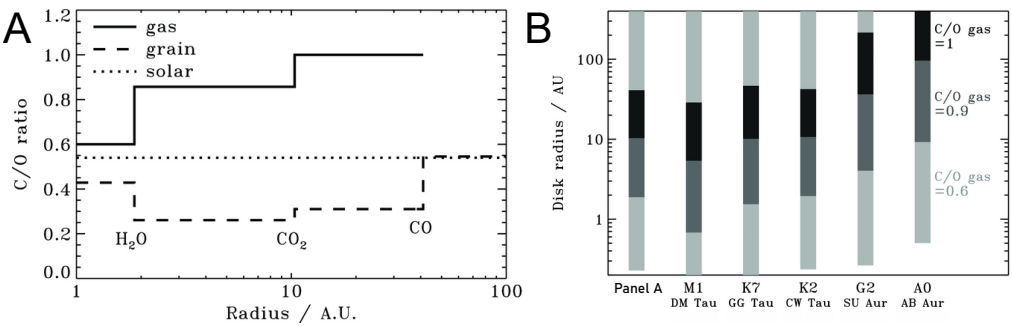

Figure 2.3: A: C/O ratio of gaseous (black line) species and grains (dashed line) in a protoplanetary disk as a function of the orbital distance. A solar-type star is assumed, and the solar C/O = 0.54 is marked by the dotted line. Also, the snowlines of different species are indicated. B: C/O ratio of the protoplanetary disk as a function of the orbital distance and stellar type. In all cases, the stellar C/O ratio is assumed to be solar (i.e., 0.54). *Image credit:* Figures adapted from Öberg et al. (2011).

temperature is lower than that for their condensation (i.e., this is known as the *snowline* of a certain compound). Naturally, the snowline of different compounds will occur at different orbital distances due to their different condensation temperatures. Hence, the C/O ratio of gases and grains will be impacted by this (Fig. 2.3A).

In addition, the snowlines and, in turn, the C/O ratios, depend on the luminosity of the host star (Fig. 2.3B). The primordial C/O ratio of the exoplanet's envelope thus depends on where the core is formed. In addition, other phenomena, such as the accretion of large icy bodies and outgassing of the core, can also impact the C/O ratio of the primordial atmosphere of a planet. Interestingly, the models of Öberg et al. (2011) predict enhanced C/O ratios (i.e., *supersolar*) at the orbital distances where gas giants are expected to form (see Fig. 2.3B). Moreover, supersolar C/O is found to be consistent only with atmospheres forming mainly by accretion beyond the H_2O and CO_2 snowlines.

The observation of exoplanets with high C/O ratios orbiting very close to their host stars thus supports the occurrence of planetary migration in the disks. That is, these gas giants likely formed at larger orbital distances and then migrated inwards (Öberg et al., 2011). For instance, this is the case for the hot Jupiters WASP-12 b (Madhusudhan et al., 2011a), HD 189733 b (Swain et al., 2008), and for the hot Neptune GJ 436 b (Madhusudhan and Seager, 2011), for which supersolar C/O ratios have been reported. Consequently, these exoplanets are thought to have migrated inwards.

Furthermore, high C/O ratios could yield a depletion in compounds such as H_2O and thus, could result in optically thinner atmospheres in the near infrared, where this molecule absorbs strongly. This also means that the atmosphere cools less efficiently and thus, the atomic lines (e.g., alkali lines) absorb a larger

portion of the incoming stellar radiation. In hot atmospheres, this might yield observable temperature inversions. That is, temperatures increasing towards lower pressures (Madhusudhan et al., 2011b).

With the objective of characterizing the disequilibrium chemistry in high C/O environments, species with up to six carbon atoms with ~ 4000 possible chemical reactions are now being studied in the disequilibrium models discussed in Sect. 2.1.4 (Venot et al., 2015). It is worth noting that heavy hydrocarbons could play a major role in some exo-atmospheres. For instance, this is the case in Saturn's moon Titan, in our Solar System. The hydrocarbon haze in Titan's stratosphere has been shown to be a result of large abundances of polycyclic aromatic hydrocarbons (PAH) in the upper atmosphere (Lavvas et al., 2013; López-Puertas et al., 2013). PAH compounds absorb UV solar photons, hence producing the Titan's stratopause. In fact, an ionosphere is formed in the upper atmosphere by charged particles, which quickly grow in size by ion chemistry and, subsequently, descend to the lower layers of Titan's atmosphere. Similar processes might take place in exoplanets with abundant PAHs (Bilger et al., 2013). Hence, we might be able to infer the presence of these heavy carbon-bearing molecules in exo-atmospheres by studying the potential haze extinction.

2.1.6 Atmospheric circulation

The atmospheric circulation refers to the large-scale motion of the atmospheric gases in a planetary atmosphere, which is fuelled by the incident stellar irradiation and acts redistributing the energy around the planet. In order to study this, several *General Circulation Models* (GCM) have been developed in the past years in order to solve for the 3D structure of the atmosphere by using its bulk parameters and the radiation coming from the host star (Parmentier et al., 2013; Showman et al., 2013; Kataria et al., 2016; Rauscher, 2017; Zhang et al., 2017).

Due to its relevance for the context of this thesis, we will focus our discussion mainly on hot Jupiter atmospheres. There are two major processes driving the circulation in these hot planets. Firstly, the temperature gradients between the equator and the poles of these tidally-locked hot Jupiters give rise to the so-called *Rossby waves*, planetary-scale standing latitudinal oscillations (in the north-south direction) that propagate gases to the west (i.e., transverse waves) at low latitudes. Interestingly, the anisotropy induced by the variations of the Coriolis force with latitude (the so-called β-effect), induces a vortex-like rotation in the gas transported by the waves[5]. And, secondly, the often extreme temperature gradient between the bright and the dark sides of these exoplanets[6] trigger

[5]Because of this, fluids turn clockwise in the northern hemisphere and anticlockwise in the southern hemisphere.

[6]For hot Jupiters, the radiative cooling timescale is expected to be sufficiently short for the appearance of large day-to-night temperature constrasts.

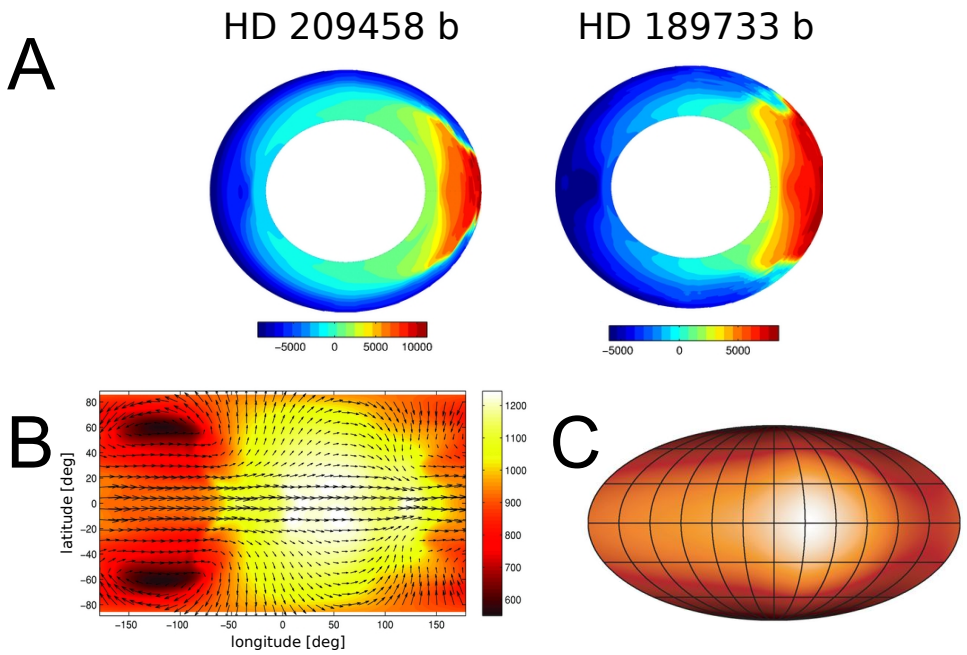

Figure 2.4: A: Model atmospheric winds (including the planet's rotation) towards the Earth (blueshifted, in blue) and away from the Earth (redshifted, in red) for HD 209458 b (left) and HD 189733 b (right). The shown pressure layers range from 200 bar (inner part of the rings) to 2 μbar (outer layers). The color scale indicates the wind velocity in m/s. In both exoplanets, a superrotating jet appears (see text). B: GCM predictions of atmospheric winds in HD 189733 b showing the superrotation and shifted hot spot. The color scale indicates the temperature in K. C: Brightness map for HD 189733 b obtained from Spitzer's IRAC 8 μm band measurements also showing the shift of the hot spot from the substellar point. *Image credit:* Panel A adapted from Showman et al. (2013). Lower row from Madhusudhan (2019), with panel B adapted from Showman and Polvani (2011) and panel C adapted from Knutson et al. (2007a).

another kind of equatorial waves called the *Kelvin waves*, which propagate to the east.

The eddies (i.e., regions of swirling gas) resulting from the interaction of Rossby and Kelvin waves move south-east in the northern hemisphere and north-east in the southern hemisphere (Showman and Polvani, 2011). The gases are thus pushed from high latitudes to the equator with an overall eastward momentum and hence, a strong jet of gas appears flowing eastwards in the equator of the exoplanet. This is typically known as the *superrotation* that, in the case of many hot Jupiters, is responsible for the redistribution of thermal energy between the day- and the night-side (see Figs. 2.4A and 2.4B).

However, a strong dampening of the jet may occur in some exoplanets either due to strong radiative cooling or frictional drag. In these cases, the circulation is dominated by a global day-to-night wind flow at high altitudes (i.e., towards lower pressures, $p < 1$ bar) and a slow (due to the larger density) night-to-day

flow at low altitudes (i.e., towards larger pressures, $p > 1$ bar), with an increasing temperature gradient between the day and night hemispheres (see dampened equatorial jet for HD 209458 b, with respect to HD 189733 b, according to GCM models in Fig. 2.4A and Showman et al., 2013).

The effects of the atmospheric circulation and/or superrotation in the temperature profiles, in the day-to-night temperature gradient, and in the efficiency of the heat transport can be observed in phase curve monitoring (Knutson et al., 2008; Crossfield et al., 2010; Knutson et al., 2012; Demory et al., 2016) and emission observations (Deming et al., 2005; Grillmair et al., 2008; Line et al., 2016; Piskorz et al., 2018) of exo-atmospheres.

In the presence of a strong jet and efficient redistribution, the exo-atmosphere is faster in transporting the energy than in cooling to space and hence, the temperature gradient between the day- and the nigh-side is reduced. In addition, the observable substellar point in the atmosphere (i.e., the hot spot at which the star is at the zenith) is displaced slightly to the east by the jet (see, e.g., Fig. 2.4B and Fig. 2.4C and Knutson et al., 2008; Crossfield et al., 2010; Heng et al., 2011a,b). As seen above, the jet-dominated dynamics in these extreme environments translates into strong atmospheric winds in the exoplanet's terminator that move towards and away from the Earth, depending of the atmospheric region. This causes a broadening and a Doppler-shift of the exo-atmospheric molecular lines, which can be detected using different instrumentation (Snellen et al., 2010; Showman et al., 2013; Alonso-Floriano et al., 2019a; Sánchez-López et al., 2019). In the jet-dampened scenario, the overall wind flow towards the Earth would result in larger blue-shifts of the atmospheric signal. We will discuss more about the detection of winds in exo-atmospheres in the following chapters that cover the high dispersion spectroscopy technique and its application to hot Jupiters. In particular, we will analyze the presence of atmospheric winds in HD 189733 b and HD 209458 b, which are expected to show weak-to-moderate superrotation.

2.2 The width and shape of spectral lines

The different species absorb (emit) photons at specific wavelengths that excite (de-excite) their internal rotational and vibrational energy levels. The strength and shape of the absorption lines are significantly affected by the temperature and pressure conditions in the atmosphere. The spectral line shapes are far from Dirac delta functions (i.e., infinetly narrow), but are broadened. That is, the photons of a range of energies around the transition energy will be absorbed, with a lower probability the more different their frequency is from the one corresponding to the transition. In the following, we introduce and discuss the different contributions to the broadening of the spectral lines.

2.2.1 *Natural broadening*

Heisenberg's uncertainty principle itself creates an unavoidable blurring of the lines as:

$$\Delta E \Delta t \sim \frac{h}{2\pi}, \tag{2.17}$$

where Δt is the transition time between the ground state and the excited state, which has an energy E. ΔE is thus the uncertainty in this energy. Therefore, the frequency of the photon that will trigger this transition is not unique, but a range (i.e., uncertainty in the frequency) given by the line width

$$\alpha_N = \frac{1}{2\pi c \Delta t}, \tag{2.18}$$

where c is the speed of light. However, the natural width of the lines is really small when compared to other sources of broadening and hence, it is rarely observed in practical cases.

2.2.2 *Doppler broadening*

Any pool of gases in the atmosphere presents particles that move in a wide range of velocities given by the Maxwell-Boltzmann distribution. In fact, the number of molecules with a mass m and a velocity v with respect to the observer is given by

$$\frac{dN(v)}{N(v)} = \sqrt{\frac{m}{2\pi\kappa_B T}} \exp\left[-\frac{mv^2}{2\kappa_B T}\right] dv, \tag{2.19}$$

where $dN(v)/N(v)$ is the fraction of particles moving at velocities comprised between v and dv. Taking into account that the photons that interact with molecules, which move at a velocity v, suffer a frequency shift of a factor of $(1 - v/c)$, the *line shape* resulting from the Doppler broadening (see red curve in Fig. 2.5) is

$$\phi(\nu) = \frac{1}{\sqrt{\pi}\alpha_D} \exp\left[-\frac{(\nu - \nu_0)^2}{\alpha_D^2}\right], \tag{2.20}$$

where ν is the observed frequency of the photon, ν_0 is the original frequency and α_D is the so-called *Doppler width* calculated as

$$\alpha_D = \frac{\nu_0}{c}\sqrt{\frac{2RT}{M}}, \tag{2.21}$$

where R is the ideal gas constant and M is the molecular weight. Due to the ν_0 dependence, the effect of the Doppler broadening is stronger at larger frequencies.

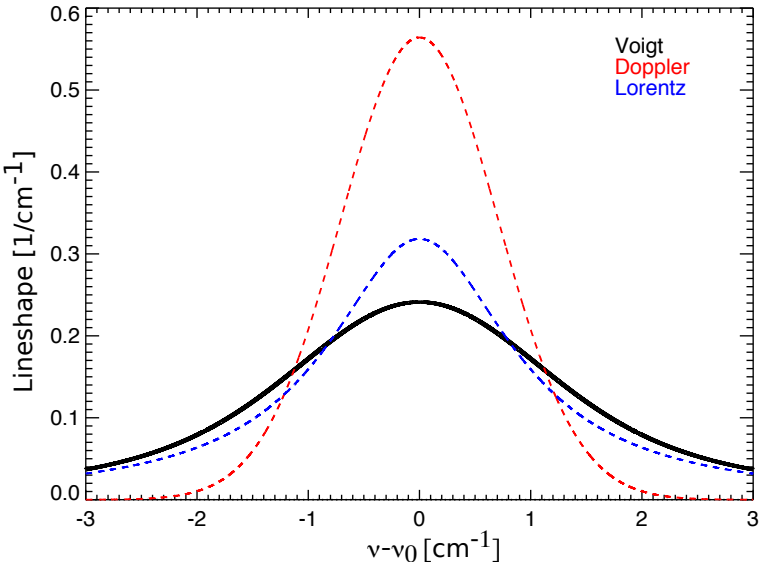

Figure 2.5: Line profiles arising from the Doppler broadening (red curve), Lorentz broadening (blue), and the convolution of both mechanisms, that is, the Voigt line profile (black curve).

2.2.3 *Pressure broadening*

The larger the pressure (e.g., in the deepest atmospheric layers where the density is high), the more collisions the particles will experience. A high rate of collisions shortens the lifetime of the excited states. In the case of standard conditions for temperature and pressure (STP)[7] the line width, in this case referred to as *Lorentz width*, becomes

$$\alpha_L = \frac{1}{2\pi\, c\, t_0}, \tag{2.22}$$

where $1/t_0$ is the collision frequency at STP conditions (i.e., t_0 is the mean time that passes between collisions at STP conditions). In fact, the nature of pressure broadening is the same as for the natural mechanism, which explains why the Lorentz width is so similar to that presented in Eq. 2.18 for the natural broadening. However, the former has a larger contribution to the overall line profile, especially at high pressures (low altitudes above the planet's surface).

We can now calculate the line shape arising from the Lorentz broadening by integrating the square of the frequency distribution of a sine wave of duration t_0 multiplied by the probability of having that finite t_0. The resulting shape (see blue curve in Fig. 2.5) is given by

$$\phi(\nu) = \frac{1}{\pi} \frac{\alpha_L}{(\nu - \nu_0)^2 + \alpha_L^2}. \tag{2.23}$$

[7]These conditions aim at allowing easier comparisons of experimental measurements and correspond to a temperature of 293.15 K and a pressure of 1 atm.

In the case of $p-T$ conditions different from those of STP, we can re-write the Lorentz width as

$$\alpha_L(p,T) = \alpha_L(STP)\,\frac{p}{p_0}\sqrt{\frac{T_0}{T}}. \tag{2.24}$$

2.2.4 Convolution of different broadening mechanisms

The total line shape for a given transition is thus affected by all the broadening mechanisms discussed in the previous section. Naturally, certain scenarios allow us to neglect the contribution for some of these effects. For instance, the natural broadening can almost always be neglected, since the natural lifetime of the excited states is much longer than the usual timescale between collisions ($\alpha_N \ll \alpha_L$). In addition, $\alpha_N \ll \alpha_D$ unless the system has an extremely low temperature. Moreover, in the lowest atmospheric layers where the pressure is the largest, the line profile will be dominated by the Lorentz broadening since α_L can be roughly two orders of magnitude larger than α_D under STP conditions. Actually, the line profile arising from the Lorentz profile decreases much more slowly than the Doppler profile when we depart from the center frequency. Thus, the line wings are dominated by the Lorentz contribution.

However, α_D gains importance in the case of hot atmospheres, such as those in hot Jupiters, or in the case of really low pressures such as those in the highest atmospheric layers. In general, the core of the lines will have its stronger contribution from these regions at which the Doppler mechanism becomes relevant.

In the intermediate cases, when both contributions are to be accounted for, we can obtain the combined effect of both mechanisms by calculating the convolution of the two line shapes (see black curve in Fig. 2.5). This is the so-called *Voigt line profile* given by

$$\phi_{\text{Voigt}}(\nu-\nu_0) = \frac{1}{\alpha_D\sqrt{\pi}}\frac{y}{\pi}\int_{-\infty}^{+\infty}\frac{e^{-t^2}dt}{y^2+(x-t)^2}, \tag{2.25}$$

where $y = \alpha_L/\alpha_D$ and $x = (\nu-\nu_0)/\alpha_D$.

Unfortunately, the integral expression for the Voigt line shape cannot be solved analytically. However, a widely-used and fast numerical approximation is that of Humlíček (1982).

2.3 Notions of radiative transfer

Once the $p-T$ and abundance profiles for the exo-atmosphere are set, we can compute the absorption cross-sections of the different compounds in each atmospheric layer. Consecutively, we can solve for the radiative transfer at each atmospheric layer and frequency. This, in turn, will allow us to determine the state of the radiation field in the atmosphere. To do so, let us consider a basic

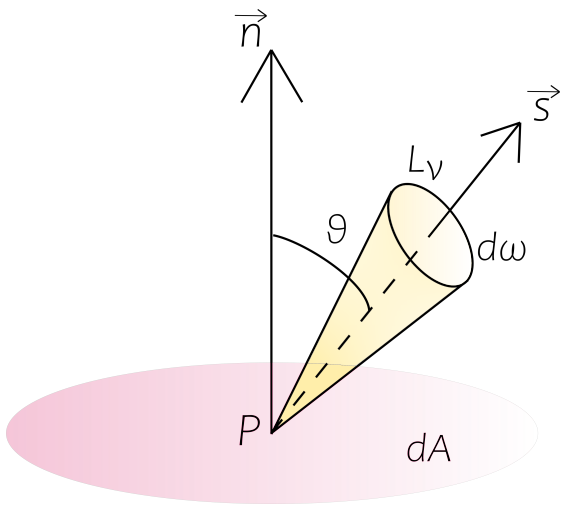

Figure 2.6: Sketch of the radiance at a point P in the atmosphere.

atmosphere in which photons travel in all directions and have all frequencies. We can accurately describe how photons propagate through the different atmospheric layers restricting ourselves to a point P in the atmosphere (see Fig. 2.6). We can now describe the *radiation field* at P by considering a differential area dA with normal unit vector $\vec{n}$. The *specific intensity* of a light ray in an arbitrary direction following the unit vector $\vec{s}$, at a point P, and forming an angle θ with $\vec{n}$, is given by

$$L_\nu\left(P,\,\vec{s}\right) = \frac{dE_\nu}{\cos\left(\theta\right)\,dA\,d\omega\,d\nu\,dt}, \tag{2.26}$$

where dE_ν is the energy transported by the radiative field at a certain $d\nu$ across dA in all directions within the differential solid angle $d\omega$ centred around the direction $\vec{s}$ in the infinitesimal time dt. The quantity expressed in Eq. 2.26 is also referred to as the *radiance*.

The integration of $L_\nu\left(P,\,\vec{s}\right)$ over the frequency interval $(\nu,\,\nu + d\nu)$ yields the total radiance which has dimensions of $W\,m^{-2}sr^{-1}$. Interestingly, Eq. 2.26 tells us that the energy that passes through the considered area changes if we consider another arbitrary direction or a different point in the atmosphere. Integrating over all $\vec{s}$ directions in $d\omega$ allows us to obtain the *net radiative flux* through the area dA:

$$F_{\nu,\,n}\left(P\right) = \int_\omega L_\nu\left(P,\,\vec{s}\right)\cos\left(\theta\right)d\omega. \tag{2.27}$$

Similarly, we can calculate the mean radiance of the radiation field at a certain frequency ν by averaging over all solid angles as

$$\overline{L}_\nu = \frac{1}{4\pi}\int_\omega L_\nu\left(P,\,\vec{s}\right)d\omega. \tag{2.28}$$

Naturally, the radiation that propagates in the atmosphere interacts with matter. Hence, we need to take into account the processes that result in loss and production of photons. The decrease in the radiance of the radiation field due to absorption and scattering processes as the photons travel a differential distance ds is

$$dL_\nu = -\alpha_\nu n_a L_\nu ds, \tag{2.29}$$

where n_a is the number density of the absorbing species and α_ν is the extinction coefficient, which is given by:

$$\alpha_\nu = k_\nu + k_{\nu,\,\mathrm{scat}}, \tag{2.30}$$

where k_ν is the absorption coefficient and $k_{\nu,\,\mathrm{scat}}$ is the extinction coefficient due to scattering processes. By the same token, the production of photons due to emission processes and scattering can be written as

$$dL_\nu = j_\nu n_a ds, \tag{2.31}$$

where j_ν is the emission coefficient.

Making use of the *Kirchhoff's law* of thermal radiation, the ratio of the emission and the absorption coefficients must be equal to a universal function of the frequency and the temperature[8], $\mathcal{F}_\nu(\mathcal{T})$. In mathematical form:

$$\frac{j_\nu}{\alpha_\nu} = \mathcal{F}_\nu(\mathcal{T}). \tag{2.32}$$

In the case of thermodynamic equilibrium, this universal function is non other than the Planck's function:

$$\mathcal{F}_\nu(\mathcal{T}) = \mathcal{B}_\nu(T) = \frac{2h\nu^3}{c^2}\frac{1}{\exp\left(\frac{h\nu}{\kappa_B T}\right) - 1}. \tag{2.33}$$

This relation can also be defined for processes out of thermodynamic equilibrium by introducing a general *source function* as

$$S_\nu = \frac{j_\nu}{\alpha_\nu}. \tag{2.34}$$

Introducing the source function in Eq. 2.31 we obtain

$$dL_\nu = \alpha_\nu n_a S_\nu ds, \tag{2.35}$$

[8]In fact, the mathematical expression of Kirchhoff's law was found by Max Planck (Planck's law) forty years after Kirchhoff postulated the existence of the relation between the emission and absorption coefficients.

and hence, the change in the radiance of the radiation field when travelling through a pool of gases must be dictated by the so-called *radiative transfer equation* (RTE) given by

$$\frac{dL_\nu\left(P,\ \overrightarrow{s}\right)}{ds} = -\alpha_\nu n_a \left[L_\nu\left(P,\ \overrightarrow{s}\right) - S_\nu\left(P,\ \overrightarrow{s}\right)\right]. \tag{2.36}$$

By defining the *single-scattering albedo* as the fraction of all extinction that is produced by scattering processes,

$$\eta_\nu = \frac{k_{\nu,\,\mathrm{scat}}}{\alpha_\nu}, \tag{2.37}$$

and, also, the *photon destruction probability* as the fraction of all extinction that is due to absorption,

$$\epsilon_\nu = \frac{k_\nu}{\alpha_\nu} = 1 - \eta_\nu, \tag{2.38}$$

we can express the general source function as

$$S_\nu = \epsilon_\nu \mathcal{B}_\nu\left(T\right) + \eta_\nu \int_{4\pi} L_\nu\left(\overrightarrow{s}'\right) p_\nu\left(\overrightarrow{s}',\ \overrightarrow{s}\right) d\omega', \tag{2.39}$$

where p_ν is the normalized probability distribution function that is referred to as *scattering phase function*. p_ν gives us the probability of a light ray traveling in a direction $\overrightarrow{s}'$ being scattered into a direction $\overrightarrow{s}$. Usually, the phase function is only dependent on the angle between both directions and hence, it holds that $p_\nu\left(\overrightarrow{s}',\ \overrightarrow{s}\right) = p_\nu\left(\overrightarrow{s},\ \overrightarrow{s}'\right) = p_\nu\left(\overrightarrow{s}' \cdot\ \overrightarrow{s}\right)$, where $\overrightarrow{s}' \cdot\ \overrightarrow{s}$ is simply the cosine of the angle between both directions, since both are unit vectors. This quantity is usually called μ.

In the lowest atmospheric layers, where density and pressure are large, the probability of a photon being absorbed or scattered is high. This is known as the *diffusive regime* of the atmosphere in which the scattering processes are non-isotropic. In this scenario, we can define the scattering anisotropy, g_ν, as the mean value of $\mu = \overrightarrow{s}' \cdot\ \overrightarrow{s}$ as follows:

$$g_\nu = \int_{4\pi} \left(\overrightarrow{s}' \cdot\ \overrightarrow{s}\right) p_\nu\left(\overrightarrow{s}',\ \overrightarrow{s}\right) d\omega'. \tag{2.40}$$

Consequently, the source function can be re-written as (see, e.g., Wang and Wu, 2012):

$$S_\nu = \epsilon_\nu \mathcal{B}_\nu\left(T\right) + \eta_\nu\left(1 - g_\nu\right)\overline{L}_\nu. \tag{2.41}$$

Therefore, we need to solve for the radiance L_ν at each layer using Eq. 2.36, which depends on the source function. However, the source function depends, in turn, on the radiance we are trying to find (Eq. 2.41). Hence, this is a system of coupled equations with a non-trivial solution. Some usual approaches

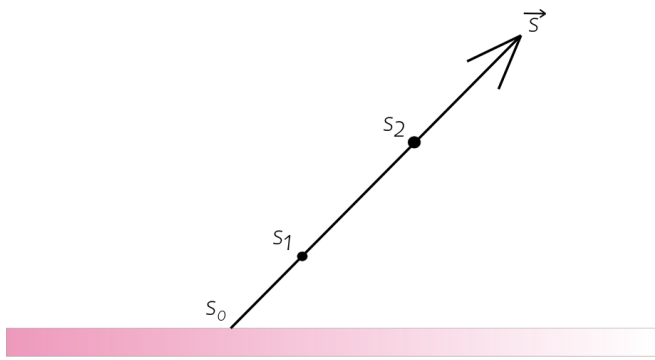

Figure 2.7: Sketch of the optical path travelled by a light ray in the atmosphere.

for solving the RTE are, for instance, the Feautrier method (see, e.g., Gandhi and Madhusudhan, 2017; Mollière, 2017), the Lambda iteration, or the Curtis matrix method (see, e.g., Lopez-Puertas and Taylor, 2002; Funke et al., 2012).

For later use, we will also write the RTE (Eq. 2.36), neglecting all scattering processes, in terms of the optical depth of the chord depicted in Fig. 2.7, for the case of photons of frequency ν traveling between the points s_1 and s_2 as

$$\tau_\nu\left(s_1, s_2\right) = \int_{s_1}^{s_2} k_\nu\left(s''\right) n_a\left(s''\right) ds'', \tag{2.42}$$

where we have considered that $s_2 > s_1$ and thus, $d\tau_\nu/ds < 0$ since $\tau_\nu > 0$. Therefore, the RTE (Eq. 2.36) at a distance s_1 can be re-written as:

$$\frac{dL_\nu\left(s_1, \vec{s}\right)}{d\tau_\nu} = L_\nu\left(s_1, \vec{s}\right) - S_\nu\left(s_1, \vec{s}\right). \tag{2.43}$$

In this way, the RTE has the form of an ordinary differential equation and describes the radiance at a point s_2 in the direction $\vec{s}$ for photons that have traveled from s_0 through a medium with a certain optical depth. The formal solution would then be:

$$L_\nu\left(s_2, \vec{s}\right) = L_\nu\left(s_0, \vec{s}\right) e^{-\tau_\nu(s_0, s_2)} + \int_0^{\tau_\nu(s_0, s_2)} S_\nu\left(s_1, \vec{s}\right) e^{-\tau_\nu(s_1, s_2)} d\tau_\nu. \tag{2.44}$$

The first term in the right hand side (RHS) of the equation reflects the initial radiance at s_0, attenuated by the medium's optical depth when travelling from s_0 to s. The second term in the RHS is then the contribution to the radiation field by the emission of the gas in the volume elements at each s' along $\vec{s}$, also attenuated by the medium's optical depth.

Lastly, we can introduce here the concept of *transmittance*, $\mathcal{T}$, between the points s_1 and s_2 in a direction $\vec{s}$ as

$$\mathcal{T}_\nu\left(s_1, s_2\right) = \exp\left[-\tau_\nu\left(s_1, s_2\right)\right] = \exp\left[-\int_{s_1}^{s_2} k_\nu\left(s''\right) n_a\left(s''\right) ds''\right]. \tag{2.45}$$

2.4 The Karlsruhe Optimized and Precise Radiative Transfer Algorithm

The Karlsruhe Optimized and Precise Radiative Transfer Algorithm (KOPRA; Stiller et al., 2002) calculates the monochromatic radiances line-by-line by solving the radiative transfer (Eq. 2.44) at all defined atmospheric layers using the Curtis-Godson approximation, which is based on replacing an inhomogeneous optical path segment with an equivalent homogeneous path that has the same transmittance (Krakow et al., 1966). Thus, for each path element in the line of sight of the observer, KOPRA calculates the partial gas columns and the Curtis-Godson means for temperature, pressure, and Local Thermodynamic Equilibrium (LTE) population ratios[9].

KOPRA models the spectral lines using a Voigt line shape as described in previous sections, hence taking into account the convolution of the Doppler and the Lorentz broadening for the specific $p - T$ conditions at each layer. To obtain the line positions, it makes use of spectroscopic databases such as the HITRAN 2016 compilation (Gordon et al., 2017) or the HITEMP 2010 compilation (Rothman et al., 2010), which has a special relevance in the frame of this thesis for studying hot Jupiters. However, other spectroscopic databases can be coupled with it. KOPRA includes an adaptive scheme that allows us to include or reject spectral lines of a given strength, which is most useful when working with gases in very hot atmospheres. This is because the line lists for the different species in such extreme environments contain a huge number of lines, and their calculation has a high computational cost.

Originally, KOPRA was developed for the analysis of the emission of rovibrational spectral bands measured by the MIPAS instrument (Fischer et al., 2007) and was validated with respect to GENLN2, Reference Forward Model (RFM) and Simulation Program for Infrared Radiative Transfer (SPIRT) (Von Clarmann et al., 2002). Later, the non-LTE algorithm GRANADA was introduced and coupled with KOPRA by the Instituto de Astrofísica de Andalucía, IAA (Funke et al., 2012). Moreover, KOPRA has been adapted and validated for the study of Titan and Jupiter (García-Comas et al., 2011; Montañés-Rodríguez et al., 2015; López-Puertas et al., 2018). Within the frame of this thesis, we have adapted KOPRA for our purposes involving the geometry of the primary transit of exoplanets (Alonso-Floriano et al., 2019a and see next sections).

Generally, KOPRA accepts as input files the $z-p-T$ profile of the exoplanet, where 'z' is the height of each layer, and the Volume Mixing Ratio (VMR) profiles that indicate the abundance for each species at the given atmospheric layers. The user can then specify the frequency[10] interval for the calculations and

[9] In addition, the algorithm GRANADA (Funke et al., 2012) can be used to calculate the non-LTE population ratios, which can then be used in KOPRA.

[10] In fact, KOPRA works internally using wavenumber (in cm^{-1}).

whether the calculations should be performed at a very high *spectral resolution*, R (i.e., specified by the user), and if a certain input *Instrumental Line Shape* (ILS) should be used. With these inputs, KOPRA returns, in the case of a limb geometry (i.e., used for transit observations), the transmittances (or radiances) at each frequency for each specified atmospheric layer.

2.4.1 Adaptation for the primary transit geometry of exoplanets

Integration over the atmospheric annulus for the primary transit

In order to derive the so-called *spectrum ratio* of the transiting system, we will follow, mainly, Brown (2001) and Ehrenreich et al. (2006). Let us consider the ratio, $\mathcal{R}$, of the flux received from the star during transit, $F_{\rm in}$, with respect to the flux received out-of-transit, $F_{\rm out}$, when there is no occultation of the stellar photons. The spectrum ratio is usually defined as

$$\mathcal{R}' = \mathcal{R} - 1 = \frac{F_{\rm in} - F_{\rm out}}{F_{\rm out}}, \tag{2.46}$$

which is, essentially, the fraction of blocked flux introduced in Eq. 1.4. In this form, the spectrum ratio is essentially giving us information about two major absorption contributions. Namely, the absorption of the planetary disk (i.e., opaque at all wavelengths), and the absorption of the exo-atmosphere. The former is directly proportional to the area of the planet's disk, πR_p^2, whereas the latter must be proportional to the frequency dependent area of the exo-atmosphere, $\mathcal{A}_\nu$, which can be calculated by (see, e.g., Brown, 2001; Wit and Seager, 2013; Heng and Kitzmann, 2017):

$$\mathcal{A}_\nu = 2\pi \int_{R_{\rm ref}}^{\infty} (1 - \mathcal{T}_\nu)\, r dr. \tag{2.47}$$

For the computation of $\mathcal{A}_\nu$, let us assume a ray of light travelling through a model atmosphere of $j = 1, ..., N$ layers with impact parameters r_i, as devised in the sketch of Fig. 2.8. In this configuration, $\mathcal{A}_\nu$ can be discretized as

$$\mathcal{A}_\nu = \pi \sum_{j=i}^{N-1} \left[(1 - \mathcal{T}_{\nu,\,j+1}) - (1 - \mathcal{T}_{\nu,\,j})\right] \left[(R_p + r_{j+1})^2 - (R_p + r_j)^2\right], \tag{2.48}$$

where $\mathcal{T}_{\nu,j}$ is the total transmittance of the atmosphere for photons travelling at the j-th layer. In essence, we are calculating the equivalent absorption (i.e., $1 - \mathcal{T}_\nu$) for each atmospheric annulus and multiplying this value by the area of the annulus. By summing over $N - 1$ atmospheric layers, we obtain the total desired contribution from all the atmospheric annuli. Therefore, the spectrum ratio is given by:

$$\mathcal{R}'(\nu) = \frac{\mathcal{A}_\nu + \pi R_p^2}{\pi R_*^2}. \tag{2.49}$$

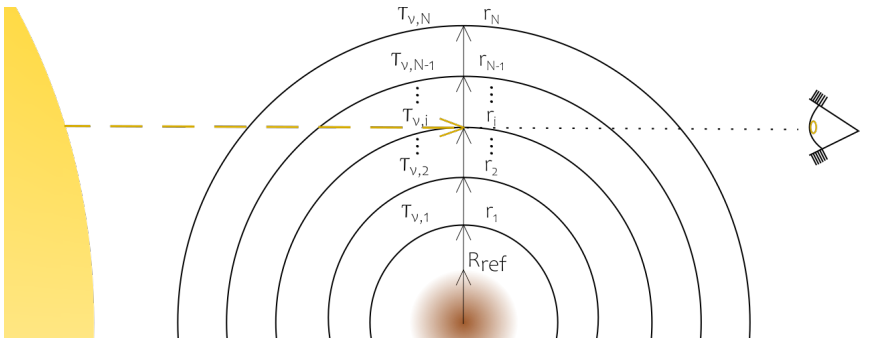

Figure 2.8: Sketch (not to scale) of the atmospheric integration for the obtention of the total transmittance in the primary transit.

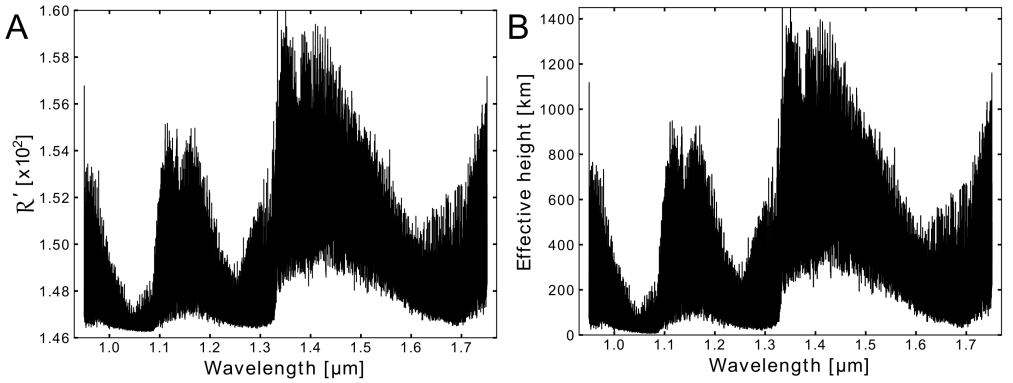

Figure 2.9: Model transmission spectrum for a typical hot Jupiter. The spectrum ratio computed with Eq. 2.49 ($\times 10^2$) is shown in panel A. The same spectrum, but expressed in terms of the effective height (Eq. 2.50), is shown in panel B.

A model spectrum ratio computed with KOPRA for a typical hot Jupiter is shown in Fig. 2.9A.

Some authors do not work with the spectrum ratio as calculated with the previous expression. Instead, the effective height of the atmosphere is shown directly (see Sect. 1.2.1 and, e.g., Rauer et al., 2011; Scheucher et al., 2018). The effective height, at a certain frequency, of the grid exo-atmosphere is calculated as

$$r_{\mathrm{eff},\,\nu} = \sum_j \left(1 - \mathcal{T}_{\nu,\,j}\right) \Delta r_j, \tag{2.50}$$

where Δr_j is the altitude difference between consecutive atmospheric layers[11]. A model transmission spectrum computed with KOPRA and expressed in terms of the effective height is shown in Fig. 2.9B.

[11]The effective height is typically represented as $h_{\mathrm{eff},\,\nu}$. However, we used $r_{\mathrm{eff},\,\nu}$ so as to be consistent with the notation of this section and, also, Fig. 2.8.

From the effective height, the spectrum ratio is calculated as follows:

$$\mathcal{R}'(\nu) = \left(\frac{R_p + r_{\mathrm{eff},\nu}}{R_*}\right)^2, \tag{2.51}$$

which is equivalent to Eq. 2.49. In fact, the effective height and the atmospheric annular area can be related by taking into account that, at a certain frequency, it holds that

$$\mathcal{A}_\nu = \pi\left(R_p + r_{\mathrm{eff},\nu}\right)^2 - \pi R_p^2 = \pi r_{\mathrm{eff},\nu}^2 + 2\pi R_p r_{\mathrm{eff},\nu}, \tag{2.52}$$

and, hence, the effective height can be written in terms of the area of the exo-atmospheric annulus as follows:

$$r_{\mathrm{eff},\nu} = \sqrt{R_p^2 + \mathcal{A}_\nu/\pi} - R_p. \tag{2.53}$$

By inserting this latter expression in Eq. 2.51, we recover the spectrum ratio of Eq. 2.49.

Alternatively, we could neglect the term $\propto r_{\mathrm{eff},\nu}^2$ in Eq. 2.52, since $r_{\mathrm{eff},\nu} \ll R_p$. Hence, an approximated solution for the effective height would be given by:

$$r_{\mathrm{eff},\nu} \sim \frac{\mathcal{A}_\nu}{2\pi R_p}. \tag{2.54}$$

Contribution of the Rayleigh scattering

The atmosphere of hot gas giants is mainly constituted by hydrogen ($\sim 85\%$) and helium ($\sim 15\%$). As a ray of light traverses such an atmosphere, they collide frequently with particles that are smaller than their wavelength (λ) and hence, scatter. At first order, we can consider such collisions as being elastic and model the extinction by using the usual Rayleigh scattering: the efficiency of scattering is inversely proportional to λ^{-4}. In fact, the incoming photons (i.e., an oscillating electromagnetic wave) interact with matter by imprinting their oscillation in the particle's internal charges, creating radiating dipoles that emit a photon of the same wavelength as the original. Thus, globally, the effect is analogous to an original photon being scattered.

We included the effects of Rayleigh scattering by molecular hydrogen and helium in our calculations, which resulted in a significant additional opacity contributing mainly at optical wavelengths. The optical cross-sections for H_2 were taken from Ford and Browne, 1973, and from Chan and Dalgarno, 1965 for He. The effects of RS, along with the collision-induced absorption (see Sect. 2.4.1), on the computed transmission spectra can be observed in both panels of Fig. 2.10 for different wavelength intervals.

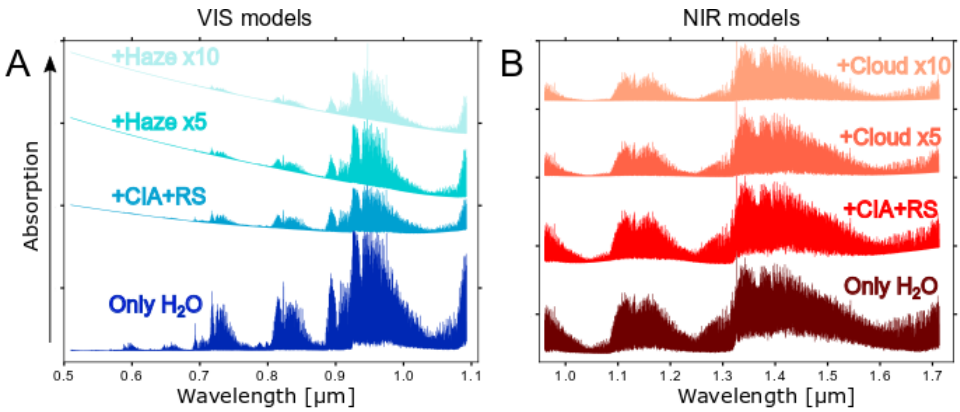

Figure 2.10: Synthetic transmission models for the absorption of water vapor in a hot Jupiter atmosphere. An arbitrary offset has been introduced in the baseline of each model for clarity. A: Models of H_2O at optical wavelengths. The effect of Rayleigh Scattering (RS), collision-induced absorption (CIA), and different levels of extinction by hazes (see text) are perceptible. B: Models of H_2O at near infrared wavelengths. The effects of the RS, CIA, and different contributions of a cloud deck are shown.

Contribution of the collision-induced absorption of H_2-H_2 and H_2-He

Due to the dominant abundance of molecular hydrogen and helium in gas giants, the collisions between pairs of H_2-H_2 and H_2-He are ubiquitous in their atmospheres. Although symmetric molecules (e.g., H_2) do not possess permanent dipole moments and hence, do not emit or absorb strongly, these inelastic collisions can, in some cases, create transient dipole moments and, hence, allow for excited internal energy levels to exist. In fact, they can even form ephemeral supramolecular entities which have spectral features different from those of its original constituents. These new absorption features are the so-called Collision-Induced Absorption (CIA) which, in the case of H_2-H_2 and H_2-He pairs, appear as a smooth absorption peaking in the $0.6-0.9$, $1.0-1.4$, and $2.0-2.5\,\mu$m spectral intervals. We included the Collision-Induced Absorption (CIA) by using the opacities for high temperatures derived by Borysow (2002) for H_2-H_2 collisions and by Borysow et al. (1989) and Borysow and Frommhold (1989) for H_2-He collisions. The effects of the CIA (along with RS) on the computed transmission spectra can be seen in both panels of Fig. 2.10 for different wavelength intervals. In particular, the effects of CIA are observed by comparing the models including only H_2O with those including also CIA+RS in the $1.0-1.5\,\mu$m spectral region in Fig. 2.10A, and in the $1.6-1.7\,\mu$m interval in Fig. 2.10B.

A simple model for clouds and hazes

We modeled the extinction by hazes and the effects of cloud decks in the transmission spectra by following the prescription used in Sing et al. (2016). That

is, the aerosol extinction was introduced as being similar to a Rayleigh scattering opacity with a cross-section $\sigma = \sigma_0 \, (\lambda/\lambda_0)^{-4}$, where the reference cross section is that of molecular hydrogen, $\sigma_0 = 5.31 \times 10^{-27}$ cm^2 at a $\lambda_0 = 350$ nm. Thereby, we did not model the Rayleigh scattering of specific haze compounds, but estimated the overall contribution of a potential haze, regardless of its composition.

The presence of clouds in the exo-atmosphere results in a partial to complete blockage of the potential spectral features that would come from the atmospheric layers below the cloud top deck and, hence, prevent us from obtaining information from the atmospheric regions below. Thus, the effects of cloud coverage usually manifests as flat transmission spectra where the remaining spectral features are mostly those of strong and deep absorption lines such as the atomic transitions coming from the upper layers (e.g., sodium doublet lines). Thus, a simple model for clouds covering the terminator can be included by assuming a constant cross-section (i.e., wavelength-independent), which can be set to, as for the haze model, the σ_0 for molecular hydrogen at λ_0. The effect of haze extinction and cloud top decks blockage of the spectral features can be seen in Fig. 2.10A and Fig. 2.10B, respectively. Larger haze factors indicate the presence of more aerosols contributing to a stronger extinction (i.e., steeper scattering slope observable in the optical). Larger cloud factors are equivalent to a cloud top deck at higher altitudes (i.e., blocking more atmospheric layers and yielding flatter spectra).

2.4.2 Validation of KOPRA against other algorithms

KOPRA is a well tested algorithm for solving the RTE in atmospheric studies in our solar system (see, e.g., García-Comas et al., 2011; Montañés-Rodríguez et al., 2015). With the objective of ensuring that our calculations of the spectra of exoplanets are also correct, we have compared the spectra obtained with KOPRA with those obtained by other well tested algorithms, which are used by other groups for exoplanetary and exo-atmospheric studies. In the following, we briefly discuss our results.

Comparison with GARLIC in transmission

The Generic Atmospheric Radiation Line-by-line Infrared Code (GARLIC, see Schreier et al., 2014) is an algorithm for the computation of transmittances or radiances in a planetary atmosphere for any observational geometry, field of view, etc. To set up the comparison, we assumed an Earth-like exoplanet orbiting around the M-dwarf ADLeo (see also Scheucher et al., 2018). The exoplanet is assumed to have a surface temperature of 288.15 K and its atmosphere includes N_2, N_2O, O_2, O_3, H_2O, CO, CO_2, CH_4, NO, SO_2, NO_2, HNO_3, OH, HCL, ClO, H_2CO, HOCl, H_2O_2, H_2S, HO_2, and $ClNO_3$. Also, the continuum

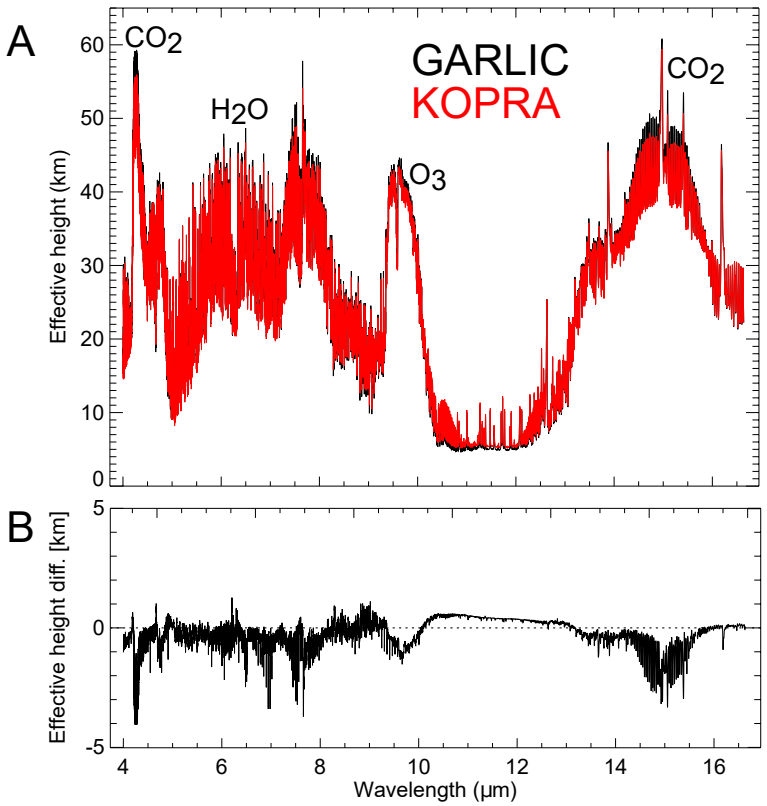

Figure 2.11: A: Comparison of transmission spectra during the primary transit of an exo-Earth generated with KOPRA (red) and GARLIC (black). The quantity shown in the vertical axis is the effective height, calculated following Eq. 2.50. Some spectral features of important atmospheric constituents are indicated. B: Relative differences between both models.

absorption by N_2, O_2, H_2O, and CO_2 is included. Both algorithms made use of the HITRAN2012 spectroscopic database.

The resulting transmission spectra in the primary transit computed with both algorithms are shown in Fig. 2.11A. In particular, KOPRA calculations were performed at a very high resolution and then convolved by using a Gaussian line shape with a full width at half maximum of $0.4\,\mathrm{cm}^{-1}$. The transmission spectra computed with both algorithms agree remarkably well (see differences in Fig. 2.11B). There is a general discrepancy of, roughly, 0.5 km at all wavelengths. That is, the effective heights calculated with GARLIC are slightly larger than those computed by KOPRA. It is important to note that the GARLIC spectrum was computed by performing the integration over altitude introduced in Eq. 2.50, whereas for the KOPRA results the effective height was calculated from the area of the atmospheric annuli (see Eqs. 2.48 and 2.53). The different integration over altitude in both procedures is likely the cause of the observed differences.

Additionally, there are also noticeable differences ($\sim 3-4\,\mathrm{km}$) in the core

of the strongest absorption bands (see, e.g., CO_2 features at 4.3 μm and 15 μm, O_3 at 10 μm). Several reasons could explain this. Firstly, there is a different line cut-off in both codes. Whereas KOPRA calculates the absorption of the lines up to 25 cm^{-1} away from the line center, GARLIC cuts this absorption at 10 cm^{-1}. Secondly, KOPRA considers the effects of line mixing for CO_2, whereas it is not accounted for in GARLIC calculations. Thirdly, we examined the transmittance of the upper layers individually and found that, for the KOPRA calculations, many lines were completely saturated (i.e., zero transmittance, complete absorption) even at the highest altitudes (e.g., ∼61 km). This suggests that the altitude integration grids were different in both calculations. Also, the altitude grid used in KOPRA should be extended to higher altitudes in order to account for the complete absorption. This would enhance the resemblance of both spectra. These reasons combined are likely the cause of the observed small differences.

Comparison with GARLIC in emission

We compared also the spectra computed with GARLIC and KOPRA in emission. To do so, we simulated the nadir radiances of the Earth seen as an exoplanet. The atmospheric species included were CH_4, N_2O, O_2, O_3, H_2O, CO, and CO_2, for which both algorithms obtained the spectroscopic information from the HITRAN2012 database.

The resulting spectra are shown in Fig. 2.12A. Both calculations agree remarkably well in a wide wavelength interval and across multiple orders of magnitude in radiance. In fact, this is better observed in Fig. 2.12B, where the mean differences are below the 5% level. However, there are noticeable differences in the radiances computed for water vapor near 6 μm, where the GARLIC radiances are, roughly, 25% larger than those of KOPRA. In addition, the radiance computed with GARLIC is nearly 20% larger in a short wavelength interval of the blue wing of the CO_2 band at 4.3 μm. That is, despite the band core being in very good agreement in both calculations. These differences are likely due to the different line cut-offs discussed above (i.e., 25 cm^{-1} for KOPRA and 10 cm^{-1} for GARLIC). In general, both spectra are very similar and, therefore, the transmission and emission comparisons performed here serve as a validation of KOPRA for its application to exoplanetary geometries.

2.4.2.1 Comparison with ARIEL

We performed an additional comparison of the transmission spectra produced by KOPRA with those provided by the ARIEL retrieval Working Group. These spectra are a part of the recently conducted retrieval challenge within the ARIEL Working Groups, which aims at optimizing the data analysis tools once this telescope begins its operation (see, e.g., Tinetti et al., 2018). For this comparison we

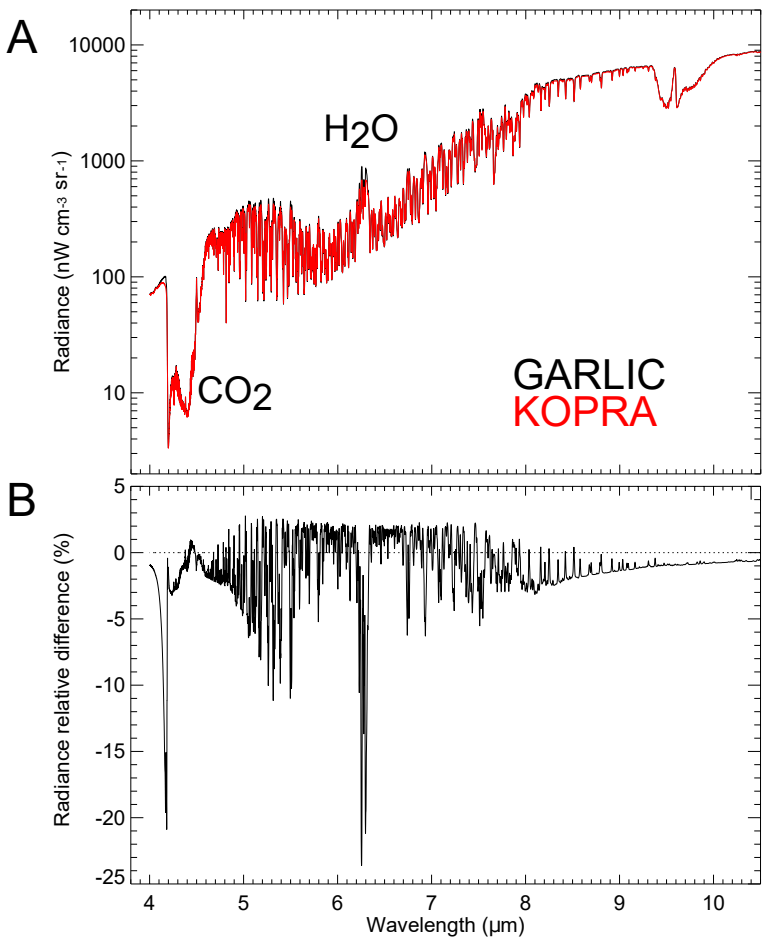

Figure 2.12: A: Comparison of nadir emission spectra of an exo-Earth with KOPRA (red) and GARLIC (black). The quantity shown in the vertical axis is the effective height, calculated following Eq. 2.50. Some spectral features of important atmospheric constituents are indicated. B: Relative differences between both models.

computed the transit spectra of the hot Jupiter HD 209458 b assuming chemical equilibrium abundances in the exo-atmosphere for H_2O, CO, CO_2, CH_4, SO_2, NH_3, HCN, C_2H_2, and C_2H_4. The spectroscopic information was obtained from HITEMP2010 in the case of KOPRA, whereas the Exomol database was used in the ARIEL calculations. The resulting spectra are shown in Fig. 2.13A.

Overall, both spectra agree very well. Moreover, the relative differences are below the 2% level at all wavelengths (see Fig. 2.13B), which reinforces the confidence of both calculations. There are, however, significant differences in the transit depth computed around the CO absorption band at $\sim 2.3\,\mu$m and, also, around the CH_4 band near $3.3\,\mu$m. Both bands are found to have a larger absorption in the ARIEL spectrum. The different spectroscopic databases used in

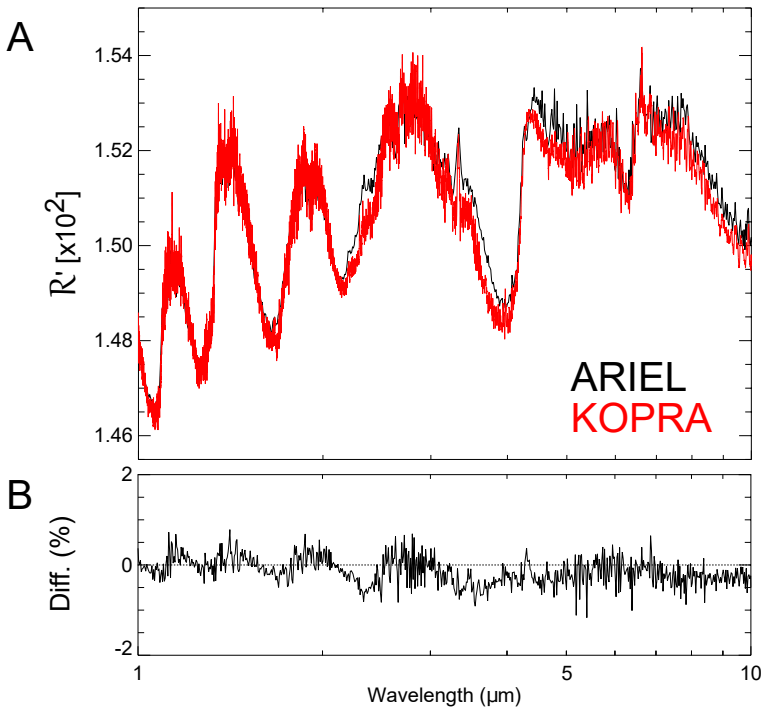

Figure 2.13: A: Comparison of model transmission spectra during the primary transit of the hot Jupiter HD 209458 b generated with KOPRA (red) and those provided by the ARIEL retrieval challenge Working Group (black). The quantity shown in the vertical axis is the spectrum ratio, calculated following Eq. 2.49, multiplied by 10^2. B: Relative differences between both models.

both algorithms for these molecules is very likely the source of these discrepancies. However, the HITEMP2010 and Exomol spectroscopic information for water vapor are much more similar. This explains the very good agreement we observed in the $1.0 - 1.7\,\mu$m spectral range, in which H_2O is the dominant absorbent species.

As for the minor differences observed at other wavelengths (see, e.g., at $1.15\,\mu$m or at $1.4\,\mu$m), there are different possible explanations. On the one hand, the aforementioned different spectroscopic databases. On the other hand, the ARIEL spectrum was computed directly at the low resolution expected for the instrument's observations, whereas we computed a very high resolution spectrum with KOPRA that was later convolved to match such low-resolution. Both factors combined might explain these small differences.

2.4.2.2 Comparison with petitRADTRANS

petitRADTRANS (Mollière et al., 2019) is a publicly available code for the calculation of both transmission and emission spectra of exo-atmospheres at low

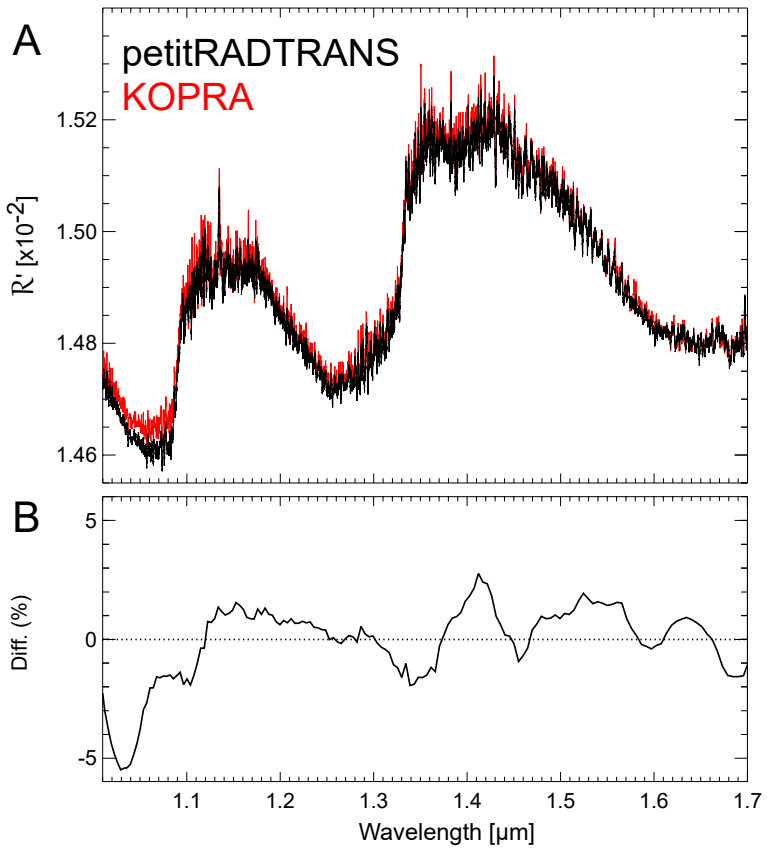

Figure 2.14: Comparison of model transmission spectra during the primary transit of the hot Jupiter HD 209458 b generated with KOPRA (red) and petitRADTRANS (black). The quantity shown in the vertical axis of the top panel is the spectrum ratio, calculated following Eq. 2.49, multiplied by 10^2. B: Relative differences between both calculations.

and high resolution. Although it is continuously being updated, this algorithm has already been validated against the algorithms petitCODE (Mollière et al., 2015, 2017), ATMO (Tremblin et al., 2015), and Exo-REM (Baudino et al., 2015; Baudino et al., 2017). The version of petitRADTRANS we have used here has been improved with respect to that used in the validation exercise with Exo-REM (Mollière et al., 2019, Per. Comm.). By using KOPRA and petitRADTRANS, we computed a model transmission spectrum during the primary transit of the hot Jupiter HD 209458 b including only water vapor with a volume mixing ratio of 10^{-5}. In addition, we used the $p-T$ profile retrieved in Brogi et al. (2017). In the case of KOPRA, the spectroscopic information was obtained from HITEMP2010, whilst the Exomol database was used in petitRADTRANS.

The computed spectra are compared in Fig. 2.14A. The fine grid calculations were smoothed with a boxcar average with a width of 1000 points. Overall,

both calculations are very consistent at all spectral intervals. We observed some minor differences across all wavelengths (see Fig. 2.14B), below the 3% level. However, there is a small discrepancy at the 5% level in the $1.0 - 1.1\,\mu$m region. We note that the KOPRA results were in very good agreement with the ARIEL spectrum in this spectral range (i.e., differences below 1%). Although we are still investigating the possible sources of this small discrepancy, a possible explanation might be related to a more restrictive cut-off of the absorption lines in petitRADTRANS. That is, the petitRADTRANS calculations might be neglecting the contribution of weak lines (i.e., below a given threshold), which are included in the KOPRA calculations.

Chapter 3

High dispersion spectroscopy with CARMENES

In this chapter we discuss in depth the cross-correlation technique applied to the very high-resolution data gathered with CARMENES with the aim of disentangling the exo-atmospheric signal from the telluric (i.e., Earth's atmosphere) and stellar contributions. As introduced in Sect. 1.2.3, close-in gas giants in extrasolar systems have large orbital velocities ($K_p \sim 150$ km/s) resulting in Doppler-shifts of the planetary lines, whereas the telluric and stellar signals can be considered quasi-static (see Fig. 3.1). The great advantage of using very high-resolution spectrographs is that they provide with the necessary spectral resolution to distinguish such wavelength shifts.

When we target the forest of absorption lines from molecules such as water vapor in the near-infrared (NIR), we are able to measure the shift from thousands of lines with a wide range of line strengths. However, these planetary lines are below the noise level. A usual approach is to merge the information from these lines by cross-correlating the spectra with a template of the expected exo-atmospheric absorption. This allows us to enhance the *signal-to-noise ratio* (S/N) of the planetary signal by a factor of $N_{\rm lines}^{1/2}$, where $N_{\rm lines}$ is a factor that takes into account the total number of planetary lines we are able to disentangle and detect[1]. Thus, the larger the covered spectral interval and the spectral resolution, the more lines we can resolve and the better our expected S/N of the planet will be. In fact, we can estimate the expected S/N of the planetary signal to first order by using this technique following Snellen et al. (2015) as

$$\mathrm{S/N}_p = \frac{S_p\, N_{\rm lines}^{1/2}}{\left(S_* + \sigma_{\rm bg}^2 + \sigma_{\rm RN}^2 + \sigma_{\rm dark}^2\right)^{1/2}}, \tag{3.1}$$

where S_p and S_* are the exoplanet's and stellar signals (in units of photons

[1]In fact, we are implicitly assuming here that all the detected lines are equally absorbent.

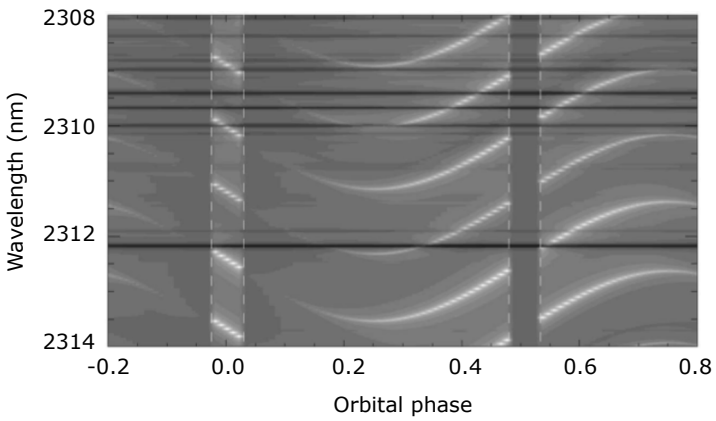

Figure 3.1: Radial velocity curve of a modeled CO absorption in the atmosphere of a close-in exoplanet. The planetary signal (bright curve) is significantly Doppler shifted as the exoplanet orbits around its host star with RV changes of $\sim$ km/s. The horizontal black lines represent the telluric absorption lines that do not move in wavelength (or the shift is very small, of the order of $\sim$ m/s, and is therefore neglected). The boxed interval around an orbital phase of 0.0 represents the primary transit. The signal from the exoplanet disappears as it is occulted by the star during the secondary eclipse (boxed at orbital phases $\sim$ 0.5). *Image credit:* Figure adapted from Snellen (2013).

per resolution element), respectively. [2] Also, $\sigma_{\rm bg}$ is the background sky noise, $\sigma_{\rm RN}$ is the readout noise, and $\sigma_{\rm dark}$ is the dark current noise in the detector. Implicitly, we have assumed that the telluric and stellar contributions have been ideally removed from the recorded spectra.

In some practical cases, the contribution from the sky background, readout noise, and dark currents can be neglected when compared to the often bright targets. Under this assumption, we are operating in the *photon-limited regime*, in which we can follow Birkby (2018) and re-write Eq. 3.1 as

$$\mathrm{S/N}_p = \left(\frac{S_p}{S_*}\right) (\mathrm{S/N})_* \, N_{\rm lines}^{1/2}, \tag{3.2}$$

where $\left(\frac{S_p}{S_*}\right)$ is defined as the signal ratio between the planet and the star, which can be estimated by their flux ratio, or by the expected transmission signal (Birkby, 2018). Here, $(\mathrm{S/N})_*$ is the total signal to noise ratio of the star, which is given by $S_*/S_*^{1/2} = S_*^{1/2}$ in the photon-limited regime.

Let's assume that we aim at observing with the NIR channel of CARMENES ($0.96 - 1.71\,\mu$m) so as to detect water vapor in the atmosphere of a transiting

[2] It is important to note that the $\sqrt{S_*}$ term in the denominator is the shot noise of the observations. The number of stellar photons that arrive to the detector (*events*) is not a constant in time, but follows a Poisson distribution. In the limit of a large number of events, the Poisson distribution approaches a Gaussian distribution. Hence, the shot noise introduced by the variable number of photons can be calculated as a gaussian noise, which has a standard deviation equal to the square root of the total number of events ($\sqrt{S_*}$).

hot Jupiter with a night-side flux ratio of $(S_p/S_*) = 10^{-5}$. If the target star is bright enough, the average signal-to-noise ratio of the star we could reach is of $S/N_* \sim 150$. Let's also assume that we can detect, on average, ~ 150000 H_2O lines (assumed as being all equally strong). If we monitor the transit of the exoplanet during 80 exposures, we should be able to detect water vapor from a exoplanetary origin with a $S/N = 10^{-5} * 150 * \sqrt{80} * \sqrt{150000} \sim 5$.

In the following sections of this chapter, we will discuss the different steps that allow us to extract the exoplanet's signal from the CARMENES raw high-resolution spectra. The characterization of the exo-atmospheres of the hot Jupiters HD 189733 b and HD 209458 b using this technique with CARMENES data within the frame of this thesis will be discussed in Chapters 4, 5 and 6.

3.1 The CARMENES instrument

CARMENES is an instrument built by a consortium of German and Spanish institutions, which is located in the coudé room of the 3.5m telescope at the Calar Alto Observatory. The main objective of the instrument is to survey nearly 300 main sequence stars, aiming at the detection of low mass planets ($\geq 2\,M_{\rm Earth}$) in their habitable zones.

CARMENES provides data with its two internal spectrographs. Their main features are:

- VIS channel: This spectrograph has a resolving power of $R = 94\,600$ and covers optical wavelengths in the interval $\Delta\lambda = 520 - 960$ nm. The full wavelength coverage is divided in 55 intervals, usually referred to as *spectral orders*. This detector is built with a 4096×4096 pixel $e2v\,231-84$ CCD.

- NIR channel: This second spectrograph provides data at a slightly lower resolving power of $R = 80\,400$ in the spectral interval $\Delta\lambda = 960 - 1710$ nm in 28 spectral orders. Its architecture consists in two 2048×2048 pixel $HAWAII-2RG$ infrared detectors, which yield a small gap in the joint of detectors at the center of each order.

The spectral orders in both channels generally overlap in their first and last wavelengths covered with their nearest neighbors so as to cover the full interval. However, the orders stop overlapping for $\lambda > 1.35\,\mu$m, resulting in gaps between orders (e.g., $0.015\,\mu$m wide between the last two orders).

Moreover, CARMENES allows us to observe with two fibers. Typically, fiber A is devoted to the target of the observations (e.g., the star hosting a transiting exoplanet), with fiber B being dedicated to either the Fabry-Pérot

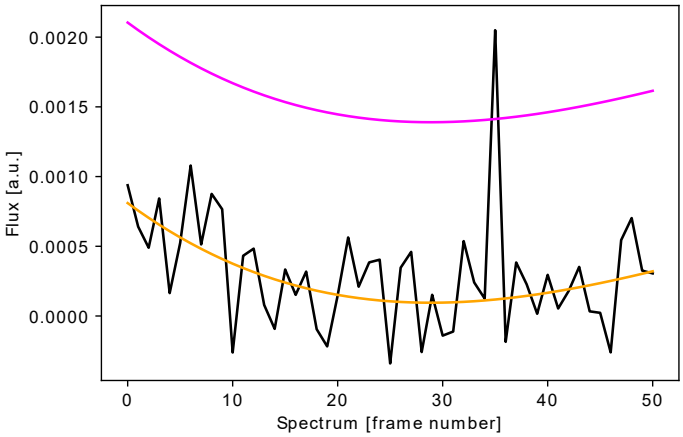

Figure 3.2: Time evolution of the flux received in a CCD pixel (i.e., at a specific wavelength) where a hot pixel was observed during the night of June 30th, 2019 (in black). The orange line represents the third-order polynomial fitted to the data. The hot pixel is identified as being deviated 5 standard deviations (in fuchsia) from the fit.

etalon[3], or to the sky (Seifert et al., 2012; Stürmer et al., 2014). However, CARMENES channels are highly stabilized for the long-term radial velocity survey and hence, an additional wavelength calibration is usually not necessary for the obtention of high quality spectra during the relatively short transits of hot Jupiters (i.e., ∼2–3 hours). Therefore, it is preferable to use fiber B for sky measurements that allow us to identify strong emission lines of the Earth's atmosphere (Alonso-Floriano et al., 2019a). Additionally, and as a safety test, the drift in wavelength of the instrument during the observations taken during one night (night drift in the following) need to be checked to guarantee a correct behaviour of the instrument. Usually, the CARMENES night drift over an entire night is below 30 m/s for both channels.

3.2 Data reduction and first steps of analysis

The CARMENES raw data are automatically processed after the observations by a dedicated data reduction pipeline called CARACAL (Zechmeister et al., 2014; Caballero et al., 2016). In the resulting spectra, we search for possible remaining bad-quality pixels with '*not a number*' (NaN) values and correct them by linear interpolation to their nearest neighbors. Next, we need to perform a correction of the outliers present in the data, which are attributable to cosmic rays (see Fig. 3.2). To do so, we fit a third order polynomial to the time evolution

[3]This is done mostly in radial velocity studies which require very high-precision simultaneous wavelength calibrations. See e.g., Reiners et al. (2018b) for an atlas of calibrated spectra with CARMENES.

of the flux received at each CCD pixel with an outlier-resistant routine, so that the cosmic ray itself does not influence the fit. Thereby, we are able to identify if and when a "hot" pixel appears when the flux exceeds five times the standard deviation of the rest of the data. In the case of a positive identification, the affected pixel is corrected by assigning the value of the outlier-resistant fit to it.

With the objective of removing strong broadband absorption contributions (i.e., the continuum), the spectrograph's *Blaze function*, and the different baseline of the spectra due to observing at different airmasses during the transit duration, we need to normalize the observed spectra (Snellen et al., 2008; Heng et al., 2015; Wyttenbach et al., 2015; Pino et al., 2018b). In order to have the same baseline in all spectra, we fitted a quadratic polynomial to the pseudo-continuum order by order as shown in Fig. 3.3. The fitting is performed usually by sufficiently sampling the pseudo-continuum of each spectral order (e.g., typically, $80-100$ points is enough for CARMENES data) by dividing each spectral order in a certain number of intervals. At each interval, we select the maximum value, avoiding the sky emission lines that are common in the reddest NIR orders of CARMENES[4]. Lastly, the data is normalized dividing it by the quadratic fit to the maxima.

However, this procedure stops working properly whenever the telluric water vapor has major absorption features in a certain spectral order. When this happens, the received flux is near zero at those wavelengths and hence, the division yields spurious values. For this reason, usually, the spectral orders that carry the strongest H_2O absorption are usually discarded (see the spectral regions around 1.15 and 1.4 μm in panel D of Fig. 3.3). Although the cross-correlation technique needs the spectra to be normalized, it is mostly insensitive to small shifts around 1 of the normalized pseudo-continuum in the different spectra. That is, the results will not be affected by small inaccuracies (although perceivable by the naked eye) in the normalization at each spectrum. For instance, this can be seen in Fig. 3.3D or in Fig. 3.4B, where the normalized continuum is not exactly one for all orders. In addition, the orders neighbouring the discarded ones may have a few strong lines which also yield spurious positive values that need to be eliminated.

The masking of spectral regions with strong absorption, emission or spurious normalization values is the next step in the data analysis (see Fig. 3.4). Firstly, the telluric absorption lines (i.e., mostly H_2O at these wavelengths) that block almost all of the incoming flux have to be masked, since very little information from the exoplanet is preserved at them (e.g., lines absorbing more than, typically, 80% of the flux). If left unmasked, these regions could hinder the telluric correction we need to perform, since such strong lines are poorly removed. The identified sky emission lines with fiber B are also masked. Furthermore, the spurious normalization values are masked if they reach, typically, the 1.05 level.

[4]These are mainly due to OH emission in the Earth's atmosphere.

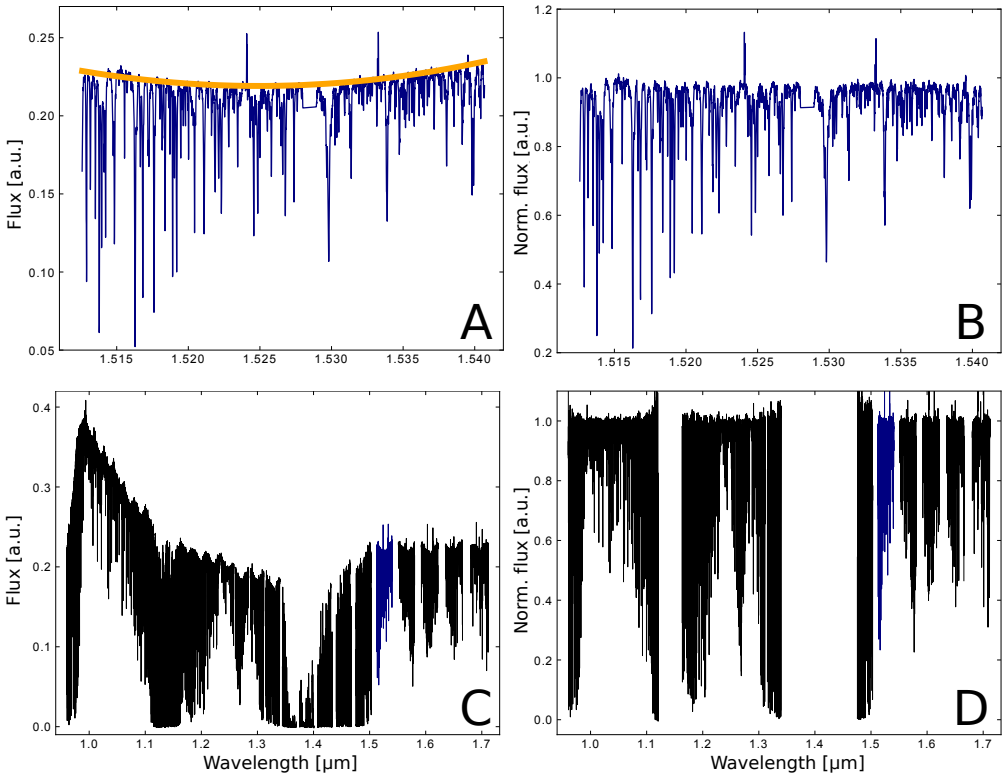

Figure 3.3: Normalization of spectra. Panels A and B depict the flux received in the NIR spectral order 41. Panel A shows the original spectrum (dark blue) and the quadratic fit to the pseudo-continuum (orange), which is used to normalize the data in panel B. Panels C and D show a typical spectrum in the entire NIR channel in its original and normalized form, respectively. All NIR orders are shown in black, except for order 41 which is shown in dark blue. The spectral regions covering $1.12 - 1.16\,\mu$m and $1.34 - 1.47\,\mu$m are excluded in panel D since the large telluric absorption in them results in almost zero flux, which precludes an accurate normalization.

An example of a normalized and masked spectra is shown in Fig. 3.4B.

The normalization and masking steps are crucial for an optimal functionality of the algorithms we used for removing the telluric and stellar features (see next section). However, they are tied to another unfortunate but unavoidable effect: the loss of the absolute level of absorption at each wavelength bin (i.e., we removed the continuum information). Because of this, this technique is not sensitive to the absolute level of absorption, but to the relative depth of the absorption lines with respect to the flux continuum. Additionally, the synthetic spectra created with different p-T and composition profiles do not show large differences after being normalized. That is, a degeneracy is introduced in the models. This mainly affects our capabilities to retrieve the exoplanet's true temperature and abundances with this technique.

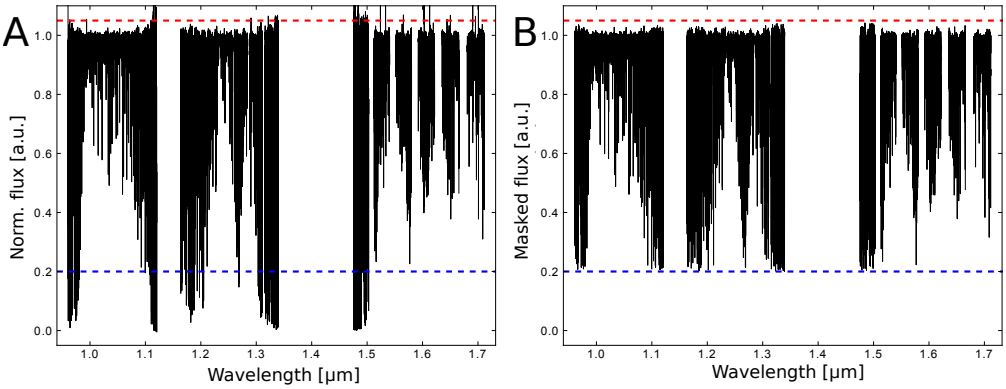

Figure 3.4: Masking procedure for telluric absorption and emission lines, and normalization artefacts (visible in panel A). The telluric lines that absorb more than 80% of the flux (in dashed blue) are masked. The masked emission lines were identified with fiber B. The normalization artefacts above 1.05 (dashed red) are also masked.

3.3 Telluric and stellar signal removal with SYSREM

Naturally, the strongest contribution to ground-based spectra comes from our own atmosphere. If we are to detect the weak exo-atmospheric signal, roughly at the $10^{-3} - 10^{-5}$ level, we need to remove the Earth's absorption and stellar features at that precision or better. Here is where we can take advantage of the fact that both contributions are almost fixed in wavelength whereas the exoplanet signal has a significant and changing Doppler shift as it orbits at high velocities. In the studies presented in the following chapters of this thesis, we removed these features by using SYSREM, a principal component analysis (PCA) algorithm (Tamuz et al., 2005). This algorithm was originally developed for light curve surveys, but it has been widely tested and used in the past for our purposes (Birkby et al., 2013; Nugroho et al., 2017; Cabot et al., 2018; Hawker et al., 2018; Alonso-Floriano et al., 2019a). The blind PCA approach for the cleaning of spectra suits well in our case, since the data not only have telluric and stellar contamination, but also unknown and/or random noise sources which are very difficult or impossible to identify and model separately.

Due to its relevance for this thesis, we present the equations and the algorithm scheme that is carried out within each SYSREM run in Appendix A. Essentially, SYSREM treats the time evolution of each of the pixels as a light-curve and removes common systematic features (also called *common modes*) that affect all wavelength bins and all the observed spectra (see Appendix A). Thus, the algorithm primarily fits and removes the largest spectral variations in wavelength and in time, which are caused by the telluric and stellar features. At the same time, SYSREM allows to weight the measurement of each spectral bin by its uncertainty. In particular, the CARMENES pipeline provides a measure-

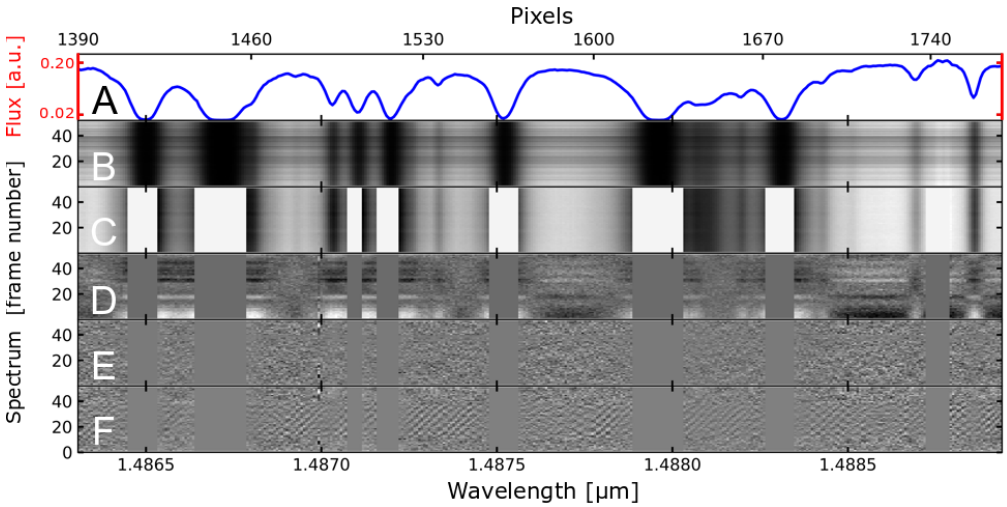

Figure 3.5: Resulting spectra at the different steps of the data analysis for the spectral region $1.486 - 1.489\,\mu$m. A: Flux measured in the first spectrum taken during the transit of HD 189733 b on the night of 30 June 2019. B: Spectral matrix with the original observations of CARMENES. The gray-scale indicates the strength of absorption of the spectral features. C: normalized and masked spectra. D: Residual matrix after the first iteration. E: Residual matrix after the 9th iteration. F: Matrix for the 9th iteration also, but with an injected artificial exo-atmospheric signal at 1000× the expected level (tilted dark patterns).

ment of the photon noise and the read out noise for each pixel at each spectrum, which constitutes the input uncertainty. Therefore, by iterating SYSREM at each spectral order individually, we are able to remove most of the telluric and stellar features, and also the variations induced by changes in the airmass, in the column depth of *precipitable water vapor* (PWV), etc.

However, SYSREM does not really fit the airmass changes nor other atmospheric parameters (see, e.g., Nugroho et al., 2017). Instead, this algorithm performs linear fits that only provide the approximated behavior of the non-linear evolution of the telluric absorption with time. Therefore, even after many iterations of the algorithm, some telluric residuals are left. We illustrate this procedure in Fig. 3.5 for the spectral region $1.486 - 1.489\,\mu$m, where we can identify the steps discussed so far.

In Fig. 3.5A we show the measured flux in the first spectrum taken during the night of 30 June 2019 during the transit of HD 189733 b with the CARMENES NIR channel in the region from 1.486 to $1.489\,\mu$m. A very useful way to visualize all spectra taken during the night is in the form of a spectral matrix (see panel B). Here, the gray-scale indicates the strength of the lines (i.e., the darker the color, the more opaque the atmosphere is at that wavelength bin). In panel C, we show the previous spectral matrix after the normalization and masking steps have been applied, as described in the previous section. Panel D shows the re-

sulting spectral matrix after the first SYSREM iteration has been applied. At this point, the algorithm has started cleaning some features. However, there are still evident residuals, which are almost completely corrected after nine iterations, as shown in panel E.

In order to visualize if the exo-atmospheric signal, which is well below the noise level, would be preserved after the PCA analysis, a usual procedure is to inject a model absorption of the exo-atmosphere in the data. In panel F, we show the result of applying nine iterations to the data with an injection at 1000× the expected strength[5]. Here, we can observe that the planetary signal is preserved in the data after nine iterations. That is, the algorithm does not identify this absorption as a common mode, since it changes in wavelength over time. The exo-atmospheric lines are thus visualized as a forest of slanted dark lines between spectra 11 and 37 (i.e., the transit duration in this case).

However, the planetary features also create a weak common mode (Birkby et al., 2017). Thus, after a certain number of SYSREM iterations, these weak features will also be perceptible by the algorithm. At this point, SYSREM starts focusing on fitting and removing the planetary signal, which is an unwanted effect. There are different ways in which this can be taken into account in order to avoid erasing the planetary signal. In the following chapters, where we apply this technique, we will discuss the approaches we used for each particular case.

There are other useful approaches to remove the telluric contamination, such as to use the European Southern Observatory MOLECFIT tool (Smette et al., 2015). MOLECFIT corrects for the telluric absorption features by using synthetic models of the Earth's atmosphere. The main advantage of this is that we do not need to normalize the spectra, which allows us to preserve the absolute level of absorption. If the modeled telluric spectrum is accurate enough, an excess absorption should be left at the wavelengths corresponding to the planetary features. However, the main disadvantage is that unknown systematics and the stellar features are untouched and hence, additional steps need to be carried out with the data (see, e.g., Brogi et al., 2016; Schwarz et al., 2016).

MOLECFIT has been applied succesfully in HDS studies to place upper limits on the strength of water vapor lines in hot Jupiters and to study the telluric water vapor and molecular oxygen spectral features (Allart et al., 2017; Ulmer-Moll et al., 2019). We also studied telluric-corrected CARMENES spectra by using MOLECFIT in collaboration with the CARMENES Consortium. However, we could not recover the exo-atmospheric signal when using this algorithm (see Sect. 4.3.1). Ulmer-Moll et al. (2019) applied this tool to CRIRES data and found a very large scatter (between 3% and 7%) in the residual spectra. Hence, the fit uncertainties over the entire wavelength coverage of the CARMENES

[5]The injection is made here strong enough so as to identify the lines by eye in the figure, but such strength also perturbs the noise level and thus, it is not useful for other purposes. In the actual analyses, this signal is injected, typically, at 5× the expected level.

channels are expected to be rather large for attempting a detection of the weak exoplanet's features with this technique. Because of this, MOLECFIT corrections were not useful for the HDS studies presented in the following chapters of this thesis.

Other works have succeeded in the removal of telluric lines by normalizing spectra and then fitting a polynomial directly to the time evolution of the pixels (Brogi et al., 2012; Brogi et al., 2013, 2014; Schwarz et al., 2015; Brogi et al., 2016; Brogi et al., 2018). This fit usually takes the form:

$$\log\left[F\left(\lambda_i,\, t\right)\right] = c_{i,\,0} + c_{i,\,1}a\left(t\right) + c_{i,\,2}a^2\left(t\right), \tag{3.3}$$

where, $F\left(\lambda_i,\, t\right)$ is the flux received at a certain wavelength bin λ_i at the time t, $c_{i,\,0}$, $c_{i,\,1}$ and $c_{i,\,2}$ are the coefficients of the fit, and $a\left(t\right)$ is the airmass at that time.

In summary, the appropriate procedure for the removal of the telluric lines depends on each particular science case and the quality of the observations. Thus, there is no 'best approach' so far (see, e.g., Cabot et al., 2018). In the frame of this thesis, we have investigated different ways to optimize the telluric removal step, which will be discussed in Chapters 4 and 5.

3.4 Cross-correlation of the data with a model of the exo-atmosphere

The exo-atmospheric lines are at this point buried below the noise level after the telluric and stellar signal removal (see e.g., Fig. 3.5E), since their individual strength is rather low. The basic idea is then to accumulate the information from the thousands of absorbing ro-vibrational lines (e.g., for water vapor) by performing a cross-correlation (CC) of the residual matrices with model spectra of the exo-atmosphere. These models are computed as described in Sect. 2.4.

The CC values provide us with a measurement of the similarity between our model template , x, and the spectra, y, as follows (see, e.g., Hoeijmakers, 2017):

$$CC\left(x, y\right) = \frac{\sum_{k=0}^{N}\left(x_k - \overline{x}\right)\left(y_k - \overline{y}\right)}{\sqrt{\sum_{k=0}^{N}\left(x_k - \overline{x}\right)^2 \sum_{k=0}^{N}\left(y_k - \overline{y}\right)^2}}, \tag{3.4}$$

where N is the number of data points, and $\overline{x}$ and $\overline{y}$ are the mean values of the model and the measured spectra, respectively. With this definition, the CC is insensitive to global changes of the model points. That is, provided that the line positions match, the CC value obtained with Eq. 3.4 for the given x and y sets is the same as the one obtained by changing the model in the forms $b \cdot x$ or $b + x$, where b is an arbitrary constant. However, the CC value will differ if a subset of the model points, x_k, is changed or if the changes introduced to the model

have a spectral dependence (e.g., a change in the line shapes, Doppler-shifting the model, etc.).

By definition, the CC values could take any value between -1 and 1, which are interpreted as anti-correlation values (< 1) and correlation values (> 1). Of course, the more accurate the template is (i.e., closer to the true absorption), the larger the CC values will be. At this point, it is interesting to discuss several critical points that determine our capabilities to enhance and extract the exo-atmospheric signal:

- Accuracy of spectral linelists: Since we aim at detecting as many atomic or molecular lines as possible via Doppler shifts at very high resolving powers[6], the accuracy and completeness of the line strengths and line positions at the required p-T conditions is crucial. For some molecules, such as CO, this task is affordable since it is a simple and well-understood molecule. However, the linelists of more complex molecules that have a forest of lines (e.g., water vapor, methane, titanium oxide, etc.) are much more difficult to know accurately, especially at high temperatures. Hence, their linelists are less complete and accurate. Often, databases are calculated by means of quantum chemistry, which imprints inaccuracies that can severely affect our templates (see e.g., the problems in TiO studies in Hoeijmakers et al., 2015). Spectroscopic linelists are also compiled from laboratory experiments for a range of temperatures (Hargreaves et al., 2015; Hörst et al., 2018). Some databases blend laboratory measurements with theoretical calculations, as is the case of the HITRAN and HITEMP databases (Rothman et al., 2010; Gordon et al., 2017) or the ExoMol database (Tennyson et al., 2016).

- Matching the spectral resolution of the template and the measurements: The instrument resolution usually changes (although slightly) across its wavelength coverage and it has a certain *Line Spread Function* (LSF). In the case of CARMENES, we have contributed to the development of an accurate LSF for the VIS and the NIR channels (Nagel et al., 2019). We model the CARMENES LSF as a Voigt line shape profile whose components, the Doppler and the Lorentz width coefficients, change with wavelength in the form:

$$\begin{aligned} \alpha_D &= \mathrm{FWHM}_D \frac{\lambda}{2\sqrt{\ln(2)}}, \\ \alpha_L &= \mathrm{FWHM}_L \frac{\lambda}{2}, \end{aligned} \tag{3.5}$$

  where the Doppler and Lorentz *full width at half maximum*, FWHM_D and

[6] At low resolutions, inaccuracies in the line positions have a lesser impact, since they appear convolved and we can only see the 'broadband' contribution.

FWHM$_L$, respectively, for the NIR and VIS channels are:

$$\begin{aligned} \mathrm{FWHM}_{D,\,\mathrm{NIR}} &= 1.18 \times 10^{-5}, \\ \mathrm{FWHM}_{L,\,\mathrm{NIR}} &= 1.70 \times 10^{-6}, \\ \mathrm{FWHM}_{D,\,\mathrm{VIS}} &= 1.01 \times 10^{-5}, \\ \mathrm{FWHM}_{L,\,\mathrm{VIS}} &= 2.10 \times 10^{-6}. \end{aligned} \tag{3.6}$$

Thus, the high resolution model spectra, which we typically compute at a spectral resolution of $\mathcal{R} \sim 4 \cdot 10^7$, is convolved with this CARMENES LSF. The convolution is performed at given wavelengths, which we choose to be those of the measured spectra.

- Normalization of the template: Ground-based data need to be normalized, as described previously. Hence, we need to normalize also the model of the exo-atmosphere so as to maximize the possible similarities.

The standard procedure is to cross-correlate the measured spectra, corrected from the telluric and stellar contributions, with the model template Doppler-shifted in a wide range of planetary radial velocities (e.g., from -200 to $+200$ km/s). The step size of the velocity grid should be sufficiently small so as to identify the shift of the planetary lines as the planet moves with respect to Earth during the observations. For instance, a good choice is the instrument pixel size (~ 1.3 km/s for the CARMENES' channels).

The CC values for each of the Doppler shifts conform the so-called *cross-correlation function* (CCF). By performing this operation for all the observed spectra, we obtain a cross-correlation matrix, $\overline{CCF}$, as the one shown in Fig. 3.6A. If detected, the exo-atmospheric signal should appear as positive (i.e., darker colors in the figure) CC values along the expected planetary velocities, given by

$$v_p\,(t, K_p) = v_{sys} + v_{bary}(t) + K_p \sin\left[2\pi\phi\,(t)\right], \tag{3.7}$$

where v_{sys} is the systemic velocity of the explored system, $v_{bary}(t)$ is the barycentric velocity during the observations, K_p is the semi-amplitude of the orbital motion of the exoplanet, $\phi(t)$ is its orbital phase, and t is time. In Fig. 3.6B we illustrate this behavior by injecting a model at $5\times$ the expected strength of the signal. Thus, the expected exoplanet's trail is easily identified (i.e., between the tilted dashed lines). Naturally, no injection is performed when evaluating the presence of a signal in the real data.

We can further enhance the planetary signal by co-adding the information contained in the $\overline{CCFs}$ over time. To do so, we first divide each row of the $\overline{CCFs}$ by their median value, in order to remove broad variations arising from the differences between the spectra and the template. Next, we shift each of the CCFs in the cross-correlation matrix to the exoplanet's rest-frame by using

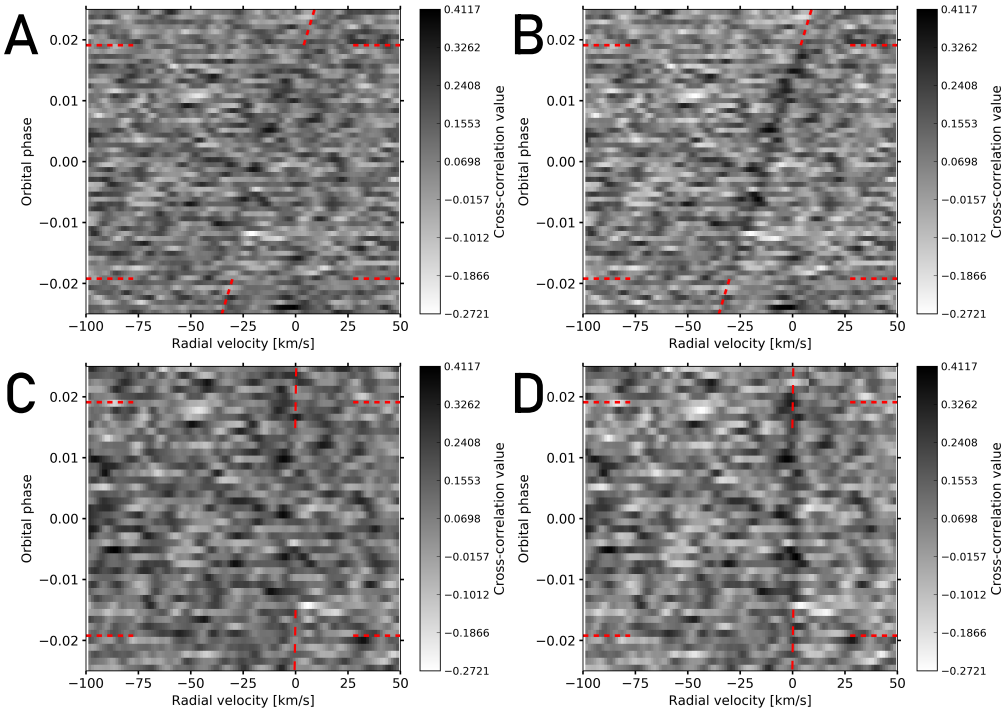

Figure 3.6: Cross-correlation values as a function of the exoplanet's radial velocity and its orbital phase (or, equivalently, time) during the observations. The matrices are shown in the Earth rest-frame (upper row, panels A and B) and in the exoplanet's rest-frame (lower row, panels C and D). The first column (A and C) correspond to real data, whilst in the second column (B and D) an additional model signal was injected at 5× the expected strength. The latter are shown only for illustration. The horizontal dashed red lines mark the orbital phase of the first and last in-transit spectra. The tilted dashed red lines in panels A and B mark the expected velocities of the exoplanet with respect to the Earth. The vertical dashed lines in panels C and D mark the rest-frame velocities of the exoplanet (i.e., zero). In particular, the planetary signal in panel C is shifted towards negative radial velocities (i.e., with respect to the vertical dashed red lines), which could be explained by winds in the exo-atmosphere (see main text and, also, Chapter 5).

Eq. 3.7. This is shown in Fig. 3.6C and, more clearly, with an injection, in Fig. 3.6D. Here, it is common to assume that the planetary K_p is unknown, regardless of previous measurements of this quantity for the specific exoplanet. Typically, we create a grid in K_p and run the entire CC analysis for each value in the grid.

Once the $\overline{CCF}$s are shifted for each value of K_p, we can co-add the information over time and obtain the total CCF. Thus, we should find the largest CCF peak at the expected planetary K_p, when the co-adding of the signal is most correct. This step allows us to directly measure K_p, although with rather large uncertainties. This is mainly because the change in the exoplanet's RV during

the transit, of only a few tens of km/s, is too small to accurately measure this quantity (Brogi et al., 2018; Alonso-Floriano et al., 2019a; Sánchez-López et al., 2019). Furthermore, we run this procedure independently for each of the spectral orders of CARMENES so as to validate the signals that might appear in each of them. At this point, if no telluric residuals or other artefacts are found in the CCF for each of the spectral orders, we can also merge their information by co-adding their total CCFs.

Consequently, the resulting CCFs encode the information of all the instrument's spectral points over time, for each K_p value. We can thus present all the results in the form of a CC map (see Fig. 3.7A). Here, a region of large CC values should be observed around the expected planetary velocities ($\sim 150\,\mathrm{km/s}$ in our example), with no significant correlation nor anti-correlation signals at other locations of the explored velocities. That is, the map should present a significant signal that is consistent with the exoplanet's velocity, and no other comparable signals should appear at other velocities in the explored velocity space. Therefore, the CCF obtained by using the expected planetary K_p should present a peak value at the rest-frame radial velocity of the exoplanet, which is ~ 0 km/s (see Fig. 3.7B). Often, the CCF peaks appear at RVs that, errors considered, are not compatible with a zero rest-frame velocity, as is the case in Fig. 3.7B (i.e., the CCF peak is displaced to negative velocities in the figure). This is usually attributed to strong winds that flow from the dayside to the nightside at the terminator of hot Jupiters, which are predicted by GCM models (Snellen et al., 2010; Showman et al., 2013; Brogi et al., 2016; Zhang et al., 2017; Brogi et al., 2018; Alonso-Floriano et al., 2019a; Sánchez-López et al., 2019). Under this assumption, we note this wind velocity as v_{wind} in this thesis.

3.4.1 Measuring the significance of the signal

The resulting cross correlation map presents a distribution of CC values that, in some cases, shows a potential detection of molecular features from the exoatmosphere. In order to quantify the significance of the potential detection, different metrics have been used in the past. We detail the two most common ones in the following.

The signal-to-noise ratio metric

We can re-express the CC map as a S/N map (Brogi et al., 2012; Brogi et al., 2013, 2014; Brogi et al., 2018; Cabot et al., 2018; Alonso-Floriano et al., 2019a). The S/N can be calculated at each K_p by dividing each CC value by the CCF standard deviation obtained from the whole RV interval, but excluding the region around the CC value (see Fig. 3.7C and Fig. 3.7D). As a result, this S/N thus depends on the width of the velocity interval. In the usual scenario, when

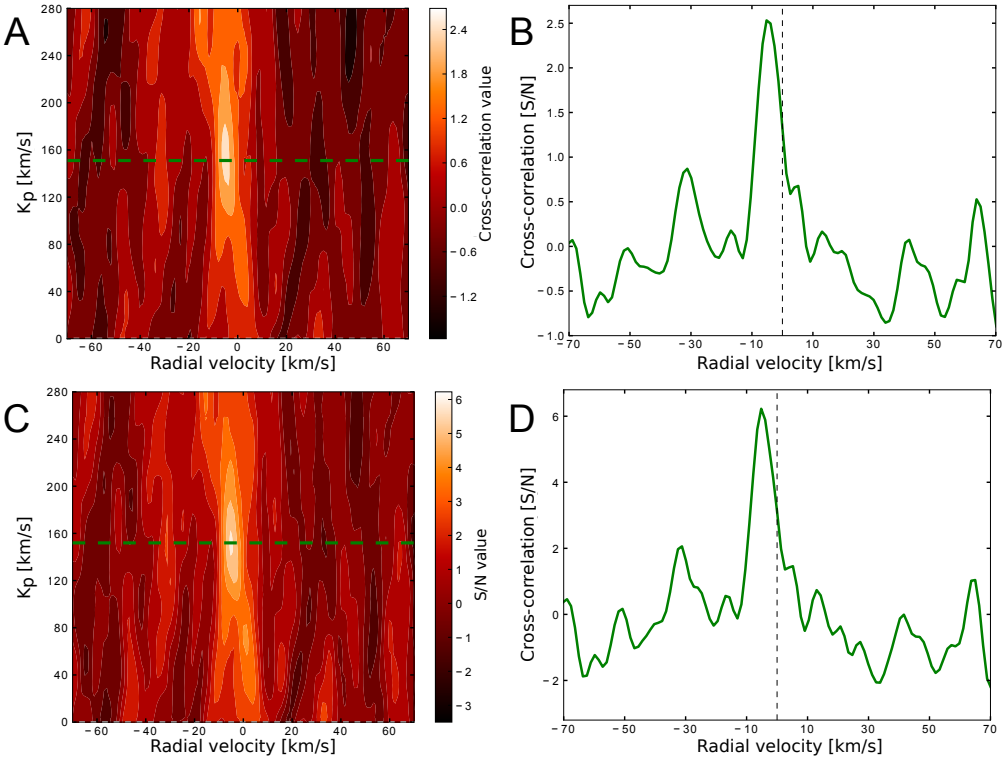

Figure 3.7: A: Typical cross-correlation map for the explored RV and K_p grids when a signal is found. The CCF with the largest CC values (green dashed line) should be consistent with the expected exoplanet's K_p, which reinforces the confidence of the detection. B: CCF with the largest peak value in the map of panel A. The dashed vertical line marks the zero velocity (rest-frame of the exoplanet). Panels C and D provide the same information as A and B, respectively,, but re-expressed in units of S/N (see text).

there is no correlated noise, the S/N metric is a very reliable way of quantifying the significance of the signals. However, in the presence of auto-correlation signals (i.e., aliases) or, in general, correlated noise that still averages to zero, the standard deviation of the CCFs might be inflated and hence, the S/N metric might underestimate the potential signal.

The Welch t-test metric

Another procedure for the calculation of the signal's significance is that based on the Welch t-test metric. The main idea is to use the fact that the distribution of correlation values, in the absence of correlated noise or planetary signals, should be a Gaussian with a zero mean (Brogi et al., 2012; Birkby et al., 2017). However, the CC values in the velocity trail of the exoplanet should not be distributed in this way. That is, the trace of positive CC values should have a

mean value significantly deviated from zero.

In the case of transit spectra, we use the $\overline{CCF}$ only in-transit, and in the Earth's rest-frame (see the CC values between the horizontal dashed red lines in Fig. 3.6A). Here, we can define two distributions:

- The *in-trail* distribution: This set covers the CC values along the planetary RVs and, typically, a three-pixel wide window centered around them (e.g., for CARMENES, this means a window from -1.3 to $+1.3$ km/s). Since the exoplanet's RVs have to be calculated using Eq. 3.7, this test also allows for a full exploration of the K_p space so as to directly measure this quantity and compare it with the S/N metric and earlier studies. In addition, we can slide the considered in-trail window at each K_p in the RV direction (i.e., from left to right) so as to measure any additional shifts of the potential signal of the exoplanet. This would be analogous to the direct identification of Doppler-shifts of the CCF peak in the S/N metric.

- The *out-of-trail* distribution: This set comprises the rest of the studied velocities, but excluding a region around the in-trail distribution (e.g., for CARMENES, this safety window is set to ± 15.6 km/s around the in-trail window). In this way, we can guarantee that the out-of-trail distribution should contain no planetary information. Therefore, the out-of-trail CC values correspond to uncorrelated noise and should be distributed normally with a zero mean.

After defining both distributions of values at each K_p, the following step is to compare them by means of a Welch t-test (Welch, 1947). If no planetary signal is present in our data and in the absence of other correlated-noise sources, the in-trail distribution should also be a Gaussian centered in zero. We thus proceed to set the initial *null hypothesis*, H_0, of both distributions having the same mean value. This test provides us with the probability that both sets are drawn from the same parent distribution and returns the value of the so-called t-statistic, which is expected to be larger the stronger the evidence against H_0 is. Each t-value can be directly converted into a $p-$value, which represents the probability of obtaining a t-value as large as observed or larger if H_0 was true. Subsequently, the p-values can be expressed in terms of standard deviations (σ-values). In this analysis, the presence of a signal of exo-atmospheric origin in the data would yield significantly different means for the two distributions. The in-trail CC values would then contain information not consistent with uncorrelated noise, hence rejecting the null hypothesis with high significance.

The resulting σ-map for an example of K_p-RV grid is shown in Fig. 3.8A. A region of high σ-values evidences the presence of a signal in our data. If the K_p and RV at which the signal appears are consistent with those of the exoplanet, then the test qualifies our signal as being highly significant. Furthermore, the

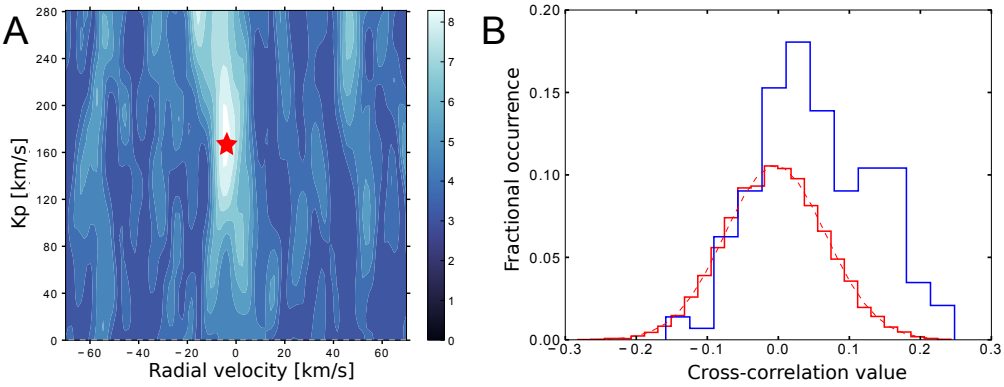

Figure 3.8: A: σ-map for an example K_p-RV grid. A region of largest significance is found near the center of the map. The red star marks the position of largest σ-value. B: In-trail (blue) and out-of-trail (red) distributions for the K_p-RV pair marked by the red star. The in-trail distribution is significantly deviated from the out-of-trail set.

exploration of the full map allows here as well to check for spurious signals or aliases[7] that would diminish our confidence in the potential exoplanetary signal. The in-trail and out-of-trail distributions for the K_p-RV pair providing the largest σ-value in this example (see the red star marking this pair in Fig. 3.8A) are shown in Fig. 3.8B. We can directly observe that the in-trail distribution is significantly deviated from zero, whereas the out-of-trail distribution agrees well with the expected Gaussian behaviour (shown as a dashed red curve).

The Welch t-test metric is also widely used in the literature (Birkby et al., 2017; Nugroho et al., 2017; Brogi et al., 2018; Cabot et al., 2018; Alonso-Floriano et al., 2019a; Sánchez-López et al., 2019). However, it has been recently suggested that this test might be more vulnerable to potentially overestimate the possible signals (Cabot et al., 2018). This, combined with the potential underestimation of signals when using the S/N metric, evidences the current lack of an ideal procedure for the calculation of the significance of the signals.

[7]False positives might appear as a result of the autocorrelation function of the template.

Chapter 4

Detection of H_2O in the atmosphere of HD 189733 b

We explore the capabilities of CARMENES for characterizing the atmosphere of hot-Jupiters from a 4-m class telescope by targeting multiple water absorption bands. In particular, we study those centred at ~ 1.15 and $\sim 1.4\,\mu$m. Previous *Hubble Space Telescope* (*HST*) observations suggest that these spectral intervals could be relevant for distinguishing the haziness and/or cloudiness of these exo-atmospheres. To do so, we observed one transit of the archetypal hot Jupiter HD 189733 b with CARMENES. We removed the telluric and stellar absorption by using SYSREM, which performs a principal component analysis including proper error propagation. Consecutively, we cross-correlated the residual spectra with model templates including the absorption of the expected molecules in the atmosphere. With this analysis, we report a CCF peak at a S/N of 6.6, revealing the presence of water vapor in the transmission spectrum of HD 189733 b. In addition, the CCF signal appeared slightly blue-shifted at -3.9 ± 1.3 km/s, which is an indication of day-to-night winds at the terminator of this hot Jupiter. Moreover, we studied the individual CCF signals of the H_2O bands at 1.15 and 1.4 μm, finding significant CCF peaks at S/N= 4.9 and S/N= 4.4, respectively. Both spectral features are consistent with those observed with the *HST*. With our results, we prove that ground-based high-resolution spectrographs can access the H_2O absorption bands individually and provide insightful information to constrain the properties of exoplanet atmospheres. Although the current multi-band detections cannot yet constrain atmospheric haze models for HD 189733 b, future observations at higher S/N could provide an alternative way to tackle such challenge.

F.J. Alonso-Floriano, A. Sánchez-López, I.A.G. Snellen, M. López-Puertas, et al., *Astronomy & Astrophysics*, 621, A74 (2019)

4.1 Introduction

For a long time since the discovery of the first exoplanet (Mayor and Queloz, 1995), it was thought that exo-atmospheric science belonged to the domain of space observations, either with the *HST* or the *Spitzer Space Telescope* (Charbonneau et al., 2002; Vidal-Madjar et al., 2003; Tinetti et al., 2007; Grillmair et al., 2008). However, this notion changed drastically with the works from Redfield et al. (2008) and Snellen et al. (2008). These authors used ground-based high-resolution instrumentation on $8-10$-m class telescopes to detect sodium in the atmospheres of HD 189733 b and HD 209458 b, respectively. Since then, the field of atmospheric characterization with highly-stabilized ground-based spectrographs has flourished, also for 4-m class telescopes, especially for the high S/N stars, such as HD 189733. For instance, Wyttenbach et al. (2015) and Louden and Wheatley (2015) used data from the High Accuracy Radial-velocity Planet Searcher échelle spectrograph (HARPS, Mayor et al., 2003) at the ESO 3.6 m telescope to study in detail the shape of the sodium transmission signature of HD 189733 b, from which the authors extract information about the temperature at different pressure levels and winds in the exo-atmosphere. Molecular features have also been succesfully studied in HD 189733 b. For instance, Brogi et al. (2018) used GIANO at the Telescopio Nazionale Galileo (TNG) to detect the presence of water vapor in the atmosphere of HD 189733 b, mainly from its absorption band around $2\,\mu$m.

Recently, Hoeijmakers et al. (2018a) used HARPS-North transmission spectra so as to find, for the first time, absorption features of heavy atomic species such as Fe, Fe^+, and Ti^+. Also in this target, Yan and Henning (2018) used CARMENES to detect the excess absorption of atomic hydrogen by observing its absorption in the Balmer Hα line during the transit of the ultra-hot Jupiter Kelt-9b. In this chapter, we also use CARMENES to study the transmission spectrum of HD 189733 b with the aim of detecting water vapor in this exo-atmosphere. As mentioned before, this hot Jupiter is one of the prototypical, most well-studied hot Jupiters since, for long, it was the brightest known transiting system ($V = 7.6$ mag, $J = 6.1$ mag). In fact, there are a myriad studies that have aimed at the characterization of this exo-atmosphere targeting its hydrogen exosphere (Etangs et al., 2010, 2012; Bourrier and Etangs, 2013), its transmission spectrum (Redfield et al., 2008; Sing et al., 2011; Gibson et al., 2012; McCullough et al., 2014; Brogi et al., 2016; Brogi et al., 2018), and its emission spectrum (Deming et al., 2006; Charbonneau et al., 2008; Grillmair et al., 2008; Swain et al., 2010; Todorov et al., 2014).

In particular, one of our objectives is to use the CARMENES NIR channel to study the two strongest water features in this wavelength interval at ~ 1.15 and $\sim 1.4\,\mu$m. Although challenging, detecting these absorption features individually would translate in a ground-based confirmation, by means

of a different technique and instrument, of the $\sim 1.4\,\mu$m band only observed previously with the Wide Field Camera 3 (WFC3) at the *HST* in several planets (see, e.g., Fig. 1.8 and Sing et al., 2016). In addition, it has been observed that HD 189733 b presents a steep Rayleigh scattering slope which is especially prominent at optical and ultraviolet wavelengths (Etangs et al., 2008a; Pont et al., 2008; Gibson et al., 2012; Pont et al., 2013; Sing et al., 2016; Pino et al., 2018b). As outlined in previous chapters, a strong extinction by hazes can mask the absorption features of water vapor and this effect has a strong wavelength dependence, being stronger at optical wavelengths than in the near infrared. Therefore, a comparison of the strength of water absorption signal over different wavelength intervals could potentially constrain the Rayleigh scattering of the high-altitude hazes in this kind of exoplanets (Stevenson, 2016; Pino et al., 2018a). Thus, our study also represents one of the first steps in this direction.

4.2 Observations and data analysis

4.2.1 CARMENES data for HD 189733 b

We used CARMENES to observe the system HD 189733 (see Table 4.1) on 7 September 2017. Unfortunately, only the NIR channel data could be considered in this work, since no spectra were recorded with the VIS channel due to shutter problems during this observing night. In addition, since the wavelength-calibration requirement for transmission spectroscopy is not very demanding, we opted to use the second fiber for sky measurements (see Sect. 3.2). These sky measurements were not used in the data calibration process, but only to visually identify sky emission lines. The observations were obtained in service mode, and consist of 46 exposures of 198 s, starting at 20:14 UT and ending at 00:00 UT, and corresponding to a planet orbital phase range of $\phi = -0.035$ to $\phi = 0.036$ (see Fig. 4.1A). During the course of the observation, the relative humidity varied between 57 and 65%. The star moved from airmass 1.08 to 1.30, during which we updated the atmospheric dispersion corrector four times by reacquisition of the target, which takes about two minutes (see, e.g, Seifert et al., 2012). A typical continuum S/N of ~ 150 was reached per spectrum. In addition, the mean S/N per pixel was ~ 120 (see bottom panel of Fig. 4.1A and Fig.4.1B).

The CARMENES data were automatically processed after the observations using the dedicated data reduction pipeline CARACAL v2.10 (Zechmeister et al., 2014; Caballero et al., 2016). The Precipitable Water vapor (PWV) was retrieved from the measured spectra using the ESO Molecfit tool (Smette et al., 2015). The PWV level during the observations was relatively high, ranging from 11.7 to 15.9 mm, compared to an average of 7 mm at Calar Alto. This made the telluric water absorption in orders $45 - 42$ ($1.34 - 1.47\,\mu$m) and $54 - 53$

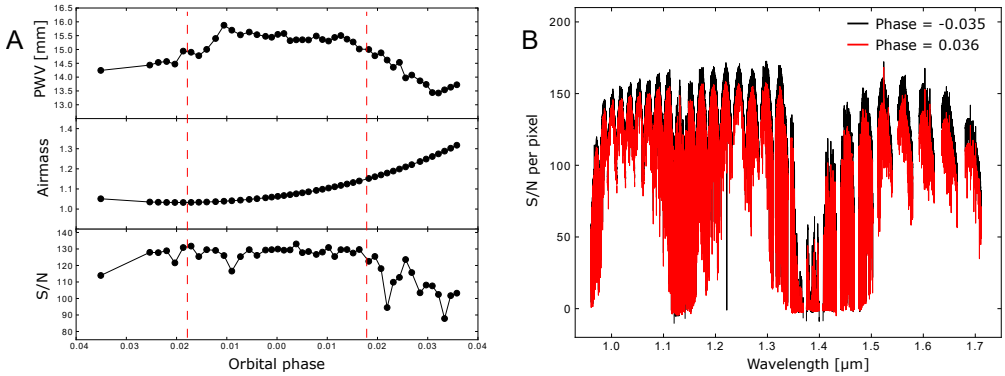

Figure 4.1: A: Column depth of Precipitable Water vapor (PWV, *top panel*), airmass (*middle panel*) and S/N (*bottom panel*) of the HD 189733 b observations on 7 September 2017. All quantities are shown as a function of the orbital phase of the exoplanet. The transit occurred at the orbital phases (i.e., times) between the vertical dashed red lines. B: Typical S/N of spectra taken at the beginning of the observations (black) and close to the end (red).

$(1.12 - 1.16\,\mu\text{m})$ too high for useful data analysis.

The spectra were processed and analyzed independently per order, using very similar techniques to those developed in previous works (Brogi et al., 2012; Brogi et al., 2016; Birkby et al., 2017; Nugroho et al., 2017; Brogi et al., 2018; Hawker et al., 2018). As described in Chapter 3, we first removed artefacts from the data that were attributable to cosmic rays (i.e., 5σ outliers) and a small number of bad quality pixels. We computed a night drift of 15 m/s (0.011 pixel) by measuring the radial velocity variation of telluric lines present in the observed spectra. This drift was so small that a wavelength correction was not necessary. Subsequently, we normalized the spectra using a quadratic polynomial fit to the pseudo-continuum and avoiding the sky emission lines identified with fiber B, which were present mainly in the reddest orders.

The expected water vapor signature from the exo-atmosphere is several orders of magnitude smaller than the stellar and telluric absorption lines. Hence, these contributions have to be removed before the planetary signal can be detected. Since we do not expect to retrieve any planet signal from the cores of the strongest telluric absorption lines (i.e., where the Earth's atmosphere is almost opaque), we masked all wavelengths that exhibit an absorption greater than 80% of the flux continuum. We also masked the wavelengths corresponding to strong sky emission lines (see Fig. 4.2). In total, we masked 10% of the spectral points.

The remaining stellar and telluric components were removed using SYSREM (see Sect. 3.3 and Fig. 4.2). We fed this algorithm with 22 spectral matrices (see Sect. 3.3) containing the data of each usable order and ran it, on each of these matrices individually, for 15 iterations. The code primarily removed the largest spectral contributions, which are the quasi-static stellar and telluric

Table 4.1: Parameters of the system HD 189733.

Parameter	Value	Reference
α [J2000]	20:00:43.71	*Gaia* DR2[a]
δ [J2000]	+22:42:35.2	*Gaia* DR2[a]
V [mag]	7.65	Koen et al. (2010)
J [mag]	6.07	Skrutskie et al. (2006)
R_*^b [$R_\odot$]	0.756 ± 0.018	Torres et al. (2008)
K_* [m/s]	$201.96\,^{+1.07}_{-0.63}$	Triaud et al. (2009)
v_{sys} [km/s]	-2.361 ± 0.003	Bouchy et al. (2005)
a [AU]	0.03120 (27)	Triaud et al. (2009)
e	$0.0041^{+0.0025}_{-0.0020}$	Triaud et al. (2009)
$P_{\rm orb}$ [days]	2.21857567 (15)	Agol et al. (2010)
T_0 [days]	2454279.436714 (15)	Agol et al. (2010)
i [deg]	85.71 ± 0.024	Agol et al. (2010)
$R_{\rm P}^b$ [$R_\uparrow$]	$1.138^{+0.027}_{-0.027}$	Torres et al. (2008)
$K_{\rm P}^c$ [km/s]	$152.5^{+1.3}_{-1.8}$	Brogi et al. (2016)
v_{wind} [km/s]	-3.9 ± 1.3	Alonso-Floriano et al. (2019a)

[a]Brown et al. (2018). [b]Equatorial radii. [c]Value derived from orbital parameters.

signals, as shown after the first SYSREM iteration in Fig. 4.2B. Since the signal of the exoplanet is Doppler-shifted, it is preserved buried in the noise of the resulting residual matrices. However, SYSREM is also prone to remove the weak exoplanetary signal after the higher order variations have been removed in the first few iterations. This effect was studied in detail by Birkby et al. (2017) and can start at a different iteration in each spectral order. We also found this effect to be dependent on the transmission spectrum model template used for the cross correlation. Since the way of assessing this effect involves the computation of the cross-correlation, we discuss how we chose the optimum iteration to halt the code in Sect. 4.2.3.

An additional telluric correction of the data performed by using MOLECFIT was not useful for our purposes. This is due to the difficult modelling of the telluric lines in the large wavelength range of the CARMENES NIR channel (see Sect. 3.3).

4.2.2 Computation of templates

We computed 12 transmission spectra of HD 189733 b during its primary transit at a very high-resolution ($R \sim 4 \cdot 10^7$) as described in Sect. 2.4 using KOPRA. The spectra were then convolved with the LSF of CARMENES. The first four

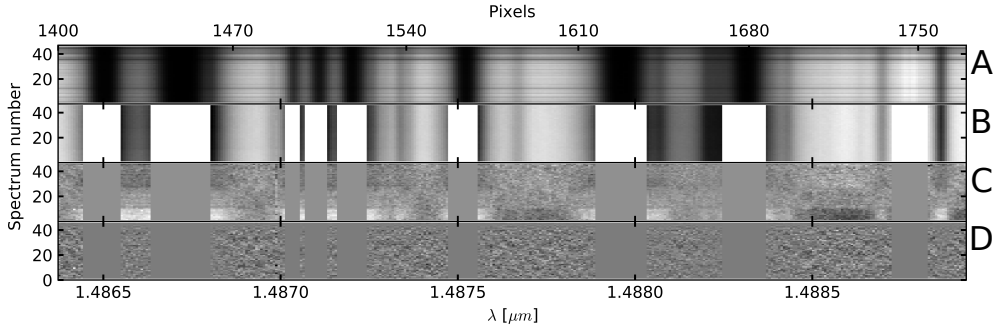

Figure 4.2: Resulting spectra of HD 189733 b on the night of 7 September 2017 at the different steps of the data analysis for the spectral region $1.486 - 1.489\,\mu$m (i.e., spectral order 41). A: Spectral matrix with the original observations of CARMENES. The color scale indicates the strength of absorption of the spectral features. B: normalized and masked spectra ready for the telluric and stellar removal process with SYSREM. C: Residual matrix after the first iteration. At this point the telluric residuals are still visible. D: Residual matrix after the 10th iteration. The telluric residuals are almost completely removed.

models included only H_2O, another four models included only CH_4, and the last four models included both molecules. For the four water-only models, we used two different pressure-temperature profiles (A and B, see Fig. 4.3A) and two constant H_2O VMRs of 10^{-5} and 10^{-4}. Although we did not expect significant differences on the results when using these models, due to the known model degeneracy (Brogi et al., 2014), it was a robustness check of our detection.
The $p-T$ profile A was obtained from our best fit to the transmission values measured with *HST*/WFC3 by and McCullough et al. (2014). The $p-T$ profile B was the one used by Brogi et al. (2018). This $p-T$ profile is hotter than profile A in the lower atmosphere, below $\sim 10^{-2}$ bar (see Fig. 4.3A), where most of the absorption takes place (i.e., where the continuum and the line wings are formed). Hence, the $p-T$ B profile yields a more extended exo-atmosphere and, consequently, produces a larger absolute absorption. The nominal transmission model used in our analysis was based on the $p-T$ profile B and a constant H_2O VMR of 10^{-4} (see Fig. 4.3B). All models were computed assuming a reference pressure of $p_{\rm ref} = 1$ bar at the reference exoplanet's radius $r_{\rm ref} = 1.138\,R_J$ (Sing et al., 2016), where R_J is the equatorial radius of Jupiter (71492 km).

Furthermore, we studied the potential presence of CH_4 in the planet atmosphere using eight models. All of them were calculated using the pressure–temperature profile B. Four of them included only methane, with CH_4 VMRs ranging from 10^{-7} to 10^{-4} in increments of one order of magnitude. The other four models included water vapor, with a VMR of 10^{-4}, and also methane with the previous set of VMRs.

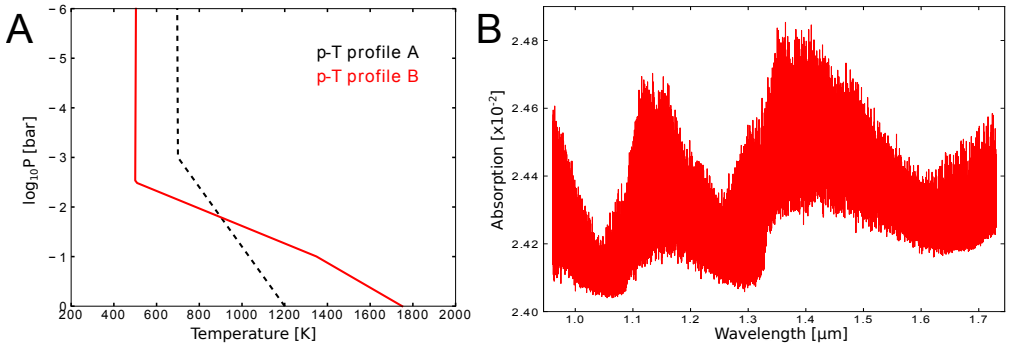

Figure 4.3: A: Pressure–temperature ($p-T$) profiles used for computing the synthetic exo-atmospheric absorption spectra. In dashed black, the $p-T$ profile A, was obtained from our best fit to the *HST*/WFC3 data of McCullough et al. (2014). In solid red, the $p-T$ profile B was taken from Brogi et al. (2018). B: Water vapor exo-atmospheric absorption model of HD 189733 b in the CARMENES NIR spectral range. The contribution of the planetary disk (i.e., opaque at all wavelengths) has been included. The calculations were performed with the the $p-T$ profile B and a constant H_2O volume mixing ratio of 10^{-4}. The model was computed at a very high spectral resolution ($R \sim 4 \cdot 10^7$) and convolved with the LSF of CARMENES.

4.2.3 Cross-correlation analysis

The radial velocity of the exoplanet changed during transit approximately from -5 to 25 km/s (see tilted dashed lines in Fig. 4.4). The cross-correlation analysis was performed for each spectral order over a wide range of planetary RVs, from -130 km/s to $+130$ km/s, in intervals of 1.3 km/s, which were set by the step-size of the CARMENES NIR pixels. We linearly interpolated the molecular transmission templates to the corresponding Doppler-shifted wavelengths. As was outlined in Chapter 3, the cross-correlation functions (CCFs) were obtained individually for each spectrum, forming a cross-correlation matrix, $\overline{CCF}$, per order. The dimension of each matrix was determined by the radial velocity shifts used in the cross-correlation and the number of spectra, i.e., 201×46 in this case. The median value from each CCF was subtracted to account for possible broadband differences between the models and the spectra. We applied the cross-correlation process after each of the 15 SYSREM iterations, thus obtaining 15 sets of 22 cross-correlation matrices (i.e., number of SYSREM iterations times the number of useful orders).

The $\overline{CCFs}$ resulting from the same or different iterations, should be combined before retrieving the planet signal in order to obtain the largest possible enhancement. In a previous work, Birkby et al. (2017) injected synthetic signals in the data to find the optimal SYSREM iteration for each of their four detectors and, subsequently, they combined the cross-correlation matrices of these different optimal iterations. However, this way of finding the optimal iteration could depend on the model used and the strength of the injection (we will explore

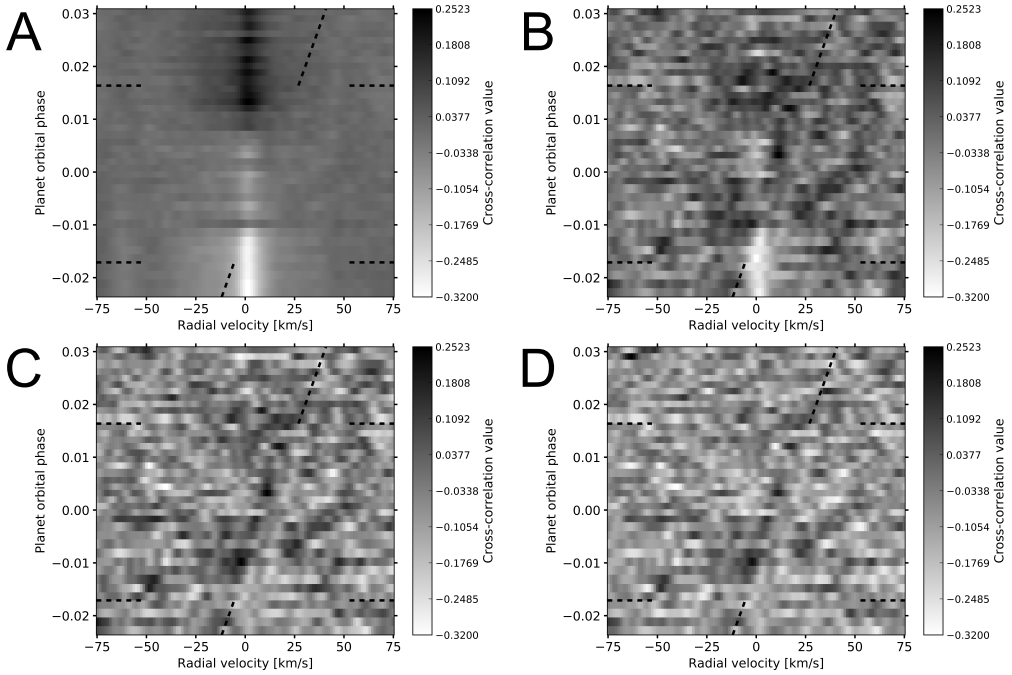

Figure 4.4: Cross-correlation values as a function of the orbital phase and planet radial velocity with respect to the Earth after one (panel A), two (panel B), three (panel C) and ten (panel D) SYSREM iterations. The orbital phase of the first and last transit spectra are indicated with horizontal dashed lines. After the first and second iteration of SYSREM the cross correlation with the telluric residuals are visible around the zero velocity. From the third iteration on, the cleaning of the telluric residuals is better and the exo-atmospheric signature appears as positive cross-correlation values (i.e., darker colors) along the planetary velocities, indicated with the tilted dashed lines (when $v_{\rm wind} = 0$ km/s).

this in the analyses performed in Chapter 5). For this analysis, however, we chose to follow the approach of Brogi et al. (2018), who minimized the model dependency of the analysis and co-added the $\overline{CCFs}$ of the different spectral orders by applying the same number of iterations to all of them. However, this approach is rather conservative. This is because it does not provide the most optimal recovery of the signal at each spectral order. In addition, a side effect of this choice is that it is possible to introduce correlation noise coming from over-corrected orders (those with the least signal) or spurious signals from under-corrected ones (those with the highest telluric contamination).

The cross-correlation matrices, for the first, second, third and tenth SYSREM iterations are shown in Fig. 4.4. In the first two iterations (panels A and B), the $\overline{CCFs}$ are dominated by major telluric residuals around zero velocity, whilst for the third and tenth iterations (panels C and D), the main telluric and stellar components are already removed.

The atmospheric signal of the planet is expected to follow its radial veloc-

ity (i.e., the dashed slanted line of all panels in Fig. 4.4) with positive cross-correlation values during the transit (i.e., from 21:01 UT to 23:11 UT or, equivalently, between the horizontal dashed lines in all panels of Fig. 4.4). Consecutively, we shifted each $\overline{CCFs}$ to the exoplanet's rest-frame by using Eq. 3.7, considering a wide range of semi-amplitudes of the radial velocity ($0 < K_p < 260$ km/s) and for an RV grid from -65 to 65 km/s. This approach allowed us to independently measure K_p and probe the radial component of the high altitude global atmospheric winds ($v_{\rm wind}$) to obtain a better estimate of the noise properties.

We then co-added the information from all orders and in time. If a water signature from the atmosphere of HD 189733 b is present, the peak of the resulting CCF should be close to 0 km/s. However, the atmospheric dynamics of the planet can lead to non-zero values, as shown in previous works (Louden and Wheatley, 2015; Brogi et al., 2016; Brogi et al., 2018). We discuss this further in Sect. 4.3.

We used that approach to study the significance of the retrieved signal as described in Sect. 3.4.1 and to verify that there are no significant spurious signals. In addition, the goodness of our telluric removal technique can be checked by exploring possible signals at low K_p, i.e., in the Earth's rest frame. The results of the two metrics (i.e., the S/N and the Welch t-test methods), when using the water absorption model computed with the $p-T$ profile B and a H_2O VMR of 10^{-4}, are shown in Fig. 4.5 (panels A and B, respectively). The maximum significances in both panels are located at similar K_p and $v_{\rm wind}$ values, corresponding to the expected velocities of the exoplanet. In addition, the distributions of CC values within the expected trail of the exoplanet and away from it show significantly different means (see Fig. 4.6). This is expected when a signal is present in the data.

We applied the S/N metric to identify the iteration at which Sysrem should be halted. The evolution of the maximum S/N recovered for the different Sysrem iterations around the expected planet K_p using the nominal transmission model is shown in Fig. 4.7. The signal steadily increases in the first three iterations, as Sysrem removes the major telluric and stellar contaminations. After this point, the S/N is very similar until the 10^{th} iteration. Beyond this iteration, Sysrem appears to mainly remove the exoplanet signal and, hence, the maximum S/N decreases. In addition, we observed a decrease of the telluric signal, observed at low K_p and $v_{\rm wind}$, as the number of iterations increases (i.e., the contamination is smaller at the tenth than at the third iteration; see Fig. 4.4). The behavior of the S/N of the recovered CCF per iteration is similar for all the water absorption model templates tested in this chapter.

By using CRIRES on the VLT ($R = 10^5$), Hawker et al. (2018) detected the H_2O+CO band at 2.3 μm and the HCN band at 3.2 μm on HD 209458 b using Sysrem and found that, for most spectral orders in their dataset, a few Sysrem

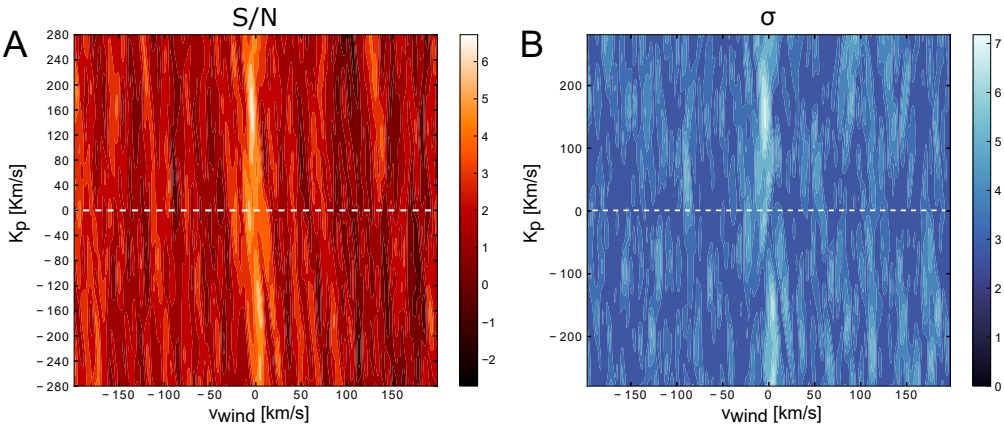

Figure 4.5: S/N results (panel A) and t-test results (panel B, in σ units) when cross-correlating, in a wide range of K_p and $v_{\rm wind}$ values, the residual matrix and the synthetic absorption model including the $p-T$ profile B and a water vapor abundance of 10^{-4}. There are no signals at the Earth's rest-frame (low K_p values), which discards the presence of significant telluric contamination.

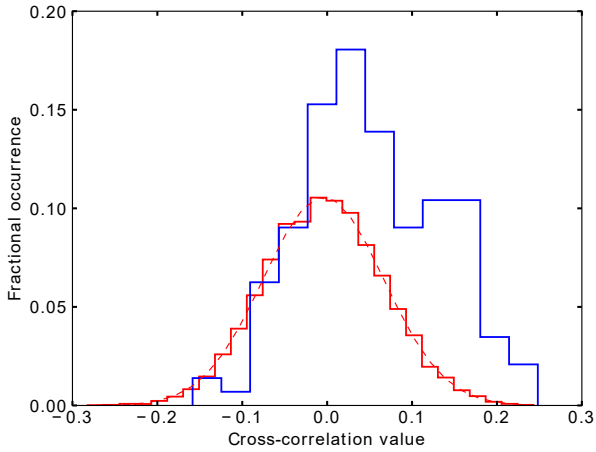

Figure 4.6: Comparison between the out-of-trail (red) and the in-trail (blue) distributions providing the largest σ-value. A Gaussian distribution with the same mean and variance as the out-of-trail curve is shown in dashed red. Both distributions show significantly different means, as it is expected in the case of an exo-atmospheric signal.

iterations were enough to remove the telluric absorption features. However, they required up to 13 iterations for those orders presenting the largest telluric contamination. Although we run 15 SYSREM iterations in total, we selected the tenth iteration for providing our results, as it is the one providing the most significant results in our analysis (see Fig. 4.7).

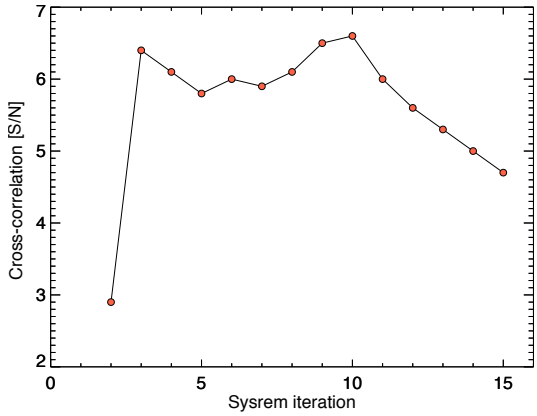

Figure 4.7: Retrieved S/N when cross-correlating the residual matrix after each SYSREM iteration with the H_2O absorption model including the $p-T$ profile B and a VMR of 10^{-4}. The values correspond to the highest S/N at the corresponding K_p and $v_{\rm wind}$ in the range of $K_p = 140$ to 180 km/s and $v_{\rm wind} = -10$ to 10 km/s. The first iteration is not shown for clarity, since it is dominated by telluric residuals.

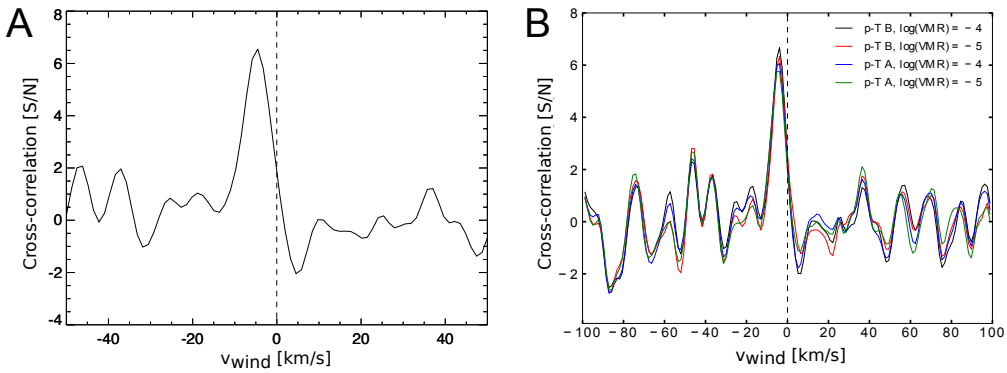

Figure 4.8: A: Total CCF when using the nominal model. The signal is blue-shifted by -3.9 ± 1.3 km/s. B: CCFs obtained for the studied H_2O absorption models. The results are very similar, hence showing a degeneracy in the tested $p-T$ profiles and H_2O abundances. A vertical dashed line marks the zero velocity value as a reference in both panels.

4.3 Results and Discussion

We detected a water vapor absorption signal in the CARMENES NIR data of the hot Jupiter HD 189733 b during the transit occurred on 7 September 2017. When cross-correlating the residual matrix of this night with the absorption model calculated with an H_2O VMR of 10^{-4} and the $p-T$ profile B, we obtained a maximum S/N of 6.6 in the total CCF (see Fig. 4.8A).

The generalized t-test analysis provided a p-value of $7.1\,\sigma$ (see Fig. 4.5B).

Moreover, we found the results obtained with the absorption models computed with H_2O VMRs of 10^{-5} and 10^{-4} and the $p-T$ profiles A and B to be similar and compatible within $1\,\sigma$ (see Fig. 4.8B). That is the analyses yielded the maximum S/N value at compatible K_p and $v_{\rm wind}$ values for all the tested model templates. From the cross correlation with the nominal model, we obtained the CCF with the largest S/N peak at a planet radial velocity semi-amplitude of $K_p = 160^{+45}_{-33}$ km/s, which is compatible with previous results found in the literature (e.g., $K_p = 194^{+19}_{-41}$ km/s was reported by Brogi et al., 2016).

Furthermore, we did not detect the signal of the exoplanet atmosphere with any of the models including only methane at abundances from 10^{-7} to 10^{-4}. In fact, the models including both H_2O and CH_4 showed decreasing S/N with increasing CH_4 abundance. Hence, we did not find any evidence of methane in the atmosphere of HD 189733 b, which is in good agreement with the results of Brogi et al. (2018).

4.3.1 Results obtained using the residual spectra from Molecfit

We investigated whether such a water vapor signal could be obtained by using the telluric-corrected spectra resulting from the Molecfit tool. To do so, we cross-correlated these residual spectra with the nominal model we chose for the exo-atmospheric absorption. The resulting $\overline{CCF}$ matrix is shown in Fig. 4.9A. There are strong spurious signals around 0 km/s, which are expected when telluric residuals are present in the spectra. Consequently, no planetary signal can be observed at the expected velocities during the observations (see tilted dashed lines).

Next, we computed the S/N map (see Fig. 4.9B). No signal consistent with a planetary origin is observed at the expected $K_p \sim 152$ km/s for this exoplanet. Instead, strong spurious signals are identified at low K_p values. That is, at the expected position of the telluric residuals. These results seem to confirm that the fit uncertainties when using Molecfit are too large to recover the H_2O signal in the wide spectral range of CARMENES (see, also, Sect. 3.3).

4.3.2 Usefulness and limitations of the inverse-injection technique

We found firm evidence of the presence of water vapor in the atmosphere of HD 189733 b. However, the CCF signal was found with similar significances K_p and $v_{\rm wind}$ values for the four water vapor models. We can now perform an additional test, which aims at providing an additional metric to identify if a certain model fits our data better than others. Such test is based on the injection of the inverse of the absorption model (i.e., $1-$model) at the exoplanet's velocities obtained from Eq. 3.7 and at the beginning of the data analysis. If the

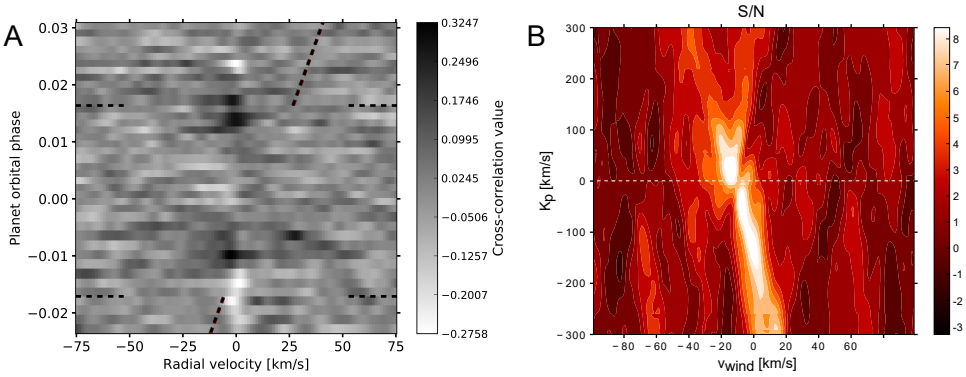

Figure 4.9: A: Cross-correlation matrix in the Earth's rest-frame obtained by using the residual data of MOLECFIT and the nominal model template. Important telluric residuals are observed around 0 km/s. Horizontal dashed black lines indicate the duration of the transit. Tilted dashed black lines mark the expected exoplanet's velocities during the observations B: S/N map computed from the cross-correlation matrix of panel A. The white dashed line marks the $K_p = 0$ km/s value for reference.

original model matches the exoplanet's transmission spectrum accurately, the injection of the inverse model should cancel the exo-atmospheric contribution. That is, the total CCF in the exoplanet's rest-frame should not present a peak around $v_{\rm wind} = 0$. Nevertheless, a succesful cancelation does not necessarily imply a S/N = 0 at $v_{\rm wind} = 0$. Even if no planetary signal is present in the data, we would expect some telluric residuals around that velocity. Naturally, the noise pattern away from the planet signal should remain unchanged. Thereby, the template that provides the most optimal cancelation of the signal of the exoplanet and, in turn, of the CCF peak, could be considered as being the best-matching model atmosphere for the exoplanet.

We tested this procedure by injecting the negative of the the four water vapor models described above. We consecutively measured the CCF at a $K_p = 160$ km/s, which yielded the maximum significance CCF peak (see Sect. 4.3). The resulting CCFs after subtracting the templates are shown in Fig. 4.10A. In this way, we found that the two models with a water vapor VMR = 10^{-5} (red and green curves) canceled best the CCF signal, leaving a maximum residual around a S/N ~ 1 or below. In particular, the model created using the $p-T$ profile A (green curve) yielded the best results. This is because the one obtained using $p-T$ profile B yielded a S/N value below 0 at $v_{\rm wind} = 0$. As discussed above, this indicates that we probably over-canceled the signal slightly, since telluric residuals are expected to also be present at that point. The two models with VMR = 10^{-4} (black and blue curves) over-canceled the signal regardless of the $p-T$ profile used. In this case, significant residuals were left at a S/N of about -3 (S/N < 0 indicate negative values of the cross–correlation).

Thus, these results suggest that the models with a VMR = 10^{-5} might

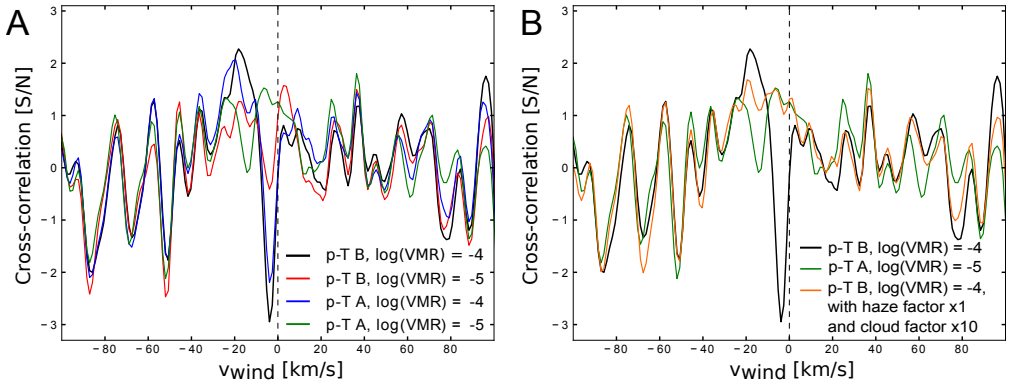

Figure 4.10: A: CCFs measured at a $K_p = 160$ km/s after subtracting the four water vapor models (see text). B: CCFs measured at a $K_p = 160$ km/s after subtracting two clear-atmosphere H_2O models and a model including the influence of hazes and clouds.

represent the abundance of H_2O in this exo-atmosphere better. In fact, this water vapor abundance is consistent with the values derived by Madhusudhan et al. (2014b), who re-analyzed the *HST*/WFC3 data from McCullough et al. (2014) and constrained the water mixing ratio to be $\log(\mathrm{VMR}) = -5.20^{+1.68}_{-0.18}$.

Nevertheless, the weak absorption of the H_2O lines with respect to the continuum could also be produced by a larger H_2O VMR in the presence of hazes in the atmosphere of this exoplanet (Madhusudhan et al., 2014b; Pino et al., 2018a). Therefore, although the clear-atmosphere models point to an atmosphere depleted in water vapor (i.e., VMR $\leq 10^{-5}$), the inclusion of clouds and hazes in the models suggest that larger VMRs could also occur (i.e., both combinations producevery similar absorptions with respect to the continuum for the H_2O lines). This is what we observe in Fig. 4.10B. The models with VMR $= 10^{-4}$ (black and orange curves) cancel the signal at the same level than those at VMR $= 10^{-5}$ (green curve) when clouds and hazes are considered.

Therefore, the inverse-injection technique provides an additional test to certify the quality of our detection, since the signal is subtracted successfully by the exo-atmospheric models. Also, the subtraction leaves the noise pattern unchanged away from the peak. Unfortunately, we cannot distinguish between clear and hazy/cloudy atmospheres, since the cross-correlation technique is only sensitive to the relative absorption of the lines with respect to the continuum (see Sect. 3.2).

Many combinations of the parameters involved in the computation of the models (e.g., the reference pressure and radius of the exoplanet, the contribution of clouds and hazes, the H_2O abundance, the temperature profile, etc.) yield very similar relative absorptions with respect to the continuum. Hence, it is possible to cancel the exo-atmospheric signal at the same level with very different atmospheres. Typically, one could assume specific values for some of

these quantities and refer the results obtained to the reference selection of parameters. However, such assumption of known physico-chemical properties of the exoplanet could be wrong, which translates in a weak statistical basis for the results (Madhusudhan, 2018). For this reason, the inverse-injection technique is not used in the following chapters of this thesis, since the information we can retrieve by using very few models is not unambiguous. Nevertheless, approaches for providing such statistical basis to the results obtained using high dispersion spectroscopy and this technique are currently being developed (Brogi et al., 2017).

4.3.3 High-altitude winds in the atmosphere of HD 189733 b

The total CCFs (Figs. 4.8A and 4.8B) show a net blueshift of the water vapor signal, of $v_{\rm wind} = -3.9 \pm 1.3$ km/s, which is compatible with previous measurements of the sodium and water vapor signals in HD 189733 b (Louden and Wheatley, 2015; Brogi et al., 2016; Brogi et al., 2018). The GCM model of Showman et al. (2013) predicted that the atmosphere of HD 189733 b is in the transition between two extreme regimes of wind patterns, being dominated either by a strong equatorial jets (i.e., superrotation), or by global day- to nightside winds at the terminator (see Sect. 2.1.6). These atmospheric winds are blue and redshifted, and the combination of their signals during the whole transit is expected to leave a net blueshifted atmospheric signal.

In particular, the application of the Showman et al. (2013) model predicts a wind velocity with a peak near -3 km/s for a fraction of about 40% of the terminator at a pressure level of 10^{-4} bar (see their Fig. 7c). Our derived value of -3.9 ± 1.3 km/s agrees well with this prediction, although it is not fully comparable because it corresponds to an average of the whole terminator (i.e., blue and redshifted signals combined). In addition, the velocity value quoted above from Showman et al. (2013) did not include the planetary rotation, which would slightly increase (i.e., larger absolute value) the wind velocity (see their Fig. 12).

4.3.4 Individual detections of H_2O from the bands around 1.15 and 1.4 μm

Besides the water vapor detection we obtained using the entire wavelength coverage of the NIR channel of CARMENES, we explored the possibility of detecting water vapor by using different absorption bands individually. In particular, we aimed at detecting H_2O by using the two strongest bands at the wavelength ranges of $1.06 - 1.26\,\mu$m (orders $58 - 50$) and $1.26 - 1.58\,\mu$m (orders $49 - 40$). For this analysis, we used the nominal transmission model and computed the S/N values at the optimal K_p and $v_{\rm wind}$ for four wavelength ranges. The results are shown in Table 4.2 and plotted in Fig. 4.11A.

Table 4.2: Signal-to-noise ratios and p-values (expressed as σ values) of the CCFs for the four analyzed wavelength ranges.

$\Delta\lambda$ [μm]	S/N	p-values [σ]	K_p [km/s]	$v_{\rm wind}$ [km/s]
$0.96 - 1.06$	2.2	3.8	153	-3.9
[a] $1.06 - 1.12$, $1.16 - 1.26$	4.9	6.8	146 ± 46	$-3.9^{+1.3}_{-2.6}$
[a] $1.26 - 1.37$, $1.47 - 1.58$	4.4	5.7	156^{+39}_{-31}	-3.9 ± 1.3
$1.59 - 1.71$	0.25	0.49	153	-3.9

[a]Band obtained by the combination of both wavelength ranges. The S/N and p-values were computed as in Sect. 3.4.1. Since the water vapor signals at the bluest ($0.96 - 1.06\,mu$m) and reddest ($1.26 - 1.58\,mu$m) bands are not detected, we list the results obtained at the fixed values of $K_p = 153$ km/s and $v_{\rm wind} = -3.9$ km/s.

Furthermore, in Fig. 4.11B, we show the water vapor transmission model that provided the best fit of the *HST*/WFC3 data of McCullough et al. (2014) for this exoplanet for us. This has a twofold purpose. On the one hand, it better illustrates the spectral ranges used in the study of the different H_2O bands. On the other hand, it shows that the results we obtained for the two water vapor bands individually are consistent with the *HST*/WFC3 measurements. In particular, we found the H_2O signals for the strongest bands at similar signal-to-noise ratios, of $S/N_{1.15} = 4.9$ and $S/N_{1.4} = 4.4$. Although the H_2O band near $1.15\,\mu$m is expected to be weaker than that at $1.4\,\mu$m, more spectral orders were discarded during the analysis on the latter, leaving a similar number of spectral points in both bands (see high-resolution transmission model in Fig. 4.11B). This could explain the similarity between the retrieved S/N values.

The bluest ($0.96 - 1.06\,mu$m) and reddest ($1.26 - 1.58\,mu$m) wavelength ranges do not provide a significant signal from the exo-atmosphere. On the one hand, the H_2O absorption at the reddest orders is rather weak. On the other hand, the bluest orders cover only a fraction of the water vapor band, which might be strongly affected by extinction due to aerosols, or partially obscured by clouds (Sing et al., 2016; Pino et al., 2018a). In the work by Pino et al. (2018a), the authors suggested to use the cross-correlation method in high-resolution transit spectra to detect water bands at optical and near-infrared wavelengths. A comparison of the signal from these different spectral ranges could diagnose the presence of broad-band spectroscopic features, such as the scattering by aerosols. According to their work, the maximum CCF relative contrast[1] (in the case of a clear atmosphere and no telluric contamination) expected between the

[1]Assuming a water vapor detection obtained from two different absorption bands, the relative contrast between their CCFs can be calculated by dividing the S/N ratio of the respective CCF peaks.

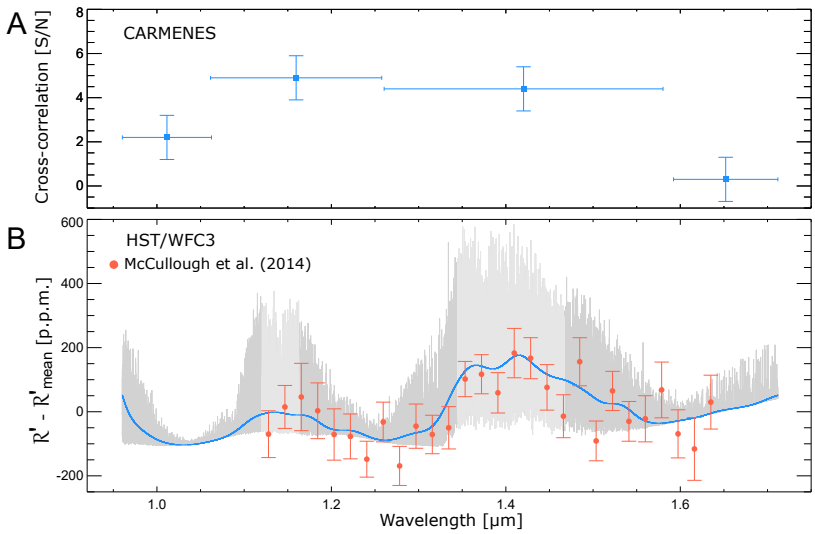

Figure 4.11: A: S/N values of the CCF peaks obtained for the different bands (see Table 4.2). B: Model H_2O absorption spectrum at the CARMENES resolution (in grey) and Gaussian-smoothed to the *HST*/WFC3 resolution (in blue), calculated by using the $p-T$ profile A and a H_2O VMR $= 10^{-5}$. The quantity that is shown in the vertical axis is the mean-subtracted spectrum ratio of Eq. 2.49, multiplied by 10^6. The lighter grey areas are the wavelength regions covered by the orders discarded in the analysis. Over-plotted in red are the *HST*/WFC3 measurements provided by McCullough et al. (2014). The reader should note that the S/Ns shown in the top panel cannot be directly compared to the *HST* absorption signals in the bottom panel.

bands at $\sim 1.15\,\mu$m and $1.4\,\mu$m is of the order of 100 p.p.m., which is about a factor of 5 smaller than the absorption of the band we have detected at $1.4\,\mu$m. Unfortunately, we are not sensitive to such low CCF contrasts (i.e., low difference in absorption between the two bands) with the S/N of our observations. Therefore, we could perform a more in-depth study of the possible aerosols in the atmosphere of HD 189733 b.

Interestingly, the maximum CCF contrast reported in Pino et al. (2018a) between the H_2O features at shorter wavelengths and those studied here could be over 200 p.p.m. in the absence of telluric contamination, which could, in principle, facilitate the detection of the haze effect with an instrument like CARMENES. However, the presence of telluric residuals in the data greatly hinders our sensitivity to these contrast ratios. Thus, it is not clear whether such a study is feasible with current instrumentation.

Future instrumentation with a redder wavelength coverage than CARMENES, such as CRIRES+ (Follert et al., 2014), could attempt the detection of water vapor spectral features at the K, L, and/or M bands. These H_2O bands are intrinsically stronger than the ones probed with the CARMENES NIR channel. Also, the effects of hazes should be weaker than in the J band. In Brogi

et al. (2016), the authors detected the water vapor absorption signal in the atmosphere of HD 189733 b using CRIRES at 2.3 μm, implying a transit depth at the wavelengths of these absorption lines of $\sim 1.3 \times 10^{-3}$, which is a factor of two stronger than those at the CARMENES wavelengths. By comparing these strong spectral features with the weakest bands covered by CARMENES, we might be able to provide a better estimation of the presence of aerosols in exoatmospheres. However, the uncertainties are currently too large to provide an accurate constraint.

Chapter 5

H_2O in the atmosphere of HD 209458 b

We aim at detecting water vapor in the atmosphere of the hot Jupiter HD 209458 b and perform a multi-band study in the near infrared with CARMENES. In the case of close-in exoplanets, the exo-atmospheric water vapor absorption lines are significantly Doppler-shifted due to the large change in its radial velocity during transit. This shift is of the order of tens of km/s, whilst the Earth's telluric and the stellar lines can be considered quasi-static. We take advantage of this shift to remove the telluric and stellar contributions using SysRem, which performs a principal component analysis including proper error propagation. The residual spectra contain the signal from thousands of planetary molecular lines well below the noise level. We retrieve the information from those lines by cross-correlating the residual spectra with models of the atmospheric absorption of the planet. We find a cross-correlation signal with a signal-to-noise ratio of 6.4, revealing H_2O in HD 209458 b. We obtain a net blueshift of the signal of $-5.2^{+2.6}_{-1.3}$ km/s, which despite the large error bars, is a firm indication of day-to-night winds at the terminator of this hot Jupiter. Additionally, we perform a multi-band study for the detection of water vapor individually from the three near infrared bands covered by CARMENES. We detect H_2O from its $0.96 - 1.06\,\mu$m band individually with a S/N of 5.8, and also find hints of a detection from the $1.06 - 1.26\,\mu$m band, with a low S/N of 2.8. No clear planetary signal is found, however, from the $1.26 - 1.62\,\mu$m band.

A. Sánchez-López, F.J. Alonso-Floriano, M. López-Puertas, I.A.G. Snellen, et al., *Astronomy & Astrophysics*, 630, A53, (2019)

5.1 Introduction

HD 209458 b is the second archetypal transiting hot Jupiter known to scientists. Several milestones in exoplanet science were achieved by studying this gas giant, since it was the first transiting exoplanet discovered. In fact, the first detection of an exo-atmosphere was accomplished in this target by Charbonneau et al. (2002), who detected sodium in its atmosphere. Moreover, the first detection of an evaporating hydrogen envelope was also achieved in this exoplanet by Vidal-Madjar et al. (2003), triggering one of the most fruitful fields of exoplanet atmospheric sciences currently (see, e.g., Nortmann et al., 2018; Oklopčić and Hirata, 2018; Salz et al., 2018; Spake et al., 2018; Alonso-Floriano et al., 2019b; Lampón et al., 2019).

This hot Jupiter orbits a bright Sun-like star (G0 V, $G \approx 7.5$ mag) with a period of ∼3.5 days (Charbonneau et al., 1999; Henry et al., 1999). This planet has been studied by analysing its transit (Charbonneau et al., 2002; Vidal-Madjar et al., 2003; Deming et al., 2013; Madhusudhan et al., 2014b; Alonso-Floriano et al., 2019b) and dayside spectra (Line et al., 2016; Hawker et al., 2018), combining low- and high-resolution spectra (Brogi et al., 2017), and by investigating its exosphere, escape, and mass-loss rate (Vidal-Madjar et al., 2004; Muñoz, 2007; Linsky et al., 2010).

Comparative studies of several hot Jupiters using *HST* and the *Spitzer Space Telescope* have shown water vapor spectral features in HD 209458 b in the $0.3 - 5.0\,\mu$m spectral region (see, e.g., Fig. 1.8 and Sing et al., 2016). These signatures were found to be weaker than expected in a solar composition cloud-free atmosphere, and have been attributed to a possible oxygen depletion and/or a partial coverage of clouds or hazes (Madhusudhan et al., 2014a). Later, MacDonald and Madhusudhan (2017) found sub-solar abundances with a partially cloudy terminator. In addition, they reported the first detection of nitrogen chemistry, with NH_3 and/or HCN being detected in *HST* transmission spectra in the $1.1 - 1.7\,\mu$m region. Moreover, Hawker et al. (2018) also detected HCN, H_2O, and CO in this planet by using CRIRES measurements in the $2.29 - 2.35\,\mu$m and $3.18 - 3.27\,\mu$m spectral ranges.

In this chapter we analyze transit spectra of HD 209458 b obtained with the near infrared (NIR) channel of CARMENES ($0.96 - 1.7\,\mu$m). After the multi-band detection of water vapor in HD 189733 b with this instrument (see Chapter 4; Alonso-Floriano et al., 2019a), we have extended this analysis to HD 209458 b, where H_2O has not been detected from the ground so far in the NIR. Detections of water vapor from bands located at different spectral regions can help to characterize aerosols in hot Jupiters (Stevenson, 2016; Pino et al., 2018a). This kind of multi-band studies is of particular interest for HD 189733 b and HD 209458 b since space observations suggest that the former is rather hazy whilst the latter has a more gentle Rayleigh scattering slope (see, e.g., Fig. 1.8

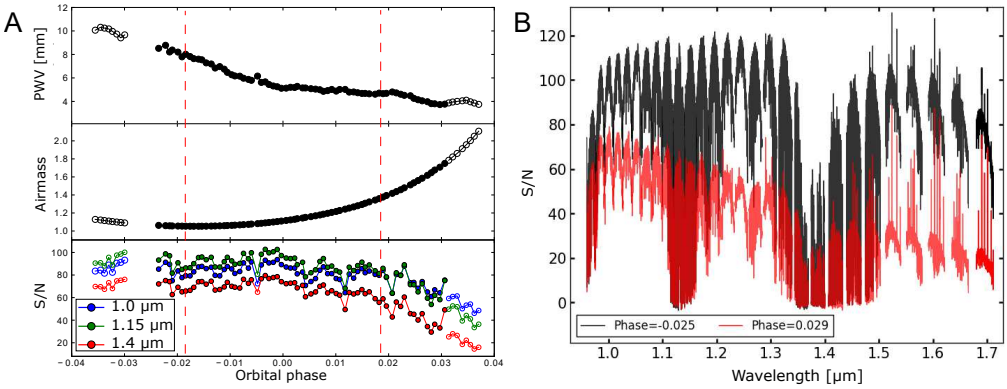

Figure 5.1: A: Column depth of Precipitable Water vapor (PWV, *top panel*), airmass (*middle panel*), and S/N (*bottom panel*) for the three H_2O bands covered by CARMENES NIR channel for the HD 209458 b observations on 5 September 2018. All quantities are shown as a function of the orbital phase of the exoplanet. The transit occurred at the orbital phases (i.e., times) between the vertical dashed red lines. Open circles represent spectra not included in the analysis. B: S/N of spectra taken at the beginning of the observations (black) and near the end (red). A strong spectral dependence of the S/N is observed in the latter.

and Sing et al., 2016). Moreover, an additional measurement of the winds in the upper atmosphere of HD 209458 b is also of high interest for characterizing the dynamics of hot Jupiter atmospheres.

5.2 Observations and data analysis

5.2.1 CARMENES data for HD 209458 b

We observed a transit of the hot Jupiter HD 209458 b (Table 5.1) on the night of 5 September 2018 using CARMENES. In this chapter, we focus solely on the data recorded with the NIR channel of the instrument (VIS data is analyzed in Chapter 6). Following the methodology introduced in Chapter 3, we used the spectra of the two fibers of the instrument. Fiber A was devoted to the target, and fiber B to the sky in order to identify telluric emission lines. The observations covered the pre-, in-, and post-transit of HD 209458 b, and are composed of 91 exposures of 198 s from 21:39 UT to 03:47 UT (see Fig. 5.1A).

Due to a brief failure in the guiding system, eight pre-transit spectra were unusable between the planetary orbital phases $\phi = -0.029$ and $\phi = -0.024$. We thus had to discard also the eight pre-transit spectra gathered before them in order to avoid sharp discontinuities in the light curve of each pixel, which could hamper our telluric corrections with Sysrem. The typical S/N per pixel of the raw spectra showed a strong spectral dependence (see Figs. 5.1A (bottom panel) and 5.1B). The mean S/N was of ∼85 for the bands at ∼1 μm and ∼1.15 μm and of ∼65 for the band at ∼1.4 μm in the first half of the observations. However,

Table 5.1: Parameters of the HD 209458 system.

Parameter	Value	Reference
α [J2000]	22:03:10.77	*Gaia* DR2[a]
δ [J2000]	+18:53:03.5	*Gaia* DR2[a]
G [mag]	7.5087 (4)	*Gaia* DR2[a]
J [mag]	6.59 (2)	Skrutskie et al. (2006)
R_*^b [$R_\odot$]	$1.155^{+0.014}_{-0.016}$	Torres et al. (2008)
K_* [m/s]	84.67(70)	Torres et al. (2008)
$v_{\rm sys}$ [km/s]	−14.7652 (16)	Mazeh et al. (2000)
a [AU]	$0.04707\,^{+0.00046}_{-0.00047}$	Torres et al. (2008)
$e\cos\omega$	0.00004 (33)	Crossfield et al. (2012)
$P_{\rm orb}$ [days]	3.52474859 (38)	Knutson et al. (2007b)
$T_0\,(HJD)$ [days]	2452826.628521 (87)	Knutson et al. (2007b)
i [deg]	86.71(5)	Torres et al. (2008)
R_p^b [$R_\nvEarth$]	$1.359^{+0.016}_{-0.019}$	Torres et al. (2008)
K_p [km/s]	140(10)	Snellen et al. (2010)
$v_{\rm wind}$ [km/s]	$-5.2^{+2.6}_{-1.3}$	This chapter

The numbers in parentheses in the middle column correspond to the error bar on the last significant digits. [a]Brown et al. (2018). [b]Equatorial radii.

it dropped below 60 towards the end for the bands at ∼1 μm and ∼1.15 μm, and below 50 for the band at ∼1.4 μm. Consequently, we also discarded the last eight out-of-transit spectra so as to avoid noisy data, which might deteriorate the potential signal. Additionally, one in-transit spectrum, taken at $\phi = -0.0066$, presented an anomalous spectral behaviour and was also excluded from the analysis. The spectra analyzed in this work thus spanned the exoplanet orbital phase interval $-0.023 < \phi < 0.031$. The airmass range was $1.06 < sec\,(z) < 1.79$ (see Fig. 5.1A) and the mean seeing was 1.5 arcsec.

The raw spectra were processed by an updated version of the CARMENES data reduction pipeline, CARACAL v2.20 (Zechmeister et al., 2014; Caballero et al., 2016). As in the previous chapter, we used the European Southern Observatory MOLECFIT tool (Smette et al., 2015) to retrieve the column depth of PWV towards the target, which dropped from 10.3 mm to 3.8 mm during the observations (see Fig. 5.1A, top panel). The mean value of the PWV was ∼ 5.8 mm, being the average PWV over Calar Alto of ∼ 7 mm. However, even with the relatively low mean PWV, there was a strong telluric absorption in the centers of the two strongest water vapor bands, which resulted in a very low flux. We thus excluded from the analysis the $1.12-1.16\,\mu$m (orders $54-53$) and $1.34-1.47\,\mu$m (orders $45-42$) spectral regions. These are the *a priori* masks

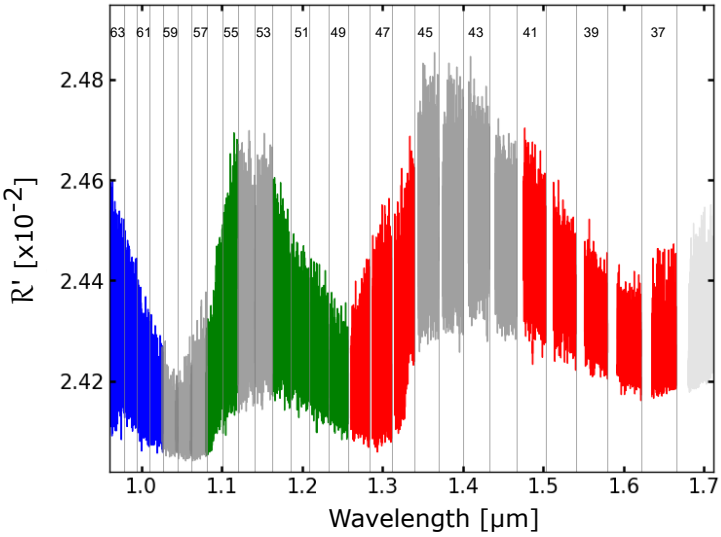

Figure 5.2: Water vapor transmission model spectra computed for the best-fitting $p-T$ profile in Brogi et al. (2017) and an H_2O volume mixing ratio of 10^{-5}. The model is shown at the same wavelengths and spectral resolution of the data (i.e., the CARMENES line spread function for the NIR channel has been applied). The 1.0 μm, 1.15 μm, and 1.4 μm bands are shown in blue, green and red, respectively. The orders in dark grey represent the *a priori* masks. The orders in light grey were masked *a posteriori*. The vertical gray lines separate the spectral orders, whose numeration is indicated.

in dark grey in Fig. 5.2.

There are three observable water vapor absorption bands within the spectral coverage of the NIR channel of CARMENES, each one covered by a different number of spectral orders (see Fig. 5.2). Firstly, the spectral region 0.96 – 1.05 μm (the 1.0 μm band from now on) was covered by five useful spectral orders (63 – 59). Secondly, the spectral interval at 1.05 – 1.26 μm (1.15 μm band in the following) was covered by eight useful orders (58 – 55, 52 – 49). And, thirdly, the spectral region of 1.26 – 1.71 μm (the 1.4 μm band in the following), which was covered by nine spectral orders (48 – 46, 41 – 36). In addition to the orders initially discarded by the *a priori* masks, we found orders 59–57 (1.03–1.08 μm) and 36 (1.68 – 1.71 μm) to present strong uncorrected telluric residuals in the analysis presented in Sect. 5.3. Therefore, we also discarded them in the analysis (see the *a posteriori* masks in Fig. 5.2). The 1.0 μm, 1.15 μm, and 1.4 μm bands were then covered by four, six, and eight useful orders, respectively.

As for previous observations, we removed from the spectra the 5 σ outliers, likely produced by cosmic rays. In addition, we derived the instrument drift during the night by measuring the shifts of the strong telluric lines as in the previous chapter, and found a value of $\sim$ 0.023 pixel ($\sim$ 30 m/s). Large sub-pixel drifts have been found to impact the data analysis of this technique. For

instance, this was the case of Brogi et al. (2013) and Birkby et al. (2017) who found ∼0.7 pixel (∼1 km/s) drifts for detector 1 in CRIRES. Thus, the authors performed a correction by aligning spectra to a common wavelength solution. As discussed in Brogi et al. (2016), the correction had an error of 0.03 pixel (∼50 m/s) in the absence of noise. Our drift is more than an order of magnitude lower than theirs and, also, lower than the ideal alignment error computed in previous works (i.e., the alignment error one would get in the absence of noise in the spectra). Therefore, we do not expect a drift correction to significantly affect our results.

The resulting spectra were stored as 18 matrices (one per order) of dimension 68×4080 (i.e., the number of spectra times the number of wavelength bins of each order). This allowed us to analyze each order independently by following the methodologies presented in the previous chapter, in previous publications (Brogi et al., 2016; Birkby et al., 2017; Brogi et al., 2018; Hawker et al., 2018; Alonso-Floriano et al., 2019a), and summarized below.

5.2.2 Optimization of the removal of telluric and stellar lines

As outlined in previous chapters, changing conditions in the Earth's atmosphere during the night (e.g., airmass variations) induce a variable pseudo-continuum level in the observed spectra (see the strong spectral dependence of the S/N in Fig. 5.1B). Thus, we normalized the spectra avoiding the telluric emission lines identified with fiber B and masked the spectra at the wavelengths where the Earth's atmospheric absorption was larger than 80% of the flux continuum. Thereby, we eliminated the spectral ranges where there is almost no flux.

In Chapter 4, we searched for the wavelength bins that satisfy the previous condition in the largest S/N spectrum of the night. This was a useful approach since the column depth of PWV during that night was stable and airmass did not change very much during the observations (see Figs. 4.1A, top and middle panels, respectively). However, we found this procedure not to be suitable for the night analyzed in this chapter due to the rather large changes in the PWV, airmass, and S/N of the observed spectra (see Fig. 5.1). For this reason, instead of selecting the spectrum with the largest S/N for masking, we chose that taken at the largest telluric water vapor absorption, which was more conservative. The masked regions represented $\sim 6\%$ of the data of the spectral orders included in the analysis.

The normalized and masked 68×4080 matrices of spectra were at this point dominated by the quasi-static telluric and stellar contributions. We removed these telluric and stellar signals also by using Sysrem (Tamuz et al. 2005; Mazeh et al. 2006).

In order to determine the optimal number of Sysrem iterations for each

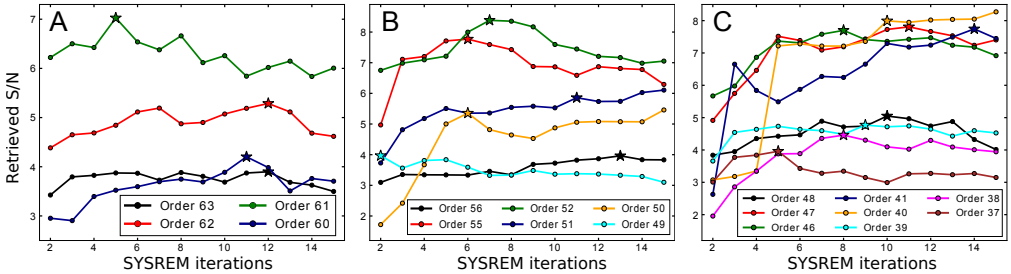

Figure 5.3: Evolution of the retrieved S/N of the injected signal with the number of SYSREM iterations for the 1.0 μm band (A), 1.15 μm band (B), and 1.4 μm band (C). The model is injected at 5× the nominal strength. For the spectral orders where a very small signal is retrieved (i.e., S/N < 3), we injected a stronger model at 10× (for orders 49 and 38) and at 12× (for order 60) the nominal strength so as to ensure the injected signal is clearly measured (i.e., S/N ≥ 3). The stars represent the selected number of iterations for each spectral order at the peak of the recovered S/N (see text).

spectral order[1], we analyzed the effect of this algorithm order by order by injecting a model planetary signal (computed as described in Sect. 2.4) into the observations, before removing the telluric contamination. In order to mimic the real signal of the planet, we Doppler-shifted the injected model planetary signal according to the expected orbital velocities of the planet at the times of the observed spectra following Eq. 3.7.

We used the cross correlation technique discussed in previous chapters to study the evolution of the S/N of the retrieved injected signal with the number of SYSREM iterations. That is, we determined the optimum number of SYSREM iterations for each spectral order by maximizing the significance of the injected CCF peak. Similar procedures have been followed in previous studies (Birkby et al., 2017; Nugroho et al., 2017; Cabot et al., 2018; Hawker et al., 2018). In order to characterize this behaviour, we visually inspected the retrieved S/N evolution for each spectral order (see Fig. 5.3).

The different performances can be broadly grouped into the following categories. Firstly, SYSREM performed well for some spectral orders where a few iterations (< 10) were enough to reach the maximum recovery of the injected signal, and the significance then dropped (e.g., orders 61, 55, 52, 49, 46, 38, 37). For other spectral orders, the peak S/N was reached more slowly (≥ 10 iterations, see, e.g., orders 60, 56, 48). Secondly, we observed a less efficient performance in some spectral orders where a maximum is achieved but the behavior is almost flat (e.g., orders 63 and 39). In these cases, since the S/N dropped afterwards, we kept the found maximum. And thirdly, for some other orders the S/N improved slightly after the first maximum (e.g., orders 62, 51, 50, 47, 41, 40). In this latter case, we kept the iteration with the first maximum of the S/N if it did not

[1]This number is expected to be different, since the telluric and stellar contributions vary from one order to another.

improve significantly (changes smaller than 5%) in subsequent iterations. We found this behavior for orders 62, 47, and 41.

As an additional test, we also explored the removal of the telluric absorption by using MOLECFIT instead of SYSREM for this dataset (not shown). However, no exo-atmospheric signal was obtained, which is line with our previous results (see Sects. 4.3.1 and 3.3). In fact, the analyses performed with MOLECFIT were more difficult for this dataset than for the one of HD 189733 b (see Sect. 4.3.1) due to the larger variability of the observational conditions.

5.3 Computation of templates and cross-correlation analysis

We computed high-resolution spectral transmission models of HD 209458 b in its primary transit by using KOPRA and afterwards convolved them with the CARMENES' near-infrared LSF (see Sect. 2.4). We used the $p-T$ profile retrieved by Brogi et al. (2017), who obtained it by combining low and high-resolution measurements for HD 209458 b. In addition, we chose H_2O, CH_4, HN_3, HCN, and CO VMRs of 10^{-5}, 10^{-8}, 10^{-8}, 10^{-6}, and 10^{-4}, respectively, which are very similar to the most probable values retrieved in that work. All models were computed assuming a reference pressure of $p_{\rm ref} = 1$ bar at the reference exoplanet's radius $r_{\rm ref} = 1.36\,R_J$, where R_J is the Jupiter equatorial radius (71492 km). In Fig. 5.2 we show the computed transmission model including only water vapor where the major absorbing bands near 1.0, 1.15, and 1.4 μm are clearly identified. In the same way as was done for the observed spectra, we normalized the model.

We cross-correlated the residual matrices with the transmission model (template) Doppler-shifted in the range of -200 to 200 km/s, in steps of 1.3 km/s, with respect to the Earth's rest-frame. In each step, the template was linearly interpolated to the corresponding Doppler-shifted wavelength grid. We obtained a CCF for each of the 68 spectra, forming $\overline{CCF}$s of dimensions 201×68. As in the previous chapter and earlier studies, these matrices were calculated independently for each spectral order and for each SYSREM iteration. Also, we subtracted the median values from each CCF of the matrix in order to remove broad variations arising from the differences between the spectra and the template.

The resulting $\overline{CCF}$ after co-adding the information of all the useful spectral orders is shown in Fig. 5.4. The trace of the planet is expected to appear during transit (i.e., between the horizontal dashed red lines) as positive cross-correlation values along the planetary velocities calculated by Eq. 3.7. During the observing night, these velocities were expected to range roughly between -34 and 15 km/s for this exoplanet (see tilted dashed lines in Fig. 5.4).

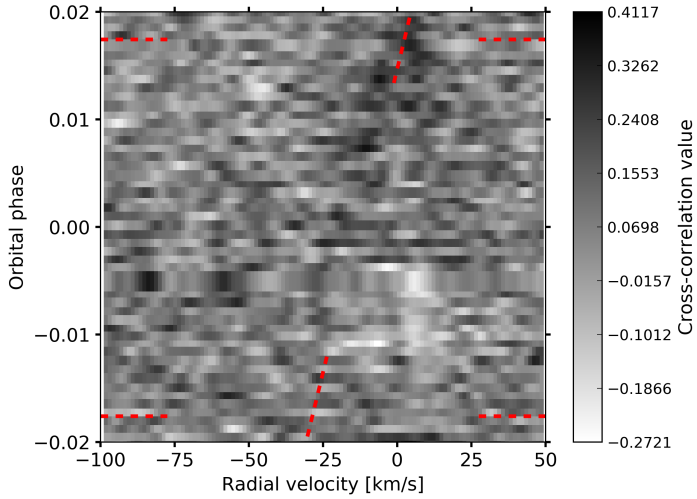

Figure 5.4: Cross-correlation values as a function of the orbital phase and planet orbital velocity in the Earth's rest-frame. The results were obtained from 18 useful NIR orders. The orbital phase of the first and last in-transit spectra are indicated by horizontal dashed red lines. A visual guide to the expected exoplanet velocities (i.e., $K_p = 140$ km/s and assuming no additional winds in the atmosphere of the planet) is indicated with tilted dashed red lines.

We aligned the rows (i.e., 68 sets of 201 spectral velocity bins) of the cross-correlation matrices to the rest frame of the exoplanet assuming K_p as unknown and performing the shifts in a grid from -280 to 280 km/s. Thus, we explored also the negative velocity space, so as to ensure that the potential signal does not present spurious aliases nor comes from uncorrected telluric residuals.

Before co-adding the $\overline{CCF}$ in time, we excluded the last seven in-transit spectra at the planetary orbital phases $0.012 < \phi < 0.018$, for which the velocity of the planet with respect to the Earth was very small (i.e., between ± 2.5 km/s) and hence, the absorption lines from the planetary atmosphere nearly overlapped with the telluric lines. At this point, if the atmospheric molecular signal were strong enough, we would expect to find a CCF peak around the zero velocity and the expected $K_p = 140$ km/s for HD 209458 b.

We explored the presence of a potential signal by means of the S/N and Welch t-test metrics (see Figs. 5.5A and 5.5B). The presence of a signal appears in both maps as a region of large S/N and σ-values at a $K_p \sim 150$ km/s, which is compatible with the K_p of HD 209458 b within the errors. In addition, no comparable signals are observed at any other velocity. Furthermore, in Fig. 5.6 we show the distributions of cross correlation values in and out of the exoplanet's trail for the K_p and $v_{\rm wind}$ pair that yielded the largest σ-value. The means of the in-trail and out-of-trail distributions are different, with the latter following a Gaussian distribution. Thus, this test also provided evidence for the presence of a planetary water vapor signal in our transit data.

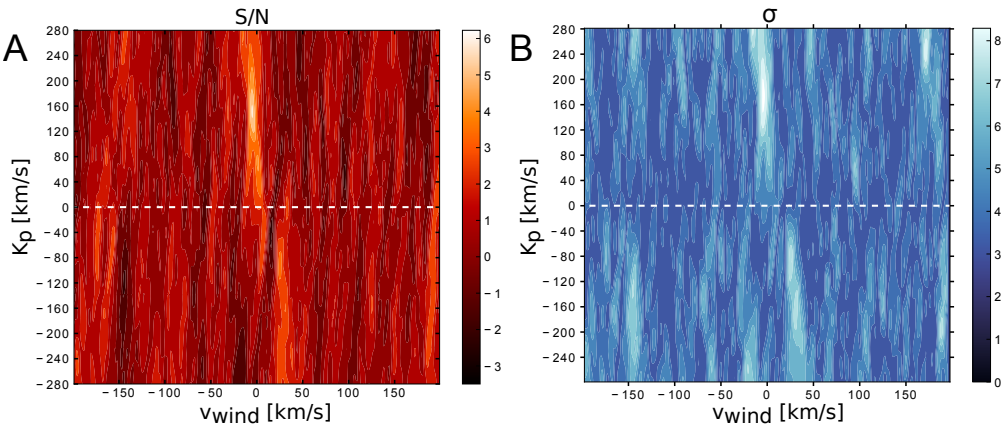

Figure 5.5: S/N map (A) and σ-values map (B) obtained after the cross-correlation of the residual spectral matrices with the atmospheric transmission template. All useful NIR orders were included. A dashed white line marks the $K_p = 0$ km/s value. Both maps show the region of maximum significance at very similar K_p values (~ 150 km/s).

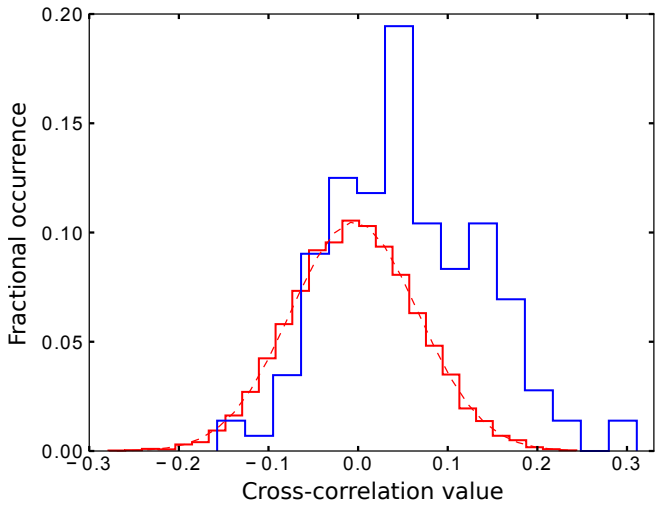

Figure 5.6: Distribution of cross-correlation values for the K_p and $v_{\rm wind}$ pair that yield the largest σ-value when including all useful NIR orders for HD 209458 b (see Table 5.2). The values around the expected planetary radial velocities (in-trail, blue), far away from the planet's velocities (out-of-trail, red), and a Gaussian distribution with the same mean and variance as the out-of-trail distribution (dashed red) are shown. As expected for a signal of planetary origin, the in- and out-of-trail distributions show significantly different means.

5.4 Results and Discussion

We have studied the detectability of water vapor in HD 209458 b transit spectra with the NIR channel of CARMENES. We computed the total CCF when including all the useful NIR spectral orders (see black curve in Fig. 5.7) and de-

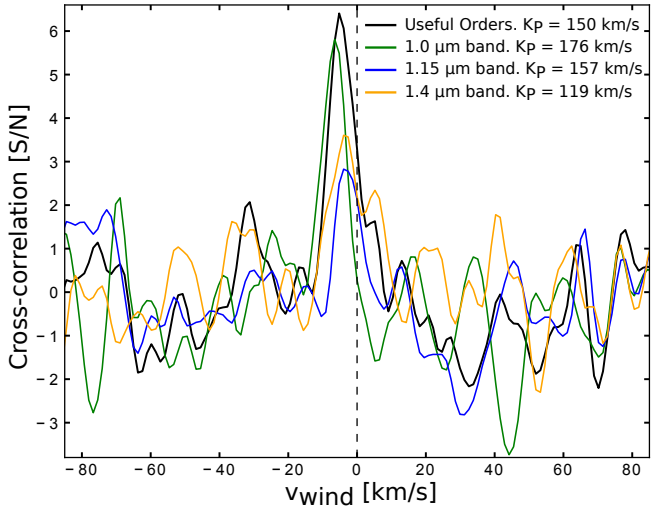

Figure 5.7: CCFs with the largest significance obtained for the 1.0 μm band (green), 1.15 μm band (blue) and including all useful NIR orders (black). Also, the CCF for the 1.4 μm band with the largest significance peak in the positive K_p space is shown (orange). The vertical dashed line marks the zero velocity value.

tected H_2O with a maximum S/N = 6.4 and a σ-value of 8.1, which was larger than its S/N. We found similar results in Chapter 4 (Alonso-Floriano et al., 2019a). In fact, this was also recently observed in Cabot et al. (2018), who suggested that the Welch's t-test might overestimate the significance of the signal more than the S/N calculation. However, as was discussed in Sect. 3.4.1, some scenarios (e.g., the presence of auto-correlation signals) might yield a potential underestimation of the signal when using the S/N metric.

We found the maximum signal at a $K_p = 150^{+28}_{-25}$ km/s, which is in line with the value derived by Hawker et al. (2018) from CRIRES observations, within the uncertainties. The cross-correlation with models including CH_4, NH_3, HCN, or CO individually did not yield any CCF peak compatible with a planetary origin. Consequently, the models including H_2O+CH_4, H_2O+NH_3, H_2O+HCN, or H_2O+CO showed noisier CCFs, and lower S/N than those obtained by including water vapor alone. However, the strongest absorption features of CH_4, NH_3, HCN, and CO occur at the reddest NIR orders of CARMENES, which presented the lowest S/N in our data[2] (see bottom panel of Fig. 5.1) and, also, the least efficient telluric removal. Therefore, our results for these molecules are not conclusive and should be validated with future observations.

[2]Here, S/N refers to the S/N of the observed spectra, not the signal-to-noise ratio of the CCF peak.

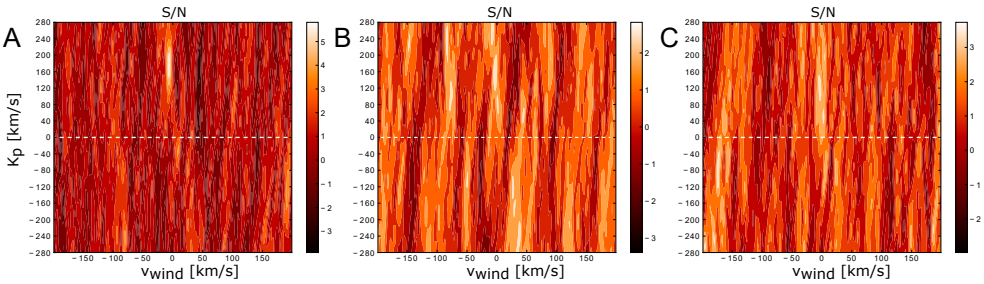

Figure 5.8: S/N maps obtained for HD 209458 b after the cross-correlation of the residual spectral matrices with the atmospheric transmission template for the 1.0 μm band (panel A), 1.15 μm band (panel B) and for the 1.4 μm band (panel C). A dashed white line marks the $K_p = 0$ km/s value in all panels.

5.4.1 Multi-band analysis

We have investigated the possibility of detecting water vapor by using separately the data in the three bands covered by the CARMENES NIR channel (see Figs. 5.2 and 5.8 and Table 5.2). Thus, we performed the cross-correlation analysis described for each water vapor absorption band individually. We detected H_2O from the 1.0 μm band with a maximum S/N of 5.8 (σ-value of 7.4) at a $K_p = 176^{+30}_{-38}$ km/s (see green curve in Fig. 5.7 and panel A in Fig. 5.8). However, H_2O was not detected in this band, covered only partially by the NIR channel, in HD 189733 b (see Chapter 4; Alonso-Floriano et al., 2019a). Actually the detection in HD 209458 b represents the first detection of water vapor from this band in any exoplanet so far.

Regarding the 1.15 μm band, we found the S/N map to be noisier than for the 1.0 μm band, possibly due to a less efficient telluric correction in this spectral region (see panel B in Fig. 5.8). We obtained the maximum significance CCF peak in the map with S/N of 2.8 (σ-value of 6.9) at a $K_p = 157^{+33}_{-47}$km/s (see blue curve in Fig. 5.7), which is consistent with the expected velocity of the planet. However, this S/N is rather low and some contamination can be seen in the form of other similar peaks. In particular, the contamination at the negative K_p space is partially carried over when including this band in all the useful NIR orders (see negative K_p space in the S/N and σ maps in Fig. 5.5). Therefore, the maximum CCF peak of the 1.15 μm band should be interpreted only as a hint of a signal, since the telluric removal in these orders was less efficient.

As for the 1.4 μm band, the S/N map obtained with these spectral orders presents different maxima (see Fig. 5.8C), being the maximum significance peak of the map located at the negative K_p space. The maximum significance CCF peak in the positive K_p space is found with a S/N = 3.6 (σ-value of 5.3) at a $K_p = 119^{+43}_{-45}$ km/s (see orange curve in Fig. 5.7), which is consistent with the expected value within the uncertainties. However, this result was insufficient for claiming a detection from this band individually.

Table 5.2: Maximum S/N and $p-$values of the CCFs at the analyzed wavelength intervals for HD 209458 b.

Band	S/N	σ-values	K_p [km/s]	$v_{\rm wind}$ [km/s]
1 μm	5.8	7.4	176^{+30}_{-38}	$-6.5^{+2.6}_{-1.3}$
1.15 μm	2.8	6.9	157^{+33}_{-47}	$-3.9^{+3.9}_{-2.6}$
1.4 μm[a]	3.6	5.3	119^{+43}_{-45}	-3.9 ± 2.6
Useful orders[b]	6.4	8.1	150^{+28}_{-25}	$-5.2^{+2.6}_{-1.3}$

[a]Maximum significance CCF peak measured in the positive K_p space (see text). [b]Combination of the 18 useful NIR spectral orders (i.e., covering the three water vapor spectral bands).

Overall, these results indicate that most of our signal arose from the 1.0 μm band, and partially from the 1.15 μm and 1.4 μm bands. Thus, including the latter in the analysis, we obtained a slightly larger signal. It is surprising though that we obtained the largest contribution to the signal from the weakest band rather than from the two strongest 1.15 μm and 1.4 μm bands. It is true that, for the strongest bands, some orders near their centers were discarded because of the absence of flux. Additionally, in these strong bands, the masking of the most absorbent absorption lines (i.e., absorbing more than 80 % of the flux) rejects many spectral points and, hence, reduces the planetary signal that we can retrieve from them. But this is in contrast with what we would expect in the light of the results obtained in Chapter 4 (see also Alonso-Floriano et al., 2019a), where we obtained the largest signals in the strongest bands of HD 189733 b. Several reasons might explain this. Firstly, the mean S/N of the observed spectra in the second half of the observations fall rapidly (see Fig. 5.1A, bottom panel). In fact, the last spectra have around half of the S/N of the first ones. Additionally, the S/N within each spectrum decreases towards longer wavelengths with typical values in the range $20 - 60$ at the reddest orders (see Fig. 5.1B). This was possibly due to the large airmasses, between 1.3 and 1.8, in the second half of the observations (see Fig. 5.1A, middle panel). Secondly, the drastic drop of the column depth of PWV (Fig. 5.1A, top panel) that occurred during the observations possibly added other trends to the data that make more difficult the telluric removal. These effects combined might have hampered an efficient signal retrieval from the 1.15 μm and 1.4 μm bands.

5.4.2 Day- to night-side winds at the terminator of HD 209458 b

The CCF peaks showed a net blueshift of $-6.5^{+2.6}_{-1.3}$ km/s for the 1 μm band and of $-3.9^{+3.9}_{-2.6}$ km/s for the 1.15 μm and the 1.4 μm bands. This could be caused by strong winds flowing from the day- to the night-side at the terminator of this hot Jupiter. The different absolute wind velocities retrieved from both bands could

be related to the different pressure levels at which the bulk of the spectrum is formed for each spectral band. However, we would expect the weaker 1.0 μm band to have its largest contribution at slightly higher pressure levels (i.e., lower altitudes) than the stronger 1.15 μm and 1.4 μm bands and hence to have a lower $v_{\rm wind}$ according to GCM models (see, e.g., Fig. 3 in Rauscher and Menou, 2012, 2013). However, this is opposite to our results and likely not the reason for the differences. Nevertheless, our large error bars make our measurements fully compatible. In addition, the cross-correlation signals of the 1.15 μm and 1.4 μm bands are rather weak and thus, the significances of our wind measurements using these bands are low.

Snellen et al. (2010) reported, from observations of a transit of this planet in the 2-μm spectral band of carbon monoxide, an overall blueshift of -2 ± 1 km/s. Our best measurement of the net blueshift obtained when considering all useful orders is larger, of $-5.2^{+2.6}_{-1.3}$ km/s, although our uncertainties also exceed theirs and, overall, both determinations are within the errors.

The circulation model of Showman et al. (2013) predicts that the atmosphere of the hot Jupiter HD 209458 b, which is exposed to a large stellar insolation, should have a circulation dominated by high-altitude, day-to-night winds, leading to a predominantly blueshifted Doppler signature at the terminator. The same model predicted for this planet a stronger high-altitude day-to-night circulation than for HD 189733 b, which should manifest in a larger net blueshift. In particular, it predicted a blueshifted signal with a peak near -3 km/s for a fraction of $\sim 40\%$ of the full terminator for HD 189733 b at a pressure level of 0.1 mbar, whilst for HD 209458 b the velocity were around -6 km/s and covering near 60% of the terminator (see their Figs. 7c and 7d).

These supersonic wind velocities were also obtained in the models of Rauscher and Menou (2012) and Amundsen et al. (2016). Rauscher and Menou (2013), however, reported slightly slower winds because they included the effects of magnetic drag which reduces the wind velocity in the upper atmosphere of HD 209458 b to about $\simeq 3$ km/s. When considering all the useful NIR spectral orders, we obtained a blue velocity of $-5.2^{+2.6}_{-1.3}$ km/s for HD 209458 b. This value is in good agreement with the predictions of Rauscher and Menou (2012) and Showman et al. (2013) and Amundsen et al. (2016). In addition, the absolute value is larger than what we derived for HD 189733 b in the previous chapter (-3.9 ± 1.3 km/s; Alonso-Floriano et al., 2019a), which is in line with the model predictions of Showman et al. (2013). However, the rather large error bars in both of our measurements prevented us from definitively confirming the prediction of Showman et al. (2013) of stronger winds in the upper atmosphere of HD 209458 b.

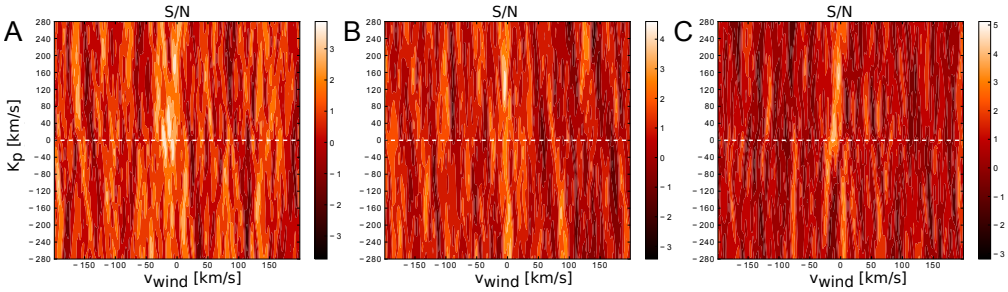

Figure 5.9: S/N maps obtained for HD 189733 b after the cross-correlation of the residual spectral matrices with the atmospheric transmission template for the 1.0 μm band (panel A), 1.15 μm band (panel B), and for the 1.4 μm band (panel C). A dashed white line marks the $K_p = 0$ km/s values in all panels.

5.5 Comparison of the H_2O detection in HD 209458 b and HD 189733 b.

We present a qualitative comparison of the results discussed above for HD 209458 b with those obtained in the previous chapter for the hot Jupiter HD 189733 b using also CARMENES transit data. In order to make it meaningful, though, we have reanalyzed the HD 189733 b dataset using the same procedure used in this chapter. That is, by maximizing the significance of the retrieved injected signal at each spectral order so as to optimize the telluric removal. The multi-band results obtained for HD 189733 b by using this new procedure are shown in Fig. 5.9 and Table 5.3.

Starting with the 1.0 μm band, water vapor was not detected in HD 189733 b from this band in the analyses performed in Chapter 4. In this reanalysis (see Fig. 5.9A), we observe a strong contamination at low K_p values, but also hints of a moderate signal of S/N = 3.7 at $K_p = 179^{+27}_{-34}$ km/s, which is consistent with the expected velocities for HD 189733 b.

Regarding the 1.15 μm and 1.4 μm bands, the results of the reanalysis (see Table 5.3) are very similar to those presented in the previous chapter (Alonso-Floriano et al., 2019a), with confident detections of H_2O in both bands (see Figs. 5.9B and 5.9C, respectively). When using all the useful NIR orders for the dataset of HD 189733 b, we detected water vapor with a $S/N = 7.7$ at $K_p = 147^{+33}_{-28}$ km/s, which represents a small, though significant, improvement with respect to the signal obtained in that work of $S/N = 6.6$. This is due to the optimization of the number of SYSREM iterations required for each spectral order, principally for the 1.0 μm band.

Comparing these results to those obtained for HD 209458 b, the hint of a water vapor detection using the 1.0 μm band in HD 189733 b is much less significant, despite the larger S/N of the gathered spectra for the latter. This could be explained by different atmospheric extinction levels in these planets.

Table 5.3: Maximum S/N of the CCFs at several wavelength intervals for HD 189733 b. Values in parenthesis extracted from Chapter 4 (Alonso-Floriano et al., 2019a).

Band	S/N	K_p [km/s]	$v_{\rm wind}$ [km/s]
1.0 μm[a]	3.7 (2.2)	$179\,^{+27}_{-34}$ (153)	-3.9 ± 2.6 (-3.9)
1.15 μm	4.6 (4.9)	116^{+65}_{-31} (146 ± 46)	$-5.2^{+2.6}_{-1.3}$ ($-3.9^{+1.3}_{-2.6}$)
1.4 μm	5.1 (4.4)	150 ± 29 (156^{+39}_{-31})	-3.9 ± 2.6 (-3.9 ± 1.3)
Useful orders[b]	7.7 (6.6)	147^{+33}_{-28} (160^{+45}_{-33})	-3.9 ± 1.3 (-3.9 ± 1.3)

[a]Value not representing the maximum of the explored map. [b]Combination of the 22 useful NIR spectral orders from Chapter 4.

HD 189733 b, compared to HD 209458 b, is expected to be a rather hazy and/or cloudy planet with a steeper Rayleigh scattering slope (Sing et al., 2016) and, hence, the extinction near 1 μm could contribute to weaken the H_2O absorbing lines in HD 189733 b.

As for the 1.15 μm and 1.4 μm bands, water vapor is hinted only from these bands in HD 209458 b. However, it was detected from both bands individually and with confidence in HD 189733 b in Chapter 4, as well as in this reanalysis. As discussed above, the lower and wavelength-dependent S/N of the measured spectra of HD 209458 b and the more variable observing conditions might be the reasons behind this difference.

Chapter 6

A search for H_2O at optical wavelengths with CARMENES

We explore the capabilities of the CARMENES VIS channel ($0.52 - 0.96\,\mu$m) to disentangle the exo-atmospheric H_2O absorption lines by means of the cross-correlation technique applied in the previous chapters. Several studies have attempted the detection of H_2O in the optical in the past by using high-resolution spectra and the cross-correlation technique. However, no clear signals of water vapor have been identified unambiguously so far from this spectral region.

These non-detections of water vapour at optical wavelengths, where its absorption bands are rather weak, could be explained by different reasons. Firstly, it is likely that detecting water vapor using these bands individually would require of several nights of observation so as to increase the overall S/N. In particular, this would be extremely important in the case of H_2O-depleted atmospheres, since the water vapor signal would be small. For instance, this would be the scenario for the super-Earth 55 Cancri e (Esteves et al., 2017). Secondly, these results could be due to a strong extinction by atmospheric hazes or to the presence of clouds in the exo-atmosphere. In the case of HD 189733 b, for which water vapor was not detected either (see, e.g., Allart et al., 2017), the aerosol extinction hypothesis is consistent with our previous results (chapters 4 and 5), and also with previous studies (Pont et al., 2008; Sing et al., 2011).

In order to investigate the detectability of water vapor at optical wavelengths, we observed several transits of HD 189733 b and HD 209458 b using the large wavelength coverage of the VIS channel of CARMENES. In this chapter, we describe the features of each night of observation and analyze the presence of H_2O in their atmospheres by computing the cross-correlation functions for each hot Jupiter.

Sánchez-López, López-Puertas, et al. (2019), in preparation

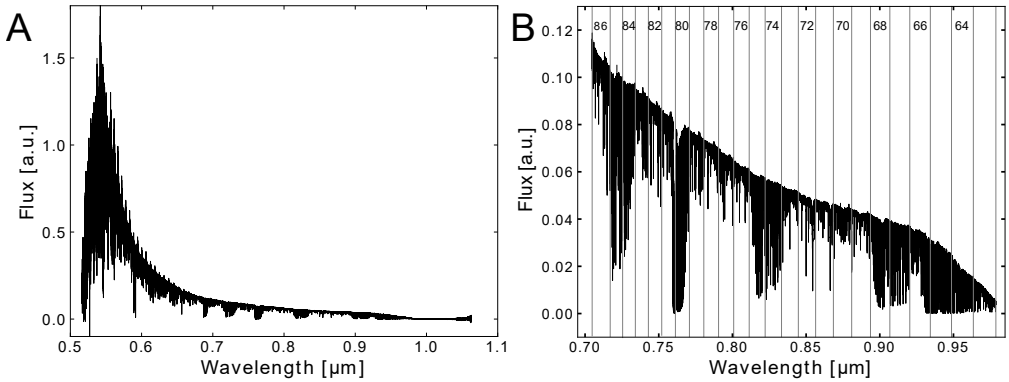

Figure 6.1: A: Flux received in the spectral range covered by the CARMENES VIS channel during the observation night of HD 209458 b on 06 September 2019. B: Zoom of the spectral range analyzed in this chapter. The vertical gray lines separate the different spectral orders of the detector, whose numeration is indicated.

6.1 Observations and data analysis

We used the VIS channel of CARMENES to observe several transits of the two most studied hot Jupiters, HD 189733 b and HD 209458 b. In all the observation nights, the spectra were obtained in service mode, with fiber A recording spectra of the target, and fiber B being dedicated to sky measurements.

Whereas the stellar emission lines were almost negligible in the NIR channel, they are prominent at $\lambda < 0.7\,\mu$m (see Fig. 6.1A. In addition, the water vapor absorption signal is the weakest in this range (see Fig. 2.10A). Therefore, we excluded this wavelength interval from the analyses performed in this chapter. Furthermore, the spectral orders covering the wavelengths beyond $0.98\,\mu$m are affected by a reduced efficiency of the detector, resulting in very noisy flux measurements, and scattered light issues. Hence, they were also discarded.

A typical VIS spectrum in the analyzed spectral range is shown in Fig. 6.1B, where the major H_2O bands in the VIS are identified at $\sim 0.72\,\mu$m, $\sim 0.82\,\mu$m, and $\sim 0.95\,\mu$m (in fact, this is the blue wing of the H_2O $1.0\,\mu$ band that provided a detection in the previous chapter). In addition, the strong molecular oxygen absorption band near $0.76\,\mu$m is observed. In the following, we describe the main parameters of each observed transit for both exoplanets.

Observations of HD 189733 b

We observed three transits of this hot Jupiter with CARMENES (see Fig. 6.2B). The main parameters of the data recorded with the VIS channel during these nights are:

- Observations taken the night of 08 August 2016 (see magenta points

in Fig. 6.2B): The data consisted of 45 exposures of 200 s, starting at 21:48:03 UT and ending at 02:17:46 UT, and spanning the exoplanet's orbital phase range $-0.047 < \phi < 0.037$, the airmass range $1.07 < \sec(z) < 1.40$, and had a mean S/N per pixel of ~ 106. Additionally, the atmospheric-dispersion corrector (ADC) was not updated during the night. Because of this, no re-acquisition of the target was performed as it moved in the sky. Thus, some stellar flux might be lost during the end of the transit and at the post-transit due to an incorrect star–telescope alignment. Also, we chose the spectrum with the largest S/N as a reference for the masking of lines absorbing more than 80% of the flux continuum.

- Observations taken the night of 17 September 2016 (orange points in Fig. 6.2B): The data consisted of 48 exposures of 200 s, starting at 19:39:13 UT and ending at 00:02:50 UT, covering an orbital phase range of $-0.058 < \phi < 0.024$ (i.e., only two post-transit spectra). The target moved from an airmass of 1.04 to 1.53 and the mean S/N per pixel of the spectra was ~ 105. The ADC was not updated during the night either. Additionally, the spectrum with the largest S/N was used for the masking of spectral regions in which the absorption was beyond 80% of the flux continuum.

- Observations taken the night of 30 June 2019 (black points in Fig. 6.2B): These observations consisted of 50 exposures of 192 s, starting at 23:32:35 UT and ending at 02:53:51 UT. The observations covered the exoplanet's orbital phase range $-0.033 < \phi < 0.029$, an airmass range of $1.03 < \sec(z) < 1.16$, and the mean S/N per pixel was ~ 125. During this night, we periodically updated the ADC so as to maximize the gathered stellar flux. As in the previous cases, a mask was set for lines absorbing more than 80% of the flux continuum in the spectrum with the largest S/N.

Observations of HD 209458 b

We observed three transits of this hot Jupiter with CARMENES (see Fig. 6.2A). The main parameters of the data recorded with the VIS channel during these nights are:

- Observations taken the night of 17 September 2016 (magenta points in Fig. 6.2A): The data consisted of 29 exposures of 180 s, starting at 19:49:58 UT and ending at 02:05:41 UT. However, we excluded from the analysis the first and last two spectra, since they had a substantially lower S/N (< 65) than the rest. Therefore, the useful spectra of this night spanned an orbital phase of the exoplanet of $-0.036 < \phi < 0.020$ (i.e., only two post-transit spectra). The target moved from an airmass of 1.29 to 1.57 and the mean S/N per pixel of the spectra was ~ 100. The ADC was

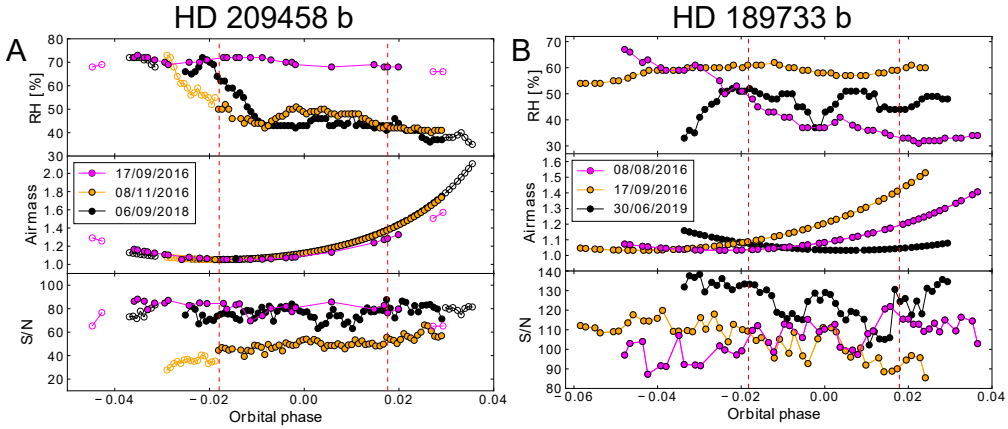

Figure 6.2: Relative humidity (RH, top panel), airmass (middle panel) and S/N (bottom panel) of the HD 209458 b (A) and HD 189733 b (B) observations with the VIS channel of CARMENES. All quantities are shown as a function of the orbital phase. The transits occurred at the orbital phases (i.e., times) between the vertical dashed lines. Open circles represent spectra not used in the analyses.

not updated during this night. In addition, a mask was applied to the spectral intervals where the absorption was greater than 80% of the flux continuum. We selected the spectrum with the largest S/N as a reference for masking. In the future, this analysis might benefit from the knowledge of the evolution of the PWV during this night, so as to better determine such reference spectrum.

- Observations taken the night of 08 November 2016 (orange points in Fig. 6.2A): The data consisted of 79 exposures of 180 s, starting at 18:04:57 UT and ending at 22:59:06 UT. However, the first fifteen spectra of the night (from 18:04:57 UT to 18:56:29 UT), which covered the pre-transit observations, presented a very low S/N (< 40). Hence, we excluded them from the analysis. Because of this, the analyzed spectra for this night consists of 64 exposures that spanned the exoplanet's orbital phase range $-0.018 < \phi < 0.029$, the airmass range $1.05 < \sec(z) < 1.74$, and had a mean S/N of ~ 61. In addition, the ADC was also not updated during this night. In this case, the masking level was set for spectral lines absorbing more than 60% of the flux continuum in the spectrum with the largest S/N. This level provided the best results for this night in the analyses performed in the following sections. In future iterations of this study, we might be able to relax the masking level of this night also by obtaining the evolution of the column depth of PWV during the night, and using the spectrum recorded at the moment of largest PWV as a reference.

- Observations taken the night of 06 September 2018 (see black points in

Fig. 6.2A): This VIS channel dataset was gathered simultaneously to the NIR data analyzed in chapter 5. Hence, it consisted of 91 exposures of 198 s, starting at 21:39:40 UT and ending at 03:47:05 UT. The observations covered the exoplanet's orbital phase range $-0.023 < \phi < 0.031$, an airmass range of $1.06 < \sec(z) < 1.79$, and the mean S/N per pixel was ~ 91 (see Sect. 5.2.1 for more details). During this transit, we periodically updated the ADC so as to maximize the gathered stellar flux. Following the results of the previous chapter, a mask was applied to the spectral intervals where the absorption was greater than 80% of the flux continuum in the spectrum taken at the time of maximum PWV (see Fig. 5.1).

6.2 Removal of the telluric and stellar lines

For both exoplanets and all the transit datasets, we removed the contributions from the Earth and the respective stars by using the methods described in Sect. 5.2.2. That is, by studying the evolution of the retrieved injected signal with the number of SYSREM iterations, and maximizing its significance at each spectral order of the VIS channel. The water vapor absorption signal is expected to be at least three times weaker in its VIS absorption bands than in those in the NIR channel. For instance, this is observed by comparing the absorption with respect to the continuum of the strongest H_2O band covered by the VIS channel, at $\sim$1.0 μm (also partially covered in the NIR), with respect to the strongest band in the NIR, at $\sim$1.4 μm (see Fig. 4.11B). The VIS water vapor signal is even weaker from the bands at $\lambda < 0.9\,\mu$m (see, e.g., Fig. 2.10). Therefore, the strength of the injected signal was set to 15$\times$ the expected level (in contrast with the 5$\times$ level used for the NIR). Thereby, we should be able to measure the injected signal above a S/N = 3 threshold. The transmission model templates that we injected were computed as outlined in Sect. 2.4 and with the $p - T$ profiles and H_2O abundances used to obtain the main results in chapters 4 and 5. Naturally, these models were computed for the VIS spectral range, where the effect of Rayleigh scattering is much stronger than at NIR wavelengths (see, e.g., Fig. 2.10).

The resulting evolution of the retrieved S/N of the injected peak for all the useful VIS spectral orders, and for the HD 189733 b transits, is shown in Figs. 6.6, 6.7, and 6.8. For the HD 209458 b transits, this information is shown in Figs. 6.3, 6.4, and 6.5. For all nights, we excluded from the analyses the spectral orders for which the 15$\times$ injected signal was not recovered at a S/N $\geq$ 3. This is because at such low significances, the measurement would be consistent with being produced by noise and hence, it would not be reliable. In particular, the excluded spectral orders for HD 189733 b and HD 209458 b are listed in Table 6.1. We observed that, with this criterion, we rejected more spectral orders for the datasets of HD 209458 b than for those of HD 189733 b, which is reasonable given

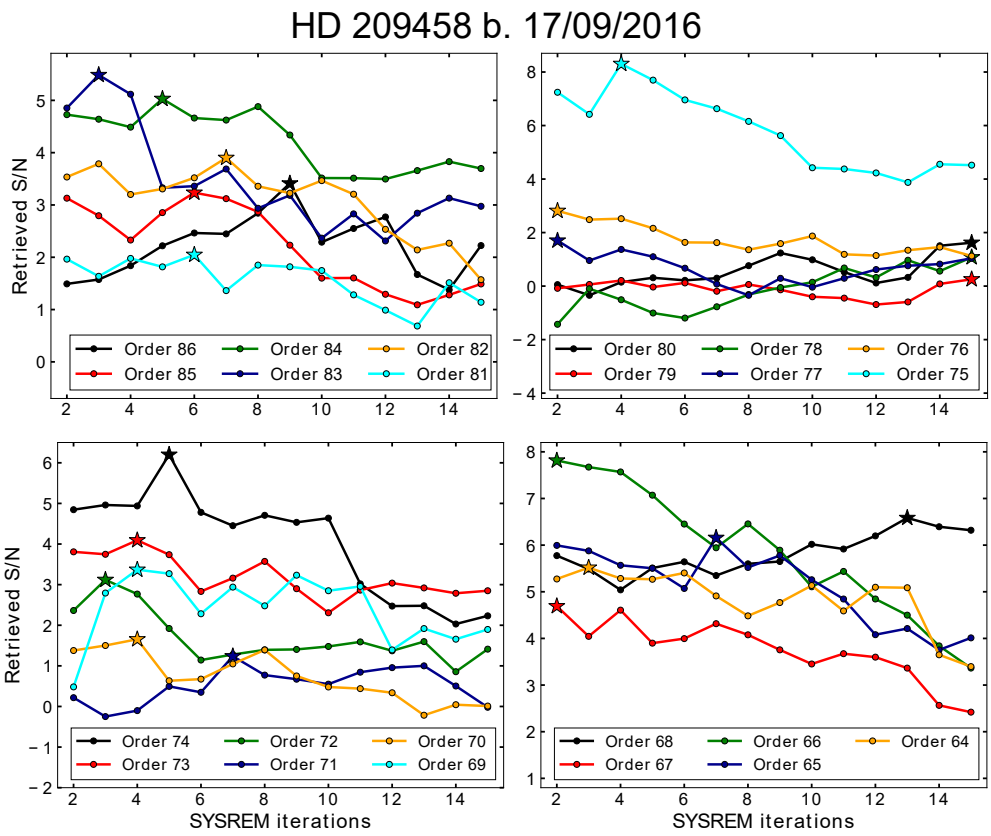

Figure 6.3: Evolution of the retrieved S/N of the injected signal in the VIS channel with the number of SYSREM iterations. The data corresponds to the transit of HD 209458 b taken on the night of 17 of September of 2016. The model signal was injected at 15× the expected strength so as to ensure that the injected signal is clearly measured (i.e., S/N $\geq$ 3). The stars represent the selected number of iterations for each spectral order at the peak of the recovered S/N. Note the different scales of the vertical axes.

the lower S/N of the observations of HD 209458 b.

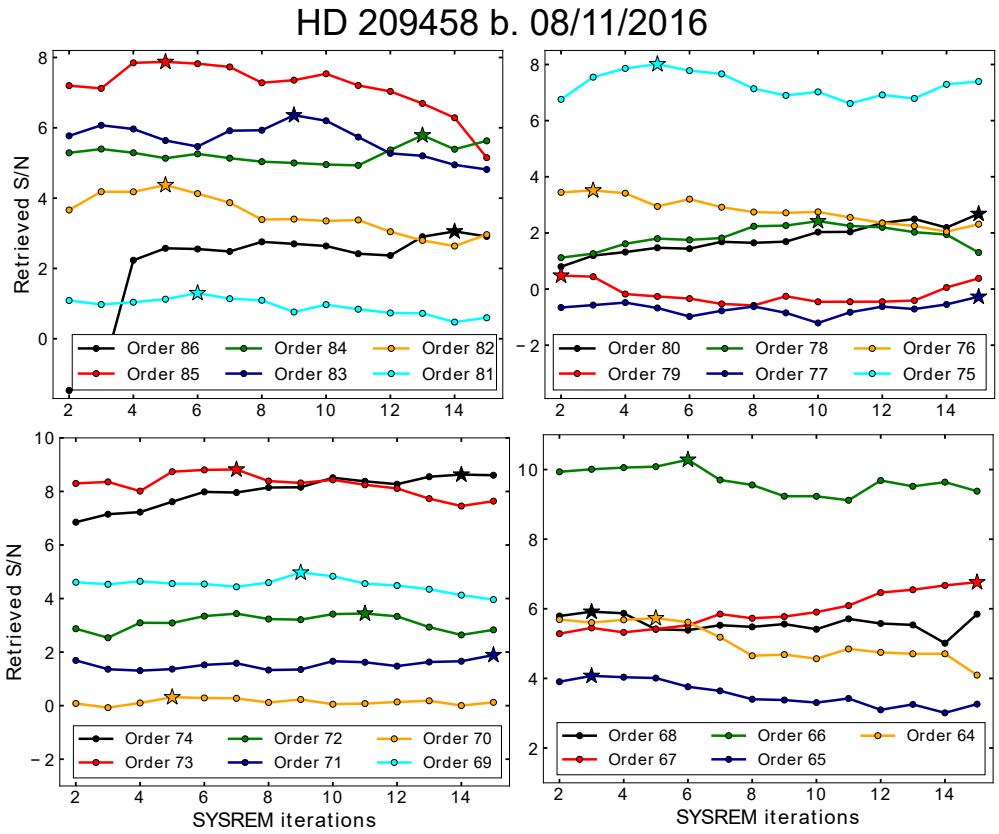

Figure 6.4: Evolution of the retrieved S/N of the injected signal in the VIS channel with the number of SYSREM iterations. The data corresponds to the transit of HD 209458 b taken on the night of 08 of November of 2016. The model signal was injected at 15× the nominal strength so as to ensure that the injected signal is clearly measured (i.e., S/N $\geq$ 3). The stars represent the selected number of iterations for each spectral order at the peak of the recovered S/N. Note the different scales of the vertical axes.

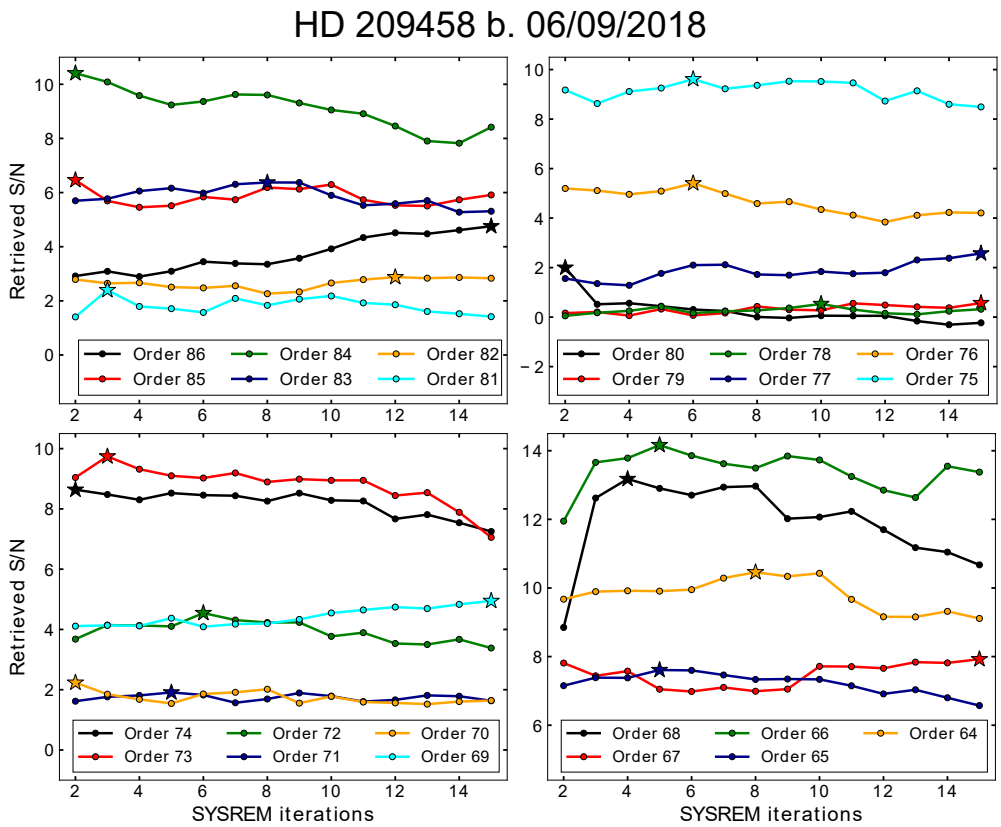

Figure 6.5: Evolution of the retrieved S/N of the injected signal in the VIS channel with the number of SYSREM iterations. The data corresponds to the transit of HD 209458 b taken on the night of 06 of September of 2018. The model signal was injected at 15× the nominal strength so as to ensure that the injected signal is clearly measured (i.e., S/N $\geq$ 3). The stars represent the selected number of iterations for each spectral order at the peak of the recovered S/N. Note the different scales of the vertical axes.

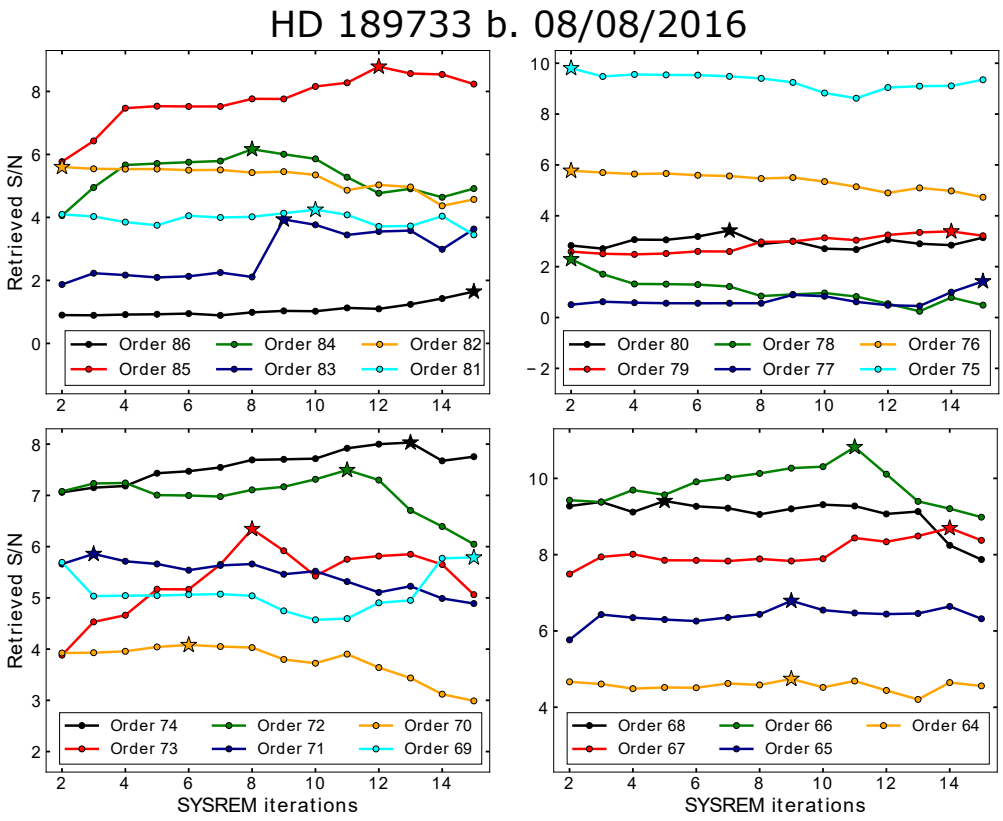

Figure 6.6: Evolution of the retrieved S/N of the injected signal in the VIS channel with the number of SYSREM iterations. The data corresponds to the transit of HD 189733 b taken on the night of 08 of August of 2016. The model signal was injected at 15× the nominal strength so as to ensure that the injected signal is clearly measured (i.e., S/N $\geq$ 3). The stars represent the selected number of iterations for each spectral order at the peak of the recovered S/N. Note the different scales of the vertical axes.

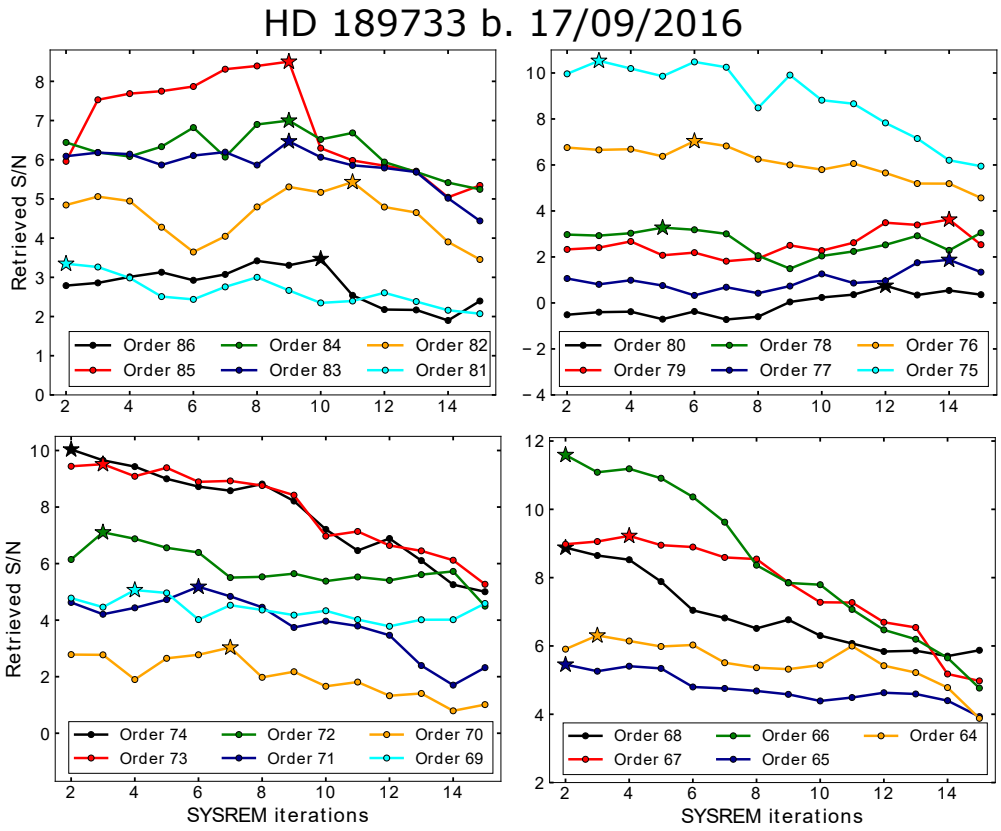

Figure 6.7: Evolution of the retrieved S/N of the injected signal in the VIS channel with the number of SYSREM iterations. The data corresponds to the transit of HD 189733 b taken on the night of 17 of September of 2016. The model signal was injected at 15× the nominal strength so as to ensure that the injected signal is clearly measured (i.e., S/N $\geq$ 3). The stars represent the selected number of iterations for each spectral order at the peak of the recovered S/N. Note the different scales of the vertical axes.

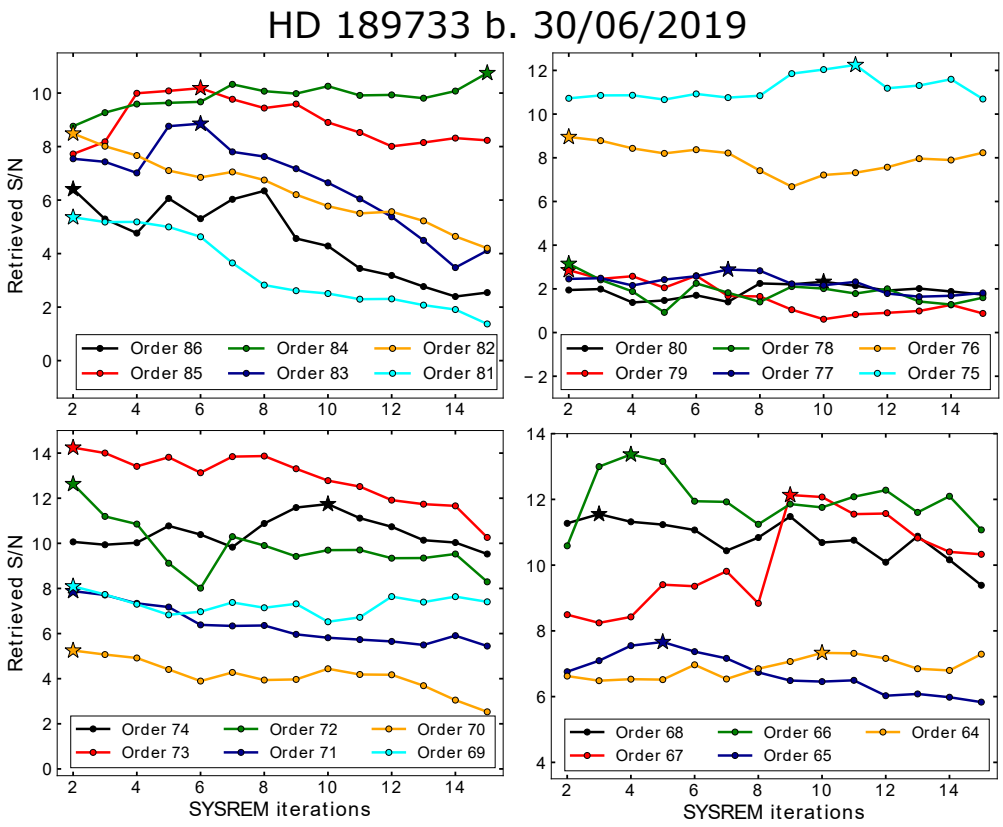

Figure 6.8: Evolution of the retrieved S/N of the injected signal in the VIS channel with the number of SYSREM iterations. The data corresponds to the transit of HD 189733 b taken on the night of 30 of June of 2019. The model signal was injected at 15× the nominal strength so as to ensure the injected signal is clearly measured (i.e., S/N $\geq$ 3). The stars represent the selected number of iterations for each spectral order at the peak of the recovered S/N. Note the different scales of the vertical axes.

Table 6.1: Spectral orders excluded from the analyses of HD 189733 b and HD 209458 b in each dataset.

Object	Night	Excluded orders
HD 189733 b	08/08/2016	86, 78, and 77
	17/09/2016	80, 77, and 70
	30/06/2019	80, 79, 78, and 77
HD 209458 b	17/09/2016	86, 85, 80, 79, 78, 77, 76, 72, 71, 70, and 69
	08/11/2016	86, 81, 80, 79, 77, 71, and 70
	06/09/2018	82, 81, 80, 79, 78, 71, and 70

6.3 Cross-correlation analysis

We computed the absorption model templates for the spectral region covered by the VIS channel of CARMENES by using the nominal $p-T$ and H_2O abundance profiles applied for HD 189733 b in chapter 4 and for HD 209458 b in chapter 5. That is, we applied the $p-T$ profile used in Brogi et al. (2018) with a water vapor VMR of 10^{-4} for HD 189733 b, and the best-fitting $p-T$ profile found in Brogi et al. (2017) with an H_2O VMR of 10^{-5} for HD 209458 b. As was the case in the previous chapters, we assumed a reference pressure of $p_{\rm ref} = 1$ bar at the reference radius of $r_{\rm ref} = 1.138\,R_J$, for HD 189733 b, and at a reference radius of $r_{\rm ref} = 1.36\,R_J$ for HD 209458 b (Sing et al., 2016), where R_J is the equatorial radius of Jupiter (71492 km). Consecutively, we computed the cross-correlation matrices in the Earth's rest-frame for each spectral order, transit and exoplanet. Following the methodology of the previous chapters, we excluded from the analyses the spectral orders for which there were moderate-to-heavy telluric residuals, which manifest as noisy patterns in the $\overline{CCFs}$, often around the 0 km/s value (i.e., in the rest-frame of the Earth).

6.3.1 Results for HD 209458 b

We co-added the cross-correlation matrices for each spectral order in a total $\overline{CCFs}$ for each transit (Fig. 6.9, row A). From these matrices, we computed the S/N maps and CCFs with largest significance peaks for the HD 209458 b transits (Fig. 6.9, rows B and C, respectively). Following the approach we introduced in chapter 5, we removed from the analyses all the in-transit spectra taken when the velocity of the planet was of ± 2.6 km/s with respect to the Earth so as to avoid an overlap of the planetary and telluric lines. That is, we left out of the co-addings seven spectra in the night of 17 September 2016 ($-0.013 < \phi < -0.01$), eight spectra on the night of 08 November 2016 ($-0.014 < \phi < -0.01$), and also seven spectra in the night of 06 September 2018 ($0.012 < \phi < 0.018$).

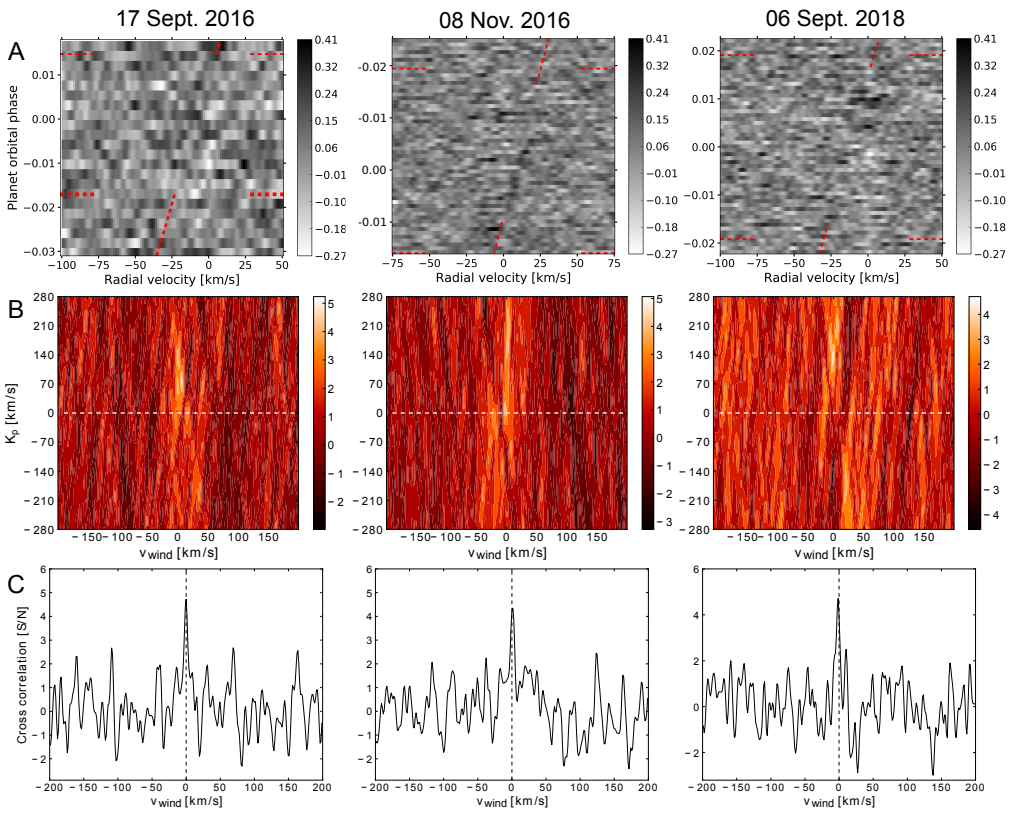

Figure 6.9: Results of the cross-correlation analyses performed on all the VIS data gathered for HD 209458 b. A: Cross-correlation matrices in the Earth's rest-frame. Horizontal dashed lines indicate the orbital phases at the beginning and end of the transit. Tilted dashed lines mark the expected exoplanet's velocities during transit with respect to the Earth. B: S/N maps. C: CCFs with the largest significance peaks found in the respective S/N maps (except for the night of 17 September 2016, see text).

All the maps presented a region of largest S/N around $K_p \sim 140$ km/s, which is the expected value for this exoplanet (Fig. 6.9B). However, this region does not represent the maximum of the explored map for the transit of 17 September 2016 (left column in Fig. 6.9), since there are other comparable signals at $K_p \sim 70$. Thereby, this night only provided hints of a potential signal and thus, in Fig. 6.9C (left column), we present the values measured at the expected Kp of 140 km/s (Snellen et al., 2010). On the contrary, the significances of the CCF peaks for the nights of 08 November 2016 and 06 September 2018 were high enough as to evidence possible H_2O detections, despite the rather noisy shape of their CCFs (see Fig. 6.9, middle and right columns, respectively).

Overall, the CCF significances are lower than those obtained for one transit in the NIR channel due to the weaker water vapor signal in the VIS. Therefore, the trace of the exoplanet is not easily identified in the $\overline{CCFs}$ in Fig. 6.9A. The

noisier behavior in the night of 17 September 2016 could be explained by the low number of spectra, the uneven coverage of the transit during that night, and the stellar flux loss due to the ADC not being updated. For the night of 08 November 2016, a trace of large cross-correlation values (i.e., darker pixels) creates the signal that we identified at orbital phases from -0.01 to 0.00, and following the expected trail of the exoplanet. However, the trace dissipates beyond $\phi \simeq 0.00$, which might also be caused by a severe loss of stellar flux towards the end of the night due to the ADC not being updated. For the night of 06 September 2018, the planetary trace is not easily identified either in the $\overline{CCF}$, suggesting that further testing of the recovered signal from this night would be useful so as to validate its origin.

In order to enhance the recovery of a planetary signal, a very useful approach is to co-add the information obtained from each night, in the same way it is carried out for each spectral order for a given night, or for every transit spectra. Thus, we created a combined S/N map by co-adding the $\overline{CCFs}$ in Fig. 6.9A, weighted by their respective mean signal-to-noise ratios. The resulting S/N map and the CCF with the largest significance, encoding the information from the three VIS observations of HD 209458 b, are shown in Fig. 6.10. Also, the S/N, K_p, and $v_{\rm wind}$ of the CCFs separately, and combined, are presented in Table 6.2. The combined S/N map showed a region of largest S/N, peaking at 6.5 at the expected velocity of the exoplanet ($K_p = 149^{+19}_{-40}$ km/s), with no comparable signals in the explored velocity space. Although preliminary, this result constitutes the first water vapor detection at optical wavelengths in any exoplanet so far. Moreover, the signal is found at a $v_{\rm wind} = 0.0 \pm 1.3$ km/s, which provides no evidence for additional winds in the atmosphere at the atmospheric layers probed by these observations.

Interestingly, the individual and combined CCFs present consistent $v_{\rm wind}$ results compatible with 0 km/s (see Table 6.2). These wind measurements are not compatible with the results we obtained in chapter 5, of $-5.2^{+2.6}_{-1.3}$ km/s. A possible explanation for this behavior is that the bulk spectrum of the weaker water vapor bands observed in the VIS might originate at lower atmospheric layers than those probed by the NIR observations. According to the GCM models of Rauscher and Menou (2013) and Showman et al. (2013), and Amundsen et al. (2016), the wind velocity is predicted to decrease towards deepest layers. In fact, in the lowest atmospheric layers, which are not probed by these observations, the winds are expected to flow from the night- to the day-side (i.e., redshifted). Thereby, the gas does not accumulate in the night hemisphere of hot Jupiters, but is returned to the illuminated side by the winds flowing in their lower atmospheres.

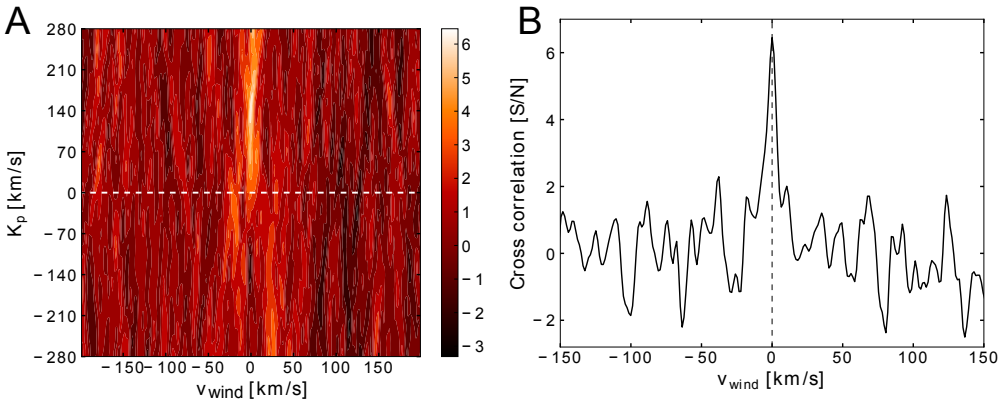

Figure 6.10: S/N map and CCF with the largest significance for the combination of the three nights of HD 209458 b observed with the VIS channel. A: S/N map encoding the information from the three nights observed for this exoplanet. A region of large S/N values is identified, with a maximum at a $K_p \sim 149$ km/s (see text), which is consistent with the expected velocity for this exoplanet. No comparable signals are observed at any other velocity. B: CCF showing the largest significance peak in the combined map.

Table 6.2: Maximum S/N of the CCFs for each night and combined for HD 209458 b.

Night	S/N	K_p [km/s]	$v_{\rm wind}$ [km/s]
17 Sept 2016	4.7^a	140^a	0.0 ± 1.3
08 Nov 2016	5.1	165^{+29}_{-26}	1.3 ± 1.3
06 Sept 2018	4.7	131 ± 22	-1.3 ± 1.3
Combined	6.5	148^{+19}_{-40}	0.0 ± 1.3

[a]Values are given at the expected $K_p = 140$ km/s (see text) .

6.3.1.1 Results for HD 189733 b

We computed the $\overline{CCFs}$ in the Earth's rest-frame for each transit of this exoplanet (see Fig. 6.11A). The exoplanet's trail cannot be visually identified in any of the matrices. This indicates that the planetary signal, if present, might still be weak and/or below the noise level. Consecutively, we computed the S/N maps (see Fig. 6.11B), leaving out of the analysis the spectra for which there was an overlapping of the planetary and telluric lines. These spectra spanned the orbital phases $-0.004 < \phi < 0.002$ (four spectra) for the night of 08 August 2016; $-0.016 < \phi < -0.012$ (three spectra) for the night of 17 September 2016; and $-0.011 < \phi < -0.017$ (five spectra) for the night of 30 June 2019.

No clear planetary signal can be observed in any of the S/N maps. In fact, the CCFs with the maximum significances we found correspond to (K_p, $v_{\rm wind}$)

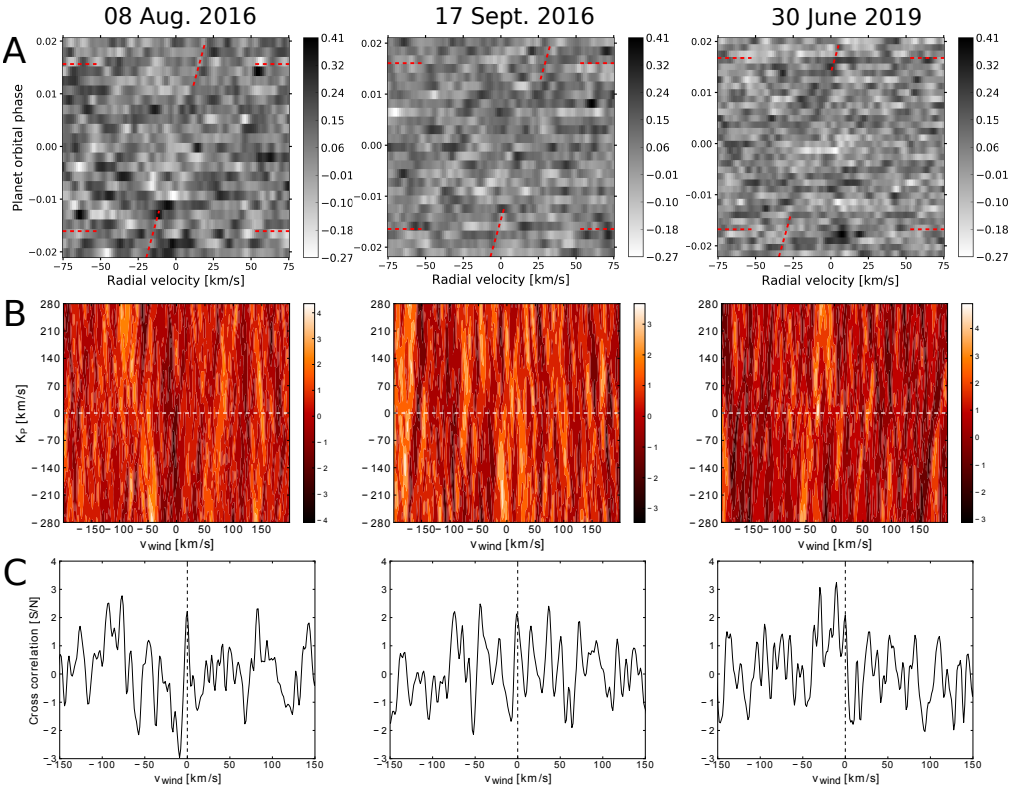

Figure 6.11: Results of the cross-correlation analyses performed for all the VIS data gathered for HD 189733 b. A: Cross-correlation matrices in the Earth's rest-frame. Horizontal dashed lines indicate the orbital phases at the beginning and end of the transit. Tilted dashed lines mark the expected exoplanet's velocities during transit with respect to the Earth. B: S/N maps. C: CCFs at the expected $K_p = 152$ km/s for this exoplanet.

tuples that are far from the expected values for this exoplanet (see Table 4.1 in chapter 4). Next, we explored the CCFs at the expected $K_p = 152$ km/s for this exoplanet (see Fig. 6.11C). As expected from the maps, no unambiguous evidence of H_2O was found in any of the CCFs above the noise level.

With the objective of enhancing a potential signal, which might still be buried at the noise level, we co-added the $\overline{CCFs}$ in the Earth's rest-frame for the three transits of this object. The combined S/N map is depicted in Fig. 6.11A. Additionally, the S/N, K_p, and $v_{\rm wind}$ of the CCFs separately, and combined, are presented in Table 6.3. There are hints of a potential water vapor signal at $K_p \sim 157$ km/s with a S/N of 3.6 (see Fig. 6.11B). However, there are more significant signals (S/N > 3.6) in the explored map (e.g., at $K_p \sim 92$ km/s, $v_{\rm wind} \sim -75$ km/s). Therefore, we could not firmly state that we found a detection of water vapor in HD 189733 b at optical wavelengths with confidence.

Table 6.3: S/N of the CCFs for each night and combined for HD 189733 b.

Night	S/N	K_p [km/s]	$v_{\rm wind}$ [km/s]
08 Aug 2016	2.2	152	$0.0^{+1.3}_{-2.6}$
17 Sept 2016	2.1	152	$-1.3^{+2.6}_{-1.3}$
30 June 2019	2.1	152	$0.0^{+1.3}_{-2.6}$
Combined	3.6	152	$0.0^{+1.3}_{-2.6}$

All values in table are measured at the expected $K_p = 152$ km/s for this exoplanet and in the $-5 < v_{\rm wind} < 5$ km/s interval, where the planetary signal is expected (see text).

6.4 Comparison of the signals in both hot Jupiters and discussion

Different studies have tackled the detection of water vapor in the optical from the ground, using HDS, and the cross-correlation technique in the past. For instance, a search of water vapor at optical wavelengths was conducted for the super-Earth 55 Cancri e by using the spectrograph/spectropolarimeter ESPaDOnS (Subaru telescope), targeting at the H_2O spectral features at $0.5-0.8\,\mu$m (Esteves et al., 2017). However, a non-detection was reported by these authors, placing a $3-\sigma$ lower limit on the mean molecular weight of this exoplanet's atmosphere, which is expected to have a C/O ratio above 1 and a low H_2O abundance (i.e., molar fractions below 10^{-6}, see Tsiaras et al., 2016).

Furthermore, Allart et al. (2017) used data from the spectrograph HARPS for the hot Jupiter HD 189733 b, focusing on the water vapor band at $\sim 0.65\,\mu$m. In that study, the authors used the Molecfit tool to remove the telluric contamination, in contrast to the PCA-based approach used in this thesis, and also reported a non-detection of water vapor using this spectral feature. In particular, they placed a $5-\sigma$ upper limit of 100 ppm in the strength of this absorption band. The presence of water vapor in the atmosphere of this hot Jupiter has been confirmed by NIR observations in the past, where H_2O bands have strengths between 200 ppm and 600 ppm (see, e.g., Fig. 4.11B and Brogi et al., 2018; Alonso-Floriano et al., 2019a). As was also discussed in Allart et al. (2017), their non-detection of H_2O in HD 189733 b in the visible, and with only one transit, is likely due to the strong extinction by atmospheric hazes, or due to dense clouds in this hot Jupiter's atmosphere. That is, the weaker the H_2O absorption band is, the more difficult it is to observe it above the Rayleigh scattering slope using transmission spectra. Thereby, more transits would have to be observed with HARPS so as to build the necessary S/N to achieve a detection.

The preliminary results we obtained in this chapter are in line with those presented in Allart et al. (2017), and also with what is expected at optical

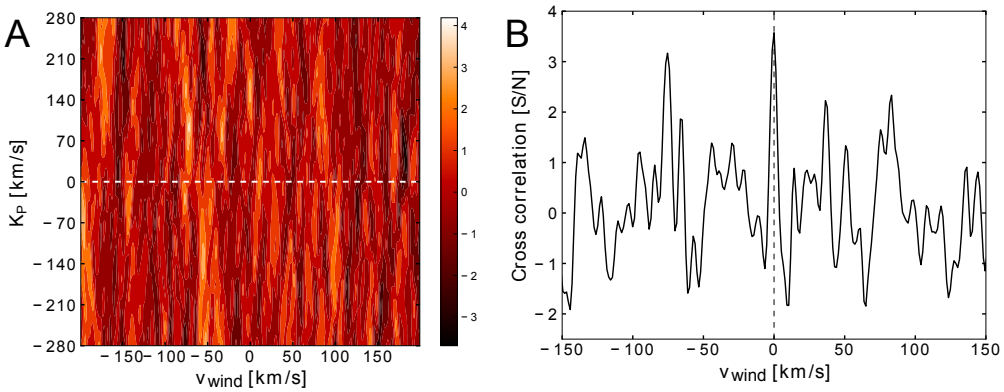

Figure 6.12: S/N map and CCF for the combination of the three nights of HD 189733 b observed with the VIS channel. A: S/N map encoding the information from all the nights observed for this exoplanet. B: CCF measured at a fixed $K_p = 152$ km/s. This CCF does not represent the maximum of the explored S/N map and hence, the value at the expected velocity of 152 km/s for this exoplanet is provided.

wavelengths for these two hot Jupiters from previous studies (Pont et al., 2008; Sing et al., 2011; Di Gloria et al., 2015; Sing et al., 2016). In addition, they are in agreement with the analyses we performed in Chapter 5, where the water vapor's absorption band at $\sim 1\,\mu$m was only hinted in HD 189733 b, whereas it provided a high-significance detection in the case of HD 209458 b. This result already suggested an atmosphere less impacted by haze extinction for the latter, which is supported by space observations (see, e.g., Sing et al., 2016).

In this context, the study presented here represents the first potential detection of water vapor using optical wavelengths on any exoplanet thus far. Furthermore, it also allows us to support the presence of a stronger atmospheric extinction in HD 189733 b, with respect to HD 209458 b, for the first time using high-dispersion spectroscopy and the cross-correlation technique in this spectral range. By using also our water vapor detections in the NIR channel of CARMENES for both hot Jupiters, we could analyze the relative intensity of the H_2O signal at very different spectral regions, from 0.52 to 1.71 μm, in a future analysis. Such study might provide new insights about the abundance of the aerosols in both exoplanets (Allart et al., 2017; Pino et al., 2018a).

Chapter 7

Summary and Outlook

"We are trying to prove ourselves wrong as quickly as possible, because only in that way can we find progress."
Richard P. Feynman

The field of exo-atmospheric characterization has reached a mature state in which revolutionary results are steadily and continuously being published. Our knowledge of the myriad stars that surround us, the exoplanets they harbor, and their exo-atmospheres is only expected to expand. In the following years, new generations of telescopes will start operating in both the outer space (e.g., JWST, ARIEL, WFIRST, HabEx, etc.) and ground-based observatories (e.g., E-ELT, TMT, etc.), that will provide us with unprecedented quality measurements of the many detected worlds that we cannot yet study, and the new ones we will discover.

While the new wave of instruments is being born, all efforts are invested in fully understanding current instrumentation, a challenge that requires the development of advanced tools for atmospheric modeling and data analysis. Interestingly, there are few available exoplanets to be characterized currently. In fact, less than a hundred exo-atmospheres have been detected out of the over 4000 exoplanets confirmed at the time of writing. It is not only possible, but expected, that our knowledge on the diversity of exo-atmospheres is biased towards the current small sample and will likely expand greatly soon. Therefore, our models and tools need to be flexible enough to allow us to understand the many surprises that await us in the new worlds of the coming decade.

In this context, this thesis represented an effort to push the boundaries of this investigation field further. With this work, we aimed at characterizing the atmospheres of exotic, very hot, and giant exoplanets that orbit very close to their host stars (i.e., hot Jupiters). These exoplanets are high signal-to-noise laboratories that provide us with high quality data with current instrumentation. We have centered our attention in the two canonical hot Jupiters, HD 189733 b

and HD 209458 b. As discussed in this thesis, these are the most well-known exoplanets to date. Hence, their study was the optimal course of action to start a new line of investigation on the Instituto de Astrofísica de Andalucía by using data from the recently installed CARMENES instrument at the Calar Alto Observatory. This faces our Group with a real challenge for learning new techniques, analyze very different datasets and study atmospheres under completely different physical conditions than those of the solar system.

In particular, the summary and main conclusions of this thesis are:

In **chapter** 2, we presented the algorithm, KOPRA, which we used to solve the radiative transfer equation (RTE) and obtain the transmittances of the atmospheric layers as a function of frequency. KOPRA is a well-tested algorithm for the study of atmospheres in the solar system and, in this chapter, we validated its use for the analysis of exo-atmospheres. In particular, we compared the transmission spectra during the primary transit of exoplanets calculated with KOPRA with those produced by other codes. Namely, the GARLIC and petitRADTRANS algorithms and the synthetic spectra produced in the framework of the ARIEL retrieval Working Group.

We have shown that our transmission models are generally in very good agreement with those calculated with those codes. Naturally, there are small differences in the computed spectra between the different algorithms. These arise, mainly, from the different methods for solving the RTE, the different spectroscopic databases used, and the different integrations of the absorption over the atmospheric annulus (i.e., as seen from Earth during transit). This general good agreement thus gives us confidence on our calculations.

In **chapter** 3, we presented an in-depth discussion of the cross-correlation technique applied to high resolution spectra. This is the state-of-the-art data analysis that is in the basis of this thesis. This technique takes advantage of the fact that close-in exoplanets move at very high orbital velocities, which, in turn, induces a Doppler shift in the exo-atmospheric lines. Although small, these shifts are detectable with high-resolution instrumentation. Moreover, this technique allows us to infer the presence of different compounds in the atmospheres of exoplanets and probe the exo-atmospheric dynamics.

We particularized our study for the case of CARMENES, a high resolution spectrograph mounted on the 3.5 m telescope at the Calar Alto Observatory (Almería, Spain). We discussed the different steps required by this technique. These were, mainly:

- The removal of bad-quality pixels not corrected by the CARMENES pipeline or, for instance, cosmic rays.

- The normalization of the spectra, which removes broadband variations

between the observations produced by airmass changes, the instrument's Blaze function, etc. Therefore, this technique is only sensitive to the relative depth of the absorption lines with respect to the continuum.

- The masking of the spectral regions most affected by the Earth's telluric absorption, mainly due to water vapor.

- The removal of the telluric and spectral features in the spectra. This was the most delicate step of this technique, since it had a direct impact on our capability to disentangle the weak exo-atmospheric signal. We made use of SYSREM, a principal component analysis algorithm. By iterating this algorithm in each spectral order, we were able to clean those contributions and extract the exo-atmospheric signal.

- Cross-correlation of the residual spectra with the transmission model templates computed with KOPRA. Such models were properly convolved with the CARMENES line spread function for the near-infrared and visible channels. Thereby, we search for potential signals that are compatible with an exo-atmospheric origin.

- The computation of the significance of the potential signals by using the signal-to-noise ratio and the Welch t-test metrics.

In **chapter** 4, we applied the cross-correlation technique to a near-infrared transit dataset of the hot Jupiter HD 189733 b obtained with CARMENES. We used the SYSREM algorithm to remove the telluric and stellar features, which was a succesful approach even at the relatively high precipitable water vapour levels of that observation night. Consecutively, we searched for water vapor in the atmosphere of this hot Jupiter and obtained a cross-correlation signal at a S/N = 6.6 ($7.1\,\sigma$). This significant value represents a firm detection of water vapor. We obtained very similar results for the currently accepted uncertainty intervals of the $p-T$ and water vapor abundance profiles, which reinforced the confidence of the detection. However, this also showed a degeneracy in this technique. That is, the cross-correlation of the data with very different models yielded very similar CCF values. Hence, it was not possible to infer the atmospheric parameters accurately with this technique (i.e., within two orders of magnitude for the H_2O concentration or several hundred Kelvin for the temperature). In addition, our analyses aiming at the detection of methane in this exo-atmosphere were not successful, since no cross-correlation signal was found when using transmission model templates containing only CH_4. In fact, the results obtained when including water vapor and methane in the models were worse than those obtained using only H_2O.

We explored the removal of the telluric contamination by using MOLECFIT instead of SYSREM. Unfortunately, our results showed that no exo-atmospheric

signal could be extracted from the residual spectra obtained with MOLECFIT, which is likely caused by the scatter of the residuals in the large wavelength coverage of the CARMENES channels.

We also studied the usefulness of the inverse-injection technique and explored whether certain models could cancel the real planetary signal better than others. We found that different combinations of water vapor abundances, temperature profiles, and contributions from clouds and hazes yielded equally successful cancelations of the exo-atmospheric absorption by using this technique. That is, as long as these parameters are kept within their expected uncertainty intervals. For instance, water vapor abundances in the range of $10^{-5} - 10^{-4}$ and overall high temperatures, above 1000 K in the lower atmosphere. This is because this technique is only sensitive to the relative depth of the absorption lines with respect to the continuum, which can be replicated by many combinations of the aforementioned parameters. Therefore, we can determine the goodness of fit of different forward models with this technique. However, providing statistically significant constraints on the atmospheric properties would require a more in-depth exploration of the parameter space.

The water vapor signal was obtained at a radial velocity semi-amplitude of $K_p = 160^{+45}_{-33}$ km/s, which is in agreement with the velocity retrieved in other works. In addition, the cross-correlation function showed a blueshifted peak at -3.9 ± 1.3 km/s, which is an indication of winds flowing from the day- to the nigh-side of HD 189733 b. This measurement of the potential winds is in line with those predicted by the model of Showman et al. (2013).

Furthermore, we were able to detect water vapor from the individual spectral bands at $\sim$1.15 μm and $\sim$1.4 μm. These two bands were only accessible from space instrumentation so far (e.g., the *HST*/WFC3). Thus, our detection of H_2O from both bands individually confirms that these absorption features can also be studied from ground-based telescopes. However, we found no clear exo-atmospheric signal when using the band at $\sim$1.0 μm individually. This is likely caused by the strong extinction by atmospheric hazes in the atmosphere of this hot Jupiter, as reported in previous works.

In **chapter** 5, we presented a detection of H_2O in the atmosphere of the hot Jupiter HD 209458 b. The signal was detected at a S/N of 6.4 (8.1 σ). We measured a net blueshift of $-5.2^{+2.6}_{-1.3}$ km/s in the signal, which indicates an average day-to-nightside strong wind at the terminator of HD 209458 b. This wind velocity is slightly larger than that reported in previous works (see, e.g., Snellen et al., 2010), although comparable within the uncertainty intervals. Moreover, this result supports the model predictions of Rauscher and Menou (2012), Showman et al. (2013), and Amundsen et al. (2016), where a stronger day-to-nightside thermospheric wind is predicted for this hotter exoplanet than for HD 189733 b.

Interestingly, we found that the largest contribution to the detection came from the 1.0 μm band, which was individually detected with a S/N of 5.8. This

result constitutes the first detection of water vapor from this band individually. In fact, it is the bluest band detected so far in any exo-atmosphere. Moreover, we observed hints of a water vapor signal from the 1.15 μm band with a low S/N of 2.8. Regarding the 1.4 μm band, we also observed hints of a potential signal, but the maximum significance cross-correlation peak was not found at the expected velocities of HD 209458 b.

The removal of the telluric contamination is the most delicate step of the cross-correlation technique applied in this study. We used SYSREM, widely tested for this purpose in previous works. We optimized the number of iterations required for each order independently by studying the behavior of an injected model signal of the planet. During the observations of the HD 209458 b transit, a sudden drop in the column depth of PWV occurred. Moreover, a significant portion of the observations was taken at large airmasses, resulting in low signal-to-noise ratios for the second half of the gathered spectra. In addition, the S/N of the spectra showed a strong wavelength dependence towards the end of the night, with the S/N decreasing significantly at the reddest wavelengths. These effects combined could be behind the less effective telluric removal in the two stronger bands covered, which would explain the lower than expected significances obtained from the 1.15 μm and 1.4 μm bands.

The comparison of the results we obtained for the CARMENES data of HD 209458 b and HD 189733 b supports the previously reported hazy nature of the latter. As discussed by Pino et al., 2018a and Alonso-Floriano et al., 2019a, the water vapor molecular bands studied here could ideally be used, along with optical data, to characterize the aerosol extinction in the atmospheres of hot Jupiters. However, the low CCF contrast ratios in the bands covered by the CARMENES NIR channel and the atmospheric variability in the HD 209458 b observation night made such a study unfeasible in this case.

In **chapter** 6, we analized several transit datasets for the hot Jupiters HD 209458 b and HD 189733 b recorded with the VIS channel of CARMENES ($0.52 - 0.96\,\mu$m). Our analyses revealed the presence of water vapor in the atmosphere of HD 209458 b, whilst only hints of a signal were obtained for HD 189733 b at these optical wavelengths. This detection of H_2O in HD 209458 b represents the first detection of water vapor in the optical in any exoplanet so far with current instrumentation. In addition, the less significant detection obtained for HD 189733 b supports our previous finding that this hot Jupiter presents a stronger atmospheric haze extinction, which is especially important in the optical. This is also in good agreement with the literature results.

Moving forward, a definitive detection of water vapor at optical wavelengths in HD 209458 b could be put in context with the detection we obtained in the near-infrared for the same exoplanet. That is, only one transit was needed to achieve a S/N = 6.4 detection in the near-infrared, whereas we had to combine three observation nights to obtain a similar S/N by using optical data. Although

the quality of the observations in each transit could play a major role in our capabilities for disentangling the planetary signal, we might be able to provide some information regarding the presence of hazes or clouds in this exoplanet by comparing both detections. Similarly, this comparison can be performed for HD 189733 b once the results are verified. In this case, a combination of three transits in the visible did not yield a detection of H_2O, whereas we detected it with confidence in the near-infrared with only one transit.

In conclusion, the results obtained in chapters 4, 5, and 6 represent an important step forward for exo-atmospheric characterization using ground-based instrumentation. In particular, this work contributed, along with previous studies (Brogi et al., 2018; Yan and Henning, 2018), to consolidate the study of exoplanet atmospheres by using 4 m-class telescopes and stabilized high-resolution spectrographs ($R > 20,000$). On the one hand, our findings verified the suitability of the NIR and, potentially, the VIS channel of CARMENES for detecting molecular features and study the dynamics of exo-atmospheres. On the other hand, our results also confirmed that large wavelength coverages, such as those of the CARMENES channels, significantly add to the performance of the cross-correlation technique by allowing the detection of molecular features using different bands separately.

We are witnessing an astonishing expansion of the research field of exoplanets and exo-atmospheres. Our knowledge is restricted to the very few quality data we can obtain from the current sample of exoplanets and instrumentation. However, our understanding of exoplanetary systems will rapidly grow as higher-quality datasets arrive. Thus, a very interesting interplay between data analysis and exo-atmospheric modeling is arising, as we try to rule out as quickly as possible the potentially wrong or incomplete conclusions we might have drawn from previous studies. As was perfectly worded by Richard P. Feynman, only this process will allow us to push our boundaries further.

Publications derived from this thesis

Main publications

Sánchez-López, A., M. López-Puertas, B. Funke, P. Amado, et al. (2017). "Simulations of transit spectra of Hot Jupiters in the wavelength range of the CARMENES infrared channel (0.96-1.7 μm)". *Differences* 5, pp. 10–5.

Sánchez López, A., F. J. Alonso Floriano, I. Snellen, M. López Puertas, et al. (2018). "Water detection in the near infrared in HD 189733 b with CARMENES". *European Planetary Science Congress*. Vol. 12.

Alonso-Floriano, F., A. Sánchez-López, I. A. G. Snellen, M. López-Puertas, et al. (2019a). "Multiple water band detections in the CARMENES near-infrared transmission spectrum of HD 189733 b". *Astronomy & Astrophysics* 621, A74.

Lampón, M., M. López-Puertas, M. L. Lara, A. Sánchez-López, et al. (2019). "Modelling the Helium triplet absorption in the atmosphere of the hot-Jupiter HD 209458 b". *to be submitted to Astronomy & Astrophysics*.

Sánchez-López, A., F. Alonso-Floriano, M. López-Puertas, I. A. G. Snellen, et al. (2019). "Water vapor detection in the transmission spectra of HD 209458 b with the CARMENES NIR channel". *Astronomy & Astrophysics* 630, A53.

Sánchez-López, A., M. López-Puertas, et al. (2019). "Detection of water vapor at optical wavelengths in the transmission spectra of CARMENES". *in preparation*.

Contributions to other publications

López-Puertas, M., P. Montañés-Rodríguez, E. Pallé, M. Höpfner, et al. (2018). "Aerosols and Water Ice in Jupiter's Stratosphere from UV-NIR Ground-based Observations". *The Astronomical Journal* 156.4, p. 169.

Nortmann, L., E. Pallé, M. Salz, J. Sanz-Forcada, et al. (2018). "Ground-based detection of an extended helium atmosphere in the Saturn-mass exoplanet WASP-69b". *Science* 362.6421, pp. 1388–1391.

Quirrenbach, A., P. Amado, I. Ribas, A. Reiners, et al. (2018). "CARMENES: high-resolution spectra and precise radial velocities in the red and infrared". *Ground-based and Airborne Instrumentation for Astronomy VII*. Vol. 10702. International Society for Optics and Photonics, 107020W.

Reiners, A., I. Ribas, M. Zechmeister, J. Caballero, et al. (2018a). "The CARMENES search for exoplanets around M dwarfs-HD147379 b: A nearby Neptune in the temperate zone of an early-M dwarf". *Astronomy & Astrophysics* 609, p. L5.

Reiners, A., M. Zechmeister, J. Caballero, I. Ribas, et al. (2018b). "The CARMENES search for exoplanets around M dwarfs-High-resolution optical and near-infrared spectroscopy of 324 survey stars". *Astronomy & Astrophysics* 612, A49.

Salz, M., S. Czesla, P. Schneider, E. Nagel, et al. (2018). "Detection of He I λ10830 Å absorption on HD 189733 b with CARMENES high-resolution transmission spectroscopy". *Astronomy & Astrophysics* 620, A97.

Trifonov, T., M. Kürster, M. Zechmeister, L. Tal-Or, et al. (2018). "The CARMENES search for exoplanets around M dwarfs-First visual-channel radial-velocity measurements and orbital parameter updates of seven M-dwarf planetary systems". *Astronomy & Astrophysics* 609, A117.

Alonso-Floriano, F., I. A. G. Snellen, S. Czesla, F. Bauer, et al. (2019b). "He I λ 10830 Å in the transmission spectrum of HD 209458 b". *arXiv preprint arXiv:1907.13425*.

Zechmeister, M., M. Dreizler, I. Ribas, A. Reiners, et al. (2019a). "VizieR Online Data Catalog: Teegarden's Star RV and Halpha curves (Zechmeister+, 2019)". *VizieR Online Data Catalog* 362.

Zechmeister, M., S. Dreizler, I. Ribas, A. Reiners, et al. (2019b). "The CARMENES search for exoplanets around M dwarfs. Two temperate Earth-mass planet candidates around Teegarden's Star". *arXiv preprint arXiv:1906.07196*.

Bibliography

Agol, E., N. B. Cowan, H. A. Knutson, D. Deming, et al. (2010). "The climate of HD 189733b from fourteen transits and eclipses measured by Spitzer". *The Astrophysical Journal* 721.2, p. 1861.

Agol, E. and D. C. Fabrycky (2018). "Transit-timing and duration variations for the discovery and characterization of exoplanets". *Handbook of Exoplanets*, pp. 797–816.

Allart, R., C. Lovis, L. Pino, A. Wyttenbach, et al. (2017). "Search for water vapor in the high-resolution transmission spectrum of HD 189733b in the visible". *Astronomy & Astrophysics* 606, A144.

Alonso-Floriano, F., A. Sánchez-López, I. A. G. Snellen, M. López-Puertas, et al. (2019a). "Multiple water band detections in the CARMENES near-infrared transmission spectrum of HD 189733 b". *Astronomy & Astrophysics* 621, A74.

Alonso-Floriano, F., I. A. G. Snellen, S. Czesla, F. Bauer, et al. (2019b). "He I λ 10830 Å in the transmission spectrum of HD 209458 b". *arXiv preprint arXiv:1907.13425*.

Amundsen, D. S., N. J. Mayne, I. Baraffe, J. Manners, et al. (2016). "The UK Met Office global circulation model with a sophisticated radiation scheme applied to the hot Jupiter HD 209458b". *Astronomy & Astrophysics* 595, A36.

Angerhausen, D., E. DeLarme, and J. A. Morse (2015). "A comprehensive study of Kepler phase curves and secondary eclipses: temperatures and albedos of confirmed Kepler giant planets". *Publications of the Astronomical Society of the Pacific* 127.957, p. 1113.

Anglada-Escudé, G., P. J. Amado, J. Barnes, Z. M. Berdiñas, et al. (2016). "A terrestrial planet candidate in a temperate orbit around Proxima Centauri". *Nature* 536.7617, p. 437.

Arcangeli, J., J.-M. Désert, V. Parmentier, K. B. Stevenson, et al. (2019). "Climate of an ultra hot Jupiter-Spectroscopic phase curve of WASP-18b with HST/WFC3". *Astronomy & Astrophysics* 625, A136.

Atri, D., J. DeMarines, and J. Haqq-Misra (2011). "A protocol for messaging to extraterrestrial intelligence". *Space Policy* 27.3, pp. 165–169.

Babcock, H. W. (1953). "The possibility of compensating astronomical seeing". *Publications of the Astronomical Society of the Pacific* 65.386, pp. 229–236.

Barragan, O. (2018). "Unveiling the Nature of Faraway Worlds: Intensive characterisation of K2 transiting exoplanets".

Barstow, J. K., S. Aigrain, P. G. Irwin, and D. K. Sing (2016). "A consistent retrieval analysis of 10 hot Jupiters observed in transmission". *The Astrophysical Journal* 834.1, p. 50.

Barstow, J. K. and P. G. Irwin (2016). "Habitable worlds with JWST: transit spectroscopy of the TRAPPIST-1 system?" *Monthly Notices of the Royal Astronomical Society: Letters* 461.1, pp. L92–L96.

Baudino, J.-L., B. Bézard, A. Boccaletti, M. Bonnefoy, et al. (2015). "Interpreting the photometry and spectroscopy of directly imaged planets: a new atmospheric model applied to β Pictoris b and SPHERE observations". *Astronomy & Astrophysics* 582, A83.

Baudino, J.-L., P. Mollière, O. Venot, P. Tremblin, et al. (2017). "Toward the analysis of JWST exoplanet spectra: Identifying troublesome model parameters". *The Astrophysical Journal* 850.2, p. 150.

Beichman, C. A. and T. P. Greene (2018). "Observing Exoplanets with the James Webb Space Telescope". *Handbook of Exoplanets*, pp. 1283–1308.

Berdyugina, S., A. Berdyugin, D. Fluri, and V. Piirola (2011). "Polarized reflected light from the exoplanet HD189733b: first multicolor observations and confirmation of detection". *The Astrophysical Journal Letters* 728.1, p. L6.

Beuzit, J.-L., M. Feldt, K. Dohlen, D. Mouillet, et al. (2008). "SPHERE: a planet finder instrument for the VLT". *Ground-based and airborne instrumentation for astronomy II*. Vol. 7014. International Society for Optics and Photonics, p. 701418.

Bilger, C., P. Rimmer, and C. Helling (2013). "Small hydrocarbon molecules in cloud-forming brown dwarf and giant gas planet atmospheres". *Monthly Notices of the Royal Astronomical Society* 435.3, pp. 1888–1903.

Birkby, J. L. (2018). "Spectroscopic Direct Detection of Exoplanets". *Handbook of Exoplanets*, pp. 1485–1508.

Birkby, J., R. de Kok, M. Brogi, E. de Mooij, et al. (2013). "Detection of water absorption in the day side atmosphere of HD 189733 b using ground-based high-resolution spectroscopy at 3.2 μm". *Monthly Notices of the Royal Astronomical Society: Letters* 436.1, pp. L35–L39.

Birkby, J., R. de Kok, M. Brogi, H. Schwarz, et al. (2017). "Discovery of water at high spectral resolution in the atmosphere of 51 Peg b". *The Astronomical Journal* 153.3, p. 138.

Board, S. S., E. National Academies of Sciences, Medicine, et al. (2019). *Exoplanet Science Strategy*. National Academies Press.

Bonnefoy, M., A. Boccaletti, A.-M. Lagrange, F. Allard, et al. (2013). "The near-infrared spectral energy distribution of β Pictoris b". *Astronomy & Astrophysics* 555, A107.

Borysow, A. (2002). "Collision-induced absorption coefficients of H2 pairs at temperatures from 60 K to 1000 K". *Astronomy & Astrophysics* 390.2, pp. 779–782.

Borysow, A. and L. Frommhold (1989). "Collision-induced infrared spectra of H2-He pairs at temperatures from 18 to 7000 K. II-Overtone and hot bands". *The Astrophysical Journal* 341, pp. 549–555.

Borysow, A., L. Frommhold, and M. Moraldi (1989). "Collision-induced infrared spectra of H2-He pairs involving 0-1 vibrational transitions and temperatures from 18 to 7000 K". *The Astrophysical Journal* 336, pp. 495–503.

Bott, K., J. Bailey, L. Kedziora-Chudczer, D. V. Cotton, et al. (2016). "The polarization of HD 189733". *Monthly Notices of the Royal Astronomical Society: Letters* 459.1, pp. L109–L113.

Bouchy, F., S. Udry, M. Mayor, C. Moutou, et al. (2005). "ELODIE metallicity-biased search for transiting hot jupiters-II. a very hot jupiter transiting the bright k star HD 189733". *Astronomy & Astrophysics* 444.1, pp. L15–L19.

Bourrier, V. and A. L. des Etangs (2013). "3D model of hydrogen atmospheric escape from HD 209458b and HD 189733b: radiative blow-out and stellar wind interactions". *Astronomy & Astrophysics* 557, A124.

Bowler, B. P. (2016). "Imaging extrasolar giant planets". *Publications of the Astronomical Society of the Pacific* 128.968, p. 102001.

Brewer, J. M., D. A. Fischer, and N. Madhusudhan (2017). "C/O and O/H Ratios Suggest Some Hot Jupiters Originate Beyond the Snow Line". *The Astronomical Journal* 153.2, p. 83.

Brogi, M., R. De Kok, S. Albrecht, I. Snellen, et al. (2016). "Rotation and winds of exoplanet HD 189733 b measured with high-dispersion transmission spectroscopy". *The Astrophysical Journal* 817.2, p. 106.

Brogi, M., R. de Kok, J. Birkby, H. Schwarz, et al. (2014). "Carbon monoxide and water vapor in the atmosphere of the non-transiting exoplanet HD 179949 b". *Astronomy & Astrophysics* 565, A124.

Brogi, M., M. Line, J. Bean, J.-M. Désert, et al. (2017). "A framework to combine low-and high-resolution spectroscopy for the atmospheres of transiting exoplanets". *The Astrophysical Journal Letters* 839.1, p. L2.

Brogi, M., I. Snellen, R. de Kok, S. Albrecht, et al. (2013). "Detection of molecular absorption in the dayside of exoplanet 51 Pegasi b?" *The Astrophysical Journal* 767.1, p. 27.

Brogi, M. (2014). "Atmospheres of hot alien Worlds". PhD thesis. Universiteit Leiden.

Brogi, M., P. Giacobbe, G. Guilluy, R. de Kok, et al. (2018). "Exoplanet atmospheres with GIANO-I. Water in the transmission spectrum of HD 189 733 b". *Astronomy & Astrophysics* 615, A16.

Brogi, M. and M. R. Line (2019). "Retrieving Temperatures and Abundances of Exoplanet Atmospheres with High-resolution Cross-correlation Spectroscopy". *The Astronomical Journal* 157.3, p. 114.

Brogi, M., I. A. Snellen, R. J. de Kok, S. Albrecht, et al. (2012). "The signature of orbital motion from the dayside of the planet τ Boötis b". *Nature* 486.7404, p. 502.

Brown, A., A. Vallenari, T. Prusti, J. De Bruijne, et al. (2018). "Gaia Data Release 2-Summary of the contents and survey properties". *Astronomy & astrophysics* 616, A1.

Brown, R. A. and C. J. Burrows (1990). "On the feasibility of detecting extrasolar planets by reflected starlight using the Hubble Space Telescope". *Icarus* 87.2, pp. 484–497.

Brown, T. M. (2001). "Transmission spectra as diagnostics of extrasolar giant planet atmospheres". *The Astrophysical Journal* 553.2, p. 1006.

Brown, T. M., D. Charbonneau, R. L. Gilliland, R. W. Noyes, et al. (2001). "Hubble Space Telescope time-series photometry of the transiting planet of HD 209458". *The Astrophysical Journal* 552.2, p. 699.

Burrows, A. S. (2014a). "Highlights in the study of exoplanet atmospheres". *Nature* 513.7518, p. 345.

— (2014b). "Spectra as windows into exoplanet atmospheres". *Proceedings of the National Academy of Sciences* 111.35, pp. 12601–12609.

Burrows, A., J. Budaj, and I. Hubeny (2008). "Theoretical spectra and light curves of close-in extrasolar giant planets and comparison with data". *The Astrophysical Journal* 678.2, p. 1436.

Butler, R. P., J. Wright, G. Marcy, D. Fischer, et al. (2006). "Catalog of nearby exoplanets". *The Astrophysical Journal* 646.1, p. 505.

Caballero, J., J. Guàrdia, M. L. del Fresno, M. Zechmeister, et al. (2016). "CARMENES: data flow". *Observatory operations: strategies, processes, and systems VI*. Vol. 9910. International Society for Optics and Photonics, 99100E.

Cabot, S. H., N. Madhusudhan, G. A. Hawker, and S. Gandhi (2018). "On the robustness of analysis techniques for molecular detections using high-resolution exoplanet spectroscopy". *Monthly Notices of the Royal Astronomical Society* 482.4, pp. 4422–4436.

Caldas, A., J. Leconte, F. Selsis, I. Waldmann, et al. (2019). "Effects of a fully 3D atmospheric structure on exoplanet transmission spectra: retrieval biases due to day–night temperature gradients". *Astronomy & Astrophysics* 623, A161.

Casasayas-Barris, N., E. Palle, G. Nowak, F. Yan, et al. (2017). "Detection of sodium in the atmosphere of WASP-69b". *Astronomy & Astrophysics* 608, A135.

Catling, D. C. and M. W. Claire (2005). "How Earth's atmosphere evolved to an oxic state: a status report". *Earth and Planetary Science Letters* 237.1-2, pp. 1–20.

Chabrier, G., I. Baraffe, and B. Plez (1996). "Mass-luminosity relationship and lithium depletion for very low mass stars". *The Astrophysical Journal Letters* 459.2, p. L91.

Chan, Y. and A. Dalgarno (1965). "The dipole spectrum and properties of helium". *Proceedings of the Physical Society* 86.4, p. 777.

Charbonneau, D., L. E. Allen, S. T. Megeath, G. Torres, et al. (2005). "Detection of thermal emission from an extrasolar planet". *The Astrophysical Journal* 626.1, p. 523.

Charbonneau, D., Z. K. Berta, J. Irwin, C. J. Burke, et al. (2009). "A super-Earth transiting a nearby low-mass star". *Nature* 462.7275, p. 891.

Charbonneau, D., T. M. Brown, D. W. Latham, and M. Mayor (1999). "Detection of planetary transits across a sun-like star". *The Astrophysical Journal Letters* 529.1, p. L45.

Charbonneau, D., T. M. Brown, R. W. Noyes, and R. L. Gilliland (2002). "Detection of an extrasolar planet atmosphere". *The Astrophysical Journal* 568.1, p. 377.

Charbonneau, D., H. A. Knutson, T. Barman, L. E. Allen, et al. (2008). "The broadband infrared emission spectrum of the exoplanet HD 189733b". *The Astrophysical Journal* 686.2, p. 1341.

Christensen, P. R. and J. C. Pearl (1997). "Initial data from the Mars Global Surveyor thermal emission spectrometer experiment: observations of the Earth". *Journal of Geophysical Research: Planets* 102.E5, pp. 10875–10880.

Christensen, U. R. (2006). "A deep dynamo generating Mercury's magnetic field". *Nature* 444.7122, p. 1056.

Crossfield, I. J. (2015). "Observations of exoplanet atmospheres". *Publications of the Astronomical Society of the Pacific* 127.956, p. 941.

Crossfield, I. J., B. M. Hansen, J. Harrington, J. Y.-K. Cho, et al. (2010). "A new 24 μm phase curve for υ Andromedae b". *The Astrophysical Journal* 723.2, p. 1436.

Crossfield, I. J., H. Knutson, J. Fortney, A. P. Showman, et al. (2012). "Spitzer/MIPS 24 μm observations of HD 209458b: Three eclipses, two and a half transits, and a phase curve corrupted by instrumental sensitivity variations". *The Astrophysical Journal* 752.2, p. 81.

Currie, T., A. Burrows, N. Madhusudhan, M. Fukagawa, et al. (2013). "A combined very large telescope and Gemini study of the atmosphere of the directly imaged planet, β PICTORIS b". *The Astrophysical Journal* 776.1, p. 15.

Dawson, R. I. and J. A. Johnson (2018). "Origins of Hot Jupiters". *Annual Review of Astronomy and Astrophysics* 56, pp. 175–221.

Deeg, H. J. and R. Alonso (2018). "Transit photometry as an exoplanet discovery method". *Handbook of exoplanets*, pp. 633–657.

Deeg, H. J. and J. A. Belmonte (2018). *Handbook of Exoplanets*. Springer.

Deming, D., J. Harrington, S. Seager, and L. J. Richardson (2006). "Strong infrared emission from the extrasolar planet HD 189733b". *The Astrophysical Journal* 644.1, p. 560.

Deming, D., S. Seager, L. J. Richardson, and J. Harrington (2005). "Infrared radiation from an extrasolar planet". *Nature* 434.7034, p. 740.

Deming, D., A. Wilkins, P. McCullough, A. Burrows, et al. (2013). "Infrared transmission spectroscopy of the exoplanets HD 209458b and XO-1b using the Wide Field Camera-3 on the Hubble Space Telescope". *The Astrophysical Journal* 774.2, p. 95.

Demory, B.-O., J. De Wit, N. Lewis, J. Fortney, et al. (2013). "Inference of inhomogeneous clouds in an exoplanet atmosphere". *The Astrophysical Journal Letters* 776.2, p. L25.

Demory, B.-O., M. Gillon, S. Seager, B. Benneke, et al. (2012). "Detection of thermal emission from a super-Earth". *The Astrophysical Journal Letters* 751.2, p. L28.

Demory, B.-O., M. Gillon, J. de Wit, N. Madhusudhan, et al. (2016). "A map of the large day–night temperature gradient of a super-Earth exoplanet". *Nature* 532.7598, p. 207.

Désert, J.-M., A. Vidal-Madjar, A. L. Des Etangs, D. Sing, et al. (2008). "TiO and VO broad band absorption features in the optical spectrum of the atmosphere of the hot-Jupiter HD 209458b". *Astronomy & Astrophysics* 492.2, pp. 585–592.

Di Gloria, E., I. Snellen, and S. Albrecht (2015). "Using the chromatic Rossiter-McLaughlin effect to probe the broadband signature in the optical transmission spectrum of HD 189733b". *Astronomy & Astrophysics* 580, A84.

Dullemond, C. P. (2012). "Lecture Notes on Radiative Transfer in Astrophysics".

Ehrenreich, D., G. Tinetti, A. L. Des Etangs, A. Vidal-Madjar, et al. (2006). "The transmission spectrum of Earth-size transiting planets". *Astronomy & Astrophysics* 448.1, pp. 379–393.

Espinoza, N., B. V. Rackham, A. Jordán, D. Apai, et al. (2018). "ACCESS: a featureless optical transmission spectrum for WASP-19b from Magellan/IMACS". *Monthly Notices of the Royal Astronomical Society* 482.2, pp. 2065–2087.

Esteves, L. J., E. J. De Mooij, and R. Jayawardhana (2013). "Optical phase curves of Kepler exoplanets". *The Astrophysical Journal* 772.1, p. 51.

— (2015). "Changing phases of alien worlds: Probing atmospheres of Kepler planets with high-precision photometry". *The Astrophysical Journal* 804.2, p. 150.

Esteves, L. J., E. J. De Mooij, R. Jayawardhana, C. Watson, et al. (2017). "A search for water in a super-earth atmosphere: high-resolution optical spectroscopy of 55Cancri e". *The Astronomical Journal* 153.6, p. 268.

Etangs, A. L. des, V. Bourrier, P. Wheatley, H. Dupuy, et al. (2012). "Temporal variations in the evaporating atmosphere of the exoplanet HD 189733b". *Astronomy & Astrophysics* 543, p. L4.

Etangs, A. L. des, D. Ehrenreich, A. Vidal-Madjar, G. Ballester, et al. (2010). "Evaporation of the planet HD 189733b observed in H i Lyman-α". *Astronomy & Astrophysics* 514, A72.

Etangs, A. L. des, F. Pont, A. Vidal-Madjar, and D. Sing (2008a). "Rayleigh scattering in the transit spectrum of HD 189733b". *Astronomy & Astrophysics* 481.2, pp. L83–L86.

Etangs, A. L. des, A. Vidal-Madjar, J.-M. Désert, and D. Sing (2008b). "Rayleigh scattering by H2 in the extrasolar planet HD 209458b". *Astronomy & Astrophysics* 485.3, pp. 865–869.

Fischer, H., M. Birk, C. Blom, B. Carli, et al. (2007). "MIPAS: an instrument for atmospheric and climate research". *Atmospheric Chemistry and Physics Discussions* 7.3, pp. 8795–8893.

Fischer, P. D., H. A. Knutson, D. K. Sing, G. W. Henry, et al. (2016). "HST hot-Jupiter transmission spectral survey: Clear skies for cool Saturn WASP-39b". *The Astrophysical Journal* 827.1, p. 19.

Fitzpatrick, R. (2001). "Thermodynamics & statistical mechanics". *University of Texas at Austin*.

Follert, R. a., R. Dorn, E. Oliva, J. Lizon, et al. (2014). "CRIRES+: a cross-dispersed high-resolution infrared spectrograph for the ESO VLT". *Ground-based and Airborne Instrumentation for Astronomy V*. Vol. 9147. International Society for Optics and Photonics, p. 914719.

Ford, A. L. and J. C. Browne (1973). "Direct-resolvent-operator computations on the hydrogen-molecule dynamic polarizability, Rayleigh, and Raman scattering". *Physical Review A* 7.2, p. 418.

Fortney, J. J. (2005). "The effect of condensates on the characterization of transiting planet atmospheres with transmission spectroscopy". *Monthly Notices of the Royal Astronomical Society* 364.2, pp. 649–653.

Funke, B., M. López-Puertas, M. García-Comas, M. Kaufmann, et al. (2012). "GRANADA: A Generic RAdiative traNsfer AnD non-LTE population algorithm". *Journal of Quantitative Spectroscopy and Radiative Transfer* 113.14, pp. 1771–1817.

Gandhi, S. and N. Madhusudhan (2017). "GENESIS: new self-consistent models of exoplanetary spectra". *Monthly Notices of the Royal Astronomical Society* 472.2, pp. 2334–2355.

García-Comas, M., M. López-Puertas, B. Funke, B. M. Dinelli, et al. (2011). "Analysis of Titan CH4 3.3 μm upper atmospheric emission as measured by Cassini/VIMS". *Icarus* 214.2, pp. 571–583.

Gibson, N., S. Aigrain, F. Pont, D. K. Sing, et al. (2012). "Probing the haze in the atmosphere of HD 189733b with Hubble Space Telescope/WFC3 transmission spectroscopy". *Monthly Notices of the Royal Astronomical Society* 422.1, pp. 753–760.

Gillon, M., E. Jehin, S. M. Lederer, L. Delrez, et al. (2016). "Temperate Earth-sized planets transiting a nearby ultracool dwarf star". *Nature* 533.7602, p. 221.

Gillon, M., A. H. Triaud, B.-O. Demory, E. Jehin, et al. (2017). "Seven temperate terrestrial planets around the nearby ultracool dwarf star TRAPPIST-1". *Nature* 542.7642, p. 456.

Goldblatt, C., T. M. Lenton, and A. J. Watson (2006). "Bistability of atmospheric oxygen and the Great Oxidation". *Nature* 443.7112, p. 683.

Gordon, I. E., L. S. Rothman, C. Hill, R. V. Kochanov, et al. (2017). "The HITRAN2016 molecular spectroscopic database". *Journal of Quantitative Spectroscopy and Radiative Transfer* 203, pp. 3–69.

Gordon, S. and B. J. McBride (1994). "Computer program for calculation of complex chemical equilibrium compositions and applications. Part 1: Analysis".

Grillmair, C. J., A. Burrows, D. Charbonneau, L. Armus, et al. (2008). "Strong water absorption in the dayside emission spectrum of the planet HD 189733b". *Nature* 456.7223, p. 767.

Guilluy, G., A. Sozzetti, M. Brogi, A. Bonomo, et al. (2019). "Exoplanet atmospheres with GIANO-II. Detection of molecular absorption in the dayside spectrum of HD 102195b". *Astronomy & Astrophysics* 625, A107.

Guyon, O. (2018). "Imaging with Adaptive Optics and Coronographs for Exoplanet Research". *Handbook of Exoplanets*, pp. 1–20.

Hansen, B. M. (2008). "On the absorption and redistribution of energy in irradiated planets". *The Astrophysical Journal Supplement Series* 179.2, p. 484.

Hargreaves, R. J., P. F. Bernath, J. Bailey, and M. Dulick (2015). "Empirical line lists and absorption cross sections for methane at high temperatures". *The Astrophysical Journal* 813.1, p. 12.

Hawker, G. A., N. Madhusudhan, S. H. Cabot, and S. Gandhi (2018). "Evidence for multiple molecular species in the hot Jupiter HD 209458b". *The Astrophysical Journal Letters* 863.1, p. L11.

Heller, R. (2018). "Formation of hot Jupiters through disk migration and evolving stellar tides". *arXiv preprint arXiv:1806.06601*.

Heng, K., D. M. W. Frierson, and P. J. Phillipps (2011a). "Atmospheric circulation of tidally locked exoplanets: II. Dual-band radiative transfer and

convective adjustment". *Monthly Notices of the Royal Astronomical Society* 418.4, pp. 2669–2696.

Heng, K. and D. Kitzmann (2017). "The theory of transmission spectra revisited: a semi-analytical method for interpreting WFC3 data and an unresolved challenge". *Monthly Notices of the Royal Astronomical Society* 470.3, pp. 2972–2981.

Heng, K., K. Menou, and P. J. Phillipps (2011b). "Atmospheric circulation of tidally locked exoplanets: a suite of benchmark tests for dynamical solvers". *Monthly Notices of the Royal Astronomical Society* 413.4, pp. 2380–2402.

Heng, K., A. Wyttenbach, B. Lavie, D. K. Sing, et al. (2015). "A Non-isothermal Theory for Interpreting Sodium Lines in Transmission Spectra of Exoplanets". *The Astrophysical Journal Letters* 803.1, p. L9.

Henry, G. W., G. W. Marcy, R. P. Butler, and S. S. Vogt (1999). "A transiting "51 Peg-like" planet". *The Astrophysical Journal Letters* 529.1, p. L41.

Hoeijmakers, H. J., D. Ehrenreich, K. Heng, D. Kitzmann, et al. (2018a). "Atomic iron and titanium in the atmosphere of the exoplanet KELT-9b". *Nature* 560.7719, p. 453.

Hoeijmakers, H., R. de Kok, I. Snellen, M. Brogi, et al. (2015). "A search for TiO in the optical high-resolution transmission spectrum of HD 209458b: Hindrance due to inaccuracies in the line database". *Astronomy & Astrophysics* 575, A20.

Hoeijmakers, H., H. Schwarz, I. Snellen, R. de Kok, et al. (2018b). "Medium-resolution integral-field spectroscopy for high-contrast exoplanet imaging-Molecule maps of the β Pictoris system with SINFONI". *Astronomy & Astrophysics* 617, A144.

Hoeijmakers, J. (2017). "Spectroscopic Characterization of Exoplanets: from Loupe to Sinfoni". PhD thesis. Universiteit Leiden.

Hörst, S. M., C. He, N. K. Lewis, E. M.-R. Kempton, et al. (2018). "Haze production rates in super-Earth and mini-Neptune atmosphere experiments". *Nature Astronomy* 2.4, p. 303.

Hu, R., B.-O. Demory, S. Seager, N. Lewis, et al. (2015). "A semi-analytical model of visible-wavelength phase curves of exoplanets and applications to Kepler-7 b and Kepler-10 b". *The Astrophysical Journal* 802.1, p. 51.

Humlíček, J. (1982). "Optimized computation of the Voigt and complex probability functions". *Journal of Quantitative Spectroscopy and Radiative Transfer* 27.4, pp. 437–444.

Jakosky, B. M., D. Brain, M. Chaffin, S. Curry, et al. (2018). "Loss of the Martian atmosphere to space: Present-day loss rates determined from MAVEN observations and integrated loss through time". *Icarus* 315, pp. 146–157.

Jaupart, C. and J.-C. Mareschal (2010). *Heat generation and transport in the Earth*. Cambridge university press.

Kasper, M., J.-L. Beuzit, C. Verinaud, R. G. Gratton, et al. (2010). "EPICS: direct imaging of exoplanets with the E-ELT". *Ground-based and Airborne Instrumentation for Astronomy III*. Vol. 7735. International Society for Optics and Photonics, 77352E.

Kasting, J. F., D. P. Whitmire, and R. T. Reynolds (1993). "Habitable zones around main sequence stars". *Icarus* 101.1, pp. 108–128.

Kataria, T., D. K. Sing, N. K. Lewis, C. Visscher, et al. (2016). "The atmospheric circulation of a nine-hot-jupiter sample: probing circulation and chemistry over a wide phase space". *The Astrophysical Journal* 821.1, p. 9.

Kippenhahn, R., A. Weigert, and A. Weiss (2012). *Stellar structure and evolution*. Springer-Verlag.

Kirchhoff, G. (1860). "Ueber das Verhältniss zwischen dem Emissionsvermögen und dem Absorptionsvermögen der Körper für Wärme und Licht". *Annalen der Physik* 185.2, pp. 275–301.

Knutson, H. A., B. Benneke, D. Deming, and D. Homeier (2014). "A featureless transmission spectrum for the Neptune-mass exoplanet GJ 436b". *Nature* 505.7481, p. 66.

Knutson, H. A., D. Charbonneau, L. E. Allen, J. J. Fortney, et al. (2007a). "A map of the day–night contrast of the extrasolar planet HD 189733b". *Nature* 447.7141, p. 183.

Knutson, H. A., D. Charbonneau, N. B. Cowan, J. J. Fortney, et al. (2008). "Multiwavelength constraints on the day-night circulation patterns of HD 189733b". *The Astrophysical Journal* 690.1, p. 822.

Knutson, H. A., D. Charbonneau, R. W. Noyes, T. M. Brown, et al. (2007b). "Using stellar limb-darkening to refine the properties of HD 209458b". *The Astrophysical Journal* 655.1, p. 564.

Knutson, H. A., N. Lewis, J. J. Fortney, A. Burrows, et al. (2012). "3.6 and 4.5 μm phase curves and evidence for non-equilibrium chemistry in the atmosphere of extrasolar planet HD 189733b". *The Astrophysical Journal* 754.1, p. 22.

Koen, C., D. Kilkenny, F. Van Wyk, and F. Marang (2010). "UBV (RI) C JHK observations of Hipparcos-selected nearby stars". *Monthly Notices of the Royal Astronomical Society* 403.4, pp. 1949–1968.

Kok, R. J. de, M. Brogi, I. A. Snellen, J. Birkby, et al. (2013). "Detection of carbon monoxide in the high-resolution day-side spectrum of the exoplanet HD 189733b". *Astronomy & Astrophysics* 554, A82.

Komacek, T. D. and A. N. Youdin (2017). "Structure and Evolution of Internally Heated Hot Jupiters". *The Astrophysical Journal* 844.2, p. 94.

Krakow, B., H. J. Babrov, G. J. Maclay, and A. L. Shabott (1966). "Use of the Curtis–Godson Approximation in Calculations of Radiant Heating by Inhomogeneous Hot Gases". *Applied optics* 5.11, pp. 1791–1800.

Kreidberg, L. (2017). "Exoplanet atmosphere measurements from transmission spectroscopy and other planet star combined light observations". *Handbook of Exoplanets*, pp. 1–23.

Kreidberg, L., J. L. Bean, J.-M. Désert, B. Benneke, et al. (2014). "Clouds in the atmosphere of the super-Earth exoplanet GJ 1214b". *Nature* 505.7481, p. 69.

Kreidberg, L. and A. Loeb (2016). "Prospects for characterizing the atmosphere of Proxima Centauri b". *The Astrophysical Journal Letters* 832.1, p. L12.

Kulikov, Y. N., H. Lammer, H. Lichtenegger, N. Terada, et al. (2006). "Atmospheric and water loss from early Venus". *Planetary and Space Science* 54.13-14, pp. 1425–1444.

Lammer, H., H. Lichtenegger, H. Biernat, N. Erkaev, et al. (2006). "Loss of hydrogen and oxygen from the upper atmosphere of Venus". *Planetary and Space Science* 54.13-14, pp. 1445–1456.

Lampón, M., M. López-Puertas, M. L. Lara, A. Sánchez-López, et al. (2019). "Modelling the Helium triplet absorption in the atmosphere of the hot-Jupiter HD 209458 b". *to be submitted to Astronomy & Astrophysics*.

Lavvas, P., R. V. Yelle, T. Koskinen, A. Bazin, et al. (2013). "Aerosol growth in Titan's ionosphere". *Proceedings of the National Academy of Sciences* 110.8, pp. 2729–2734.

Liang, M.-C., C. D. Parkinson, A. Y.-T. Lee, Y. L. Yung, et al. (2003). "Source of atomic hydrogen in the atmosphere of HD 209458b". *The Astrophysical Journal Letters* 596.2, p. L247.

Lin, D. N., P. Bodenheimer, and D. C. Richardson (1996). "Orbital migration of the planetary companion of 51 Pegasi to its present location".

Line, M. R., M.-C. Liang, and Y. L. Yung (2010). "High-temperature photochemistry in the atmosphere of HD 189733b". *The Astrophysical Journal* 717.1, p. 496.

Line, M. R., K. B. Stevenson, J. Bean, J.-M. Desert, et al. (2016). "No thermal inversion and a solar water abundance for the hot Jupiter HD 209458b from HST/WFC3 spectroscopy". *The Astronomical Journal* 152.6, p. 203.

Line, M. R., A. S. Wolf, X. Zhang, H. Knutson, et al. (2013). "A systematic retrieval analysis of secondary eclipse spectra. I. A comparison of atmospheric retrieval techniques". *The Astrophysical Journal* 775.2, p. 137.

Linsky, J. L., H. Yang, K. France, C. S. Froning, et al. (2010). "Observations of mass loss from the transiting exoplanet HD 209458b". *The Astrophysical Journal* 717.2, p. 1291.

Lockwood, A. C., J. A. Johnson, C. F. Bender, J. S. Carr, et al. (2014). "Near-IR direct detection of water vapor in Tau Boötis b". *The Astrophysical Journal Letters* 783.2, p. L29.

López-Puertas, M., B. Dinelli, A. Adriani, B. Funke, et al. (2013). "Large abundances of polycyclic aromatic hydrocarbons in Titan's upper atmosphere". *The Astrophysical Journal* 770.2, p. 132.

Lopez-Puertas, M. and F. Taylor (2002). "Non-LTE Radiative Transfer in the Atmosphere".

López-Puertas, M., P. Montañés-Rodríguez, E. Pallé, M. Höpfner, et al. (2018). "Aerosols and Water Ice in Jupiter's Stratosphere from UV-NIR Ground-based Observations". *The Astronomical Journal* 156.4, p. 169.

Louden, T. and P. J. Wheatley (2015). "Spatially resolved eastward winds and rotation of HD 189733b". *The Astrophysical Journal Letters* 814.2, p. L24.

Lovis, C., I. Snellen, D. Mouillet, F. Pepe, et al. (2017). "Atmospheric characterization of Proxima b by coupling the SPHERE high-contrast imager to the ESPRESSO spectrograph". *Astronomy & Astrophysics* 599, A16.

MacDonald, R. J. and N. Madhusudhan (2017). "HD 209458b in new light: evidence of nitrogen chemistry, patchy clouds and sub-solar water". *Monthly Notices of the Royal Astronomical Society* 469.2, pp. 1979–1996.

Madhusudhan, N. and S. Seager (2011). "High metallicity and non-equilibrium chemistry in the dayside atmosphere of hot-Neptune GJ 436b". *The Astrophysical Journal* 729.1, p. 41.

Madhusudhan, N. and S. Seager (2009). "A temperature and abundance retrieval method for exoplanet atmospheres". *The Astrophysical Journal* 707.1, p. 24.

Madhusudhan, N. (2018). "Atmospheric retrieval of exoplanets". *Handbook of Exoplanets*, pp. 1–30.

— (2019). "Exoplanetary Atmospheres: Key Insights, Challenges and Prospects". *arXiv preprint arXiv:1904.03190*.

Madhusudhan, N., M. A. Amin, and G. M. Kennedy (2014a). "Toward chemical constraints on hot Jupiter migration". *The Astrophysical Journal Letters* 794.1, p. L12.

Madhusudhan, N., B. Bitsch, A. Johansen, and L. Eriksson (2017). "Atmospheric signatures of giant exoplanet formation by pebble accretion". *Monthly Notices of the Royal Astronomical Society* 469.4, pp. 4102–4115.

Madhusudhan, N., N. Crouzet, P. R. McCullough, D. Deming, et al. (2014b). "H2O abundances in the atmospheres of three hot Jupiters". *The Astrophysical Journal Letters* 791.1, p. L9.

Madhusudhan, N., J. Harrington, K. B. Stevenson, S. Nymeyer, et al. (2011a). "A high C/O ratio and weak thermal inversion in the atmosphere of exoplanet WASP-12b". *Nature* 469.7328, p. 64.

Madhusudhan, N., O. Mousis, T. V. Johnson, and J. I. Lunine (2011b). "Carbon-rich giant planets: Atmospheric chemistry, thermal inversions, spectra, and formation conditions". *The Astrophysical Journal* 743.2, p. 191.

Marcy, G. W., R. P. Butler, E. Williams, L. Bildsten, et al. (1997). "The planet around 51 Pegasi". *The Astrophysical Journal* 481.2, p. 926.

Marley, M. S., A. S. Ackerman, J. N. Cuzzi, and D. Kitzmann (2013). "Clouds and hazes in exoplanet atmospheres". *Comparative Climatology of Terrestrial Planets* 1, pp. 367–391.

Marois, C., B. Macintosh, T. Barman, B. Zuckerman, et al. (2008). "Direct imaging of multiple planets orbiting the star HR 8799". *Science* 322.5906, pp. 1348–1352.

Marois, C., B. Zuckerman, Q. M. Konopacky, B. Macintosh, et al. (2010). "Images of a fourth planet orbiting HR 8799". *Nature* 468.7327, p. 1080.

Mayor, M., F. Pepe, D. Queloz, F. Bouchy, et al. (2003). "Setting new standards with HARPS". *The Messenger* 114, p. 20.

Mayor, M. and D. Queloz (1995). "A Jupiter-mass companion to a solar-type star". *Nature* 378.6555, p. 355.

Mazeh, T., D. Naef, G. Torres, D. W. Latham, et al. (2000). "The spectroscopic orbit of the planetary companion transiting HD 209458". *The Astrophysical Journal Letters* 532.1, p. L55.

Mazeh, T., O. Tamuz, and S. Zucker (2006). "The sys-rem detrending algorithm: Implementation and testing". *arXiv preprint astro-ph/0612418*.

Mbarek, R. and E. M.-R. Kempton (2016). "Clouds in Super-Earth Atmospheres: Chemical Equilibrium Calculations". *The Astrophysical Journal* 827.2, p. 121.

McBride, B. J. and S. Gordon (1996). "Computer Program for Calculation of Complex Chemical Equilibrium Compositions and Applications II. Users Manual and Program Description. 2; Users Manual and Program Description".

McCullough, P., N. Crouzet, D. Deming, and N. Madhusudhan (2014). "Water vapor in the spectrum of the extrasolar planet HD 189733b. I. The transit". *The Astrophysical Journal* 791.1, p. 55.

Mollière, P., J. Wardenier, R. van Boekel, T. Henning, et al. (2019). "petitRADTRANS: a Python radiative transfer package for exoplanet characterization and retrieval". *Astronomy & Astrophysics* 627, A67.

Mollière, P. M. (2017). "Modeling of Exoplanet Atmospheres". PhD thesis. Max-Planck-Institut für Astronomie.

Mollière, P., R. van Boekel, J. Bouwman, T. Henning, et al. (2017). "Observing transiting planets with JWST-Prime targets and their synthetic spectral observations". *Astronomy & Astrophysics* 600, A10.

Mollière, P., R. van Boekel, C. Dullemond, T. Henning, et al. (2015). "Model atmospheres of irradiated exoplanets: The influence of stellar parameters, metallicity, and the C/O ratio". *The Astrophysical Journal* 813.1, p. 47.

Montañés-Rodríguez, P., B. González-Merino, E. Pallé, M. López-Puertas, et al. (2015). "Jupiter as an exoplanet: UV to NIR transmission spectrum reveals hazes, a Na layer, and possibly stratospheric H2O-ice clouds". *The Astrophysical Journal Letters* 801.1, p. L8.

Morley, C. V., J. J. Fortney, E. M.-R. Kempton, M. S. Marley, et al. (2013). "Quantitatively assessing the role of clouds in the transmission spectrum of GJ 1214b". *The Astrophysical Journal* 775.1, p. 33.

Moses, J., N. Madhusudhan, C. Visscher, and R. Freedman (2012). "Chemical consequences of the C/O ratio on hot Jupiters: examples from WASP-12b, CoRoT-2b, XO-1b, and HD 189733b". *The Astrophysical Journal* 763.1, p. 25.

Moses, J. I., C. Visscher, J. J. Fortney, A. P. Showman, et al. (2011). "Disequilibrium carbon, oxygen, and nitrogen chemistry in the atmospheres of HD 189733b and HD 209458b". *The Astrophysical Journal* 737.1, p. 15.

Moutou, C., J.-F. Donati, R. Savalle, G. Hussain, et al. (2007). "Spectropolarimetric observations of the transiting planetary system of the K dwarf HD 189733". *Astronomy & Astrophysics* 473.2, pp. 651–660.

Muñoz, A. G. (2007). "Physical and chemical aeronomy of HD 209458b". *Planetary and Space Science* 55.10, pp. 1426–1455.

— (2018). "On Mapping Exoplanet Atmospheres with High-dispersion Spectropolarimetry: Some Model Predictions". *The Astrophysical Journal* 854.2, p. 108.

Muñoz, A. G. and K. G. Isaak (2015). "Probing exoplanet clouds with optical phase curves". *Proceedings of the National Academy of Sciences* 112.44, pp. 13461–13466.

Nagel, E., S. Czesla, A. Kaminski, et al. (2019). "The CARMENES search for exoplanets around M dwarfs. Telluric absorption correction in high-resolution optical and near infrared CARMENES spectra". *to be submitted to Astronomy & Astrophysics*.

Noecker, M. C., F. Zhao, R. Demers, J. Trauger, et al. (2016). "Coronagraph instrument for WFIRST-AFTA". *Journal of Astronomical Telescopes, Instruments, and Systems* 2.1, p. 011001.

Nortmann, L., E. Pallé, M. Salz, J. Sanz-Forcada, et al. (2018). "Ground-based detection of an extended helium atmosphere in the Saturn-mass exoplanet WASP-69b". *Science* 362.6421, pp. 1388–1391.

Nugroho, S. K., H. Kawahara, K. Masuda, T. Hirano, et al. (2017). "High-resolution Spectroscopic Detection of TiO and a Stratosphere in the Day-side of WASP-33b". *The Astronomical Journal* 154.6, p. 221.

Öberg, K. I., R. Murray-Clay, and E. A. Bergin (2011). "The effects of snowlines on C/O in planetary atmospheres". *The Astrophysical Journal Letters* 743.1, p. L16.

Odunlade, A. and A. E. Pauline (2010). "Transiting exoplanets: characterisation in the presence of stellar activity".

Oklopčić, A. and C. M. Hirata (2018). "A new window into escaping exoplanet atmospheres: 10830 Å line of helium". *The Astrophysical Journal Letters* 855.1, p. L11.

Owen, J. E. (2019). "Atmospheric Escape and the Evolution of Close-In Exoplanets". *Annual Review of Earth and Planetary Sciences* 47, pp. 67–90.

Pallé, E., M. Z. Osorio, and A. G. Muñoz (2011). "Characterizing the atmospheres of transiting rocky planets around late-type dwarfs". *The Astrophysical Journal* 728.1, p. 19.

Parmentier, V., A. P. Showman, and Y. Lian (2013). "3D mixing in hot Jupiters atmospheres-I. Application to the day/night cold trap in HD 209458b". *Astronomy & Astrophysics* 558, A91.

Pasquini, L., G. Avila, H. Dekker, B. Delabre, et al. (2008). "CODEX: the high-resolution visual spectrograph for the E-ELT". *Ground-Based and Airborne Instrumentation for Astronomy II*. Vol. 7014. International Society for Optics and Photonics, p. 70141I.

Pepe, F., P. Molaro, S. Cristiani, R. Rebolo, et al. (2014). "ESPRESSO: The next European exoplanet hunter". *Astronomische Nachrichten* 335.1, pp. 8–20.

Pepe, F. and C. Lovis (2008). "From HARPS to CODEX: exploring the limits of Doppler measurements". *Physica Scripta* 2008.T130, p. 014007.

Pepe, F. A., S. Cristiani, R. R. Lopez, N. C. Santos, et al. (2010). "ESPRESSO: the Echelle spectrograph for rocky exoplanets and stable spectroscopic observations". *Ground-based and Airborne Instrumentation for Astronomy III*. Vol. 7735. International Society for Optics and Photonics, 77350F.

Pino, L., D. Ehrenreich, R. Allart, C. Lovis, et al. (2018a). "Diagnosing aerosols in extrasolar giant planets with cross-correlation function of water bands". *Astronomy & Astrophysics* 619, A3.

Pino, L., D. Ehrenreich, A. Wyttenbach, V. Bourrier, et al. (2018b). "Combining low-to high-resolution transit spectroscopy of HD 189733b-Linking the troposphere and the thermosphere of a hot gas giant". *Astronomy & Astrophysics* 612, A53.

Piskorz, D., B. Benneke, N. R. Crockett, A. C. Lockwood, et al. (2016). "Evidence for the Direct Detection of the Thermal Spectrum of the Non-Transiting Hot Gas Giant HD 88133 b". *The Astrophysical Journal* 832.2, p. 131.

Piskorz, D., B. Benneke, N. R. Crockett, A. C. Lockwood, et al. (2017). "Detection of Water Vapor in the Thermal Spectrum of the Non-transiting Hot Jupiter Upsilon Andromedae b". *The Astronomical Journal* 154.2, p. 78.

Piskorz, D., C. Buzard, M. R. Line, H. A. Knutson, et al. (2018). "Ground-and Space-based Detection of the Thermal Emission Spectrum of the Transiting Hot Jupiter KELT-2Ab". *The Astronomical Journal* 156.3, p. 133.

Planck, M. (1901). "On the law of distribution of energy in the normal spectrum". *Annalen der physik* 4.553, p. 1.

Pont, F., H. Knutson, R. Gilliland, C. Moutou, et al. (2008). "Detection of atmospheric haze on an extrasolar planet: the 0.55–1.05 μm transmission

spectrum of HD 189733b with the Hubble Space Telescope". *Monthly Notices of the Royal Astronomical Society* 385.1, pp. 109–118.

Pont, F., D. K. Sing, N. Gibson, S. Aigrain, et al. (2013). "The prevalence of dust on the exoplanet HD 189733b from Hubble and Spitzer observations". *Monthly Notices of the Royal Astronomical Society* 432.4, pp. 2917–2944.

Quirrenbach, A., P. Amado, J. Caballero, R. Mundt, et al. (2016). "CARMENES: an overview six months after first light". *Ground-based and Airborne Instrumentation for Astronomy VI*. Vol. 9908. International Society for Optics and Photonics, p. 990812.

Quirrenbach, A., P. Amado, I. Ribas, A. Reiners, et al. (2018). "CARMENES: high-resolution spectra and precise radial velocities in the red and infrared". *Ground-based and Airborne Instrumentation for Astronomy VII*. Vol. 10702. International Society for Optics and Photonics, 107020W.

Rameau, J., G. Chauvin, A.-M. Lagrange, A. Boccaletti, et al. (2013a). "Discovery of a probable 4-5 Jupiter-mass exoplanet to HD 95086 by direct imaging". *The Astrophysical Journal Letters* 772.2, p. L15.

Rameau, J., G. Chauvin, A.-M. Lagrange, T. Meshkat, et al. (2013b). "Confirmation of the Planet around HD 95086 by Direct Imaging". *The Astrophysical Journal Letters* 779.2, p. L26.

Rasio, F., C. Tout, S. Lubow, and M. Livio (1996). "Tidal decay of close planetary orbits". *arXiv preprint astro-ph/9605059*.

Rauer, H., S. Gebauer, P. v. Paris, J. Cabrera, et al. (2011). "Potential biosignatures in super-Earth atmospheres-I. Spectral appearance of super-Earths around M dwarfs". *Astronomy & Astrophysics* 529, A8.

Rauscher, E. (2017). "Models of Warm Jupiter Atmospheres: Observable Signatures of Obliquity". *The Astrophysical Journal* 846.1, p. 69.

Rauscher, E. and K. Menou (2012). "A general circulation model for gaseous exoplanets with double-gray radiative transfer". *The Astrophysical Journal* 750.2, p. 96.

— (2013). "Three-dimensional atmospheric circulation models of HD 189733b and HD 209458b with consistent magnetic drag and ohmic dissipation". *The Astrophysical Journal* 764.1, p. 103.

Redfield, S., M. Endl, W. D. Cochran, and L. Koesterke (2008). "Sodium absorption from the exoplanetary atmosphere of HD 189733b detected in the optical transmission spectrum". *The Astrophysical Journal Letters* 673.1, p. L87.

Reiners, A., I. Ribas, M. Zechmeister, J. Caballero, et al. (2018a). "The CARMENES search for exoplanets around M dwarfs-HD147379 b: A nearby Neptune in the temperate zone of an early-M dwarf". *Astronomy & Astrophysics* 609, p. L5.

Reiners, A., M. Zechmeister, J. Caballero, I. Ribas, et al. (2018b). "The CARMENES search for exoplanets around M dwarfs-High-resolution optical and near-

infrared spectroscopy of 324 survey stars". *Astronomy & Astrophysics* 612, A49.

Ribas, I., M. Tuomi, A. Reiners, R. Butler, et al. (2018). "A candidate super-Earth planet orbiting near the snow line of Barnard's star". *Nature* 563.7731, p. 365.

Robinson, T. D., V. S. Meadows, D. Crisp, D. Deming, et al. (2011). "Earth as an extrasolar planet: Earth model validation using EPOXI Earth observations". *Astrobiology* 11.5, pp. 393–408.

Roche, D. P. dit de la, H. Hoeijmakers, and I. Snellen (2018). "Molecule mapping of HR8799b using OSIRIS on Keck-Strong detection of water and carbon monoxide, but no methane". *Astronomy & Astrophysics* 616, A146.

Rothman, L., I. Gordon, R. Barber, H. Dothe, et al. (2010). "HITEMP, the high-temperature molecular spectroscopic database". *Journal of Quantitative Spectroscopy and Radiative Transfer* 111.15, pp. 2139–2150.

Ruiz, J. (2014). "The early heat loss evolution of Mars and their implications for internal and environmental history". *Scientific reports* 4, p. 4338.

Sagan, C., A. Druyan, S. Soter, A. Malone, et al. (1980). "Cosmos: A personal voyage [Television series]". *Arlington, VA: Public Broadcasting Service*.

Sagan, C. (1997). *Pale blue dot: A vision of the human future in space*. Random House Digital, Inc.

Sagan, C. and F. Drake (1975). "The search for extraterrestrial intelligence". *Scientific American* 232.5, pp. 80–89.

Salz, M., S. Czesla, P. Schneider, E. Nagel, et al. (2018). "Detection of He I λ10830 Å absorption on HD 189733 b with CARMENES high-resolution transmission spectroscopy". *Astronomy & Astrophysics* 620, A97.

Sánchez López, A., F. J. Alonso Floriano, I. Snellen, M. López Puertas, et al. (2018). "Water detection in the near infrared in HD 189733 b with CARMENES". *European Planetary Science Congress*. Vol. 12.

Sánchez-López, A., F. Alonso-Floriano, M. López-Puertas, I. A. G. Snellen, et al. (2019). "Water vapor detection in the transmission spectra of HD 209458 b with the CARMENES NIR channel". *Astronomy & Astrophysics* 630, A53.

Sánchez-López, A., M. López-Puertas, et al. (2019). "Detection of water vapor at optical wavelengths in the transmission spectra of CARMENES". *in preparation*.

Sánchez-López, A., M. López-Puertas, B. Funke, P. Amado, et al. (2017). "Simulations of transit spectra of Hot Jupiters in the wavelength range of the CARMENES infrared channel (0.96-1.7 μm)". *Differences* 5, pp. 10–5.

Scheucher, M., J. Grenfell, F. Wunderlich, M. Godolt, et al. (2018). "New Insights into Cosmic-Ray-induced Biosignature Chemistry in Earth-like Atmospheres". *The Astrophysical Journal* 863.1, p. 6.

Schreier, F., S. G. García, P. Hedelt, M. Hess, et al. (2014). "GARLIC—A general purpose atmospheric radiative transfer line-by-line infrared-microwave

code: Implementation and evaluation". *Journal of Quantitative Spectroscopy and Radiative Transfer* 137, pp. 29–50.

Schwarz, H., M. Brogi, R. de Kok, J. Birkby, et al. (2015). "Evidence against a strong thermal inversion in HD 209458b from high-dispersion spectroscopy". *Astronomy & Astrophysics* 576, A111.

Schwarz, H., C. Ginski, R. J. de Kok, I. A. Snellen, et al. (2016). "The slow spin of the young substellar companion GQ Lupi b and its orbital configuration". *Astronomy & Astrophysics* 593, A74.

Seager, S. (2014). "The future of spectroscopic life detection on exoplanets". *Proceedings of the National Academy of Sciences* 111.35, pp. 12634–12640.

Seager, S., W. Bains, and J. Petkowski (2016). "Toward a list of molecules as potential biosignature gases for the search for life on exoplanets and applications to terrestrial biochemistry". *Astrobiology* 16.6, pp. 465–485.

Seager, S. and D. D. Sasselov (2000). "Theoretical transmission spectra during extrasolar giant planet transits". *The Astrophysical Journal* 537.2, p. 916.

Seifert, W., M. S. Carrasco, W. Xu, M. Cárdenas, et al. (2012). "CARMENES. II: optical and opto-mechanical design". *Ground-based and airborne instrumentation for astronomy IV*. Vol. 8446. International Society for Optics and Photonics, p. 844633.

Showman, A. P., J. J. Fortney, N. K. Lewis, and M. Shabram (2013). "Doppler signatures of the atmospheric circulation on hot jupiters". *The Astrophysical Journal* 762.1, p. 24.

Showman, A. P. and L. M. Polvani (2011). "Equatorial superrotation on tidally locked exoplanets". *The Astrophysical Journal* 738.1, p. 71.

Sing, D. K. (2018). "Observational Techniques With Transiting Exoplanetary Atmospheres". *Astrophysics of Exoplanetary Atmospheres*. Springer, pp. 3–48.

Sing, D. K., J. J. Fortney, N. Nikolov, H. R. Wakeford, et al. (2016). "A continuum from clear to cloudy hot-Jupiter exoplanets without primordial water depletion". *Nature* 529.7584, p. 59.

Sing, D. K., F. Pont, S. Aigrain, D. Charbonneau, et al. (2011). "Hubble Space Telescope transmission spectroscopy of the exoplanet HD 189733b: high-altitude atmospheric haze in the optical and near-ultraviolet with STIS". *Monthly Notices of the Royal Astronomical Society* 416.2, pp. 1443–1455.

Sing, D. K., H. Wakeford, A. Showman, N. Nikolov, et al. (2014). "HST hot-Jupiter transmission spectral survey: detection of potassium in WASP-31b along with a cloud deck and Rayleigh scattering". *Monthly Notices of the Royal Astronomical Society* 446.3, pp. 2428–2443.

Skrutskie, M., R. Cutri, R. Stiening, M. Weinberg, et al. (2006). "The two micron all sky survey (2MASS)". *The Astronomical Journal* 131.2, p. 1163.

Smette, A., H. Sana, S. Noll, H. Horst, et al. (2015). "Molecfit: A general tool for telluric absorption correction-I. Method and application to ESO instruments". *Astronomy & Astrophysics* 576, A77.

Snellen, I. A. G. (2013). *Probing exoplanet atmospheres at high spectral dispersion with METIS and HIRES.* Talk notes. ESO2013, Leiden Observatory.

Snellen, I., S. Albrecht, E. de Mooij, and R. Le Poole (2008). "Ground-based detection of sodium in the transmission spectrum of exoplanet HD 209458b". *Astronomy & Astrophysics* 487.1, pp. 357–362.

Snellen, I., J.-M. Désert, L. Waters, T. Robinson, et al. (2017). "Detecting Proxima b's Atmosphere with JWST Targeting CO2 at 15 μm Using a High-pass Spectral Filtering Technique". *The Astronomical Journal* 154.2, p. 77.

Snellen, I. A., B. R. Brandl, R. J. de Kok, M. Brogi, et al. (2014). "Fast spin of the young extrasolar planet β Pictoris b". *Nature* 509.7498, p. 63.

Snellen, I. A., R. J. De Kok, E. J. De Mooij, and S. Albrecht (2010). "The orbital motion, absolute mass and high-altitude winds of exoplanet HD 209458b". *Nature* 465.7301, p. 1049.

Snellen, I., R. de Kok, J. Birkby, B. Brandl, et al. (2015). "Combining high-dispersion spectroscopy with high contrast imaging: Probing rocky planets around our nearest neighbors". *Astronomy & Astrophysics* 576, A59.

Spake, J., D. Sing, T. Evans, A. Oklopčić, et al. (2018). "Helium in the eroding atmosphere of an exoplanet". *Nature* 557.7703, p. 68.

Steffen, J. H., D. C. Fabrycky, E. Agol, E. B. Ford, et al. (2012). "Transit timing observations from Kepler–VII. Confirmation of 27 planets in 13 multiplanet systems via transit timing variations and orbital stability". *Monthly Notices of the Royal Astronomical Society* 428.2, pp. 1077–1087.

Stevenson, K. B. (2016). "Quantifying and predicting the presence of clouds in exoplanet atmospheres". *The Astrophysical Journal Letters* 817.2, p. L16.

Stevenson, K. B., J.-M. Désert, M. R. Line, J. L. Bean, et al. (2014). "Thermal structure of an exoplanet atmosphere from phase-resolved emission spectroscopy". *Science* 346.6211, pp. 838–841.

Stiller, G. P., T. von Clarmann, B. Funke, N. Glatthor, et al. (2002). "Sensitivity of trace gas abundances retrievals from infrared limb emission spectra to simplifying approximations in radiative transfer modelling". *Journal of Quantitative Spectroscopy and Radiative Transfer* 72.3, pp. 249–280.

Stiller, G. P., M. Hoepfner, M. Kuntz, T. von Clarmann, et al. (1998). "Karlsruhe optimized and precise radiative transfer algorithm. Part I: requirements, justification, and model error estimation". *Optical Remote Sensing of the Atmosphere and Clouds.* Vol. 3501. International Society for Optics and Photonics, pp. 257–269.

Stürmer, J., O. Stahl, C. Schwab, W. Seifert, et al. (2014). "CARMENES in SPIE 2014. Building a fibre link for CARMENES". *Advances in optical and*

mechanical technologies for telescopes and instrumentation. Vol. 9151. International Society for Optics and Photonics, p. 915152.

Swain, M. R., P. Deroo, C. A. Griffith, G. Tinetti, et al. (2010). "A ground-based near-infrared emission spectrum of the exoplanet HD 189733b". *Nature* 463.7281, p. 637.

Swain, M., G. Vasisht, G. Tinetti, J. Bouwman, et al. (2008). "Molecular signatures in the near-infrared dayside spectrum of HD 189733b". *The Astrophysical Journal Letters* 690.2, p. L114.

Tamuz, O., T. Mazeh, and S. Zucker (2005). "Correcting systematic effects in a large set of photometric light curves". *Monthly Notices of the Royal Astronomical Society* 356.4, pp. 1466–1470.

Tarnas, J. D. (2016). "Transit, Secondary Eclipse, and Phase Curve Analysis to Characterize Kepler Exoplanets".

Tennyson, J., S. N. Yurchenko, A. F. Al-Refaie, E. J. Barton, et al. (2016). "The ExoMol database: molecular line lists for exoplanet and other hot atmospheres". *Journal of Molecular Spectroscopy* 327, pp. 73–94.

Tinetti, G., P. Drossart, P. Eccleston, P. Hartogh, et al. (2018). "A chemical survey of exoplanets with ARIEL". *Experimental Astronomy* 46.1, pp. 135–209.

Tinetti, G., A. Vidal-Madjar, M.-C. Liang, J.-P. Beaulieu, et al. (2007). "Water vapour in the atmosphere of a transiting extrasolar planet". *Nature* 448.7150, p. 169.

Todorov, K. O., D. Deming, A. Burrows, and C. J. Grillmair (2014). "Updated Spitzer emission spectroscopy of bright transiting hot Jupiter HD 189733b". *The Astrophysical Journal* 796.2, p. 100.

Torres, G., J. N. Winn, and M. J. Holman (2008). "Improved parameters for extrasolar transiting planets". *The Astrophysical Journal* 677.2, p. 1324.

Tremblin, P., D. S. Amundsen, P. Mourier, I. Baraffe, et al. (2015). "Fingering convection and cloudless models for cool brown dwarf atmospheres". *The Astrophysical Journal Letters* 804.1, p. L17.

Triaud, A. H., D. Queloz, F. Bouchy, C. Moutou, et al. (2009). "The Rossiter-McLaughlin effect of CoRoT-3b and HD 189733b". *Astronomy & Astrophysics* 506.1, pp. 377–384.

Trifonov, T., M. Kürster, M. Zechmeister, L. Tal-Or, et al. (2018). "The CARMENES search for exoplanets around M dwarfs-First visual-channel radial-velocity measurements and orbital parameter updates of seven M-dwarf planetary systems". *Astronomy & Astrophysics* 609, A117.

Tsiaras, A., M. Rocchetto, I. Waldmann, O. Venot, et al. (2016). "Detection of an atmosphere around the super-Earth 55 Cancri e". *The Astrophysical Journal* 820.2, p. 99.

Turbet, M., J. Leconte, F. Selsis, E. Bolmont, et al. (2016). "The habitability of Proxima Centauri b-II. Possible climates and observability". *Astronomy & Astrophysics* 596, A112.

Turnbull, M. C., W. A. Traub, K. W. Jucks, N. J. Woolf, et al. (2006). "Spectrum of a habitable world: Earthshine in the near-infrared". *The Astrophysical Journal* 644.1, p. 551.

Ulmer-Moll, S., P. Figueira, J. Neal, N. Santos, et al. (2019). "Telluric correction in the near-infrared: Standard star or synthetic transmission?" *Astronomy & Astrophysics* 621, A79.

Venot, O., B. Drummond, Y. Miguel, I. P. Waldmann, et al. (2018). "A better characterization of the chemical composition of exoplanets atmospheres with ARIEL". *Experimental Astronomy* 46.1, pp. 101–134.

Venot, O., E. Hébrard, M. Agúndez, L. Decin, et al. (2015). "New chemical scheme for studying carbon-rich exoplanet atmospheres". *Astronomy & Astrophysics* 577, A33.

Venot, O., E. Hébrard, M. Agúndez, M. Dobrijevic, et al. (2012). "A chemical model for the atmosphere of hot Jupiters". *Astronomy & Astrophysics* 546, A43.

Vidal-Madjar, A., A. L. Des Etangs, J.-M. Désert, G. Ballester, et al. (2003). "An extended upper atmosphere around the extrasolar planet HD209458b". *Nature* 422.6928, p. 143.

Vidal-Madjar, A., J.-M. Désert, A. L. Des Etangs, G. Hébrard, et al. (2004). "Detection of oxygen and carbon in the hydrodynamically escaping atmosphere of the extrasolar planet HD 209458b". *The Astrophysical Journal Letters* 604.1, p. L69.

Visscher, C. and J. I. Moses (2011). "Quenching of carbon monoxide and methane in the atmospheres of cool brown dwarfs and hot Jupiters". *The Astrophysical Journal* 738.1, p. 72.

Von Clarmann, T., A. Dudhia, D. Edwards, B. Funke, et al. (2002). "Intercomparison of radiative transfer codes under non-local thermodynamic equilibrium conditions". *Journal of Geophysical Research: Atmospheres* 107.D22, ACH–12.

Walker, J. C. (1978). "The early history of oxygen and ozone in the atmosphere". *Pure and applied geophysics* 117.3, pp. 498–512.

Wang, L. V. and H.-i. Wu (2012). *Biomedical optics: principles and imaging*. John Wiley & Sons.

Welch, B. L. (1947). "The generalization ofstudent's' problem when several different population variances are involved". *Biometrika* 34.1/2, pp. 28–35.

Winn, J. N. (2010). "Exoplanet transits and occultations". *Exoplanets* 1, pp. 55–77.

Wit, J. de and S. Seager (2013). "Constraining exoplanet mass from transmission spectroscopy". *Science* 342.6165, pp. 1473–1477.

Wit, J. de, H. R. Wakeford, M. Gillon, N. K. Lewis, et al. (2016). "A combined transmission spectrum of the Earth-sized exoplanets TRAPPIST-1 b and c". *Nature* 537.7618, p. 69.

Wolszczan, A. and D. A. Frail (1992). "A planetary system around the millisecond pulsar PSR1257+ 12". *Nature* 355.6356, p. 145.

Wolszczan, A. (1994). "Confirmation of Earth-mass planets orbiting the millisecond pulsar PSR B1257+ 12". *Science* 264.5158, pp. 538–542.

Wright, J. T. and B. S. Gaudi (2013). "Exoplanet detection methods". *Planets, Stars and Stellar Systems: Volume 3: Solar and Stellar Planetary Systems*, pp. 489–540.

Wright, J. T. (2017). "Radial Velocities as an Exoplanet Discovery Method". *Handbook of Exoplanets*, pp. 1–13.

Wyttenbach, A., D. Ehrenreich, C. Lovis, S. Udry, et al. (2015). "Spectrally resolved detection of sodium in the atmosphere of HD 189733b with the HARPS spectrograph". *Astronomy & Astrophysics* 577, A62.

Yan, F. and T. Henning (2018). "An extended hydrogen envelope of the extremely hot giant exoplanet KELT-9b". *Nature Astronomy* 2.9, p. 714.

Zahnle, K., M. Marley, and J. Fortney (2009a). "Thermometric soots on warm Jupiters?" *arXiv preprint arXiv:0911.0728*.

Zahnle, K., M. Marley, R. S. Freedman, K. Lodders, et al. (2009b). "Atmospheric sulfur photochemistry on hot Jupiters". *The Astrophysical Journal Letters* 701.1, p. L20.

Zechmeister, M., G. Anglada-Escudé, and A. Reiners (2014). "Flat-relative optimal extraction-A quick and efficient algorithm for stabilised spectrographs". *Astronomy & Astrophysics* 561, A59.

Zechmeister, M., M. Dreizler, I. Ribas, A. Reiners, et al. (2019a). "VizieR Online Data Catalog: Teegarden's Star RV and Halpha curves (Zechmeister+, 2019)". *VizieR Online Data Catalog* 362.

Zechmeister, M., S. Dreizler, I. Ribas, A. Reiners, et al. (2019b). "The CARMENES search for exoplanets around M dwarfs. Two temperate Earth-mass planet candidates around Teegarden's Star". *arXiv preprint arXiv:1906.07196*.

Zhang, J., E. M.-R. Kempton, and E. Rauscher (2017). "Constraining hot Jupiter atmospheric structure and dynamics through doppler-shifted emission spectra". *The Astrophysical Journal* 851.2, p. 84.

Appendix A

The Sysrem algorithm

A.1 Introduction

In this appendix, we will outline the origin and main features of the Sysrem algorithm (Tamuz et al., 2005; Mazeh et al., 2006), used within the frame of this thesis to fit and remove common modes in the ground-based high-resolution data. By means of iterating the fit and removal procedure, we eliminate the telluric and stellar contributions from the recorded spectra, leaving the information from the exo-atmospheres buried below the noise-level.

Sysrem was originally developed with the aim of removing atmospheric extinction effects in the light curves of photometric surveys. Later, in Tamuz et al. (2005), it was adapted for the fitting and removal of linear approximations to systematic effects affecting all light curves in a photometric survey (e.g., changes in the observing conditions due to changes in the Earth's atmosphere, changes in the instrument's point spread function, etc.).

The algorithm is particularly useful for this task, since it allows each frame within each light curve to participate in the fitted trends with a different amplitude. That is, each pixel can be weighted by its uncertainty[1]. Interestingly, these features are also of great help for the telluric removal procedure within high dispersion spectroscopy due to the unequal performance of the pixels across a detector, the different strength of the Earth tellurics and the stellar absorptions at different wavelength bins, etc. Thus, it has been used widely in the past (Birkby et al., 2013; Nugroho et al., 2017; Cabot et al., 2018; Hawker et al., 2018; Alonso-Floriano et al., 2019a; Sánchez-López et al., 2019).

[1]In the case of all pixels having the same uncertainty, Sysrem works as a principal component analysis algorithm.

A.2 The iterating scheme

We will describe how this algorthm works by following, mainly, the concise discussion by Nugroho et al. (2017). Let us assume the following scenario: during our observations of, for instance, an exoplanet transiting its host star, we record N spectra in a certain wavelength interval. SYSREM treats the flux received at each pixel λ_i (i.e., wavelength bin) during the N exposures as a light curve. The algorithm's aim is to determine the airmass a_j and the effective extinction coefficient c_i that best describe the atmospheric absorption r_{ij} at each exposure ($j = 0$, ..., N) and pixel (i).

Although this algorithm requires no prior knowledge of the systematics, the observed airmass a is used as an input to initialize the run. With the input airmass, the set of extinction coefficients is calculated as:

$$c_i = \frac{\sum_j \left(r_{ij} a_j / \sigma_{ij}^2\right)}{\sum_j \left(a_j^2 / \sigma_{ij}^2\right)}, \tag{A.1}$$

where σ_{ij} is the uncertainty of the pixel i in the exposure j. In the case of CARMENES, this includes the photon noise and the read our noise of the detector (see Chapter 3). By using the newly obtained c_i, we can now re-calculate an optimal airmass as follows:

$$a_j = \frac{\sum_i \left(r_{ij} c_i / \sigma_{ij}^2\right)}{\sum_i \left(c_i^2 / \sigma_{ij}^2\right)}. \tag{A.2}$$

Our objective is to describe r_{ij} with the product $a_i c_j$ and hence, we aim at minimizing

$$R_i^2 = \sum_j \frac{\left(r_{ij} - c_i a_j\right)^2}{\sigma_{ij}^2}. \tag{A.3}$$

Thereby, after evaluating R_i, we can use the optimized airmass a_i tom obtain a new set of c_j and, in turn, a new a_i so as to re-evaluate R_i and compare it with the previous one until a converge criterion is satisfied. Once R_i^2 is minimized, $c_i a_j$ is subtracted from the data and thus, the first SYSREM iteration is finished:

$$r_{ij}^{1_{st}} = r_{ij} - c_i a_j. \tag{A.4}$$

By iterating SYSREM up to 15 times (see Chapters 4 and 5), we obtain $r_{ij}^{1_{st}}$, ..., $r_{ij}^{15_{th}}$, where up to the fifteenth systematic effect (i.e., common mode) has been subtracted from the data. As discussed in this thesis, we can now search for the optimal iteration at each wavelength interval so as to maximize the possibility of finding a signal from an exoplanetary origin in our dataset.

By inspecting Eq. A.4, one can see that the effective extinction coefficient is in fact the slope of the best linear fit to r_{ij} (a_j). That is, SYSREM only approximates these atmospheric quantities linearly. Therefore, this is likely the main reason behind the presence of residuals in the data after each iteration. In particular, these are strong in the case of rapidly changing atmospheric conditions, especially in the strongest absorption lines covered (see Chapter 5).